

ASSESSMENT OF DIFFERENT RAINFALL PRODUCTS
IN FLOOD SIMULATIONS

A THESIS SUBMITTED TO
THE GRADUATE SCHOOL OF NATURAL AND APPLIED SCIENCES
OF
MIDDLE EAST TECHNICAL UNIVERSITY

BY

ARZU ÖZKAYA

IN PARTIAL FULFILLMENT OF THE REQUIREMENTS
FOR
THE DEGREE OF DOCTOR OF PHILOSOPHY
IN
CIVIL ENGINEERING

JUNE 2017

Approval of the thesis:

**ASSESSMENT OF DIFFERENT RAINFALL PRODUCTS
IN FLOOD SIMULATIONS**

submitted by **ARZU ÖZKAYA** in partial fulfillment of the requirements for the degree of **Doctor of Philosophy in Civil Engineering Department, Middle East Technical University** by,

Prof. Dr. Gülbin Dural Ünver
Dean, Graduate School of **Natural and Applied Sciences** _____

Prof. Dr. İsmail Özgür Yaman
Head of Department, **Civil Engineering** _____

Prof. Dr. Zuhâl Akyürek
Supervisor, **Civil Engineering Dept., METU** _____

Examining Committee Members:

Assoc. Prof. Dr. İsmail Yücel
Civil Engineering Dept., METU _____

Prof. Dr. Zuhâl Akyürek
Civil Engineering Dept., METU _____

Assoc. Prof. Dr. Koray K. Yılmaz
Geological Engineering Dept., METU _____

Assoc. Prof. Dr. Ahmet Emre Tekeli
Civil Engineering Dept., Çankırı Karatekin University _____

Assist. Prof. Dr. Ahmet Öztopal
Meteorological Engineering Dept., Istanbul Technical University _____

Date: June 09, 2017

I hereby declare that all information in this document has been obtained and presented in accordance with academic rules and ethical conduct. I also declare that, as required by these rules and conduct, I have fully cited and referenced all material and results that are not original to this work.

Name, Last Name : Arzu Özkaya

Signature :

ABSTRACT

ASSESSMENT OF DIFFERENT RAINFALL PRODUCTS IN FLOOD SIMULATIONS

Özkaya, Arzu

Ph.D., Department of Civil Engineering
Supervisor: Prof. Dr. Zuhâl Akyürek

June 2017, 180 pages

Floods happening due to heavy rainfall are one of the most widespread natural hazards. To predict such events, accurate rainfall products and well calibrated hydrologic models are essential especially in urban settlements for life savings. With the objective of assessing the rain detection potential of rainfall data products, several hourly rainfall datasets are used as forcing inputs in two hydrologic models. Physic-based distributed model, WRF-Hydro, and conceptual based lumped model, HEC-HMS, are used to simulate the three catastrophic flood events those occurred in Terme Basin in Samsun. For the calibration of both models, gauge data belonging to 22nd November 2014 flood event are used. Furthermore, stream network density effect in rainfall-runoff modeling is investigated in WRF-Hydro model. In model evaluations, two different flood events with different rainfall datasets are used. The datasets contain weather radar data and satellite rainfall estimates from Hydro-Estimator (HE) as nowcasting products; Weather Research and Forecasting Model (WRF) precipitation data as a forecasting product and gauge-based data. Among these datasets bias correction is applied to the weather radar data by using Kalman Filtering and their use in flood modeling is also evaluated in the simulations. Results show that all products have different limitations

and potentials depending on the rainfall type. Among them, the HE product generally indicates poor performance in the simulations in this basin. Whereas, gauge data located in close proximity to the study area is good at representing the flood peak occurrence time but has a weakness in the flood magnitude estimation. WRF precipitation data are superior in detecting the rain with some time inaccuracy but as a forecasted product it can be useful as an early warning system to take initial precautions. Bias corrected radar data using the gauging stations in close proximity to the studied one has an affirmative effect on results especially in frontal rainfall type. Results of the models show that both models are generally close to each other in representing hydrograph shape and peak time. The average value of correlation (r) and root mean square error (RMSE) for all events and rainfall products indicate that WRF Hydro (0.61 for r , 62.6 m^3/s for RMSE) showed a slightly better success compared to the HEC HMS (0.59 for r , 67.6 m^3/s for RMSE). However, one of the flood event that has mainly convective origin makes the difference between the models. In this event, WRF-Hydro model presents the physical-based model's ability in showing hydrograph peak discharge and time to peak accurately. The overall results indicate that the use of well calibrated hydrologic model with rainfall data that compound of calibrated radar, WRF precipitation forecast and observations in ungauged or poorly gauged areas can help to take necessary precautions against flooding and provide benefit in saving life and property.

Keywords: WRF-Hydro, HEC-HMS, bias correction, Kalman Filter, satellite based rainfall

ÖZ

FARKLI YAĞIŞ ÜRÜNLERİNİN TAŞKIN SİMÜLASYONLARINDA DEĞERLENDİRİLMESİ

Özkaya, Arzu

Doktora, İnşaat Mühendisliği Bölümü
Tez Yöneticisi: Prof. Dr. Zuhal Akyürek

Haziran 2017, 180 sayfa

Şiddetli yağışların neden olduğu seller, en yaygın doğal afetlerden biridir. Güvenilir yağış ürünleri ve iyi kalibre edilmiş hidrolojik modeller bu tür olayları öngörmeye, özellikle kentsel yerleşim yerlerinde hayat kurtarma için önemlidir. Yağış veri kaynaklarının yağış algılama potansiyelini değerlendirmek amacıyla, birçok yağış verisi iki hidrolojik modelde saatlik olarak kullanılmıştır. Samsun'daki Terme Havzasında meydana gelen üç sel olayını simüle etmek için, fizik temelli dağıtılmış model WRF-Hydro ve deneysel tabanlı model HEC-HMS modeli kullanılmıştır. Her iki model kalibrasyonu için 22 Kasım 2014 sel olayına ait ölçüm verileri kullanılmıştır. Ayrıca, WRF-Hydro modelinde akarsu ağ yoğunluğunun yağış-akış modellemesine etkisi araştırılmıştır. Model değerlendirmelerinde, farklı yağış verilerine sahip iki farklı sel olayı kullanılmıştır. Yağış verileri, anlık veri olarak radar verisi ve uydu yağış tahmini olan Hydro-Estimator (HE) ürünü; tahmin verisi olarak Weather Research and Forecasting Model (WRF) yağış ürünü; ve yer verisinden oluşmaktadır. Bu veri setleri arasında, radar yağış verilerine Kalman Filtrelemesi uygulanarak yanlışlık düzeltilmesi yapılmış ve bunların taşkın modellemesinde kullanımı da simülasyonlarda değerlendirilmiştir. Sonuçlar, tüm ürünlerin yağış türüne bağlı olarak farklı sınırlamaları ve potansiyelleri olduğunu göstermektedir. Bunların arasında, HE ürünü

genel olarak bu havzadaki simülasyonlarda zayıf performans göstermiştir. Çalışma alanının yakınında bulunan yer yağış verileri, taşkın pik oluşum zamanını temsil etmede iyi olmasına karşın, taşkın büyüklüğü tahmini açısından zayıflık göstermiştir. WRF yağış verileri sel olayını tespit etmede bir miktar zaman yanlışlığı ile üstündür; bu sebeple, tahmin ürünü olarak, erken uyarı sistemlerinde ilk önlemleri almak için yararlı olabilir. Yanlılık düzeltmesi çalışma alanına yakın istasyonlar kullanarak yapılan radar verilerinin özellikle cephesel yağış tipinde başarılı sonuçlar verdiği görülmüştür. Modellerin sonuçları, her iki modelin de hidrograf şekli ve pik süresini temsil etmede birbirine genellikle yakın olduğunu göstermiştir. Tüm olaylar ve yağış ürünleri için ortalama korelasyon (r) ve ortalama karekök hata (RMSE) değeri, WRF Hydro modelinin (r için 0.61, RMSE için $62.6 \text{ m}^3/\text{s}$), HEC-HMS modeline (r için 0.59, RMSE için $67.6 \text{ m}^3/\text{s}$) kıyasla daha iyi bir başarı gösterdiğini ortaya koymaktadır. Ancak, konvektif kökenli sel olayında modeller arasında fark görülmektedir. Bu olayda, WRF-Hydro modeli fiziksel tabanlı model özelliğini kullanarak, hidrograf pik ve zamanını doğru bir şekilde ortaya çıkarmıştır. Sonuçların geneli, iyi kalibre edilmiş hidrolojik model ile yanlılığı düzelmiş radar, WRF yağış tahminleri ve gözlemlerden oluşan yağış verisinin ölçüm istasyonları olmayan veya yetersiz olan alanlarda taşkınlara karşı gerekli önlemleri almaya ve hayat ve varlık korunumunda fayda sağlamaya yardımcı olabileceğini göstermektedir.

Anahtar Kelimeler: WRF-Hydro, HEC-HMS, sapma düzeltme, Kalman Filtresi, uydu tabanlı yağış verileri.

To My Beloved Husband...

ACKNOWLEDGEMENTS

I would like to express my gratitude to my supervisor Prof. Dr. Zuhal Akyürek for her invaluable encouragement, endless support and helpful advice throughout the research.

I would also like to express my sincere thanks to jury members, Dr. İsmail Yücel, Dr. Koray K. Yılmaz, Dr. Ahmet Öztopal and Dr. Ahmet Emre Tekeli, for their precious comments, time and valuable input that improve the thesis.

I owe thanks to the Scientific and Technological Research Council of Turkey (TUBİTAK) - BİDEB-2211 for the national scholarship that has been received during my PhD education.

I would also like to thank the Turkish State Meteorological Service and General Directorate of State Hydraulic Works for providing meteorological and flow datasets.

I am grateful to my all friends for their motivations and advice. I am also grateful to my dear late friend, Ayça Demirbaş Öztürk. I will never forget your kindness and friendship.

Saving the best for the last; my sincere thanks go to my great uncle, parents, brother, parents-in-law, sister-in-law, nephews, my dearest husband and my little baby for their love, support and care they provided me. I would specially like to thank my grandmother for supporting me for my whole life. Lastly, I would also like to express my gratitude to my angel up above, my dearest grandfather, for his unforgettable love. I am proud to be your granddaughter. Without the patience and encouragement of my big family, this thesis would not have been completed. So glad I have you!

TABLE OF CONTENTS

ABSTRACT	v
ÖZ	vii
ACKNOWLEDGEMENTS	x
LIST OF TABLES	xv
LIST OF FIGURES	xvii
LIST OF ABBREVIATIONS	xxii
CHAPTERS	
1. INTRODUCTION	1
1.1 General	1
1.2 Problem Statement and Methodology	2
1.3 Objectives.....	7
1.4 Thesis Outline	7
2. STUDY AREA AND DATASETS	9
2.1 Description of the Study Area.....	9
2.2 Data	11
2.2.1 Rainfall Datasets	11
2.2.1.1 Rain Gauge Data.....	11
2.2.1.2 Satellite Data.....	11
2.2.1.2.1 General Information about the HE Product.....	13
2.2.1.2.2 Format of the HE Product.....	16
2.2.1.2.3 Use of the HE Product in the Study Area.....	17

2.2.1.3 WRF Model Precipitation Data.....	18
2.2.1.4 Radar-Based QPE.....	19
2.2.2 Soil Data.....	27
2.2.3 Runoff Data.....	29
3. COMPARISON OF THE RAINFALL PRODUCTS	31
3.1 General	31
3.2 Radar-based QPE Matching Techniques.....	31
3.2.1 Direct Matching Method (DMM)	31
3.2.2 Probability Matching Method (PMM)	32
3.2.3 Window Correlation Matching Method (WCMM).....	33
3.2.4 Evaluation of the Methods	33
3.5 Evaluation of the Flood Events	41
3.6 Comparison of the Rainfall Products	44
3.6.1 Comparison of the Rainfall Products in Point Based Manner	44
3.6.2 Comparison of the Rainfall Products in Areal Based Manner.....	47
3.7 Summary and Discussion of the Results	51
4. RADAR-BASED QPE BIAS CORRECTION	55
4.1 Introduction	55
4.2 Description of the Kalman Filter.....	56
4.2.1 The Time Update Step	56
4.2.2 The Measurement Update Step	57
4.3 Methodology	57
4.4 Modeling the Empirical Variance	61
4.5 Computation of the Correlation Coefficient (ρ_x) and the Empirical Variance (σ_x^2).....	65
4.6 Kalman Filter Application.....	67

4.6.1 The KF Application Type I.....	67
4.6.2 The KF Application Type II	67
4.7 Results	69
4.8 The Effect of Correlation Coefficient (ρx) and Empirical Variance (σx^2) on Results.....	73
4.9 Discussion of the Results	74
5. HYDROLOGIC MODELING	77
5.1 General	77
5.2 HEC Hydrologic Modeling System	77
5.2.1 Parameters Defined in the Model	80
5.2.1.1 Curve Number (CN) Determination.....	81
5.2.1.2 Parameters in Routing Process.....	82
5.2.2 Calibration of the Model.....	85
5.3 WRF-Hydro Modeling System	90
5.3.1 WRF Model Physics Description	91
5.3.1.1 Land Surface Model (LSM) Description.....	91
5.3.1.2 Subsurface Routing Description.....	92
5.3.1.3 Surface Overland Flow Routing Description.....	94
5.3.1.4 Channel Routing Description.....	96
5.3.2 Description of Input Data Files.....	98
5.3.2.1 The WRF Preprocessing System (WPS).....	99
5.3.2.2. Terrain Routing Grid Data (High Resolution Grid Data).....	102
5.3.2.3. Forcing Data Input Files.....	105
5.3.3 WRF-Hydro Model Calibration Approach	106
5.3.3.1. Model Calibration Part I.....	107
5.3.3.2 Model Calibration Part II.....	110

5.3.4 The Effect of Stream Network Density on Simulation.....	115
5.4 Evaluation of Calibration with Other Rainfall Datasets.....	121
5.5 The Physical Assessment of the Channel Parameters (WRF-Hydro).....	127
5.6 Summary and Discussion of the Results	129
6. CONCLUSIONS AND RECOMMENDATIONS.....	133
6.1 Summary	133
6.2 Conclusions	135
6.3 Recommendations	138
REFERENCES.....	141
APPENDICES	
Appendix A: CDF Curves	155
Appendix B: Statistical Measures for Stations.....	159
Appendix C: Rainfall Distributions for Sub-basins	163
Appendix D: KF Application Results for Stations.....	167
Appendix E: Soil Categories and Vegetation Type Tables.....	177
VITA	179

LIST OF TABLES

TABLES

Table 2.1 Available Satellite Precipitation Datasets (Huffman, 2015).....	12
Table 2.2 Specification of the HE Product.....	15
Table 2.3 Requested Radar-based QPE from TSMS.....	26
Table 2.4 Available Radar-based QPE with Their Time Spans and Missing Data ...	27
Table 3.1 Correlation Coefficient Results with Different Space Windows and PMM.....	35
Table 3.2 Correlation Coefficient Values for Each Events with Clustering Months and Color Coding	38
Table 3.3 Assessment Factors (cumulative radar rainfall amount /cumulative gauge rainfall amount) for Each Event and Station.....	39
Table 3.4 Number of Radar Point Data in Sub-basins	48
Table 3.5 Geometry of Sub-basins.....	49
Table 3.6 Mean Statistics of Datasets for Sub-basins.....	50
Table 3.7 Cumulative Rainfall Amounts for Four Products and Sub-basins.....	50
Table 4.1 Cumulative Rainfall Amounts for each Event (mm).....	63
Table 4.2 Correlation Coefficients and Empirical Variances for each Event with the Duration and Average of Cumulative Radar and Gauge Rainfall Amounts	66
Table 4.3 Correlation Coefficients of Gauges with Each Other Using 8 Events.....	68
Table 4.4 Summary of the Table 4.3.....	69
Table 4.5 Summary of Statistics for all Stations and Flood Events.....	72
Table 5.1 Amount of Runoff Volume for Observed and Simulated Discharges (10^6 m ³).....	85
Table 5.2 Calibrated Routing Parameters for each Reach	89
Table 5.3 Runoff Volume Ratios and Improvements for REFDK Values	110
Table 5.4 Channel Parameter Values	111
Table 5.5 Parameters Calibrated in the Model with their Nominal Ranges, Default Values and Final Values.....	115

Table 5.6 Stream Definition Based on Number of Pixel and Contributing Area.....	115
Table 5.7 Statistical Results (NSE and components) for Different Stream Network Thresholds (22 nd November 2014).....	117
Table 5.8 Statistical Results (NSE and components) for Different Stream Network Thresholds (28 th May 2016).....	119
Table 5.9 Statistical Measures for Observed and Simulated Hydrographs.....	126
Table 5.10 Adjusted and Original Channel Parameters Considering Strahler Stream Order.....	128
Table B.1 Statistical Measures for the flood observed on 22 nd November 2014.....	159
Table B.2 Statistical Measures the flood observed on 2 nd August 2015.....	160
Table B.3 Statistical Measures for the flood observed on 28 th May 2016.....	161
Table E.1 Soil Categories and Textures.....	177
Table E.2 Vegetation Type (Class), LAI and Albedo Parameters with Explanations	178

LIST OF FIGURES

FIGURES

Figure 1.1 Conceptual Framework of the Research.....	6
Figure 2.1 The sub-basins of the Study Area, the Location of the Weather Radar, Rain Gauge Stations and the Stream Flow Station.....	10
Figure 2.2 Operational Geostationary Satellites that Cover Areas of the Earth.....	14
Figure 2.3 Pixel Centers of the HE Data.....	17
Figure 2.4 Distribution of WRF Points (pixel centers).....	18
Figure 2.5 Study Area with Rain Gauge Stations on Digital Elevation Model.....	23
Figure 2.6 Topography Between Radar Location and the Stations.....	24
Figure 2.7 Topography Between Radar Location and the Study Area.....	25
Figure 2.8 Soil Data Taken from Directorate of Mineral Research and Exploration (a), Land Cover (b) and Land Use Data (c).....	28
Figure 3.1 Direct Matching Method.....	32
Figure 3.2 The Probability Matching Method.....	32
Figure 3.3 Window Correlation Matching Method (5x5 space window and 3 time window)	33
Figure 3.4 Data Extraction in 5x5 Space Window.....	34
Figure 3.5 Gauge and Radar Rainfall Distribution in a Time Series for Alaçam Station	34
Figure 3.6 Space Window Types	35
Figure 3.7 CDF Curve of the Kavak Station (a) and Rainfall Distribution with three Datasets for 2014 Flood Event Day (b).....	36
Figure 3.8 Cumulative Distribution of WRF precipitation Data for 72 hours: Columns (1), (2) and (3) show flood events on 22 nd November 2014, 2 nd August 2015 and 28 th May 2016 respectively. Rows (1), (2) and (3) show distribution of rainfall types: convective, non-convective and both respectively.	42

Figure 3.9 Cumulative Distribution of Rainfall Data: Columns (1), (2) and (3) show flood events on 22 nd November 2014, 2 nd August 2015 and 28 th May 2016 respectively. Rows (1), (2) and (3) show rain gauge, the HE Product and Radar Rainfall Datasets respectively	43
Figure 3.10 Box Plots of 3 Flood Events for Radar, WRF and the HE Product, Root Mean Squared Error (rmse) (a) and Correlation Coefficient (b) (Averaged for 13 Rain Gauge Stations).....	46
Figure 3.11 Averaged Bias (mm) of Radar, WRF and the HE Product at Hourly Interval for each Station and Flood Event Year	47
Figure 3.12 Radar Point Locations (a) and the distribution of the HE Product (b) and WRF data (c)	48
Figure 3.13 Rainfall Distribution with Time for all Rainfall Products: 2014 (a), 2015 (b) and 2016 (c).....	49
Figure 4.1 Flowchart of the Kalman Filter Procedure	56
Figure 4.2 Empirical Variance of Stations with the Distance between Stations and Radar	64
Figure 4.3 Empirical Variance of all Datasets (a) and Empirical variance model after outlier detection (b)	65
Figure 4.4 The Results for the Salıpazarı Station (2014 (a), 2015 (b) and 2016 (c)).	71
Figure 4.5 Effect of ρx (a) and σx^2 (b) on r, Cumulative Rainfall Amounts and Maximum Rainfall Amount	73
Figure 5.1 Preprocessing Steps (Dem Reconditioning (a), Fill Sinks (b), Flow Direction (c), Flow Accumulation (d), Stream Definition (e), Stream Segmentation (f), Catchment Delineation (g) and Drainage Line (h))	79
Figure 5.2 Project Area with Project Point and Drainage Line.....	80
Figure 5.3 Average Infiltration Rate vs. Lithology (Source: Pratama et al., 2016) ...	82
Figure 5.4 Simulated hydrographs obtained from CN calibration	85
Figure 5.5 Location of the Sub-basins, Reaches and Gauging Station	87
Figure 5.6 The Effect of K (a) and X (b) Parameters on Discharge	88
Figure 5.7 The Optimal Simulated Flow	89
Figure 5.8 WRF-Hydro Architecture with Model Components	91

Figure 5.9 NOAH Land Surface Model Structure	92
Figure 5.10 Saturated Subsurface Flow Components	93
Figure 5.11 Overland Flow Routing	95
Figure 5.12 The WRF Preprocessing System Flowchart	99
Figure 5.13 Terrestrial Information for Turkey and Surroundings (Dominant Soil Categories in the Bottom Layer (a) and the Top Layer (b), Land Use Index (Dominant Vegetation Types) (c), Land Mask (d), Topographic Elevation (m)(e) and Surface Albedo (units of %) (e)).....	101
Figure 5.14 (a) Elevation Data (on the left), (b) land use index (on the right)	102
Figure 5.15 Implementation of Routing Sub-grid within Coarse Grid	103
Figure 5.16 Topography (a), Flow Accumulation (b), Channel Grid (c), Flow Direction (d), Basin Mask (e) and Land Use (f)	104
Figure 5.17 The Topography of Coarse Grid (on the left) and Fine Grid (on the right) in the Model Domain	105
Figure 5.18 Model Domain over the Thiessen Polygon (a), Stretching the Edge of the Polygons (b), Splitting the Polygons over the Coarse Grid (c).....	106
Figure 5.19 Simulation Results for the Runoff Volume Ratios.....	109
Figure 5.20 NSE Results for MANN and OVROUGHRT Parameters	113
Figure 5.21 r^2 (a), α (b), β_n (c) and β (d) Results for MANN and OVROUGHRT parameters	113
Figure 5.22 Hydrograph Results for Selected Parameters (22 nd November 2014)..	114
Figure 5.23 Strahler Stream Density Network for Different Thresholds.....	116
Figure 5.24 Hydrograph Simulation Results for each Stream Network Definition. .	117
Figure 5.25 Simulated Flow for Different Stream Densities (2 nd August 2015 (a), 28 th May 2016 (b))	119
Figure 5.26 NSE Results for Models	120
Figure 5.27 The SMC change (mm) with Stream Order.....	122
Figure 5.28 Model Simulation Results with 2014 flood data (gauge (a), WRF (b) the HE product (c), radar (d), BCR (I) (e) and BCR (II) (f)).....	123
Figure 5.29 Model Simulation Results with 2015 flood data (gauge (a), WRF (b) the HE product (c), radar (d), BCR (I) (e) and BCR (II) (f)).....	124

Figure 5.30 Model Simulation Results with 2016 flood data (gauge (a), WRF (b) the HE product (c), radar (d), BCR (I) (e) and BCR (II) (f))	125
Figure 5.31 Model Simulation Results for Gauge Rainfall Data with Adjusted Cross Sections (2014 (a), 2015 (b) and 2016 (c); Stream Order 1 (1), Stream Order 2 (2), Stream Order 3 (3)) (c.s. is the abbreviation for cross section).....	128
Figure A. 1 Columns (1) and (2) show CDF Curve of Stations and Rainfall Distribution with three Datasets for 2014 Flood Event Day respectively; Rows (1), (2), (3) and (4) show stations: Bafra, Ondokuz M., Karadeniz A. and Havza respectively.....	155
Figure A.2 Columns (1) and (2) show CDF Curve of Stations and Rainfall Distribution with three Datasets for 2014 Flood Event Day respectively; Rows (1), (2), (3) and (4) show stations: Alaçam, Vezirköprü, Yakakent and Çarşamba respectively.....	156
Figure A.3 Columns (1) and (2) show CDF Curve of Stations and Rainfall Distribution with three Datasets for 2014 Flood Event Day respectively; Rows (1), (2), (3) and (4) show stations: Ayvacık, Salıpazarı, Kozluk Beldesi and Topraksu Araş. respectively.....	157
Figure C.1 2014 Flood Event Rainfall Distribution with Time for Four Sub-basins (Sub-basin 1 (a), Sub-basin 2 (b), Sub-basin 3 (c) and Sub-basin 4 (d))	163
Figure C.2 2015 Flood Event Rainfall Distribution with Time for Four Sub-basins (Sub-basin 1 (a), Sub-basin 2 (b), Sub-basin 3 (c) and Sub-basin 4 (d))	164
Figure C.3 2016 Flood Event Rainfall Distribution with Time for Four Sub-basins (Sub-basin 1 (a), Sub-basin 2 (b), Sub-basin 3 (c) and Sub-basin 4 (d))	165
Figure D.1 KF Application Results in 2014 Flood Event for Stations: Vezirköprü (a), Yakakent (b), Alaçam (c), Havza (d) and Topraksu Araştırma (e).....	167
Figure D.2 KF Application Results in 2014 Flood Event for Stations: Bafra (a), Kavak (b), Ondokuz Mayıs (c), Karadeniz Araştırma (d) and Ayvacık (e).....	168
Figure D.3 KF Application Results in 2014 Flood Event for Stations: Çarşamba (a), Salıpazarı (b) and Kozluk (c)	169
Figure D.4 KF Application Results in 2015 Flood Event for Stations: Vezirköprü (a), Yakakent (b), Alaçam (c), Havza (d) and Topraksu Araştırma (e).....	170

Figure D.5 KF Application Results in 2015 Flood Event for Stations: Bafra (a), Kavak (b), Ondokuz Mayıs (c), Karadeniz Araştırma (d) and Ayvacık (e).....	171
Figure D.6 KF Application Results in 2015 Flood Event for Stations: Çarşamba (a), Salıpazarı (b) and Kozluk (c)	172
Figure D.7 KF Application Results in 2016 Flood Event for Stations: Vezirköprü (a), Yakakent (b), Alaçam (c), Havza (d) and Topraksu Araştırma (e).....	173
Figure D.8 KF Application Results in 2016 Flood Event for Stations: Bafra (a), Kavak (b), Ondokuz Mayıs (c), Karadeniz Araştırma (d) and Ayvacık (e).....	174
Figure D.9 KF Application Results in 2016 Flood Event for Stations: Çarşamba (a), Salıpazarı (b) and Kozluk (c)	175

LIST OF ABBREVIATIONS

AE	: Auto Estimator
AF	: Assessment Factors
AFWA	: Air Force Weather Agency
AGGFACTR	: Integer Divisor
AMC	: Antecedent Moisture Condition
AR	: Autoregressive Model
BCR	: Bias Corrected Radar
Bw	: Base Width
CDF	: Cumulative Distribution Function
Ch SSlp	: Channel Slope
CN	: Curve Number
DEM	: Digital Elevation Model
DSD	: Drop Size Distribution
DSI	: General Directorate of State Hydraulic Works
EUMETSAT	: European Organization for the Exploitation of Meteorological Satellites
FSL	: Forecast Systems Laboratory
GOES	: Geostationary Operational Environmental Satellite
GRIB	: GRIdded Binary or General Regularly-distributed Information in Binary
HE	: Hydro-Estimator
HEC-HMS	: Hydrologic Engineering Center's Hydrologic Modeling System
HEC-GeoHMS	: Geospatial Hydrologic Modeling Extension
HLINK	: Initial Water Depth
HydroSHEDS	: HYDROlogical data and maps based on SHuttle Elevation Derivatives at multiple Scales

IRIS	: Interactive Radar Information System
JMA	: Japan Meteorological Agency
K	: Muskingum Parameter (wave travel time)
KF	: Kalman Filter
LANDSAT	: Land Remote Sensing Satellite
LSM	: Land Surface Model
MANN	: Channel Manning Roughness
MPE	: Multisensor Precipitation Estimation
NCAR	: National Center for Atmospheric Research
NCAR RDA	: NCAR Research Data Archive
NCEP	: National Centers for Environmental Prediction
NEH	: National Engineering Handbook
NetCDF	: Network Common Data Form
NSE	: Nash and Sutcliffe Efficiency
NWS	: National Weather Service
OU	: Oklahoma University
OVROUGHRT	: Surface Roughness
OVROUGHRTFAC	: Overland Flow Roughness Scaling Factor
PMM	: Probability matching method
PW	: Precipitable Water
QPE	: Quantitative Precipitation Estimate
R	: Rainfall rate
r	: Correlation
REFDK	: Surface Runoff Parameter
REFKDT	: Infiltration Scaling Factor
RETDEPRTFAC	: Surface Retention Depth Factor
RH	: Relative Humidity
RMSE	: Root Mean Squared Errors
SBP	: Satellite Based Precipitation
SCaMPR	: Self-Calibrating Multivariate Precipitation Retrieval
SCS	: Soil Conservation Service

SLOPECAT	: Topographic Slope
SMC	: Soil Moisture Content
SRI	: Surface Rain Intensity
SRTM	: Space Shuttle Flight for NASA's Shuttle Radar Topography Mission
STATSGO	: State Soil Geographic Soil Database
TSMS	: Turkish State Meteorological Service
USACE	: Hydrologic Engineering Center within the United States Army Corps of Engineers
USDA – NRCS	: United States Department of Agriculture, Natural Resources Conservation Service
WPMM	: Window Probability Matching Method
WPS	: WRF Preprocessing System
WRF	: Weather Research and Forecasting
WRF-Hydro	: Weather Research and Forecasting model HYDROlogical extension package
X	: Muskingum Parameter (weighting factor)
VIC	: Variable Infiltration Capacity
Z	: Reflectivity
ΔL	: Reach Length
α	: Relative Variability
β_n	: Bias Normalized by the Standard Deviation
β	: Bias
ρ_x	: Correlation Coefficient
σ_x^2	: Empirical Variance

CHAPTER 1

INTRODUCTION

1.1 General

Flood is one of the most damaging natural disasters and results in life and property losses. With global climate change, deforestation and rapid urbanization, extreme weather events are expected to occur with increasing frequencies with greater intensities (Lau et al., 2010). In Turkey, 52% of floods take place in the Black Sea Region and they most frequently occur during winter, spring and summer months (Özcan, 2006). The reasons for floods in the Black Sea region can be listed as rapid saturation of impermeable clay soil with rainfall, high slope gradient, low water carrying capacity of streams and destruction of forests into agricultural land. In addition to the physical characteristics of the region, orographic rainfall with snow melting in spring and early summer seasons leads an increase in flood effect. Hence, it is important to accurately estimate the spatial and temporal distribution of a flood event ahead of the decision making. Thus, threats to life and property can be reduced by early warnings and by implementing planned responses. Flooding may be more devastating in data sparse regions due to not only the absence of flood warning systems but also the lack of rainfall estimates. Rainfall output gathered from spatially distributed rainfall data like weather radar, satellite and numerical weather prediction model precipitation products can be a remedy to the difficulties in representing the driving force in hydrologic models for ungauged or poorly gauged regions. However, the accuracy assessment of these products especially over the mountainous regions is a necessity.

Rainfall-runoff models are tools to formalize knowledge about hydrological systems (Beven, 2011). Since the early 1960s, various model structures have been developed and implemented into software (Todini, 1988). These structures can be narrowed down into three distinct classes; metric (empirical or black box), parametric (conceptual or gray box) and mechanistic (physic-based or white box) (Wagener et al., 2004). In addition to physical process description, hydrologic model can also be classified according to the spatial description of catchment process as lumped, semi-distributed and distributed. However, hydrological model categorization can be hampered by overlapping characteristics of model classes; therefore, classification of model may change depending on justification (Jajarmizadeh et al., 2012). For example, HEC-HMS model can range from empirical to conceptual and lumped to distributed (US Army Corps of Engineers, 2000). Regardless of the category description, each hydrologic model, used for flood management, has different levels of complexity. With rapid development of sophisticated computer programs throughout the past decades, various hydrologic models capable of using the rich information content of remotely sensed geospatial data have been developed for flood simulations. Among these models, physics-based distributed hydrologic models have an emerging trend due to their better representation of watershed spatio-temporal characteristics that transform rainfall into runoff (Vieux et al, 2004). However, hydrological models are expected to have different success rates depending on the basin characteristics, initial conditions and calibration stages. For instance, in moist areas, variable infiltration capacity model (VIC) performs well and it can be used for agricultural purposes efficiently. Another model, MIKE SHE, a deterministic, fully-distributed and physically-based hydrological and water quality modeling system, is limited to smaller catchments due to the requirement of large data. Moreover, SWAT model can obtain good hydrologic predictions with little direct calibration, whereas TOPMODEL can be used in areas with shallow soil and moderate topography (Devia et al., 2015).

1.2 Problem Statement and Methodology

Flooding has the potential to cause significant impacts to economic activities as well as to disrupt or displace populations. Changing climate regimes such as extreme

rainfall events increases flood vulnerability and put additional stresses on infrastructure. The flood problem is not a recent issue neither for Turkey nor for other countries. Therefore, the need for the flood protection and flood management are not new too. There are many studies about flood management around the world. Recent researches suggest a risk-based approach in flood management (Hooijer et al., 2004; Petrow et al., 2006; van Alphen and van Beek, 2006). The necessity to move towards a risk based approach has also been recognized by the European Parliament (de Moel et al., 2009), which adopted a new Flood Directive 19 (2007/60/EC) on 23 October 2007. According to the EU Flood Directive, the member states must prepare the flood hazard and risk maps for their territory and then use these maps for flood risk management plans. Structural management measures play also important role among various mitigation facilities and flood management strategies.

Studies on floods require hydrological, hydraulic and topographical inputs to be analyzed at temporal and spatial scales. In Turkey, authorities use traditional methods in flood hydrograph calculations such as point flood frequency analysis (PFFA), regional flood frequency analysis, DSI synthetic unit hydrograph and Mockus method. However, the use of hydrological models can greatly evolve the work done in this regard. Recently, computer-based rainfall-runoff models, as previously mentioned, can provide effective tools for decision-making and flood control management measures.

Following the above considerations, in this study, a methodology is presented for sparsely gauged or ungauged areas to investigate the flooding problem with the use of different rainfall products in hydrologic models. In the first step of the methodology, to find convenient rainfall product, considering their sources, three different spatially distributed rainfall data are used; radar, satellite and numerical weather prediction model precipitation products. Samsun weather radar station is the closest station (nearly 75 km) to the study area that can provide radar-based quantitative precipitation estimates (QPE) with high spatial scale. Unlike selection of radar-based QPE, selection of satellite-derived rainfall product that is optimal for the study area is complicated. The reason for this can be explained as the sheer number of satellite derived rainfall

products currently available at high spatial and temporal resolutions suitable for hydrologic models. Among the satellite derived rainfall products used in the literature, given in detail in the second chapter, the Hydro-Estimator (HE) product is considered to be appropriate for the study area. As a *forecasting product*, Weather Research and Forecasting (WRF) Model precipitation data are selected to investigate its capacity in flood warning for the study area. In the following steps of the methodology, the emphasis is given to radar-based QPE due to its high spatial resolution by applying matching techniques that are used in the literature; direct matching method, probability matching method and window correlation matching method. The aim of applying these methods is to improve the accuracy of radar-based QPE that may have errors related to collocation and timing problems. In the next step, all rainfall products are investigated in point and areal based manner to evaluate their performances before the hydrologic model application. Among the rainfall products, radar-based QPE, which has the best spatial resolution, captures the trend of the rainfall more accurately. Therefore, in the second step of the methodology, bias correction is applied to radar-based QPE. The correction of radar-based QPE with gauge observations has been an important research topic. In the literature, there are numerous proposed methods used to reduce the error of radar estimation. Meteorological services such as Meteo France, UK MetOffice and MeteoSwiss use gauge adjustment methods and describe adjusting radar-based QPE so that it corresponds with the quantity given by gauge observations. The detail and operational use of the mentioned methods can be found in the COST 717 report (Gjertsen et al., 2004). More complex methods such as co-kriging (Sun et al., 2000), kriging with external drift (Verworn and Haberlandt, 2011), statistical objective analysis (Pereira et al., 1998) and use of the Kalman Filter (Todini, 2001) are also employed in the processing of radar-based QPE. Kriging or kriging with external drifts are methods that interpolate gauge observations before bias computations. Statistical objective analysis adjusts the radar data pixel by pixel using gauge observations (Gerstner and Heinemann, 2008). In real-time applications of radar rainfall estimates, the mean field bias adjustment method is used (Seo et al., 1999; Chumchean et al., 2006 and Habib et al., 2012). Electrical calibration errors, radar reflectivity measurement errors and systematic errors in space; such as height sampling

errors in range, are the sources of radar rainfall bias (Yoo et al., 2014). For the purpose of bias correction, Kalman Filtering (KF) algorithm is used in this study due to its appropriateness in continuously changing system and efficiency in data memory usage. The KF algorithm is applied to the dataset with two different approaches using appropriate system equation, correlation coefficient and empirical variance. In the first approach, all rain gauges except for the studied one located in the radar range are used for the computation. In the second approach, gauges that have better correlations with the studied gauge are taken into consideration. Upon completion of these approaches, two different bias corrected radar (BCR) datasets are obtained; namely, BCR (I) and BCR (II). The primary goal of the second approach is to localize the bias computation. In the third and final step of the methodology, two different hydrologic models are used. As an empirical based model, the Hydrologic Engineering Center's Hydrologic Modeling System (HEC-HMS) is used due to its wide usage in the literature and easy access. As a physic-based distributed model, the Weather Research and Forecasting model hydrological extension package (WRF-Hydro), is used due to its prediction skill of hydrometeorological forecasts using physics-based numerical prediction tools. The methodological steps are provided in Figure 1.1.

To summarize, as the physic-based model, the WRF-Hydro model in uncoupled mode and as the empirical-based model, HEC-HMS model are used to simulate heavy rainfall of 3 different events those have different rainfall types observed on 22nd November 2014, 2nd August 2015 and 28th May 2016. For each event and model, a total of six rainfall products are used in the simulations. Among the datasets, four of them have different sources that are weather radar, the Hydro-Estimator (HE) product, gauge and rainfall output obtained from WRF model and two of them are derived from radar-based QPE in which bias corrections are applied using the information provided by rain gauges. Conforming to the available data, the detailed calibration is only performed for 2014 flood event using flow data at stream gauge station for both models. Then, the rest of the rainfall products' performances are evaluated in both models with the calibrated parameters.

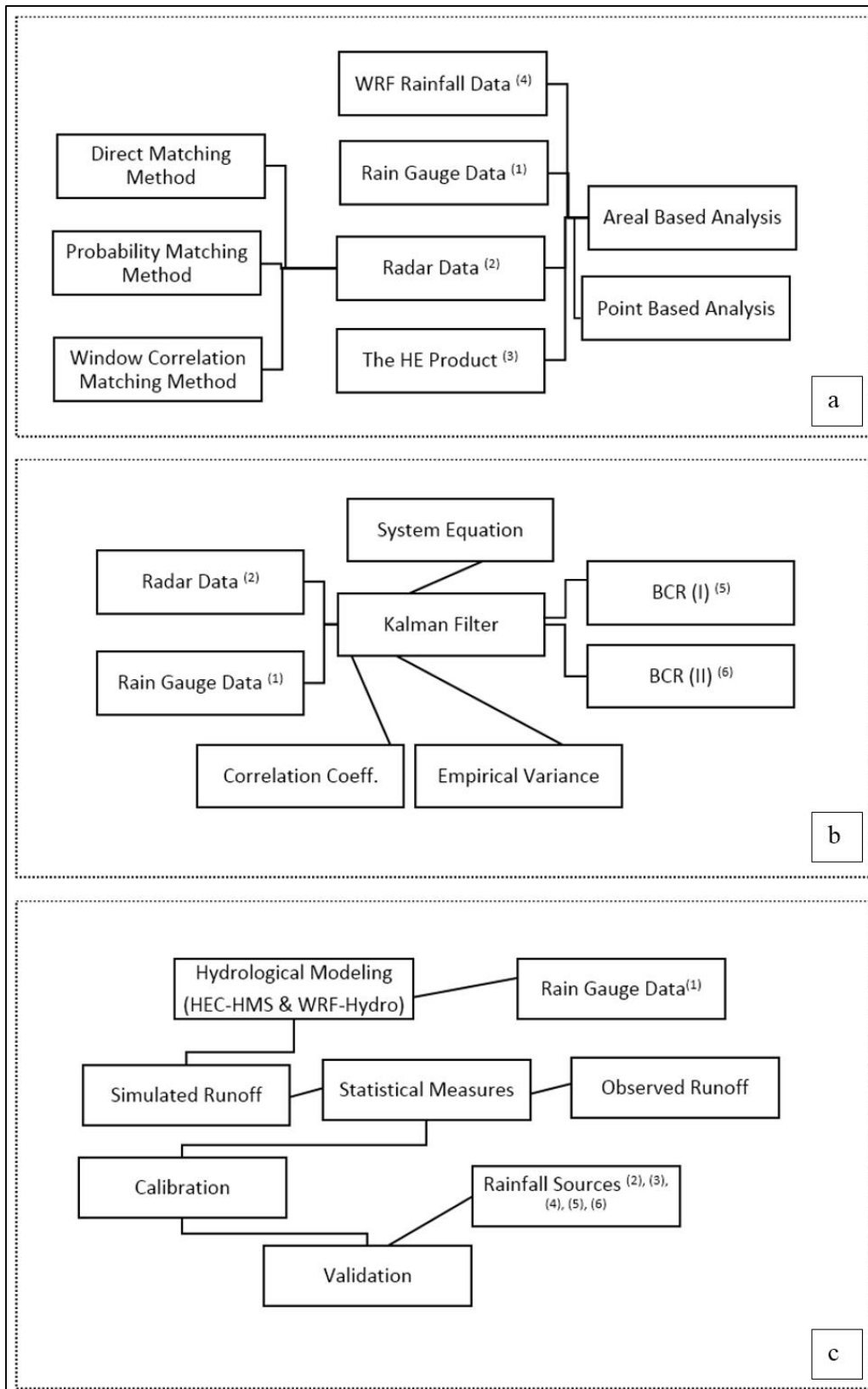


Figure 1.1 Conceptual Framework of the Research (Rainfall Comparisons (a), Kalman Filtering of Radar QPE (b) and Hydrological Modeling Studies (c))

1.3 Objectives

The main purpose of this study is to assess the rainfall products in a sparsely gauged catchment for different rainfall types; namely convective, non-convective and both. For this purpose, Samsun-Terme basin is selected for the study area due to data availability. Hourly based intervals are used throughout the analyses due to the small size of the catchment and rapid response of catchment to the rainfall. Furthermore, main objectives of this study are listed below:

- To evaluate the rainfall products, which are mentioned in the methodology, using rain gauge data in point and areal based analyses with statistical measures.
- To apply Kalman Filtering (KF) algorithm to radar-based QPE for improving the accuracy by considering the gauge correlations among each other.
- To calibrate two hydrological models using gauge data and successfully model the hydrologic behavior of the basin.
- To assess the performance of rainfall products on simulations of hydrologic models using calibrated model parameters.

1.4 Thesis Outline

The subjects described in the following chapters are given below:

In Chapter 2, the study area and the data used in the research are presented. The characteristics of different rainfall products and the studies performed in the literature are summarized.

In Chapter 3, the rainfall products and their evaluations are presented. Matching techniques are applied to radar-based QPE and their results are analyzed by statistical measures. Comparison of rainfall datasets are performed in point and areal based manner.

In Chapter 4, description of the KF and two different applications of KF methodology are presented.

In Chapter 5 the calibration of two models using the statistical measures and then the verification using the calibrated parameters are presented. This section includes the main results of the study and discusses the use of other rainfall products in the study area.

Finally, Chapter 6 presents the conclusions of the study and gives recommendations for further studies.

CHAPTER 2

STUDY AREA AND DATASETS

2.1 Description of the Study Area

The Terme River basin is located in the eastern Black Sea region of Turkey at about 40°84'-41°12' North and 36°71'-36°98' East. The Terme River has a catchment area of 436.4 km². The sub-basins, represented with the stream flow station, have an area of 231.8 km² and a mean elevation of 681.5 m (Figure 2.1). The Black Sea region is impacted by continental polar and tropical air masses originated from Russia and Siberia, and Azores Islands respectively (Sensoy, 2004). The topography of the study area emphasizes sudden flooding events and the surrounding urbanized areas may suffer serious consequences. The intense convective rainfall (especially in summer) falls on the upper parts of the basin. Due to the basin characteristics, areas close to the Terme River can be flooded in summer, even if no rainfall occurs in the Terme City center.

On 11th July 2012, Terme city center was exposed to a flood with 510 m³/s peak flood discharge passed through the city. The hydrological report of the General Directorate of State Hydraulic Works (DSI) stated that the peak flood discharge in 2012 almost equals to a 6-year return period of flood discharge. Then, the DSI 7th Regional Directorate initiated a tender, namely, Samsun Terme District, Terme River Flood Hazard Map Designation. The result of the tender showed that virtually the entire city was flooded with 500-years return period of discharge. In order to mitigate this problem, the Salıpazarı Dam tender that costs 125 million TL was made in December 2016. With the completion of the construction, this dam will serve the purpose of water

supply, irrigation and flood prevention. However, in 2015, a hydraulic modeling with unsteady flow calculations was applied in the Terme urbanized area and its upstream to propose applicable solutions to the flood problem. The studies were carried out with different discharges for different scenarios. The primary conclusions were that; the river meanders had a major effect on flood discharge and the Salıpazarı Dam flood capacity was not sufficient individually to protect Terme City against flooding. (Bozoğlu, 2015). For this reason, additional structures would be needed. Providing early flood warnings would be another remedy for the study area. In the development and implementation of a flood warning system for the area, well calibrated hydrological model and continuous meteorological forcing data are essential.

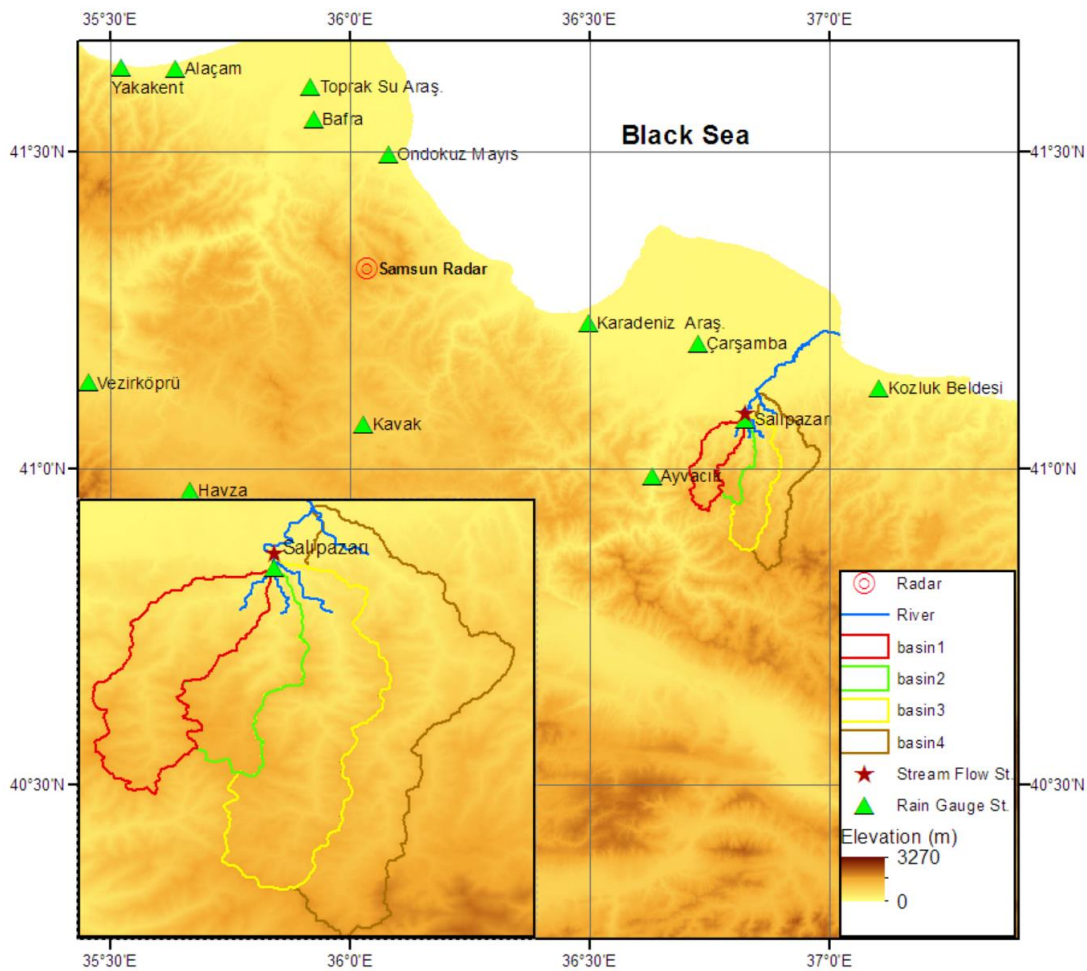


Figure 2.1 The sub-basins of the Study Area, the Location of the Weather Radar, Rain Gauge Stations and the Stream Flow Station

2.2 Data

2.2.1 Rainfall Datasets

2.2.1.1 Rain Gauge Data

There are 13 rain gauges located around the study region (Figure 2.1). In the selection of rain gauges, the topography of the radar umbrella and the region is considered; however, the stations located on the south part of the study area are not taken due to mountain blockage. The continuous gauge rainfall record during flood events at each of the 13 rain gauges is used to calculate the rainfall amount with a 1-hour duration. These data are paired with the corresponding rainfall datasets. For the Kalman Filtering application, apart from the three flood datasets, events having a cumulative rainfall amount greater than 20 mm are selected and these are used only in bias-correction methodology.

2.2.1.2 Satellite Data

Satellite based precipitation (SBP) products can be a remedy for ungauged and sparsely gauged regions. The utility of SBP estimates with recent algorithms for hydrologic forecasting and hazard monitoring have been studied by various researchers (Creutin and Borga, 2003, Hong et al., 2007, Hong and Adler, 2007 and Li et al., 2013). However, hydro climatic features of the region especially over the complex terrain influence the performance of the SBP products (Yilmaz et al., 2005). In the literature, SBP products' performance evaluation over the complex terrain is still limited (Derin and Yilmaz, 2014, Derin et al., 2016). Not only the performance of SBP product, but also the latency of product access and resolution of product in spatial and temporal manner are other significant components. Available multi-satellite precipitation estimates with information about their input data, resolution, latency and producer are given in Table 2.1.

Table 2.1 Available Satellite Precipitation Datasets (Huffman, 2015)

Algorithm	Input data	Space/time grid	Areal coverage/start date	Latency	Producer
AIRS AIRG2SSD	AIRS, AMSU, HSB sounding retrievals	Level 2G swath/orbit segments	Global/Sept. 2002	1 day	NASA/GSFC GES DISC
AIRS AIRX3STD, AIRX3ST8, AIRX3STM	AIRS, AMSU, HSB sounding retrievals	1°/daily, 1°/8-day, 1°/monthly	Global/Sept. 2002	1 day	NASA/GSFC GES DISC
CMORPH	TMI, AMSR-E, SSM/I, SSMIS, AMSU, MHS, IR vectors	8 km/30-min	50°N-S/1998	18 hours	NOAA/CPC
CMORPH V1.0 RAW	TMI, AMSR-E, SSM/I, SSMIS, AMSU, MHS, IR vectors	0.25°/3-hourly	50°N-S/1998	18 hours	NOAA/CPC
GSMaP-NRT	TMI, AMSR-E, SSM/I, SSMIS, AMSU, IR vectors	0.1°/hourly	60°N-S/Oct. 2007	4 hours	JAXA
GSMaP-MWR	TMI, AMSR-E, AMSR, SSM/I, IR vectors	0.25°/hourly, daily, monthly	60°N-S/1998-2006	-	JAXA
GSMaP-MVK	TMI, AMSR-E, AMSR, SSM/I, SSMIS, AMSU, IR vectors	0.1°/hourly	60°N-S/2000 (currently 2003-2008 data available)	Reprocess now; will become operational	JAXA
GSMaP-MVK+	TMI, AMSR-E, AMSR, SSM/I, AMSU, IR vectors	0.1°/hourly	60°N-S/2003-2006	-	JAXA
MPE	Meteosat 7, 8, 9, 10 IR and SSM/I, SSMIS Meteosat 7, 8, 9, 10 IR and SSM/I, SSMIS	MFG: original pixels/30-min MSG: original pixels/15-min	Indian Ocean 8°W-1.22°E, 65°N-S Europe/Africa 79°W-E, 65°N-S	10 min 10 min	EUMETSAT EUMETSAT
NRL Real Time	SSM/I- & F16/SSMIS-cal IR (Prob.-Matching Method)	0.25°/hourly	40°N-S/ July 2000	3 hours	NRL
PERSIANN	(TMI, AMSR-E, SSM/I, SSMIS, AMSU, MHS)-cal. IR	0.25°/30-min	60°N-S/ March 2000	1 day	UC Irvine
PR-OBS-3	SSMIS, AMSU/MHS, MSG-IR	5 km/15 min	Europe/Jan 2009	15 min	HSAF
PR-OBS-4	SSMIS, AMSU/MHS, MSG-IR	8 km/30 min	Europe/Nov 2011	3 hours	HSAF
TCI (3G68)	PR, TMI	0.5°/hourly	Global - 37°N-S/ Dec. 1997	4 days	NASA/GSFC PPS
TOVS	HIRS, MSU sounding retrievals	1°/daily	Global/1979-April 2005	1 month	NASA/GSFC 610
TRMM Real-Time HQ Version 7 (3B40RT)	TMI, SSM/I, SSMIS, AMSR-E, AMSU, MHS	0.25°/3-hourly	Global - 70°N-S/Mar. 2000	9 hours	NASA/GSFC PPS
TRMM Real-Time VAR Version 7 (3B41RT)	MW-VAR (IR)	0.25°/hourly	Global - 50°N-S/Mar. 2000	9 hours	NASA/GSFC PPS
TRMM Real-Time HQVAR Version 7 (3B42RT)	HQ, MW-VAR (IR)	0.25°/3-hourly	Global - 50°N-S/Mar. 2000	9 hours	NASA/GSFC PPS

Among the products it is seen that Multisensor Precipitation Estimation (MPE) algorithm has the best space time grid combination. It has 4 km spatial and 15 min. temporal resolution. The product is derived from the infrared (IR) data (10.8 μm) of geostationary European Organization for the Exploitation of Meteorological Satellites (EUMETSAT) by recalibration of algorithm with polar orbiting microwave sensors. The product has a monotonic function which means highest rain rate is associated with coldest temperature and lowest rain rate is related with warmest temperature. Thus, it is suitable for convective weather situations (Heinemann et al., 2002). However, Derin (2014) stated that MPE shows lowest performance among SBP products, TMPA 7A, TMPA 7RT, CMORPH and MPE in the study area located in Western Black Sea Region of Turkey. Also it is emphasized that with a wide range of scatter between studied years, MPE underestimates the rainfall amounts. Yucel and Onen (2014) studied MPE product and Weather Research and Forecasting (WRF) model over the Western Black Sea region. They concluded that in heavy rainfall events WRF captured the time of rainfall extremes and spatial distribution and magnitude of rainfall to some extent whereas MPE showed poor results in these aspects. Studies performed by the researches show that MPE product has a weakness in frontal rainfall and it is more suitable in convective systems. Therefore, as a satellite rainfall data another product which has the same spatial resolution like MPE, the Hydro-Estimator is used to assess the potential use in hydrologic modeling.

2.2.1.2.1 General Information about the HE Product

The Hydro-Estimator (HE) is an algorithm (Scofield and Kuligowski, 2003) that derives rain rate from convective and non-convective clouds separately by use of Geostationary Operational Environmental Satellite (GOES) brightness temperature (10.7- μm). For regions where GOES does not cover other geostationary satellites like METEOSAT (for Europe, Africa and western Asia) and MTSAT (for eastern Asia) products are used (Vicente et al., 1998).

Geostationary satellite is a satellite directly over the equator orbiting the earth at the same speed as the earth rotates. It monitors the region every 15 to 60 minutes. There

are two GOES that provide data to Western Hemisphere; GOES West and GOES East (Figure 2.2). They are centered at 135° W and 75° W respectively. Meteosat is located at 0° E and covers mainly Europe and Africa. Feng Yun 2 (FY-2), is located at 105° E and covers China. Last, the Japan Meteorological Agency's (JMA) Satellite called MT-SAT is located at 135° E and serves eastern Asia.

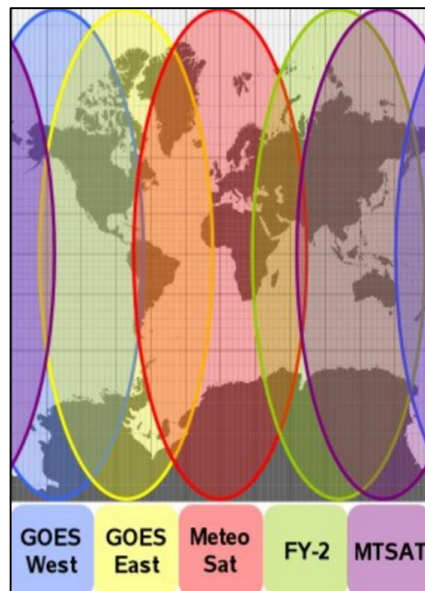


Figure 2.2 Operational Geostationary Satellites that Cover Areas of the Earth
 (Source: <http://www.automatedsciences.com/intro/intro.shtml>)

The HE product is a fully automatic method that calculates rainfall rate as a function of IR window brightness temperature and numerical weather prediction model fields from the NOAA /National Weather Service (NWS) National Service for Environmental Prediction (NCEP) North American Model or global forecast system. These fields are atmospheric moisture (the product of precipitable water (PW) and relative humidity (RH)), orography and convective equilibrium level (Kuligowski, 2014). The HE product was developed as an enhancement of original Auto-Estimator (AE) planned for moist convective systems (Vicente et al., 1998). The HE algorithm uses pixel brightness temperatures in GOES and its value relative to surrounding pixels. Pixels that are warmer than surroundings are denoted as lower clouds and no rain, while pixels colder than surroundings are associated with updraft regions.

The HE product has been operational since 2002 and available in ASCII format for global scale via this address ftp://ftp.star.nesdis.noaa.gov/pub/smcd/emb/f_f/hydroest/world/world/. Files contain 1 hour rainfall accumulation data. The specification of product is given in Table 2.2.

Table 2.2 Specification of the HE Product

Temporal Resolution	15 min to 1 hr
Spatial Resolution	4-km in GOES coverage region; Global file is 0.045 degrees (lat/lon).
Spatial Coverage	Global between 60°S and 60°N.
Product webpage	http://www.star.nesdis.noaa.gov/smcd/emb/ff/auto.html
Latency (Operational Availability)	60 minutes
Satellites	GOES (15 min), METEOSAT (30 min), MTSAT (60 min)

The HE product is powerful in convective rainfall mesoscale systems. Also, moisture corrections perform well in highly arid regions where evaporation takes place rapidly after rainfall reaches to the ground. However, in stratiform rainfall type, rainfall relationship between cloud top brightness temperature and surface rainfall rates is weak so algorithm is insufficient for cool season. Moreover, on tropical islands, algorithm does not perform well in extremely warm top convection systems (Kuligowski, 2014).

Vicente et al. (2002) implemented two approaches to correct the HE product for orographic effects and parallax dislocation. These factors mainly influence the distribution of rainfall and position of the cloud tops as viewed by the satellite respectively. For orographic correction wind data taken from ETA model with 48 km resolution grid and local terrain height data taken from a composite map of North America with 20 m vertical resolution are used. This approach is only applied over North America. For parallax correction three parameters are used; the height of the cloud, the apparent position of the cloud on Earth and the position of the satellite. The purpose of parallax correction is to get better location of the rainfall cores. The effect of this correction on the result is little on synoptic scale studies but it has a major role on the mesoscale and the storm scale rain systems. Due to the insufficient number of

rainfall stations, comprehensive validation was not applied for orographic correction. The mentioned parallax adjustments have been incorporated into the HE algorithm globally (Kuligowski, 2014).

Yucel et al. (2011) studied the HE product algorithm over mountainous region in North West Mexico during two summer monsoon periods. The research showed that HE estimates generally captured the rainfall characteristics in spatial and temporal manner. However, the HE product overestimates the rainfall at lower elevation while underestimates the light rainfall in high elevation. Results showed that orographic correction has a positive impact on rainfall but it is not sufficient to eliminate elevation dependent bias in magnitude. For this reason, the improved orographic correction was needed by the HE algorithm to reduce elevation - dependent bias. Akcelik (2013) applied orographic and temperature correction methods to enhance the Self-Calibrating Multivariate Precipitation Retrieval (SCaMPR) rainfall algorithm over North West Mexico. The results are compared with the operational HE orographic correction results over North American Monsoon Experiment (NAME) region. It is found out that proposed formulation improves the correlation between SCaMPR estimates and gauge measurements by 9% in 1 hour data and 8% in 6 hour data, whereas this improvement in operational HE algorithms is limited to 3.8% and 5.8 % for 1 hour and 6 hour temporal resolution respectively. In 2015, Yucel assessed the flash flood event in İstanbul, Ayamama basin using different rainfall datasets (Yucel, 2015). In his study as nowcasting products the HE product and radar-based QPE, as a forecasting product Weather Research and Forecasting (WRF) dataset were used. Among these products, the HE product showed least negative bias and lowest mean RMSE for all time intervals. However, the HE product algorithm underestimated the peaks and it could not capture the light rainfall in stratiform systems.

2.2.1.2.2 Format of the HE Product

Files are stored in ASCII and named in Julian day format. The first line of the file contains date and time, remaining lines contain values between 0 and 256 that related to rainfall accumulation. Using the equation below rainfall amount, R can be found;

$$R = (value - 2) * 0.3048$$

Equation (2.1)

Value of 0 and 2 mean missing value and no rainfall respectively.

For the study area, data are extracted from file with generic name “world”. This file “world1hr” contains (8001x3111) 24891111 number of data stored in one row. Location data procured, there is a file named “zworld” contains lat/long information which corresponds to point in “world1hr” files. GrADS software can be used to visualize data and to split data Hex editor can be used. Further information can be obtained from: ftp://ftp.star.nesdis.noaa.gov/pub/smcd/emb/f_f/hydroest/world/world/README

2.2.1.2.3 Use of the HE Product in the Study Area

Satellite data covering entire world is downloaded for the flood events. Next, data are split and relevant data are extracted for the boundary of the study region. The product has a 4X4 km spatial resolution. Due to the way of acquiring data (point wise) the centers of pixels are represented as points (Figure 2.3). Unlike radar-based QPE, there are fewer HE points that represent the rainfall distribution of the study area.

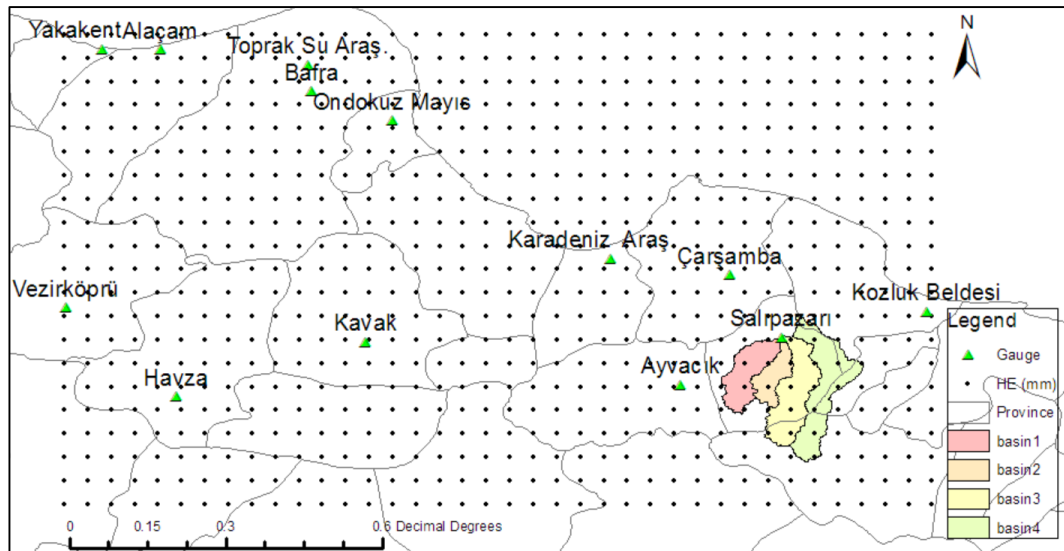


Figure 2.3 Pixel Centers of the HE Data

2.2.1.3 Weather Research and Forecasting (WRF) Model Precipitation Data

In cases of extreme events, numerical weather prediction models play a major role in weather forecasting (Nasrollahi et al., 2012). The Weather Research and Forecasting Model (WRF) is developed in a collaborative effort by the National Center for Atmospheric Research (NCAR), the National Centers for Environmental Prediction (NCEP), the Forecast Systems Laboratory (FSL), the Air Force Weather Agency (AFWA) and Oklahoma University (OU) (Skamarock et al., 2001). WRF is a regional atmospheric model in mesoscale weather research and shows skillful performance in representing a wide variety of precipitation processes over different geographical regions (Chen et al., 2010; Liu et al., 2013; Yucel and Onen, 2014).

The use of different sources of rainfall datasets may increase the potential to find the best dataset for the study area considering the event type. For this purpose, in addition to radar, gauge and satellite rainfall datasets, numerical weather prediction model precipitation forecasts are used for the flood events. For the study area, the data are requested from the Turkish State Meteorological Service (TSMS) in netcdf format. The distribution of WRF pixel centers can be seen in Figure 2.4. The spatial resolution of the WRF precipitation dataset is the same as the HE product, 0.045° nearly 4 km.

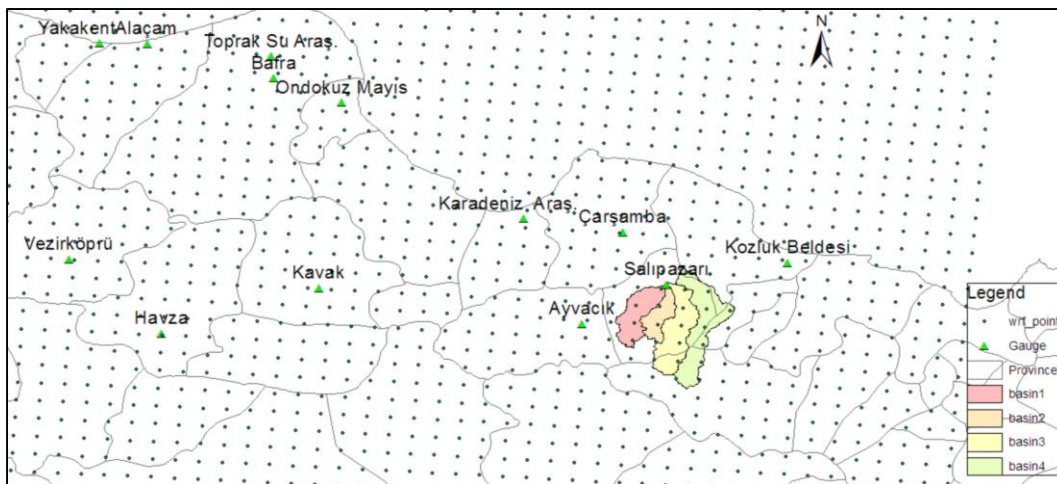


Figure 2.4 Distribution of WRF Points (pixel centers)

The WRF precipitation data are output of WRF model. The lead time of this data can be 24, 48 and 72 hrs. With the increasing of lead time the accuracy of WRF precipitation data decreases as does the capability of flood forecasting (Li et al., 2017). In this study, WRF precipitation data with 72 hrs duration are obtained from the TSMS that runs WRF model once a day at time 00:00 AM. In order to detect accurate rain and catch the hydrograph peak time and hydrograph shape in the hydrological models properly, the data is selected one day ahead of the observed hydrograph peak time. The selected WRF precipitation data are the WRF model products of 21st November 2014, 1st August 2015 and 27th May 2016 those are used for the floods observed on 22nd November 2014, 2nd August 2015 and 28th May 2016 respectively.

In production of the meteorological data, WRF model offers multiple physics options that can range from simple to complex. The supplied data are constructed by TSMS using WRF Single-Moment 5-class Scheme in microphysics option, Rapid Radiative Transfer Model in longwave radiation option, Dudhia Scheme in shortwave radiation option, Noah Land Surface Model in surface physics option and Kain-Fritsch Scheme in cumulus parameterization physics.

2.2.1.4 Radar-Based QPE

In the fields of meteorology and hydrology, weather radars have been used for decades (Maynard, 1945; Battan, 1973). Although, rainfall estimates from weather radars serve as an important feature in hydrology and water resource applications, their precision is affected by factors such as the reflectivity measurement operation and the Z-R conversion process (Joss and Waldvogel, 1970). Weather radar systems do not measure rainfall depth directly. The Z-R relationship, an empirical equation between radar reflectivity (Z) and rainfall rate (R), is generally used to calculate rainfall depth. The procedure to estimate reflectivity (Z), which is the amount of power returned to the radar, is subject to various independent sources of error such as ground and sea clutter (Collier, 1996), refraction and anomalous propagation (Battan, 1973), bright bands (Kitchen et al., 1994), beam blockage (Bech et al., 2003), attenuation (Hildebrand, 1978), temporal and spatial sampling errors (Harrold et al., 1974), and non-meteorological targets. These error sources demonstrate complex

interdependencies; therefore, their impact on measurement accuracy is difficult to evaluate. Each error type in reflectivity measurement operation has been studied and has given rise to correction methods (Andrieu et al., 1997).

The Z-R conversion process, frequently used in the literature, is not unique. Considering the study region, researchers attempted to determine the most appropriate Z-R relationship from a large number of empirical Z-R relationships available in the literature ($Z=aR^b$). Z-R parameters (a and b) show high variability according to the geographic location and season, the rainfall phase and intensity (storm type and drop size distribution), as well as the variability within the same storm and from storm to storm. For this reason, the selection of the individual Z-R type changes the precision of rainfall rates or accumulations (Vieux and Bedient, 1998). To obtain an accurate radar rainfall estimation, it is important to determine and express the errors derived from the reflectivity measurement and the Z-R conversion process. When establishing the Z-R relationship, the availability of the drop size distribution (DSD) instrument, the disdrometer, is of great importance. The disdrometer data consist of the number of raindrops n of diameter D . This instrument provides data for the number and size of rainfall droplets within the sampling volume. Marshall and Palmer (1948) published a Z-R relationship using the exponential DSD data with general parameters of $a=200$ and $b=1.6$. Battan (1973) published a list with 69 different Z-R relationships for varied climatic conditions. However, lack of DSD data restrain the detection of the accurate Z-R relation.

Calheiros and Zawadzki (1987) and Rosenfeld et al. (1993) revealed an approach to determine the relationship of datasets between recorded rainfall intensity by rain gauge and measured reflectivity by weather radar (Z) at the pixel over the rain gauge. However, the lack of synchronizations like incompatibility of volume of rain gauge and radar reflectivity and timing mismatches, reduce the accuracy of Z-R conversion for radar rainfall estimates. To overcome this problem, Calheiros and Zawadzki (1987) proposed a technique, called probability matching, to derive Z-R relation from radar and rain-gauge measurements. In this method equal percentiles of the probability density functions of two datasets are matched. Probability matching method (PMM)

ensures better results in estimating Z–R relationships for non-synchronous datasets as compared to previous method (Atlas et al., 1997). This method seems to be more useful but it requires large and homogeneous sample of simultaneous radar and gauge data (Krajewski and Smith, 1991). In PMM, nature of probability density function of R varies with storm structure and drop size distribution so stratification by rain type is essential (Rosenfeld et al., 1993). Rosenfeld et al. (1994) developed the window probability matching method (WPMM) to improve the deficiency of PMM. WPMM is performed by matching the two datasets taken from small windows centered at the gauges. This radar field window must be small enough to represent rainfall area and large enough to represent rainfall depth. In this method, errors related to displacement of the rain from the center of the radar window may be diminished. Piman et al. (2007) developed a new method, called the window correlation matching method (WCMM) to correct collocation and timing errors in Z-R pairs. These errors are caused by wind and height of the radar. According to the study performed by Piman et al. (2007), errors caused by wind (geometric mismatch) are reduced with the growing space window and errors caused by height of the radar measurement (time mismatch) are decreased with the growing time window.

In the study region, the closest weather radar is located at 1303 m, which is 40 km away from Samsun City (Figure 2.1). This radar is a C-band Doppler weather radar, and it has been serving the Central Black Sea region since July 2012, providing short-term weather forecasts over a 120-km range with 333.33-m spatial resolution. The radar rainfall estimates are obtained from the TSMS, where the Interactive Radar Information System (IRIS) radar software is used to process the radar-based QPE. IRIS was developed by the SIGMET Company, and it uses the Fourier Transform technique to eliminate clutter. The rain product is obtained from the surface rain intensity (SRI) product that uses the Marshall-Palmer (1948) relationship ($a=200$ and $b=1.6$).

Figure 2.5 shows the distribution of gauge stations, location of radar and study area on Digital Elevation Model (DEM). Arrows are drawn on this figure to show radar signal direction on the DEM. Topography between Samsun radar location and gauge stations are demonstrated in Figure 2.6. This figure indicates that there is no blockage of the

radar beam between radar and gauge stations. For the study area, 5 arrows in red color are drawn on the DEM (Figure 2.5). Change in topography through the selected arrows are depicted in Figure 2.7. In this figure, black dots show the boundary of sub-basins in the study area. In all topographic figures, it is seen that there is not any obstruction throughout the radar signal path. Thus, working of weather radar with minimum elevation angle (0.2°) is suitable for the study area and gauge locations.

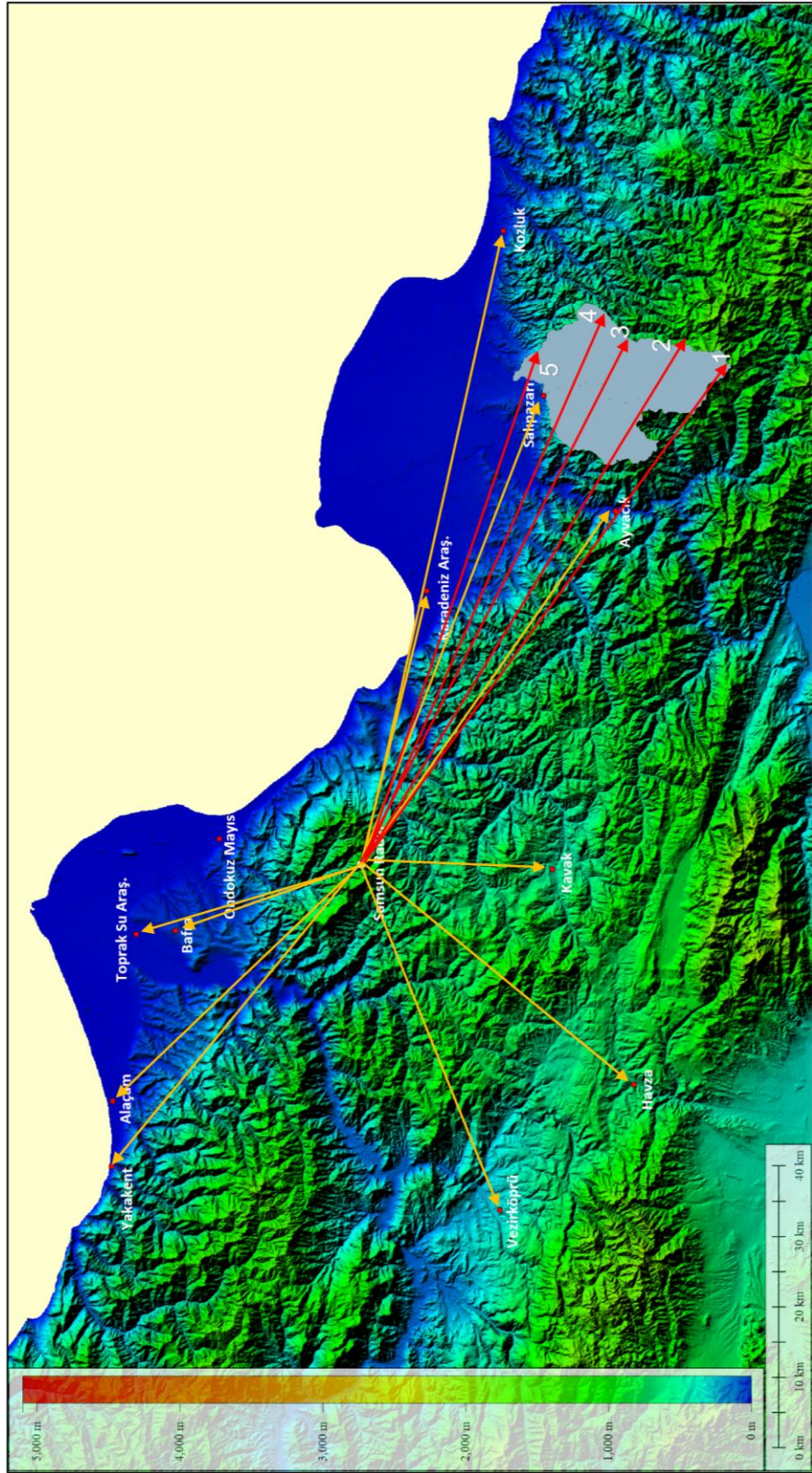


Figure 2.5 Study Area with Rain Gauge Stations on Digital Elevation Model

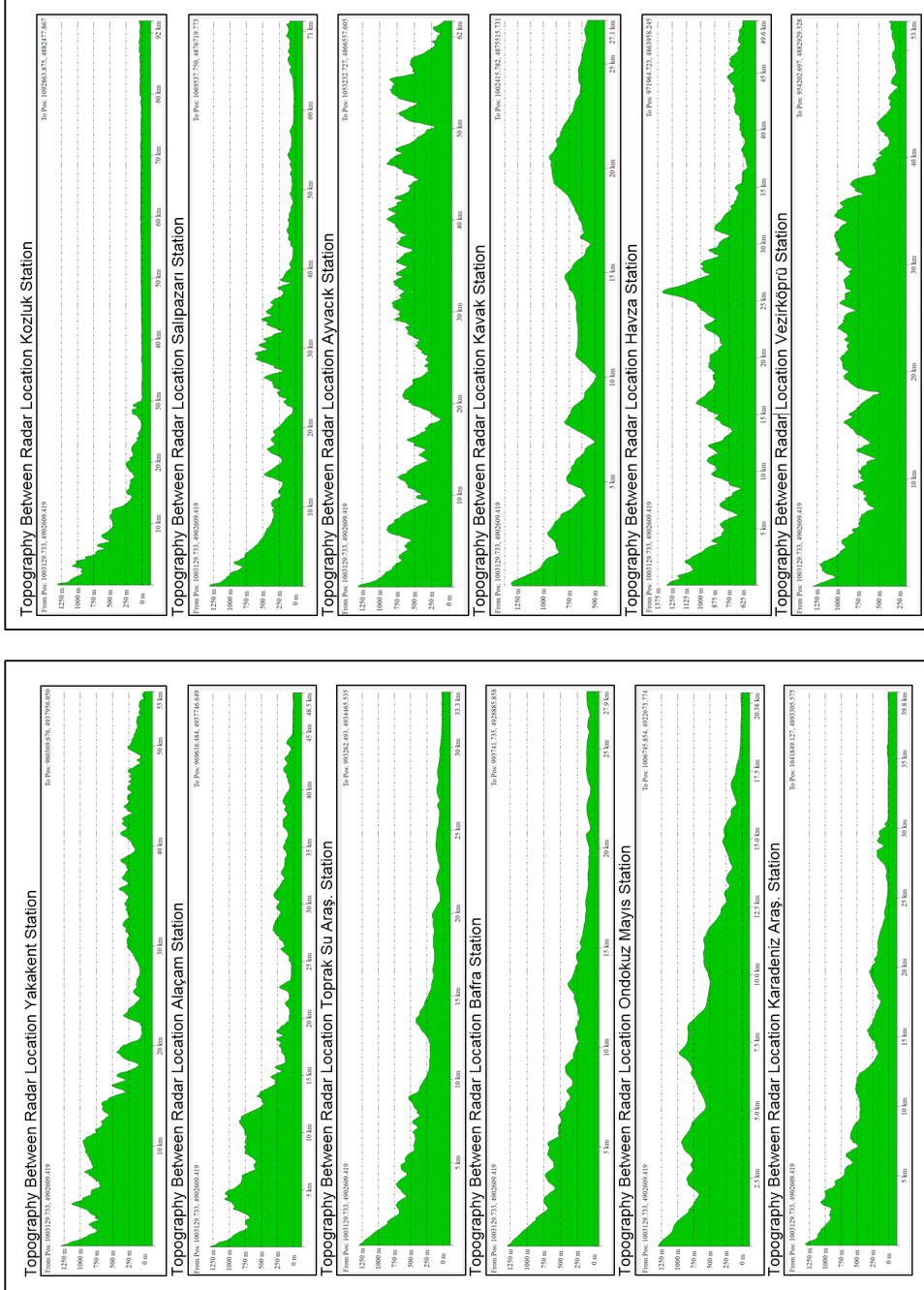


Figure 2.6 Topography Between Radar Location and the Stations

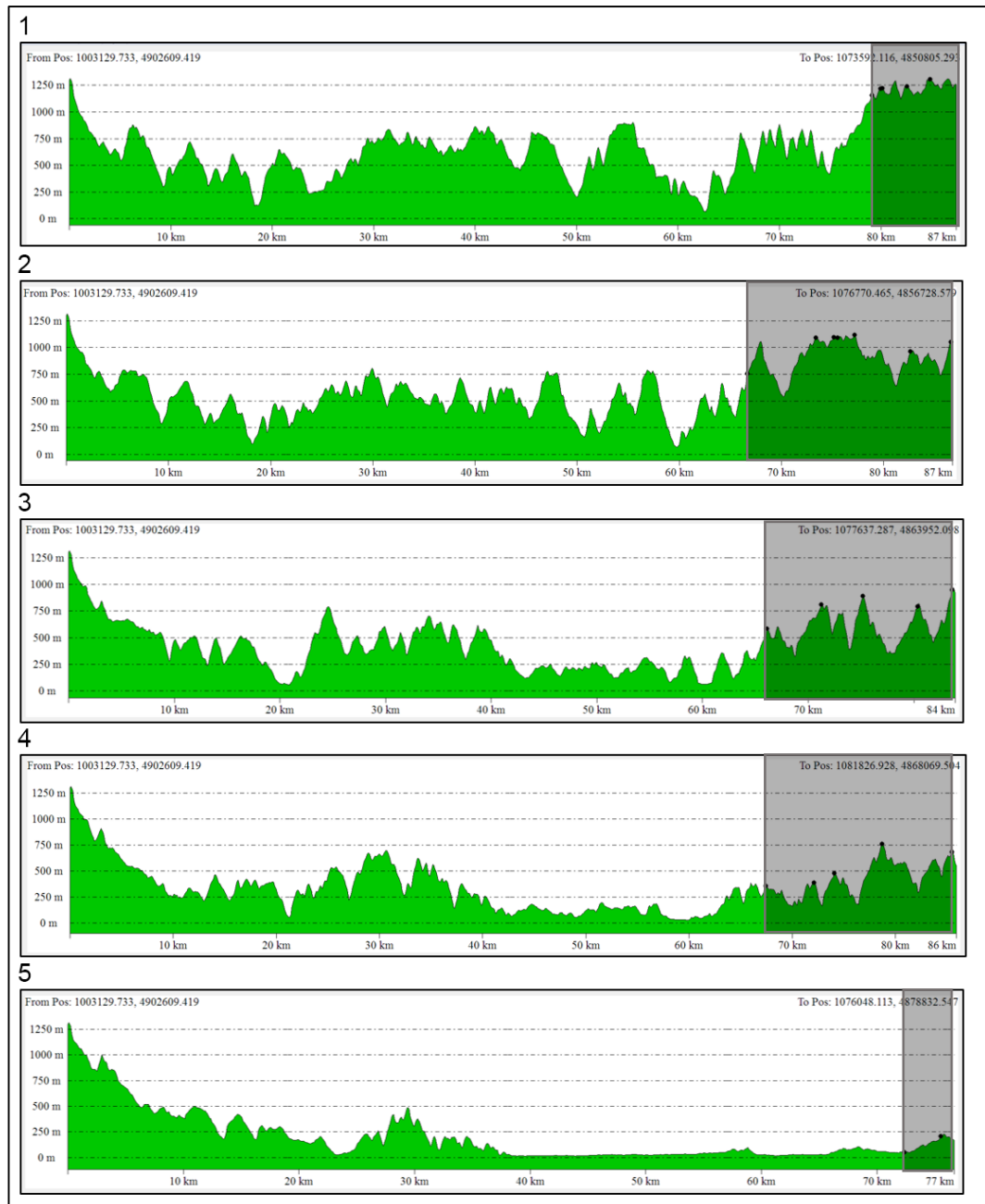


Figure 2.7 Topography Between Radar Location and the Study Area (Grey boxes show the study area)

Samsun weather radar is in operation since July 2012. From this time, events in which cumulative rainfall amounts above 20 mm are inquired and selected. According to these events, data requested from TSMS is presented in the Table 2.3. In this table, stations measuring rainfall over 20 mm are listed with event duration, date and time. Stations in boldface are the closer ones to the study area.

Table 2.3 Requested Radar-based QPE from TSMS

Event	Start		End		Dur. (hr)	Cumulative Rainfall Amount (mm)												
	Date	Time	Date	Time		17622	17623	18132	18133	18134	18536	18539	18540	18541	18542	18544	18538	18545
1	28.02.2012	14:00	01.03.2012	04:00	39	21.8	6											
2	30.05.2012	11:00	31.05.2012	13:00	14	52.2	1.4											
3	30.06.2012	16:00	01.07.2012	08:00	17	82	30.4	14.4	33.7									
4	01.07.2012	16:00	02.07.2012	20:00	29	35.6	37.2	22	22.4	11								
5	07.08.2012	05:00	08.08.2012	17:00	37	110.2	107											
6	18.08.2012	10:00	20.08.2012	15:00	54	48.8	3.4											
7	08.09.2012	10:00	08.09.2012	16:00	7	32.2	3.6											
8	07.11.2012	13:00	12.11.2012	01:00	103	134	119.4	136.8	57.7	61.4								
9	12.12.2012	18:00	14.12.2012	03:00	34	54	49.4	32.7	0.4	25.6								
10	01.08.2013	21:00	02.08.2013	00:00	4	45.4			36.4									
11	20.09.2013	15:00	21.09.2013	19:00	29	22.8	27.4	19.5	19.9	9.7								
12	18.10.2014	03:00	19.10.2014	08:00	30	37	10.4		42.1	6.5	13.4	11.6	41.9	76.3	67.7	33.6		
13	21.11.2014	09:00	22.11.2014	14:00	30	39.8	34	49.3	43.7	30.2	42.4	36.8	33.5	98.9	57.4	24		
14	29.12.2014	22:00	01.01.2015	18:00	69	50.6	86	62	68.7	3.4	32.6	39.9	70	41.3	41.4	28.6		
15	29.03.2014	10:00	30.03.2014	10:00	25	1	3.6	19.1	1.9	0.3	6.6	18.7	3	28	14.4	7.9		
16	05.05.2014	15:00	07.05.2014	02:00	36	5.4	4.6	2.9	0	7.7	16.3	21.3	6.3	39.9	21.7	12.1		
17	25.05.2014	15:00	26.05.2014	09:00	19	12	12.4	10.1	19	0.8	0.9	6.7	4.9	16.6	2.2	0.5		
18	21.07.2014	11:00	21.07.2014	22:00	12	7.4	0	0	11.8	1	0	3.8	64.8	24.2	0.3	22.1	0	
19	06.01.2015	00:00	06.01.2015	22:00	23	41.8	74.4	49.5	42.9	0.7	39.1	42.4	52.1	58	43.8	57.2	46.3	
20	08.04.2015	21:00	11.04.2015	09:00	61	32	28	46.2	23.7	21.3	26.1	40.9	31.1	54.8	55.5	45.9	50.2	

The Salıpazarı Station is located on the boundary and the Kozluk Station is 24 km far away from the Salıpazarı Station. According to this request, it is informed that events observed before the year 2014 have 240 km radar range format. However, the coordinate information about the data taken from the TSMS is in 120 km radar range format and there is not any information about the coordinate transformation between 240 km range of radar and gauge data. For this reason, workable number of events is restricted from 20 to 8. Workable radar-based QPE received from TSMS are given in Table 2.4. Since event 13 includes 2014 flood event, it is excluded from the dataset in Table 2.4. In this table number of missing values and their dates and times are also listed.

Table 2.4 Available Radar-based QPE with Their Time Spans and Missing Data

Event	Start		End		Dur. (hr)	Number of missing data	Missing Data (Date, Time)
	Date	Time	Date	Time			
12	18.10.2014	03:00	19.10.2014	08:00	30	1	18.10.2014,03:00
14	29.12.2014	22:00	01.01.2015	18:00	69	7	between 31.12.2014,01:00 and 31.12.2014,07:00
15	29.03.2014	10:00	30.03.2014	10:00	25	0	-
16	05.05.2014	15:00	07.05.2014	02:00	36	0	-
17	25.05.2014	15:00	26.05.2014	09:00	19	1	26.05.2014,09:00
18	21.07.2014	11:00	21.07.2014	22:00	12	0	-
19	06.01.2015	00:00	06.01.2015	22:00	23	1	06.01.2015,21:00
20	08.04.2015	21:00	11.04.2015	09:00	61	4	10.04.2015,10:00, between 08.04.2015, 11:00 and 08.04.2015, 13:00

2.2.2 Soil Data

The geology map needed for the study area is obtained from General Directorate of Mineral Research and Exploration and the soil data pertaining to land cover and land use are provided by CORINE (Coordinate Information on the Environment) land data base and the Ministry of Agriculture respectively, both of which indicating that the study area has uniform soil type and land cover. From soil data, it is seen that majority of the study area has basalt-andesite agglomerate soil type (Figure 2.8 (a)) and forest and podzolic soil (grey and brown) take part in almost all area (Figure 2.8 (b) and (c)).

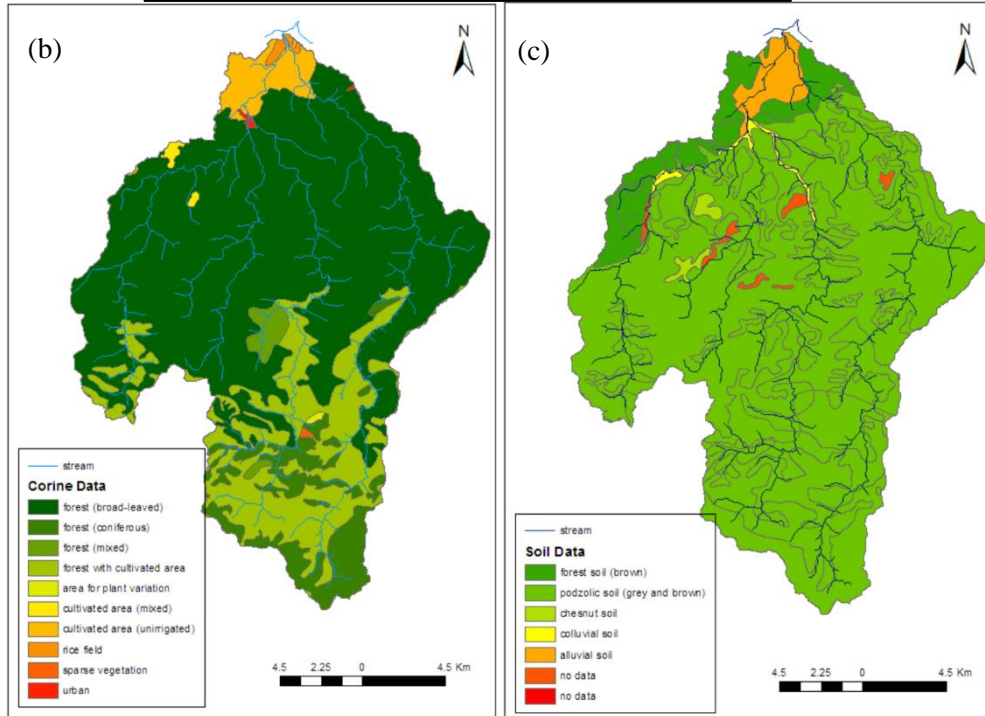
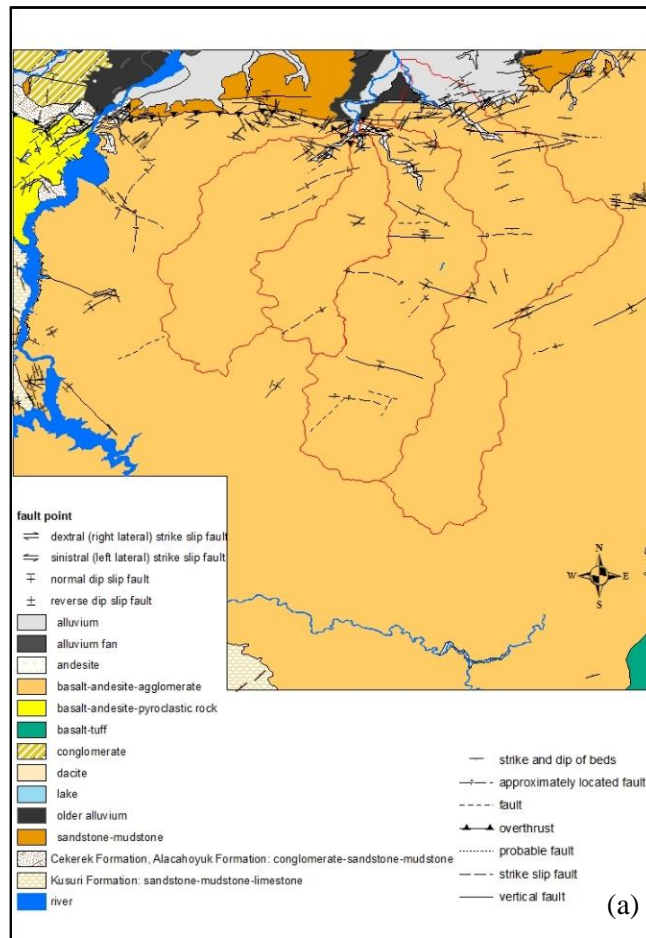


Figure 2.8 Soil Data Taken from Directorate of Mineral Research and Exploration (a), Land Cover (b) and Land Use Data (c)

2.2.3 Runoff Data

For the runoff data, hourly discharge values, obtained from State Water Works (DSI), which are observed at the Gökçeli Station during the flood events are used (Figure 2.1).

CHAPTER 3

COMPARISON OF THE RAINFALL PRODUCTS

3.1 General

Accurate rainfall observations with high spatial and temporal resolutions are required for hydrological modeling and flood studies. Rain gauges, satellite products, numerical model forecasts and weather radar rainfall estimates are generally used for this purpose. In this section, first, radar-based QPE is analyzed using the matching techniques that are used in the literature and evaluations are done using the statistical measures. Second, flood events are evaluated by the information provided from WRF model. Third, comparison of rainfall products is performed in point and areal based manner. Last, summary of the processes and discussion of results are presented.

3.2 Radar-based QPE Matching Techniques

In this study, to find appropriate matching technique and similarity between radar and gauge data, three methods namely; direct matching method, probability matching method and window correlation matching method are studied.

3.2.1 Direct Matching Method (DMM)

In the literature this approach is called traditional matching method (Piman et al., 2007). In this method (Figure 3.1) it is assumed that rainfall drops from the atmosphere to the rain gauge vertically and radar rain intensity at the measured altitude is the same as at the surface of rain gauge (Calheiros and Zawadzki, 1987).

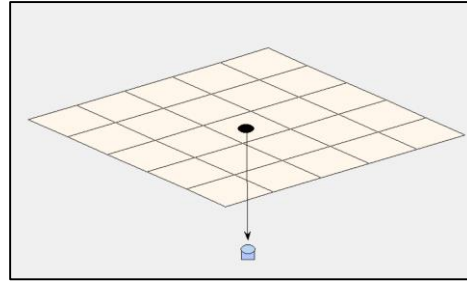


Figure 3.1 Direct Matching Method

3.2.2 Probability Matching Method (PMM)

This method was proposed by Calheiros and Zawadzki (1987) to eliminate errors coming from timing and collocation problems. The idea behind this method is assumption of reflectivity observed from radar and rain intensity measured from the rain gauge has the same probability of occurrence. Therefore, this method is based on matching the CDFs of radar and gauge datasets as described in Equation 3.1 and Figure 3.2.

$$\int_{R_i}^{\infty} P(R)dR = \int_{Z_i}^{\infty} P(Z)dZ \quad \text{Equation (3.1)}$$

$P(R)$ and $P(Z)$ are the probability density function of gauge rainfall intensity and radar reflectivity respectively.

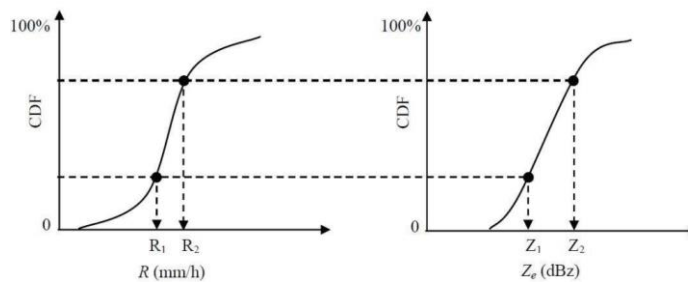


Figure 3.2 The Probability Matching Method (Source Piman et al, 2007)

3.2.3 Window Correlation Matching Method (WCMM)

This method was proposed by Piman et al. (2007) to reduce timing and collocation errors caused by wind and height of the radar measurement, respectively. The possible matching areas in this method consist space and time window (Figure 3.3). Space window is used to reduce geometric mismatch caused by wind, time window is used to reduce time error caused by the height of the radar measurement. The process of this method consists of matching two datasets searching for the value that gives maximum correlation coefficient.

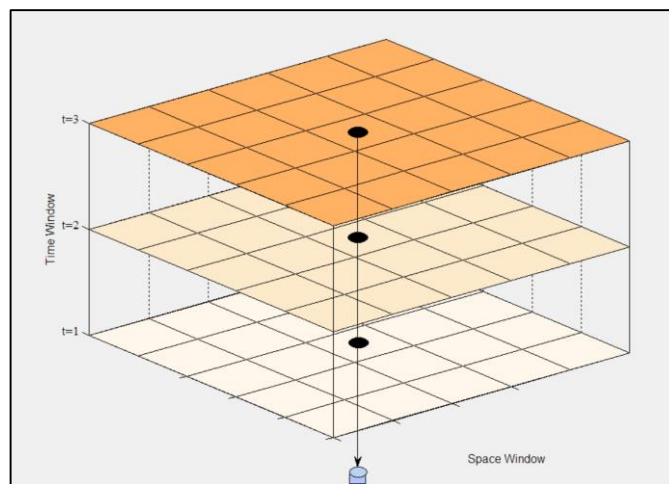


Figure 3.3 Window Correlation Matching Method (5x5 space window and 3 time window)

3.2.4 Evaluation of the Methods

Output data with 333.33 m. spatial resolution obtained from IRIS software are processed with Matlab to extract radar-based QPE in 5x5 window with correct coordinates (Figure 3.4).

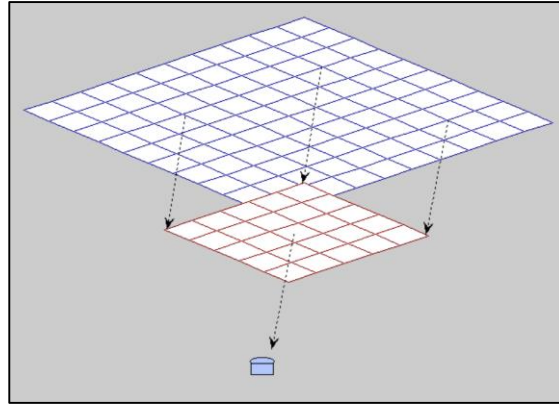


Figure 3.4 Data Extraction in 5x5 Space Window

Before starting the study, datasets which are rainfall estimation from radar and rainfall measurement from rain gauge are analyzed in a time series. It is seen that for all stations, there is a one hour synchronization error. This means that, there is a timing mismatch between two datasets. For Alaçam Station, time mismatch can be seen in Figure 3.5. Although, histogram is more appropriate to demonstrate the distribution of rainfall, time series graph can be useful to detect timing mismatch (Figure 3.5). In Figure 3.5, it is seen that radar captures the start of rainfall at time 12, but gauge records at time 11. Also the second peak of the flood event is captured by radar at time 29 and recorded by gauge at time 28. The label “radar_average” means the average of 25 radar cell rainfall amount in a 5x5 space window.

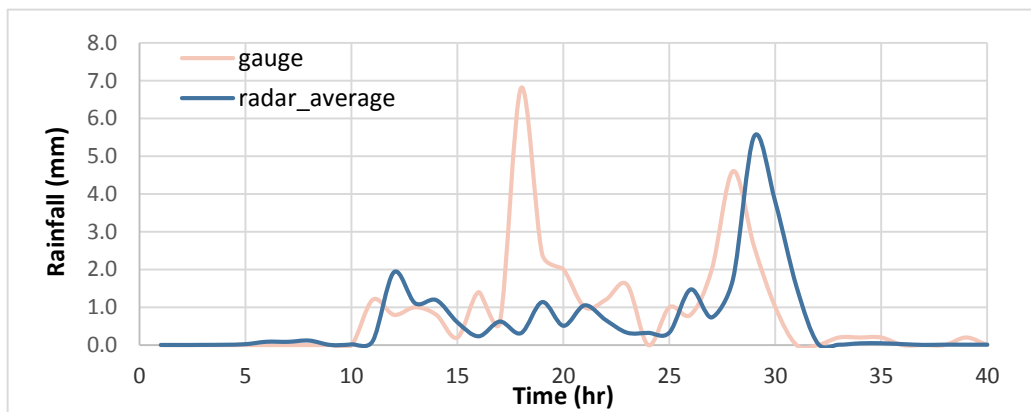


Figure 3.5 Gauge and Radar Rainfall Distribution in a Time Series for Alaçam Station from 21/11/2014 (00:00 AM) to 22/11/2014 (15:00 PM)

This error is confirmed by TSMS. For the same time zone, radar-based QPE is initiated with the start of the hour, whereas ground data are referenced to the end of the hour, which is the reason of the time shift between two datasets. As TSMS is mostly interested in cumulative rain amount, this error was unnoticed.

After time correction, mentioned techniques are applied to the dataset. Direct matching method is the same as 1X1 space window in window correlation matching method. In order to see space effect (Figure 3.6) on results, r values computed for all stations regarding space window. 1x1, 3x3 and 5x5 space window results and can be seen in Table 3.1.

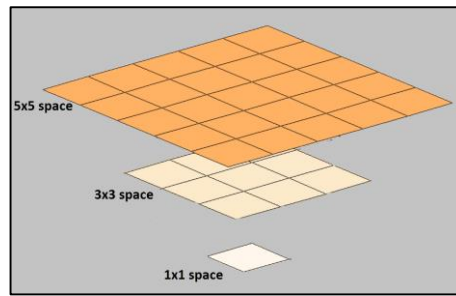


Figure 3.6 Space Window Types

Table 3.1 Correlation Coefficient Results with Different Space Windows and PMM

Station Name	2014				2015				2016			
	Space Window			PMM	Space Window			PMM	Space Window			PMM
	1X1	3X3	5X5		1X1	3X3	5X5		1X1	3X3	5X5	
Bafra	0.78	0.78	0.79	0.81	-	-	-	-	0.93	0.94	0.94	0.56
Alaçam	0.67	0.67	0.67	0.55	-	-	-	-	0.94	0.94	0.93	0.76
Karadeniz A.	0.9	0.91	0.91	0.88	0.98	0.98	0.99	0.19	0.85	0.85	0.85	0.84
Topraksu A.	0.91	0.91	0.92	0.91	0.83	0.84	0.85	0.82	0.79	0.80	0.80	0.89
Vezirköprü	0.9	0.90	0.89	0.86	-	-	-	-	0.87	0.87	0.88	0.73
Ayvacık	0.45	0.45	0.43	0.18	0.83	0.82	0.81	0.76	0.52	0.53	0.54	0.53
Çarşamba	0.87	0.87	0.87	0.85	0.58	0.67	0.78	0.77	0.58	0.61	0.63	0.64
Havza	0.71	0.70	0.70	0.71	-	-	-	-	0.40	0.40	0.40	0.53
Kavak	0.91	0.91	0.91	0.93	0.47	0.49	0.52	0.47	0.85	0.85	0.85	0.81
Ondokuz M.	0.83	0.84	0.85	0.77	0.51	0.50	0.51	0.50	0.41	0.41	0.42	0.43
Salıpazarı	0.85	0.86	0.85	0.73	-	-	-	-	0.61	0.61	0.61	0.66
Kozluk	0.61	0.62	0.63	0.63	0.96	0.96	0.96	0.07	0.55	0.55	0.55	0.52
Yakakent	0.82	0.82	0.82	0.72	-0.01	-0.01	-0.01	-0.02	0.88	0.88	0.88	0.32

The results of space windows (Table 3.1) show that change of space window 1x1 type to 5x5 type does not improve the results dramatically. However, studying with 5x5 window type seems to be more appropriate because majority of the stations give best result in 5X5 window space.

Using received data (Table 2.4, 8 events), first, probability matching method is applied for each station. In this method, flood events data are excluded from the general dataset for verification. Using remaining dataset, rainfall magnitudes are ranked and according to this, cumulative probability curves are constructed for each station. Figure 3.7 (a) shows the cumulative distribution function (CDF) of two datasets where 261 rainfall data pairs are used.

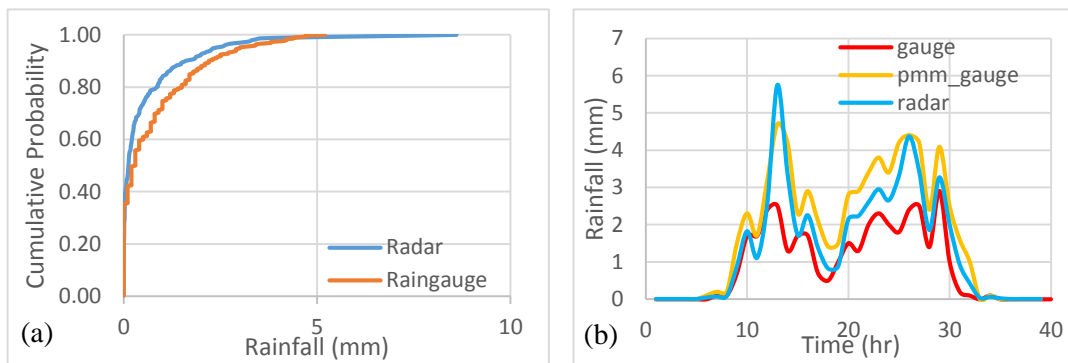


Figure 3.7 CDF Curve of the Kavak Station (a) and Rainfall Distribution with three Datasets for 2014 Flood Event Day (b)

Using radar-based QPE that corresponds to Kavak Station for the flood event day, new gauge values are read from CDF curve of Kavak Station (Figure 3.7 (a)). For the 2014 flood event day, rainfall values of observed gauge, radar and estimated gauge values (pmm_gauge) from CDF curve are drawn in time series graph (Figure 3.7 (b)). From Figure 3.7 (b), it is seen that estimated gauge values (pmm_gauge) seem not to be closer to the observed gauge values. The first peak of the rainfall is captured well from CDF curve reading. However, it is noticed that the bottom and the peak values rather than the first one (pmm_gauge) do not approach the observed ones; values are overestimated and become distant. In overall, all estimated values are shifted by some proportion. This method is applied to all stations for three flood events and their CDF

curves and time series rainfall graphs of the 2014 flood event are given in Appendix A. The correlation coefficients between estimated gauge values and observed gauge ones for PMM are given in Table 3.1. Table 3.1 shows that, only 2 stations for the 2014 flood event and 5 stations for the 2016 flood event give better correlation results in PMM compared to WCMM. For the 2015 flood event, all stations show better correlation results in WCMM. Therefore, it can be said that for these events remarkable enhancement is not achieved in PMM computation. For this reason, in the next stages of this study WCMM (5X5 data window) will be used for point based comparisons.

For the events, excluding flood data, correlation coefficients between two datasets and their assessment factors, AF, (cumulative radar rainfall/ cumulative gauge rainfall) are calculated and results are presented in Table 3.2 and Table 3.3 respectively.

Table 3.2 Correlation Coefficient between Estimated and Observed Rainfall Amounts for Each Events with Clustering Months and Color Coding

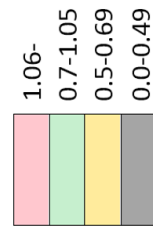
Event	Date	Dur (hr)	Cluster	17622	18541	18540	18132	17623	18539	18134	18545	18538	18536	18542	18544	18133
				Baġra	Ondokuz Mayıs	Kavak	Karadeniz Arş.	Alaçam	Havza	Veir- Köprü	Yakakent	Çarşamba	Ayvacak	Salıpazarı	Kozluk	Toprak Su Arş.
18	21.07.2014	12	1	0.98	0.92	0.97	#DIV	#DIV	#DIV	1.00	#DIV	0.68	0.79	0.95	0.21	0.91
12	18.10.2014	29	2	0.96	0.81	0.71	#DIV	#N/A	0.71	0.95	0.66	0.94	#N/A	0.78	0.60	0.86
19	06.01.2015	22	3	0.75	0.48	0.89	0.89	0.35	0.85	0.02	0.66	0.85	#N/A	0.91	0.82	0.82
14	29.12.2014	62	3	0.71	0.55	0.44	0.34	0.43	0.58	0.01	-0.03	0.76	#N/A	0.77	0.61	0.61
15	29.03.2014	25	4	0.80	0.58	0.56	0.51	0.61	0.18	0.28	0.66	0.15	0.44	0.69	0.52	0.84
16	05.05.2014	36	4	0.94	0.95	0.90	0.98	0.79	0.94	0.99	0.62	0.82	0.82	0.78	0.76	#DIV
17	25.05.2014	18	4	0.98	0.86	0.92	0.95	0.98	0.46	0.98	0.71	0.83	0.85	0.95	0.29	0.79
20	08.04.2015	57	4	0.40	0.68	0.63	0.78	0.45	0.71	0.83	0.35	0.87	0.71	0.65	0.67	0.47

cluster	months
1	6-7-8
2	9-10-11
3	12-1-2
4	3-4-5

0	very weak
0.20	weak
0.40	moderate
0.60	strong
0.80	very strong

Table 3.3 Assessment Factors (cumulative radar rainfall amount /cumulative gauge rainfall amount) for Each Event and Station

Event No.	17622	18541	18540	18132	17623	18539	18134	18545	18538	18536	18542	18544	18133
	Bafra	Ondokuz Mayıs	Kavak	Karadeniz Araş.	Alaçam	Havza	Vezirköprü	Yakakent	Çarşamba	Ayvacık	Salıpazarı	Kozluk	Toprak Su Araş.
12	0.30	0.22	0.22	#DIV	#N/A	0.21	0.51	0.31	0.42	#N/A	0.37	0.46	0.26
14	0.40	0.30	1.00	0.43	0.36	1.05	9.56	1.02	0.53	#N/A	0.47	0.35	0.30
15	4.59	2.23	0.34	0.50	0.87	0.44	4.64	0.39	0.60	0.22	0.30	0.25	2.16
16	0.90	0.69	0.37	0.39	0.76	0.25	0.61	0.34	0.36	0.25	0.25	0.34	#DIV
17	0.77	0.79	0.87	0.52	0.67	0.19	0.68	12.92	0.97	0.34	0.30	0.52	0.54
18	0.91	0.30	0.41	#DIV	#DIV	#DIV	0.67	#DIV	0.96	0.35	0.24	0.36	0.85
19	0.41	0.41	0.54	0.44	0.33	0.56	31.30	0.55	0.53	#N/A	0.62	0.82	0.42
20	0.80	0.65	0.49	0.61	0.71	0.56	0.94	0.42	0.56	0.63	0.57	0.59	0.94



In Table 3.2, for each event and station, r computation results are given. In order to see season and event duration effects on r results, color coding with respect to r values is applied on the table. Evans (1996) separated absolute r values between 0 and 1 into 5 categories with 0.20 unit interval. And these intervals are defined as very weak (0-0.20), weak (0.20-0.40), moderate (0.40-0.60), strong (0.60-0.80) and very strong (0.80-1). For season effect to get easier representation, months are clustered into 4 categories. Clustering and color coding of r indicate that r values are not related to specific season or length of the event duration. Although, Marshall-Palmer relation generally behaves well on stratiform type of rainfall in cold season, which corresponds to cluster 3 in our case, results do not show significant increase with respect to the other clusters. Moreover, events that take long time like event 14 and event 20 do not affect the correlation results positively. In Table 3.2, abbreviation of “#DIV” and “#N/A” show that station does not measure rainfall which means sum of the rainfall amount during event is zero and station is not in operation respectively. In order to get more significant expression and generalize the situation, there should be more data to study on each season.

The assessment factors (AF) (cumulative rainfall amount of radar to cumulative rainfall amount of gauge) are divided into 4 categories with color coding and listed in Table 3.3. The results demonstrate that the majority of the AF values (98/117) are smaller than 1.05. This means radar rainfall estimates with Marshall-Palmer relation for this study area underestimate the rainfall amounts regardless of the season type. The rational assessment of very strong values (in dark green) in Table 3.3 has a significant point. For instance, comparing to the other events, in event 18 (21.07.2014) less or no rainfall is observed by stations Karadeniz Araş, Alaçam, Havza, Vezirköprü and Yakakent. Among these stations Vezirköprü has high r results due to the short rainfall duration, small cumulative rainfall amount and being a number of zeros (no rainfall observation) during the event. However, excluding zero pairs from both datasets for r computation may change the data continuity in time. That means, after the event starts, in some hours rain may take a pause, in this time exclusion may decrease the performance of the study. Because of this reason, especially in point

comparison study, start and end of the event time are selected carefully and time extending is not carried out in events.

3.5 Evaluation of the Flood Events

Since the operational use of Samsun weather radar, three flood events observed in the study area. Information about the rainfall types related to these events are obtained from the WRF precipitation estimates (Figure 3.8). According to the rainfall forecast results of the WRF Numerical Model, 22nd November 2014, only 2% of the total rainfall is identified as convective rainfall in the grid where the Salıpazarı Station is located (Figure 3.8 (a)). In the same grid, the WRF model forecasts a total rainfall amount of 111 mm for the flood event day and roughly that amount of rain mainly distributed over the study area (Figure 3.8 (c)). In terms of gauge, radar and the HE product, cumulative rainfall amount is calculated as 107.7 mm, 73.5 mm and 21.9 mm respectively. Gauge and radar-based QPE show similar distribution pattern like WRF data but the HE product shows underestimation, nearly value of between 30 – 40 mm (Figure 3.9 (a), (b) and (c)).

According to Figure 3.8 (d), the forecasted rainfall on 2nd August 2015 is mainly convective and that takes place along the river direction. In the Salıpazarı Station, the total forecasted rainfall in 72 hours is calculated as 139.2 mm and 91% of this amount (127.20 mm) is defined as cumulative type of rainfall and the rest (12.02 mm) is defined as non-cumulative type of rainfall by WRF data (Figure 3.8 (e) and (f)). The cumulative rainfall amount observed by the rain gauge stations is given in Figure 3.9 (d). According to this figure, it is seen that the flow monitoring station is represented by three rain gauge stations, Ayvacık (75.25%), Çarşamba (23.0 %) and Kozluk Beldesi (1.75 %). The closest station to the study area, the Salıpazarı Station, was not in operation during the flood event. Hence, using Thiessen Polygon method, rainfall amount is calculated as 45.8 mm for the location of Salıpazarı Station. The cumulative rainfall amounts of other datasets, radar and the HE product, are depicted in Figure 3.9 (f) and (e) respectively.

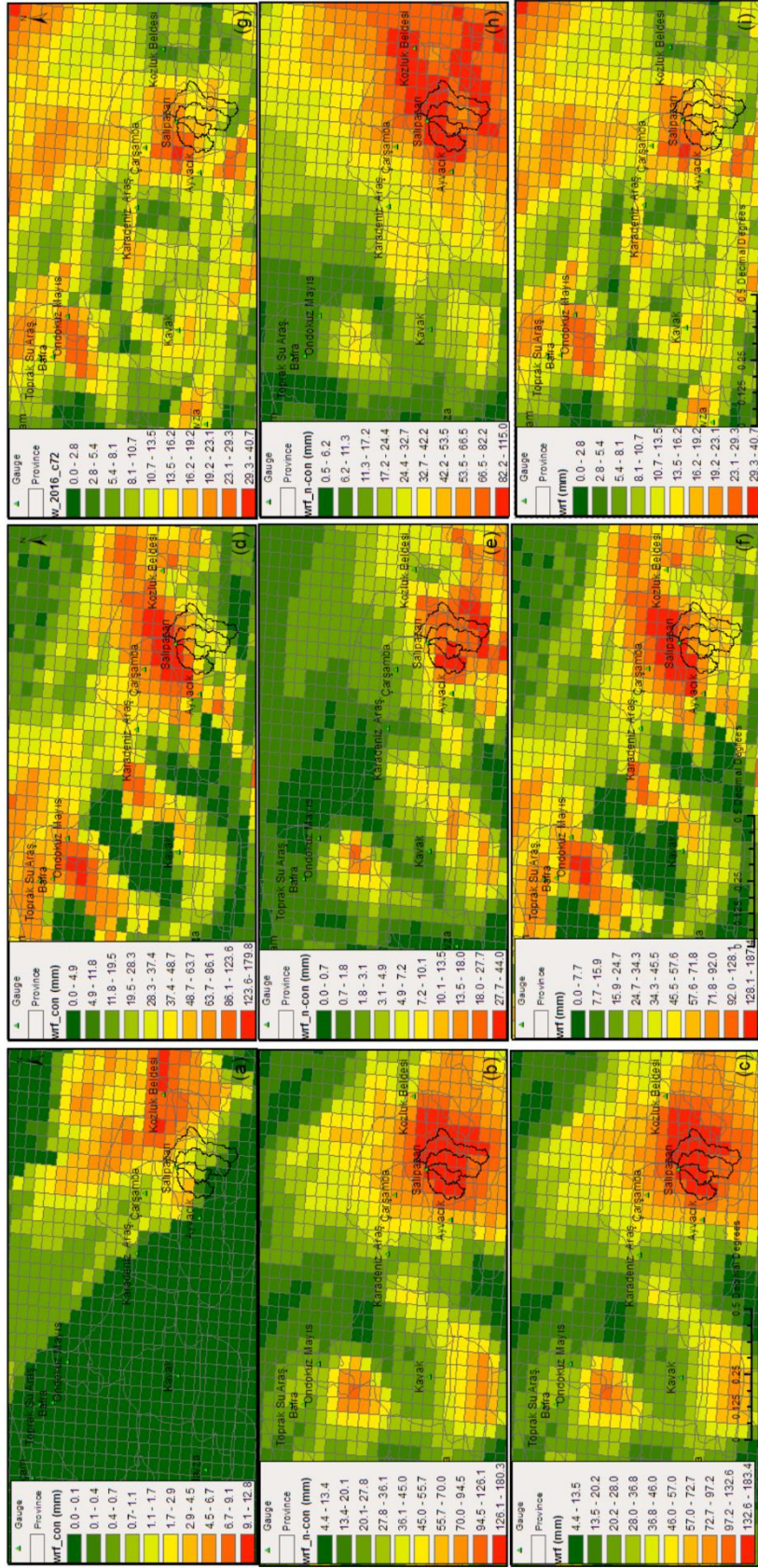


Figure 3.8 Cumulative Distribution of WRF Precipitation Data (mm) for 72 hours: Columns (1), (2) and (3) show flood events on 22nd November 2014, 2nd August 2015 and 28th May 2016 respectively. Rows (1), (2) and (3) show distribution of rainfall types: convective, non-convective and both respectively.

From these figures, it is seen that the spatial distribution of radar rainfall data resembles to WRF precipitation but the cumulative amounts of rain are quite different. At Salıpazarı Station, radar-based QPE is 56.43 mm which is 2/5 of the WRF result. Comparison with the observed rain shows that cumulative of radar rainfall amount is 1.23 times of cumulative of rain gauge amount. On the other hand, the lowest amount of rain is estimated by the HE product. According to Figure 3.9 (e), the HE product estimates almost no rain in near location to the Salıpazarı Station. In upstream part of the sub basins 3 and 4, the HE product estimates cumulative rainfall approximately 8 mm.

Unlike the flood event occurred on 2nd August 2015, the forecasted rainfall on 28th May 2016 is partly convective. According to WRF precipitation dataset, the total forecasted rainfall in 72 hours is calculated as 107.85 mm and 21% of this amount (22.58 mm) is defined as convective type of rainfall and the rest (85.27 mm) is defined as non-cumulative type of rainfall at the location of the Salıpazarı Station (Figure 3.8 (g), (h) and (i)). The cumulative rainfall distribution of the rain gauge stations (Figure 3.9 (g)) shows that the Salıpazarı Station represents the study area best and the cumulative rainfall amount is calculated as 95.2 mm. The distributions of cumulative rainfall amounts of other datasets show that radar-based QPE and the HE product resemble to WRF precipitation data. However, the cumulative rainfall amounts are different. At Salıpazarı Station, radar-based QPE and the HE product estimate rainfall value as 43.66 mm and 75.6 mm respectively (Figure 3.9 (i) and (h)).

3.6 Comparison of the Rainfall Products

3.6.1 Comparison of the Rainfall Products in Point Based Manner

The performance of radar, WRF and the HE product in estimating heavy rainfall events are summarized in Figure 3.10 and Figure 3.11 respectively. Box plots show the root mean squared errors (rmse) (Figure 3.10 (a)) and correlation coefficients (Figure 3.10 (b)) obtained from the average of 13 stations' results for each rainfall sources and events. The necessary data for box plots can be seen in appendix B. The mean statistic equations for bias (mm), RMSE (mm) and r are demonstrated below.

$$RMSE = \sqrt{\frac{\sum_{i=1}^n (X_{obs,i} - X_{est,i})^2}{n}} \quad \text{Equation (3.2)}$$

$$BIAS = \frac{1}{n} \sum_{i=1}^n (X_{obs,i} - X_{est,i}) \quad \text{Equation (3.3)}$$

$$r = \frac{\sum_{i=1}^n (X_{obs,i} - \bar{X}_{obs})(X_{est,i} - \bar{X}_{est})}{\sqrt{\sum_{i=1}^n (X_{obs,i} - \bar{X}_{obs})^2 \sum_{i=1}^n (X_{est,i} - \bar{X}_{est})^2}} \quad \text{Equation (3.4)}$$

where X_{obs} is the observed rainfall value (gauge) and X_{est} is the estimated rainfall value at time i . As evidenced by higher median correlation coefficient value and lower median of RMSE value, radar-based QPE shows the most accurate estimate with respect to other two rainfall sources for all events. Considering the events, on 22nd November 2014, radar-based QPE shows the best results, which is most probably due to the stratiform rainfall type. As mentioned earlier, the radar-based QPE is achieved by using Marshall Palmer relationship ($a=200$ and $b=1.6$) that is optimum for general stratiform rainfall. With this relation, general trend of the rainfall in 2014 is well captured by the radar rainfall estimation, but within that sequence, the radar data underestimates the rainfall amounts, especially at peak values. Considering the rainfall types, WRF and the HE product show their best results in 2014 because the results of RMSE are lower and correlation coefficients are higher for both datasets. However, interquartile range of the box plots show an increase in flood events observed on 2nd August 2015 and 28th May 2016 for all rainfall sources due to the spatio-temporal dynamic range of the convective rainfall. Among the rainfall sources, the HE product shows an exception for the box plot range in 2015 due to failing to estimate rainfall in 72 hrs. time span. Bias results based on stations' averages for radar, WRF and the HE product are shown for hourly rainfall and for each event in Figure 3.11. Generally, radar-based QPE and the HE product have negative biases, regardless of the rainfall type. Also, WRF precipitation data shows negative biases except the flood event observed in 2015, which is mainly convective rainfall type. Although the performance of the HE product is expected to be better in convective rain, neither distribution of

the product (Figure 3.9 (e)) nor statistical measures (Figure 3.10 and Figure 3.11) shows sensible results for the flood observed on 2nd August 2015. However, considering all flood events, the HE product shows similar bias like other datasets in 2016 flood event, which is partly convective rainfall. Box plots related to 2016 flood event show that estimated rainfall amounts of WRF and the HE product have time inconsistencies with the rain gauge data. Therefore, hydrologic model application including these rainfall sources may reveal valuable insight about the rainfall assessment.

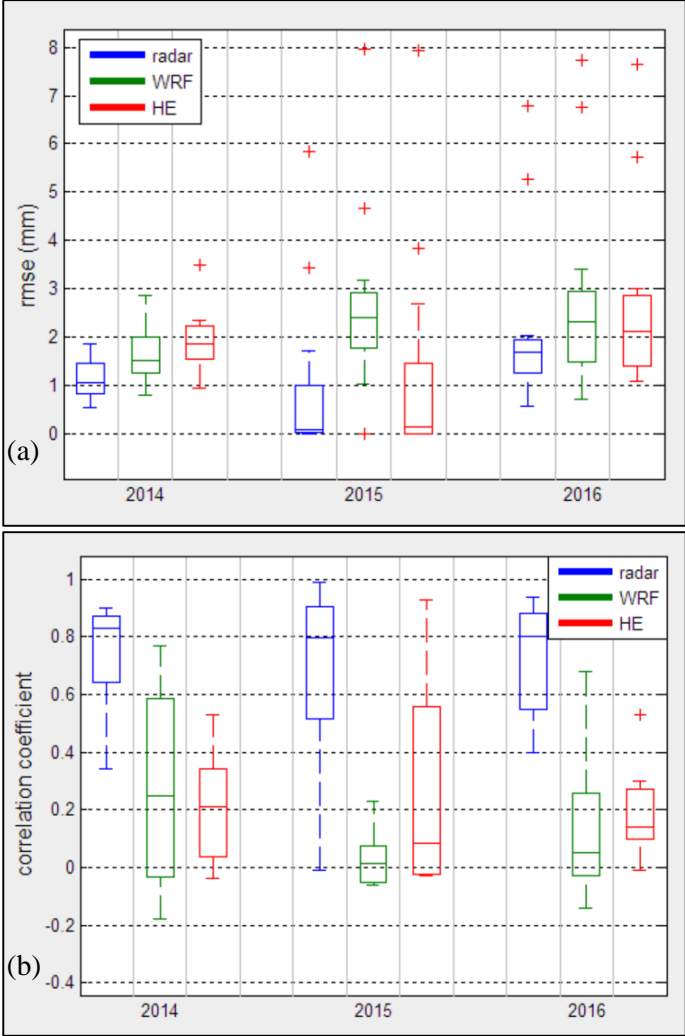


Figure 3.10 Box Plots of 3 Flood Events for Radar, WRF and the HE Product, Root Mean Squared Error (rmse) (a) and Correlation Coefficient (b) (Averaged for 13 Rain Gauge Stations)

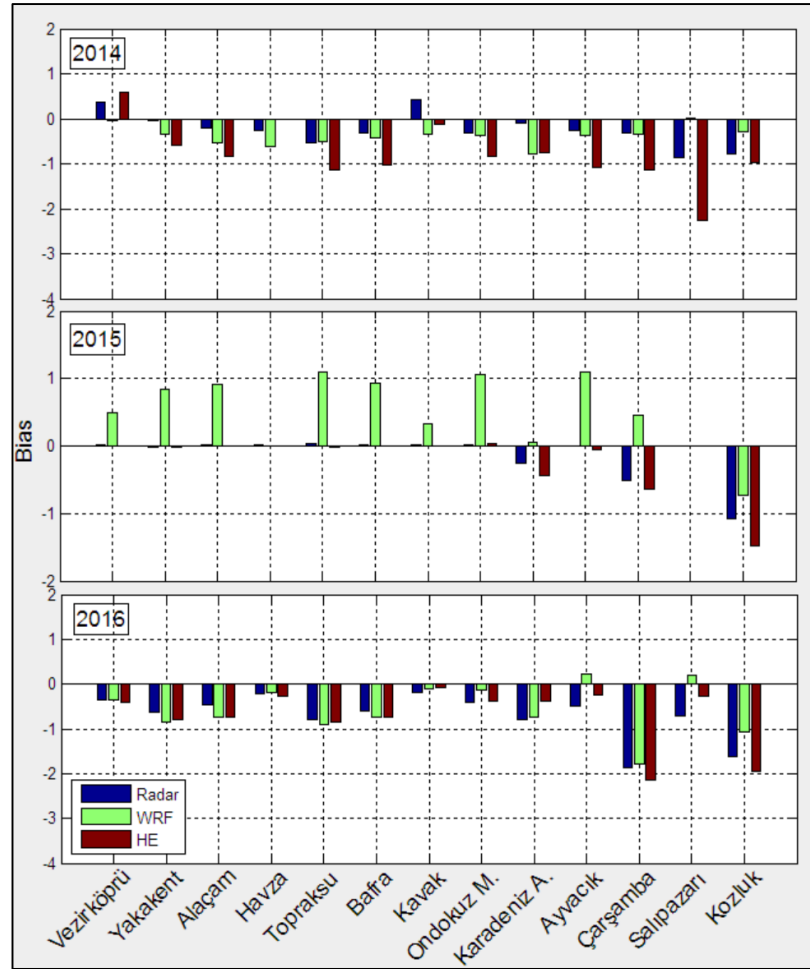


Figure 3.11 Averaged Bias (mm) of Radar, WRF and the HE Product at Hourly Interval for each Station and Flood Event Year

3.6.2 Comparison of the Rainfall Products in Areal Based Manner

In areal comparisons, Thiessen Polygon method is applied to rain gauge data to determine the mean rainfall of the basin. Figure 3.9 (a), (d) and (g) show the Thiessen polygons for flood events. It is seen that for 2014 and 2016 flood events, areal mean rainfall of the study area is calculated using two stations, Salıpazarı and Ayvacık whereas, for the flood event observed on 2nd August 2015, due to the breakdown of Salıpazarı Station, calculations are done using Çarşamba, Ayvacık and Kozluk Beldesi Stations.

For radar-based QPE, areal rainfall in the subbasins is calculated using arithmetic mean method due to the excess number of data. The number of radar points in the subbasins and their locations are given in Table 3.4 and Figure 3.12 (a) respectively. It should be stated that the radar point depicted in Figure 3.12 (a) represents the center of radar pixel. The spatial resolution of radar data is 333.33 m.

Table 3.4 Number of Radar Point Data in Sub-basins

basin	basin1	basin2	basin3	basin4	total
number of data	669	422	983	1214	3288

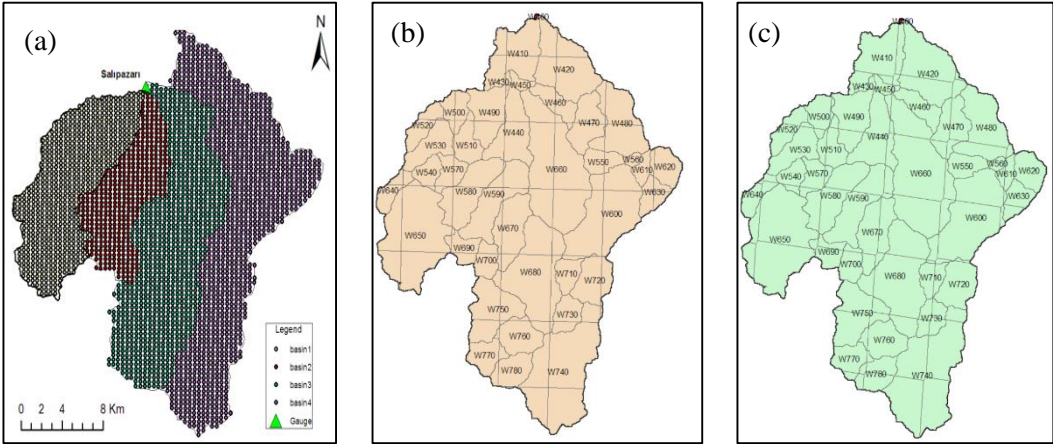


Figure 3.12 Radar Point Locations (a) and the distribution of the HE Product (b) and WRF data (c)

The rainfall amounts related to the HE product and WRF data are calculated for each sub-basin proportional to areas of the products over the sub-basins (Figure 3.12 (b) and (c)).

For the three flood events, the rainfall distribution in time is represented by Figure 3.13. Rainfall products in the figure show the average of sub-basins that have contributions to the flow monitoring station, these are sub-basin 1, sub-basin 2 and sub-basin 3. Other individual graphs for the sub-basins are given in Appendix C.

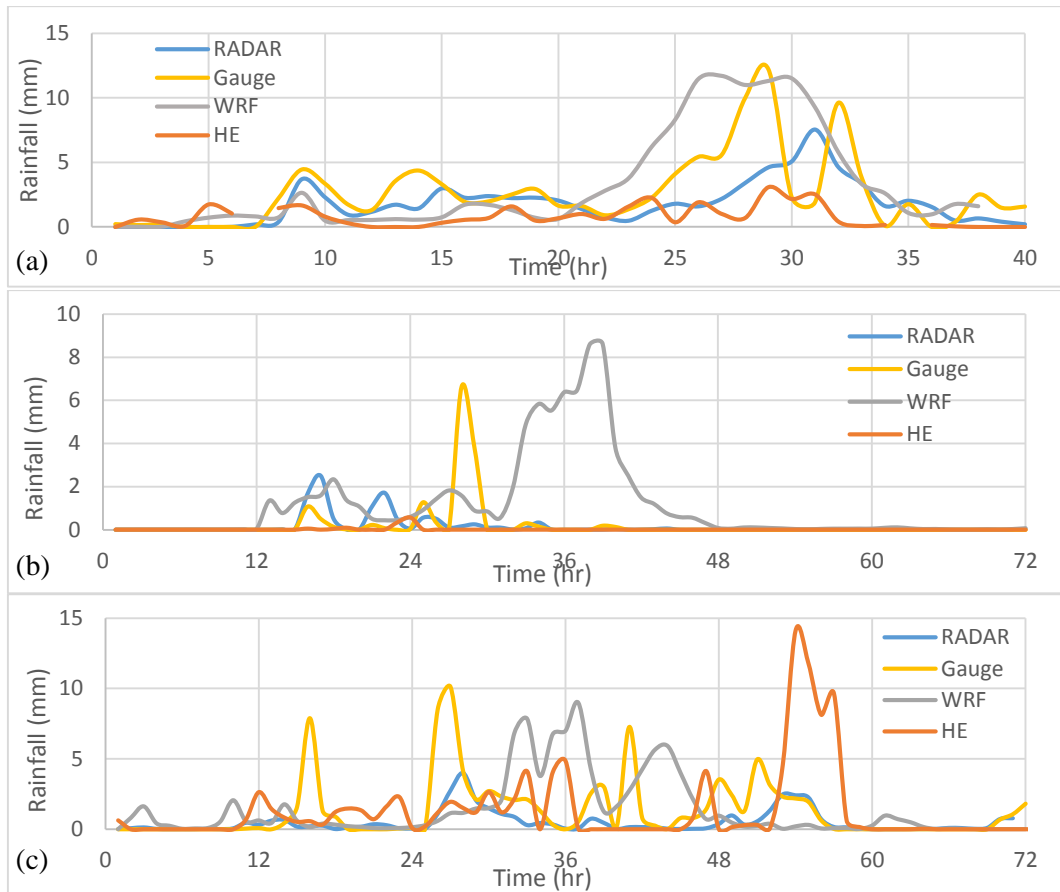


Figure 3.13 Rainfall Distribution with Time for all Rainfall Products: 2014 (a), 2015 (b) and 2016 (c)

Geometry of sub-basins are given in Table 3.5 Statistical measures and cumulative rainfall amounts for flood events considering the sub-basins are presented in Table 3.6 and Table 3.7 respectively.

Table 3.5 Geometry of Sub-basins

Basin	Area (km ²)	Average Elevation (m)	Surface Area (3D) (km ²)
basin1	75.14	616.35	80.71
basin2	46.66	720.52	50.19
basin3	109.97	707.69	118.23
basin4	134.88	635.32	142.9
basin 123	231.77	681.52	249.13

Table 3.6 Mean Statistics of Datasets for Sub-basins

Basin	BIAS (1 hr)			RMSE (mm)			r		
	Radar	WRF	HE	Radar	WRF	HE	Radar	WRF	HE
22nd November 2014									
Basin 1	-0.18	0.63	-1.65	1.63	2.78	2.67	0.70	0.64	0.18
Basin 2	-0.57	0.44	-1.98	2.46	3.16	3.50	0.60	0.64	0.24
Basin 3	-1.03	0.22	-1.94	2.75	3.15	3.42	0.50	0.62	0.33
Basin 4	-1.14	0.33	-2.01	2.83	3.21	3.42	0.47	0.64	0.39
Basin 123	-0.59	0.43	-1.85	2.28	3.03	3.20	0.60	0.63	0.25
2nd August 2015									
Basin 1	0.02	1.30	-0.17	1.00	2.81	0.84	0.07	0.03	-0.03
Basin 2	-0.05	0.94	-0.18	0.97	2.41	0.95	0.12	0.05	-0.03
Basin 3	-0.13	0.68	-0.22	0.98	2.06	1.01	0.16	0.04	-0.02
Basin 4	-0.67	0.18	-0.82	3.27	3.95	3.87	0.83	0.14	0.21
Basin 123	-0.05	0.97	-0.19	0.99	2.43	0.93	0.12	0.04	-0.03
28th May 2016									
Basin 1	-0.69	0.36	0.32	1.53	2.94	3.37	0.68	0.04	0.06
Basin 2	-0.81	0.06	0.06	2.20	3.07	3.47	0.47	0.03	0.07
Basin 3	-0.83	-0.07	-0.11	2.27	3.02	3.38	0.41	0.01	0.07
Basin 4	-0.77	0.09	-0.23	2.26	3.28	3.24	0.38	-0.01	0.09
Basin 123	-0.78	0.12	0.09	2.00	3.01	3.41	0.52	0.03	0.06

Table 3.7 Cumulative Rainfall Amounts for Four Products and Sub-basins

Basin	Gauge	Radar	WRF	HE
22nd November 2014				
Basin 1	93.5	86.3	119.6	29.5
Basin 2	107.7	85.1	127.6	30.7
Basin 3	107.7	66.5	119.2	32.1
Basin 4	107.7	62.1	123.5	29.6
Basin 123	103.0	79.3	122.1	30.8
2nd August 2015				
Basin 1	12.3	14.0	105.7	0.1
Basin 2	13.5	9.9	80.9	0.3
Basin 3	17.5	8.4	66.2	2.0
Basin 4	61.1	13.2	74.1	2.2
Basin 123	14.4	10.8	84.3	0.8
28th May 2016				
Basin 1	84.8	35.0	110.8	107.6
Basin 2	95.2	36.7	99.3	99.6
Basin 3	95.2	35.2	90.1	87.6
Basin 4	95.2	40.0	101.5	78.5
Basin 123	91.7	35.6	100.0	98.3

3.7 Summary and Discussion of the Results

In this chapter, rainfall products used in the study are presented. Among the datasets, relation between gauge and radar-based QPE rather than the radar reflectivity measurement is investigated. Radar-based QPE is obtained from IRIS software using Marshall and Palmer relation with parameters, $a=200$ and $b=1.6$ ($Z=200R^{1.6}$). Three matching methods are used to do comparison for the flood events. Then, it is found that WCMM with 5x5 space window is the most suitable technique to represent radar-based QPE. Based on this result, radar data extraction is done using WCMM (5X5 space window) for other flood events. Then, flood events are categorized using the information provided from WRF precipitation data. The rainfall datasets of flood events which were observed on 22nd November 2014, 2nd August 2015 and 28th May 2016 are analyzed. Among all rainfall datasets, only the WRF dataset has accumulated rainfall fields; namely, convective (RAINNC), shallow convective (RAINSH) and non-convective (RAINNC). RAINC contains the total accumulated rainfall from the convective, shallow convective, and microphysics schemes respectively (Lighezzolo, 2014). By the help of this data, the rainfall type of flood events (convective or non-convective) is categorized. After then, comparisons of all products in point and areal based manner are performed. The key results of this chapter can be listed as follow:

- All stations have timing mismatch error of 1 hour so applications are done after time adjustments.
- In rainfall-time graphics, it is seen that, general trend of the rainfall is captured by the radar-derived QPE well but radar underestimates the peaks.
- The assessment factor (gauge rainfall/ radar rainfall estimation) does not depend on the distance between radar and gauge station.
- Change of space window 1x1 type to 5x5 type does not improve the results dramatically. Therefore, the increase of window such as 7x7 or 9x9 are not taken into consideration.
- Dataset's time resolution is one hour, so time window study is not performed.
- Radar rainfall estimation, performed with Marshall-Palmer parameters, underestimate the rainfall peaks. Therefore, Z-R relation with other parameters may change the results.

- CDF curves do not represent the homogeneity due to the less number of data. However, rain type stratification using reflectivity data may improve the PMM.

In point based comparisons, it is inferred that;

- For the 2014 flood event day, using CDF curves and radar-based QPE, gauge data are estimated. The correlation between the estimated gauge data and the observed gauge data shows that PMM does not reveal remarkable outcome.
- r computations for each event and station demonstrate that event duration and season do not affect the results. However, to get more significant insight and generalize the situation, there should be more data to study on each season.
- AF calculation shows that the radar rainfall estimates carried out with Marshall-Palmer relation underestimate the rainfall amounts regardless of the season type.
- Topography change between Samsun radar location and gauge location together with study area indicate that there is no blockage in the direction of radar beam (Figure 2.7 and Figure 2.8).
- The HE product generally underestimates the cumulative rainfall amount in all stations and flood events.
- Radar data underestimates the results in cumulative sense but keeps the consistency in the results. On the other hand, almost all stations in WRF mean statistics computations have better results than the HE product but worse than the radar-based QPE.

In areal based comparisons, it is deduced that;

- The distribution of the HE product in time series does not show similarity with other datasets.
- It is seen that geometry of the sub-basins, size of the area in 2D and 3D and average elevation do not have an impact on the mean statistics, RMSE, r and bias calculation for three products.
- Poor results in mean statistics are observed in the HE product and gauge datasets with respect to Radar and Gauge datasets.

- Closeness of the sub-basin to the radar location gives better results in frontal rainfall types (2014 and 2016). In other words, the closest sub-basin (basin1) has the best results whereas, the furthestmost sub-basin (basin4) has the poorest.
- The HE product rainfall distribution does not resemble any dataset. WRF and radar-based QPE have similar spatial distribution but the location of the core of rainfall seems different.
- Contrary to other datasets, the bias of WRF is positive due to the overestimation of rainfall forecasts.

CHAPTER 4

RADAR-BASED QPE BIAS CORRECTION

4.1 Introduction

In 1960, R. E. Kalman published his famous paper to formulate and solve the Wiener problem from the state point of view (Kalman, 1960). Kalman defined the discrete-data linear filtering problem using a set of mathematical equations that provides computational means to estimate the state of a process, in a way that minimizes the mean of the squared error (Welch and Bishop, 2006). Kalman Filter (KF) is an optimal and recursive data processing algorithm (Grewal and Andrew, 1993) that estimates the *state* of a noisy linear dynamic system. KF is optimal with respect to selected criterion (e.g. mean square error) that makes sense. KF is recursive that means knowledge gained in previous step is incorporated into the latest result so not all data needs to be kept.

The state of a system is a vector x consisting of n variables that define the system properties. Location of an aircraft with x , y and z coordinates and orientation of aircraft can be a state. However, the variables of the state might be noisy. In order to estimate the state of aircraft, KF uses the measurements. The measurements are related to state and contain noise. If noise sources are Gaussian distributed, then KF is statistically optimal (Grewal and Andrew, 1993). KF uses the probabilistic descriptions of the system, measurement noises, and available data about the initial values of the state (Negenborn, 2003).

4.2 Description of the Kalman Filter

In this section, the principle of the Kalman Filter procedure is described using the notation proposed by Ide et al (1997). The KF procedure involves two steps: the time update (predicted) step and the measurement update (corrected) step (Figure 4.1).

The change in the discrete model from t_i to t_{i+1} is defined by Equation 4.1:

$$x_{(t_{i+1})}^t = M_i[x_{(t_i)}^t] + \eta(t_i); \quad \eta \sim N(0, \sigma_\eta) \quad \text{Equation(4.1)}$$

where x^t is the true value of the state vector, M is the system operator and η is the independent normally distributed system noise with zero mean and standard deviation σ_η .

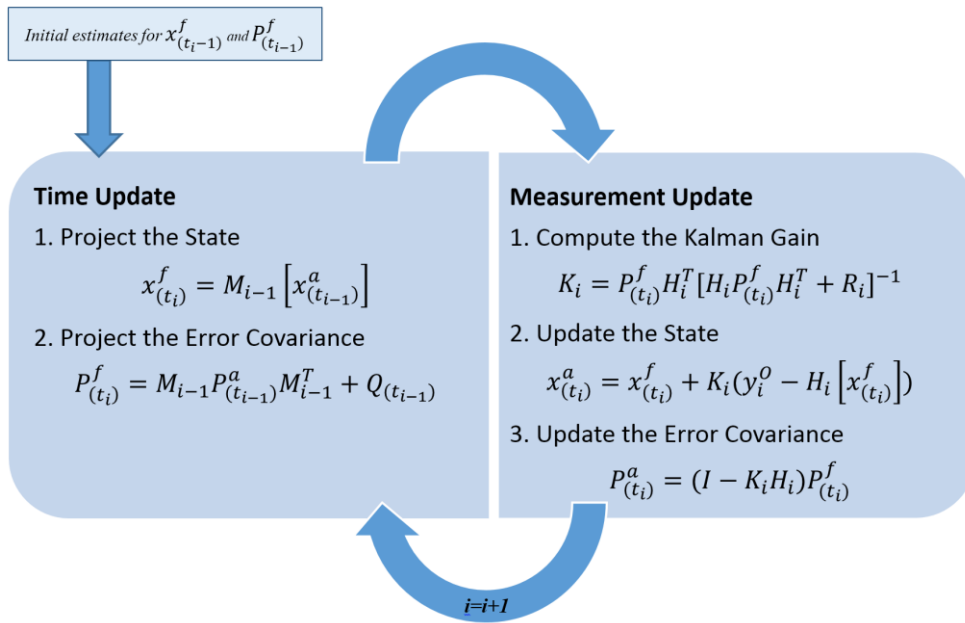


Figure 4.1 Flowchart of the Kalman Filter Procedure

4.2.1 The Time Update Step

In the forecast step, the priori estimate of the state (x^f) and process covariances (P^f) can be estimated as follows:

$$x_{(t_i)}^f = M_{i-1} [x_{(t_{i-1})}^a] \quad \text{Equation (4.2)}$$

$$P_{(t_i)}^f = M_{i-1} P_{(t_{i-1})}^a M_{i-1}^T + Q_{(t_{i-1})} \quad \text{Equation (4.3)}$$

where Q is the estimated process error covariance.

4.2.2 The Measurement Update Step

In the second step of KF, the priori estimate of the state and process covariances is updated based on the actual measurements.

The relationship between the observation (y^o) and the state at time t_i is defined by Equation 4.4.

$$y_i^o = H_i [x_{(t_i)}^t] + \varepsilon_i; \quad \varepsilon \sim N(0, \sigma_\varepsilon) \quad \text{Equation (4.4)}$$

where H is the observation operator and ε is the independent normally distributed observation error with zero mean and standard deviation σ_ε . In the following equations, the state and process covariances and the Kalman gain are estimated:

$$x_{(t_i)}^a = x_{(t_i)}^f + K_i (y_i^o - H_i [x_{(t_i)}^f]) \quad \text{Equation (4.5)}$$

$$P_{(t_i)}^a = (I - K_i H_i) P_{(t_i)}^f \quad \text{Equation (4.6)}$$

$$K_i = P_{(t_i)}^f H_i^T [H_i P_{(t_i)}^f H_i^T + R_i]^{-1} \quad \text{Equation (4.7)}$$

where R is the estimated measurement error covariance.

4.3 Methodology

Ideally, it is expected that the ratio of the rainfall amount observed from the gauge and that estimated from the weather radar is 1.0. However, the errors arising from the reflectivity measurement operation and the Z-R conversion process affect the precision of the radar estimates. For this reason, before applying the statistical analyses,

implementation of physical methods to eliminate the inaccuracies related to the mentioned errors is significant (Chumchean et al., 2006). In our case, radar rainfall data obtained from IRIS software are in the rainfall depth form, which is the output of the predetermined Z-R conversion process. Therefore, foreground processing to eliminate the errors cannot be implemented; instead, statistical analyses are carried out directly to reduce the systematic errors.

The mean field bias correction is the approach used to correct the mean difference between the amount of rainfall observed from the gauge and that estimated from the weather radar. For this purpose, in the bias-correction approach, the mean of the ratio of gauged rainfall amount and radar rainfall amount (G/R) is generally used (Smith and Krajewski, 1991; Chumchean et al., 2003). The mean field radar rainfall logarithmic bias, x , is defined as follows:

$$x_{t_i} = \frac{1}{n} \sum_{j=1}^n \log_{10} \left(\frac{G_{j,i}}{R_{j,i}} \right) \quad \text{Equation (4.8)}$$

where $R_{j,i}$ is the hourly radar rainfall amount (mm) retrieved from the location of gauge j for hour i , $G_{j,i}$ is the hourly rainfall amount (mm) observed from gauge j for hour i and n is the number of radar-gauge pairs.

When estimating the G/R ratio, a problem may be encountered, such as the presence of abnormally high or low G/R ratios in the computations. Apart from the errors related to radar reflectivity or Z-R conversion, rainfall intermittency may be the main reason for this problem (Kim and Yoo, 2014). Within the selected time span, increasing the data pairs considering the time range can help alleviate the problem. Moreover, applying a certain threshold to the data pairs can also alleviate the problem (Chumchean et al., 2006).

Describing the rainfall pattern both spatially and temporally can be imprecise, especially in complex terrain. Mountainous regions can experience an increase in rainfall in high altitudes or a mixture of storm types. The variability in the DSD may cause the G/R ratio to fluctuate, particularly when using constant Z-R parameters in

radar rainfall estimates. Using various stochastic process models, Ahnert et al. (1986) used the Kalman Filtering approach for the first time to simulate the bias in the radar field. To address the uncertainty of the time-varying behaviour of the mean field bias, the autoregressive model of order 1, the $AR(1)$ model, is selected due to its wide usage in the literature (Smith and Krajewski, 1991; Anagnostou et al., 1998; Seo et al., 1999; Chumchean et al., 2006). The autoregressive model is a stochastic process that specifies the output variable based on a weighted sum of past values. $AR(1)$ is a first order process, meaning that the current value is linearly based on the preceding value. The $AR(n)$ model can be defined as follows:

$$x_t = c + \sum_{i=1}^n \Phi_i x_{t-i} + \varepsilon_t \quad \text{Equation (4.9)}$$

where Φ is the parameter, c is the constant and ε is the white noise.

The estimation of logarithmic mean field bias ‘ x ’ is carried out with the Kalman Filter using the $AR(1)$ process system equation. Using the previous equations, the Kalman Filter algorithm has the following form:

The system equation or state is assumed to follow the $AR(1)$ process:

$$x_{(t_{i+1})}^t = \rho_x x_{(t_i)}^t + \eta(t_i); \quad \eta \sim N(0, \sigma_\eta) \quad \text{Equation (4.10)}$$

where ρ_x is the correlation coefficient of the logarithmic mean field bias and η is the system error with zero mean and constant standard deviation σ_η .

Observation (measurement) equation:

$$y_i^O = x_{(t_i)}^t + \varepsilon_i; \quad \varepsilon \sim N(0, \sigma_{\varepsilon_i}) \quad \text{Equation (4.11)}$$

where ε is the independent normally distributed observation error with mean zero and standard deviation σ_{ε_i} .

Prediction equations:

$$x_{(t_i)}^f = \rho_x x_{(t_{i-1})}^a \quad \text{Equation (4.12)}$$

$$P_{(t_i)}^f = \rho_x^2 P_{(t_{i-1})}^a + \sigma_\eta^2 \quad \text{Equation (4.13)}$$

Updating equations (in these equations, the observation operator H is taken as unity):

$$x_{(t_i)}^a = x_{(t_i)}^f + K_i (y_i^o - x_{(t_i)}^f) \quad \text{Equation (4.14)}$$

$$P_{(t_i)}^a = (I - K_i) P_{(t_i)}^f \quad \text{Equation (4.15)}$$

$$K_i = P_{(t_i)}^f [P_{(t_i)}^f + \sigma_{\varepsilon_i}^2]^{-1} \quad \text{Equation (4.16)}$$

One of the most serious difficulties in the KF procedure is determining the error variances σ_η^2 and $\sigma_{\varepsilon_i}^2$:

$$\sigma_\eta^2 = (1 - \rho_x^2) \sigma_x^2 \quad \text{Equation (4.17)}$$

where σ_x^2 is the empirical variance of the logarithmic bias

$$\sigma_{\varepsilon_i}^2 = \sigma_{y_i}^2 - \sigma_x^2 \quad \text{Equation (4.18)}$$

To estimate the empirical variance, $\sigma_{y_i}^2$, Chumchean et al. (2003) proposed a model based on the 1.5-km CAPPI, 1-km² grid resolution reflectivity data. The proposed model can be expressed as follows:

$$\sigma_{y_{i,t}}^2 = -0.015 \bar{G}_t + 0.14; \quad r_i \leq 55 \text{ km} \quad \text{Equation (4.19)}$$

$$\sigma_{y_{i,t}}^2 = -0.015 \bar{G}_t + 0.13 \frac{(r_i - 55)}{P} + 0.14; \quad r_i > 55 \text{ km} \quad \text{Equation (4.20)}$$

where \bar{G}_t is the conditional mean of the rainfall amount observed from the gauge at hour t , r_i is the distance of the i^{th} gauge from the radar location and P is the number of pulses used in the reflectivity measurement over each range.

The empirical variance, the sample variance of the $\log G - \log R$ difference, is evaluated for each gauge location and was defined by Anagnostou et al. (1998) as follows:

$$\sigma_{y_i}^2 = \frac{1}{n} \sum_{i=1}^n \{[\log G - \log R]^2 \mid G > r\} \quad \text{Equation (4.21)}$$

where $\sigma_{y_i}^2$ is the variance at the gauge, n is the number of the gauge, G is the rainfall amount at gauge i (mm), R is the rainfall estimate by the radar (mm) and r is the minimum rainfall amount. Anagnostou et al. (1998) stated that a rainfall amount below the value of 0.5 mm/h causes the variability of the $\log G - \log R$ difference to be significant. The authors selected the value of 0.5 mm/h as a threshold using more than 4500 wet data pairs.

It is well known that factors such as study area location, storm type and season greatly affect the variance of the rainfall dataset. The proposed model equations formulated by Chumchean et al. (2003) to determine the empirical variance and the threshold value defined by Anagnostou et al. (1998) to avoid significance of log transformations are crucial components of the approaches used in the bias computation.

4.4 Modeling the Empirical Variance

In modeling the empirical variance, past records from the gauging stations, namely, Salipazari and Ayvacik, which are the closest stations to the study area, are used. Stations that measure cumulative rainfall amounts greater than the threshold value of 20 mm are listed in Table 4.1. The reasons for selecting this threshold are the successful results in radar studies at high rainfall amounts and the avoidance of measurement error of low rainfall amounts (Chumchean et al., 2003). In Table 4.1, stations depicted in bold are closest to the study area and are used in the Thiessen Polygon method to calculate the mean areal rainfall for the study area. The gaps in the table show that data for the station are unavailable for this event. The number of paired data for a station (wet and non-wet) has a maximum value of 304. A breakdown in the stations or installation time of the gauge reduces the number of data pairs. Therefore,

the threshold (0.5 mm/h) defined by Anagnostou et al. (1998) is not applied to the dataset. Under normal conditions, the value of variance increases as the radar range increases due to the decrease in reflectivity measurement sensitivity. Figure 4.2 shows the change in variance with distance between the stations and the radar. Remoteness does not influence the variance computation for the study area. Taking small rainfall values ($0 < r \text{ (mm)} < 0.5$) and having few rain gauges in regions of remote distance, particularly more than 60 km, may cause this result. The increase in the number of stations in the radar range can result in a rigid conclusion about the variance changes.

Table 4.1 Cumulative Rainfall Amounts for each Event (mm)

Station	1 29.03.2014	2 05.05.2014	3 25.05.2014	4 21.07.2014	5 18.10.2014	6 29.12.2014	7 06.01.2015	8 08.04.2015
Vezirköprü	0.3	7.7	0.8	1.0	6.5	3.1	0.5	21.1
Yakakent	8.5	12.4	0.5	0.0	33.6	28.9	43.0	48.6
Alaçam	3.6	4.8	12.4	0.0	10.4	76.6	69.4	28.0
Havza	6.6	16.3	0.9	0.0	13.4	31.9	39.5	26.4
Topraksu	2.5	0.0	19.2	17.5	41.7	57.1	42.3	23.7
Bafra	2.4	5.4	12.0	8.6	35.4	42.2	39.6	31.6
Kavak	17.9	21.3	11.9	3.8	11.6	34.7	41.0	42.7
Ondokuz Mayıs	3.6	6.3	4.9	84.1	41.6	59.9	46.0	31.1
Karadeniz	19.2	25.1	10.1	0.0	-	53.9	41.7	47.8
Ayvacık	38.8	30.4	35.7	45.8	25.1	6.8	-	45.1
Çarşamba	14.4	21.7	2.2	22.1	66.4	36.2	46.9	46.5
Salpazarı	28.5	39.0	16.6	3.9	74.0	36.8	50.6	55.8
Kozluk Bel	22.6	25.7	3.7	0.3	55.0	48.6	37.0	55.7

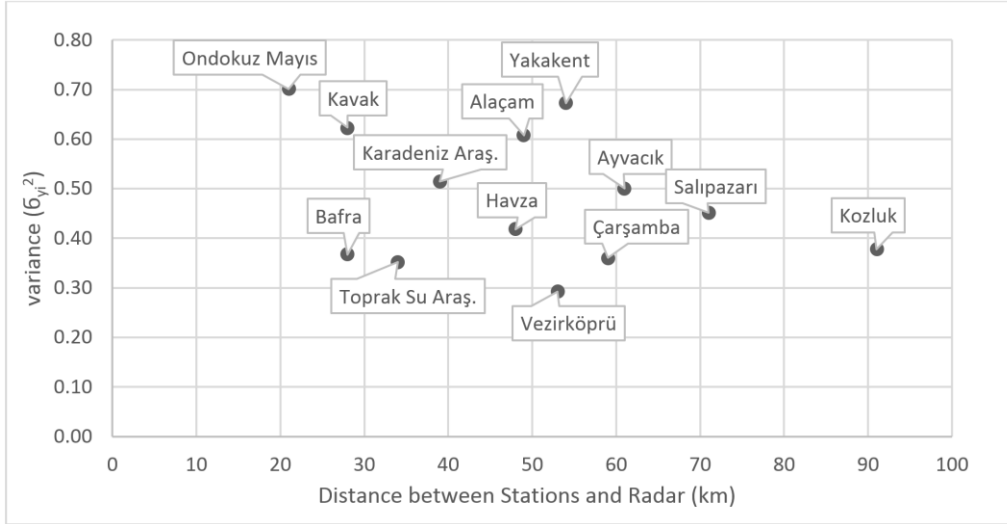


Figure 4.2 Empirical Variance of Stations with the Distance between Stations and Radar

While establishing the empirical variance model, the datasets of all rain gauges are used because of the insignificant influence of the distance on variance. Thus, the same equation (Equation (4.21)) is used for all G/R pairs. The distribution of empirical variance with respect to rainfall amounts is depicted in Figure 4.3 (a). At a low rainfall rate, the uncertainty related to the Z-R parameters (Austin, 1987) and the quantization error in gauges (Chumchen et al., 2003) are high. These assessments support the data shown in Figure 4.3 (a). It is seen that the empirical variance decreases when the rainfall amount increases. To obtain a proper model for empirical variance estimation, an outlier detection study is performed using a common method, the modified Thompson outlier detection method (Thompson, 1935). This technique is a statistical method for deciding whether to keep or remove suspected outliers in the sample. The modified Thompson (τ) value is obtained from the following equation:

$$\tau = \frac{t_{\alpha/2}(n-1)}{\sqrt{n} \sqrt{n-2 + t_{\alpha/2}^2}} \quad \text{Equation (4.22)}$$

where $t_{\alpha/2}$ is the critical value of Student's t test based on $\alpha = 0.05$ and n is the number of data points. In this case, the number of data points, n , is 1886. Using the

modified Thompson table, τ is calculated as 1.9589. After removing the outliers, the best fit model (Figure 4.3 (b)) that describes the variance with respect to the rainfall amount observed in the gauge is as follows:

$$\sigma_{y_{i,t}}^2 = -0.061 \ln(\bar{G}_t) + 0.4562 \quad \text{Equation (4.23)}$$

where \bar{G} is the mean of the rainfall amount observed from the gauges at hour t .

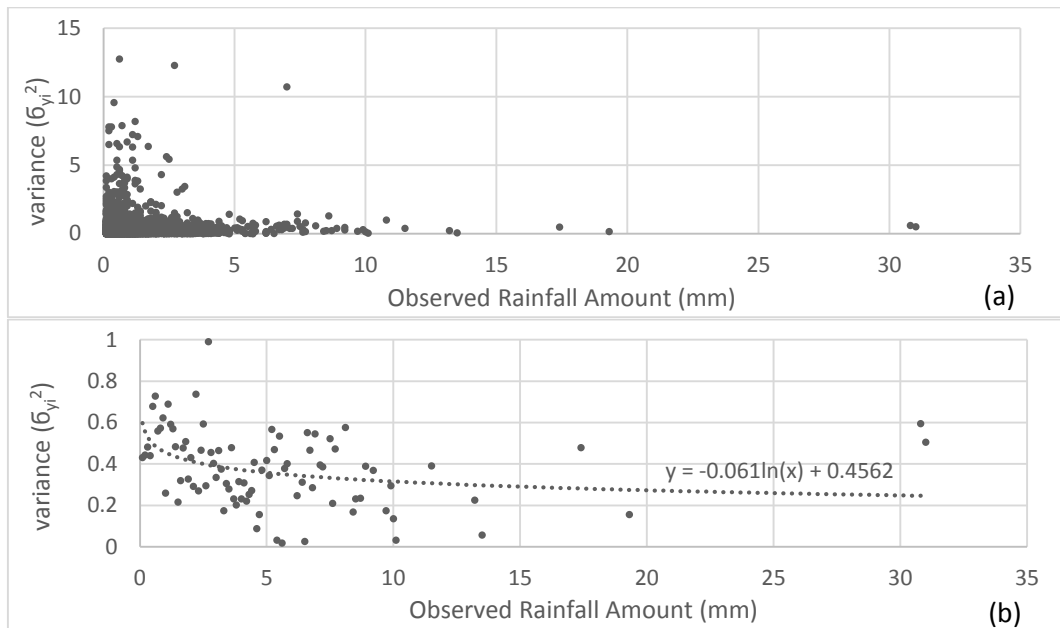


Figure 4.3 Empirical Variance of all Datasets (a) and Empirical variance model after outlier detection (b)

4.5 Computation of the Correlation Coefficient (ρ_x) and the Empirical Variance (σ_x^2)

Using all gauges, the mean field radar rainfall logarithmic bias (x_{t_i}) is calculated, and then, by applying the $AR(1)$ process, correlation coefficients (ρ_x) are computed for each event. In a similar manner, using calculated logarithmic biases (x_{t_i}), empirical variances of the logarithmic biases (σ_x^2) are calculated. The obtained parameters are given in Table 4.2.

Table 4.2 Correlation Coefficients and Empirical Variances for each Event with the Duration and Average of Cumulative Radar and Gauge Rainfall Amounts

Event #	Date (yyyy mm dd)	ρ_x	σ_x^2	Duration (hr)	Ave. of Cum. Radar Rainfall (mm)	Ave. of Cum. Gauge Rainfall (mm)
1	2014 03 29	0.48	0.22	24	5.55	12.99
2	2014 05 05	0.57	0.25	35	6.16	16.62
3	2014 05 25	0.36	0.17	17	5.48	10.07
4	2014 07 21	0.32	0.12	11	6.74	14.39
5	2014 10 18	0.74	0.22	28	13.33	35.52
6	2014 12 29	0.52	0.30	60	25.07	41.29
7	2015 01 06	-0.20	0.05	20	24.67	43.25
8	2015 04 08	0.87	0.73	58	23.69	38.78
Average		0.46	0.26	31	13.83	26.61

The ρ_x and σ_x^2 calculations depend on continuity in time. Missing data may suppress the computation. Therefore, the computations are performed by splitting the data regarding the event time. Parameter ρ_x shows the relationship of the spatial distribution of rainfall amounts at sequential time intervals. Among the results, the 7th event has the lowest ρ_x value, which may be explained by the rainfall type. Hand et al. (2004) classified and analyzed the extreme rainfall events in the United Kingdom (UK) regarding the rainfall amounts and durations. The authors grouped the events into five categories: convective, convective with frontal forcing, orographic, frontal with instability and frontal. The events having a rainfall duration equal to or less than 20 hours are classified into the convective and convective with frontal forcing categories. In Table 4.2, the average cumulative rainfall amounts are obtained by averaging the cumulative rainfall amounts observed at the gauges for each event. The results show that the cumulative rainfall distribution over the gauges is not uniform. Events with a long duration have a high average for the cumulative radar and gauge rainfall amounts and generally have high correlation coefficients. The 7th event has a 20-hour rainfall duration that may be classified into the convective type of rainfall. The convective type of rainfall is a dynamic concept because of its rapid response to neutralize an unstable vertical distribution of moist static energy (Houze, 1997). Due to this rapid response, the spatial distribution of rainfall may not be uniform. At this stage, sufficient and exact information about the rainfall types for the events is unavailable. Therefore, in

the flood day KF application, the average values of $\overline{\rho_x}$ and $\overline{\sigma_x^2}$, given in Table 4.2, are used.

4.6 Kalman Filter Application

The aim of applying the KF to radar rainfall estimates is to correct the radar rainfall estimates. The KF algorithm is applied to the dataset in two different ways. First, all rain gauges except for the studied one located in the radar range are used for the computation. Second, gauges that have better correlations with the studied gauge are taken into consideration. The primary goal of the second application is to localize the bias computation. In the first approach, the mean field bias correction is constant over the space within the time sequence. In addition, in the empirical variance modeling study, the distance between stations and radar has no influence on the empirical variance results. For this reason, rather than considering the radar distance effect, the correlations among the rain gauge stations are considered to localize the bias computation.

For both studies, at $t = 0$, the initial estimators $x_{(t_0)}^f$ and $P_{(t_0)}^f$ are taken as 0.

4.6.1 The KF Application Type I

As previously mentioned, all gauges in the radar umbrella (Figure 2.1) except for the flood events data are used in this application. The KF process is applied for the flood events using the average values of $\overline{\rho_x}$ and $\overline{\sigma_x^2}$ (Table 4.2) and the empirical variance model (Equation (4.23)).

4.6.2 The KF Application Type II

In the KF application type II, gauges that have better correlations with the studied gauge are taken into consideration. To determine the correlation coefficients among the gauges, the entire dataset except for the flood events is used. The aim of this process is to obtain the most probable gauge(s) to represent the studied gauge. The computation results for correlation coefficient (r) are given in Table 4.3 with color coding.

Table 4.3 Correlation Coefficients of Gauges with Each Other Using 8 Events

Stations	Bafra	Ondokuz.	Kavak	Karadeniz.	Alaçam	Havza	Vezirköprü	Yakakent	Çarşamba	Ayvacak	Salıpazarı	Kozluk	ToprakSu
Bafra	1.00	0.46	0.33	0.25	<u>0.61</u>	0.37	0.04	<u>0.51</u>	0.30	-0.08	0.29	0.34	<u>0.79</u>
Ondokuz	0.46	1.00	0.10	0.03	0.11	0.09	-0.03	0.15	0.19	0.10	0.12	0.07	<u>0.57</u>
Kavak	0.33	0.10	1.00	0.49	0.27	<u>0.55</u>	0.15	0.43	0.22	0.03	0.30	0.28	0.17
Karadeniz	0.25	0.03	0.49	1.00	0.34	0.48	0.11	0.28	0.22	0.03	0.26	0.24	0.13
Alaçam	<u>0.61</u>	0.11	0.27	0.34	1.00	0.35	-0.01	0.45	0.26	-0.08	0.23	0.31	<u>0.56</u>
Havza	0.37	0.09	<u>0.55</u>	0.48	0.35	1.00	0.28	0.45	0.18	-0.07	0.19	0.23	0.26
Vezirköprü	0.04	-0.03	0.15	0.11	-0.01	0.28	1.00	0.14	0.01	-0.02	-0.03	0.07	-0.03
Yakakent	<u>0.51</u>	0.15	0.43	0.28	0.45	0.45	0.14	1.00	0.34	-0.09	0.44	0.39	0.34
Çarşamba	0.30	0.19	0.22	0.22	0.26	0.18	0.01	0.34	1.00	0.12	<u>0.62</u>	0.50	0.29
Ayvacak	-0.08	0.10	0.03	0.03	-0.08	-0.07	-0.02	-0.09	0.12	1.00	0.28	0.10	-0.09
Salıpazarı	0.29	0.12	0.30	0.26	0.23	0.19	-0.03	0.44	<u>0.62</u>	0.28	1.00	<u>0.62</u>	0.21
Kozluk	0.34	0.07	0.28	0.24	0.31	0.23	0.07	0.39	0.50	0.10	<u>0.62</u>	1.00	0.20
ToprakSu	<u>0.79</u>	<u>0.57</u>	0.17	0.13	<u>0.56</u>	0.26	-0.03	0.34	0.29	-0.09	0.21	0.20	1.00

0.5<r<0.6

0.6<r

In this approach, the same values for the correlation coefficient and the same empirical variance model are used. The purpose of selecting the same values and model is to examine the effect of gauge selection. Stations having correlation coefficients greater than 0.5 are selected. Then, for the flood events, using the same $\overline{\rho_x}$, and $\overline{\sigma_x^2}$ and the empirical variance model, the KF is applied. Table 4.4 is the summary of Table 4.3 and shows stations that have better correlation coefficient results with the main gauge. Among these stations ($r>0.5$), some of them have long distance to the main gauge. Due to spatial variability of rainfall, some of the stations are subtracted to get reasonable outcome in the KF calculation.

Table 4.4 Summary of the Table 4.3

Main Gauge	Gauge that has $r>0.5$	Gauge that has $r>0.5$ and close the Main Gauge
Vezirköprü		
Yakakent	Bafra	Bafra
Alaçam	Topraksu A., Bafra	Topraksu A., Bafra
Havza	Kavak	Kavak
Topraksu Araş.	Bafra, Ondokuz Mayıs and Alaçam	Bafra
Bafra	Topraksu A., Alaçam and Yakakent	Topraksu A
Kavak	Havza	Havza
Ondokuz Mayıs	Topraksu A.	Topraksu A.
Karadeniz Araş.		
Ayvacik		
Çarşamba	Salıpazarı	Salıpazarı
Salıpazarı	Kozluk, Çarşamba	Kozluk, Çarşamba
Kozluk	Salıpazarı	Salıpazarı

4.7 Results

For the Salıpazarı Station that is the closest one to the study area, BCR (I) and BCR (II) data with respect to time are given in Figure 4.4 for all flood events. In 2014 flood event, the BCR (I) data underestimate the rainfall rate, but after 12 hours, these data overestimate the rate considering the radar estimates. From 22 to 30 hours, the BCR (I) data approach the gauge observation, and at the peak rain rate of the event (at 29 hours), the BCR (I) data exceed the gauge by 1.5 mm. The KF application results for

the remaining gauges are given in Appendix D. For the majority of the gauges at the beginning of the event, which is generally the first 15 hours, low rain rates are observed, and at the last part of the event, which is after 20 hours, high rain rates are recorded (Figure D.1, Figure D.2 and Figure D.3). Thus, the KF application adapts the Salıpazarı radar rainfall estimates to the rainfall trend observed by the majority of the gauges. In flood studies, having a value close to the peak rain rate may be significant for obtaining the actual peak flow that intensifies the hazard. Unlike the type (I), the BCR (II) overestimates the radar throughout the event period. The peak rain rate of the BCR (II) data is nearly 18 mm, which exceeds the gauge rain rate by 5 mm. In 2015 flood event, the Salıpazarı Station was not in operation (Figure 4.4 (b)). The abilities of radar-based QPE, such as gathering data in wide swath and revisiting the same place repeatedly with high spatio-temporal scale regardless of whether condition during day and night, are the unique properties for flood monitoring. These features make the radar-based QPE valuable for sparsely gauged or ungauged basins. As mentioned before, bias corrections are done using all stations except the Salıpazarı Station so application is not affected by the excluding. However, consistency of the BCR data cannot be evaluated by using gauge data. Hence, assessment of the BCR data is carried out in hydrological modeling. Regarding to rainfall amounts, it is seen that the radar data estimate rainfall as 23 and 29 mm at 16 and 17 hours respectively. Due to the convective rainfall type, the amount of the BCR (I) data is smaller than the radar-based QPE. However, the BCR (II) data show overestimation with respect to radar-based QPE because station that has better correlation with the Salıpazarı Station, the Kozluk Station observe rainfall at the same time (Figure 3.15 (f) and Figure D.6 (c)). In 2016 flood event, majority of the stations observe less rainfall amount than the Salıpazarı Station (Figure D.7, Figure D.8 and Figure D.9). Therefore, the BCR (I) data underestimate the rainfall amount with respect to the radar and the gauge data. On the contrary, the BCR (II) data overestimate the rainfall amount with respect to radar-based QPE especially in time between 20 and 35 hours because of the observed high rainfall amounts in the Çarşamba and the Kozluk Stations (Figure D.9 (a) and (c)). The Çarşamba and the Kozluk Stations give best correlation results among all stations in Table 4.3; consequently, they are used in the BCR (II) calculations.

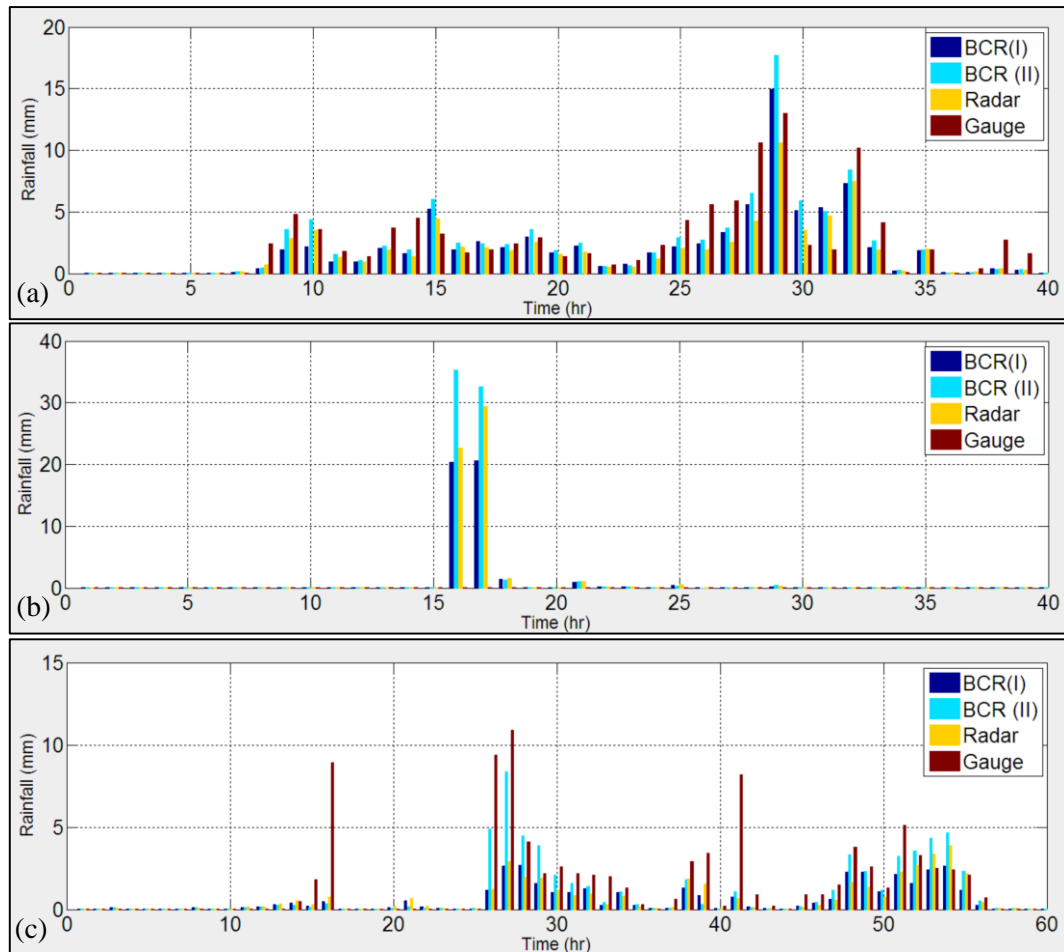


Figure 4.4 The Results for the Salıpazarı Station (2014 (a), 2015 (b) and 2016 (c))

A summary of the mean statistical values of the gauges using KF is presented in Table 4.5. In this table, there is no calculation for the Karadeniz Araş., Vezirköprü and Ayvacık Stations due to the low ($r < 0.5$) correlation coefficients. The results indicate that the weather radar underestimates the cumulative rainfall amount at generally all stations and for all flood events. After applying the KF, the general dataset maintains the underestimated values. However, for the cumulative rainfall amounts, the majority of the BCR (I) and BCR (II) datasets converges to the observed data. For the cumulative rainfall amounts, the BCR (II) data generally show appreciable progress compared with the BCR (I) data.

Table 4.5 Summary of Statistics for all Stations and Flood Events

Station Name	r			BIAS (1 hr)			Cum. rainfall (mm)			
	R	BCR-I	BCR-II	R	BCR-I	BCR-II	G	R	BCR-I	BCR-II
22nd November 2014										
Vezirköprü	0.89	0.89	-	0.20	0.19	-	33.5	48.0	47.5	-
Yakakent	0.82	0.81	0.79	-0.02	0.04	0.06	26.6	25.1	29.8	31.2
Alaçam	0.67	0.65	0.69	-0.11	-0.03	0.00	33.8	25.7	31.7	33.7
Havza	0.7	0.59	0.71	-0.15	-0.14	-0.10	45.4	34.5	35.2	37.9
Topraksu A.	0.92	0.92	0.94	-0.30	-0.22	-0.22	43.5	22.1	28.0	27.4
Bafra	0.79	0.79	0.84	-0.18	-0.09	-0.04	39.4	26.6	33.0	36.5
Kavak	0.91	0.9	0.89	0.24	0.38	0.60	37.6	55.0	64.8	80.7
Ondokuz M.	0.85	0.86	0.86	-0.17	-0.12	-0.08	33.4	20.9	25.0	27.3
Karadeniz A.	0.91	0.89	-	-0.05	0.05	-	49.2	45.5	52.9	-
Ayvacak	0.21	0.29	-	-0.15	-0.07	-	67.4	56.4	62.6	-
Çarsamba	0.86	0.9	0.87	-0.17	-0.10	0.05	59.8	47.4	52.7	63.5
Salıpazarı	0.85	0.83	0.85	-0.48	-0.34	-0.13	107.7	73.5	83.0	98.7
Kozluk	0.62	0.62	0.68	-0.43	-0.37	-0.26	66.0	34.9	39.3	47.6
2nd August 2015										
Vezirköprü	0.00	0.00	-	0.02	0.01	-	0.0	1.2	0.9	-
Yakakent	-0.01	0.00	-0.01	-0.01	-0.02	-0.02	2.2	1.6	0.9	0.9
Alaçam	0.00	0.00	0.00	0.01	0.01	0.00	0.0	0.7	0.4	0.3
Havza	0.00	0.00	0.00	0.01	0.01	0.01	0.0	0.8	0.6	0.6
Topraksu A.	0.85	0.80	0.81	0.04	0.03	0.03	1.2	4.0	3.3	3.3
Bafra	0.00	0.00	0.00	0.01	0.01	0.01	0.0	0.7	0.5	0.5
Kavak	0.52	0.51	0.55	0.02	0.01	0.02	0.3	1.6	1.4	1.6
Ondokuz M.	0.51	0.43	0.37	0.02	0.01	0.02	0.2	1.3	1.0	1.4
Karadeniz A.	0.99	0.97	-	-0.25	-0.29	-	30.9	13.0	10.1	-
Ayvacak	0.81	0.87	-	0.00	-0.01	-	3.4	3.4	2.6	-
Çarsamba	0.78	0.68	0.84	-0.52	-0.53	-0.55	45.8	8.4	7.3	6.5
Salıpazarı	-	-	-	-	-	-	-	56.4	44.7	72.0
Kozluk	0.96	0.97	0.96	-1.08	-1.11	-1.30	109.3	31.7	29.7	15.7
28th May 2016										
Vezirköprü	0.88	0.92	-	-0.35	-0.36	-	42.7	17.8	17.1	-
Yakakent	0.88	0.77	0.88	-0.63	-0.63	-0.50	76.7	31.6	31.5	40.9
Alaçam	0.93	0.93	0.90	-0.47	-0.45	-0.29	68.8	34.8	36.1	47.6
Havza	0.40	0.43	0.53	-0.21	-0.23	-0.25	37.3	22.4	20.8	19.4
Topraksu A.	0.80	0.81	0.83	-0.78	-0.73	-0.60	87.1	30.6	34.9	43.9
Bafra	0.94	0.96	0.90	-0.60	-0.52	-0.38	77.8	34.9	40.1	50.3
Kavak	0.85	0.89	0.90	-0.20	-0.17	-0.06	35.1	20.7	22.7	30.6
Ondokuz M.	0.42	0.41	0.44	-0.40	-0.39	-0.34	44.1	15.2	15.9	19.5
Karadeniz A.	0.85	0.81	-	-0.78	-0.76	-	90.4	34.5	35.7	-
Ayvacak	0.54	0.51	-	-0.48	-0.49	-	65.8	31.5	30.3	-
Çarsamba	0.63	0.67	0.40	-1.87	-1.90	-1.73	189.7	55.1	52.7	65.0
Salıpazarı	0.61	0.65	0.74	-0.72	-0.79	-0.43	95.2	43.7	38.2	64.0
Kozluk	0.55	0.53	0.63	-1.62	-1.67	-1.33	173.1	56.1	53.2	77.5

4.8 The Effect of Correlation Coefficient (ρ_x) and Empirical Variance (σ_x^2) on Results

So far, the parameters ρ_x and σ_x^2 have been calculated for each event reported in the previous sections. However, to observe the direct effects of these parameters on the Salipazarı Station on the 2014 flood event day, the parameter values are changed gradually. The effects of changing ρ_x (rho) between 0 and 1 and changing σ_x^2 (sigma) between 0 and 0.35 are shown in Figure 4.5.

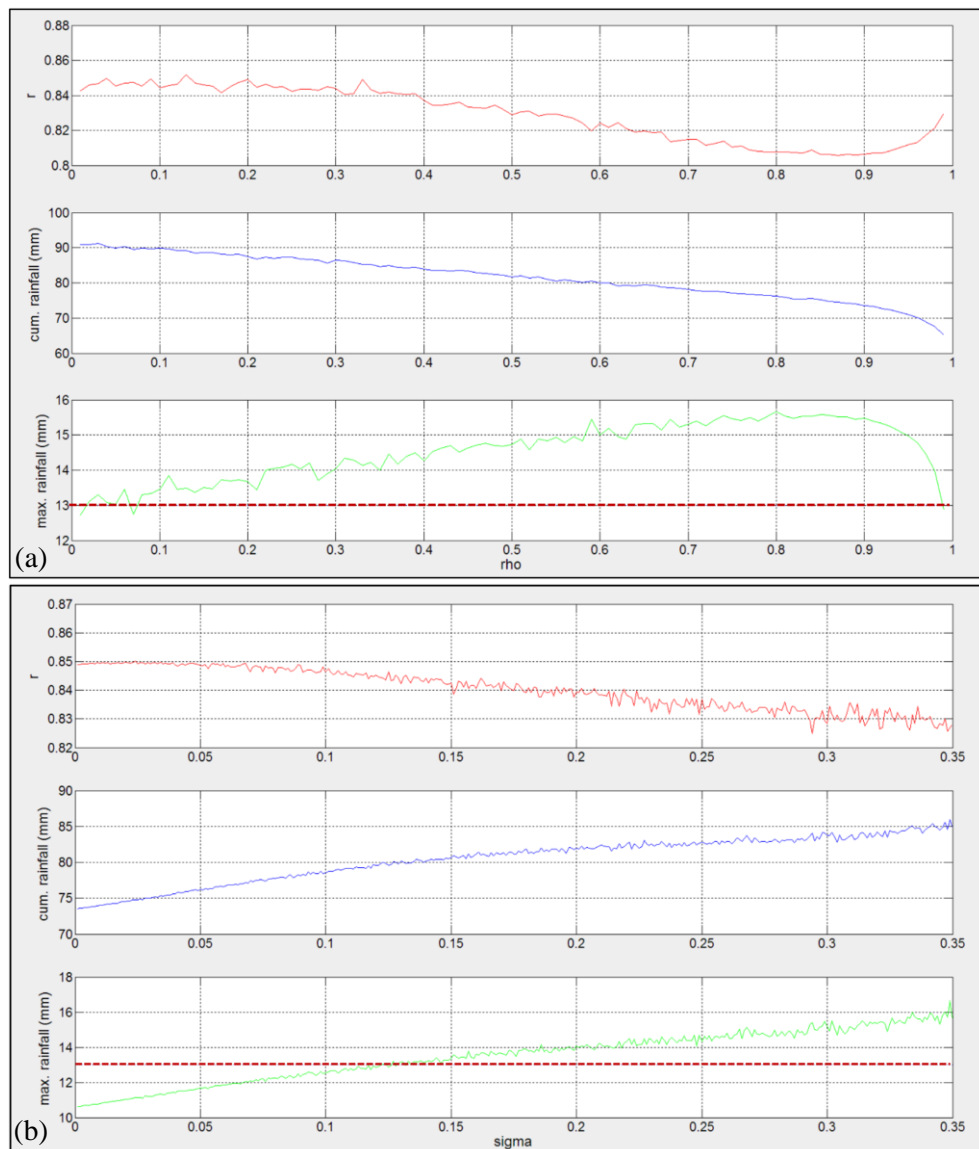


Figure 4.5 Effect of ρ_x (a) and σ_x^2 (b) on r , Cumulative Rainfall Amounts and Maximum Rainfall Amount

In Figure 4.5, the stability and magnitude of r show a decreasing pattern as ρ_x and σ_x^2 increase. However, the sensitivity is observed in the second digit of r ; therefore, in general, the r results do not strictly depend on the parameters. In contrast, the cumulative and maximum rainfall amounts show an increasing trend as ρ_x and σ_x^2 increase. Instead of the correlation coefficient, the values of cumulative and maximum rainfall are good indicators for the changes in the parameters. In flood studies, the maximum rainfall amount observed in the measurements is significant because it may be a driving force for discharge formation, which has a devastating power at the downstream site of urbanized areas. Therefore, the maximum rainfall amount is depicted in red dotted lines in the figures. For the Salıpazarı Station, suitable ρ_x and σ_x^2 values are determined as 0.36 and nearly 0.15, respectively.

4.9 Discussion of the Results

The aim of applying the Kalman Filter to radar-based QPE is to correct mean field bias in the data. The KF algorithm is applied to the datasets in two different ways. First, all rain gauges except for the studied one located in the radar range are considered for computation. Second, gauges with better correlations with the studied gauge are considered. The major outcomes of this study are as follows:

- The radar-based QPE are retrieved from IRIS outputs that are generated from the Marshall-Palmer relationship. The state of this product with the rain gauge data in the time sequence shows that the general trend of the rainfall is well captured by the radar rainfall estimation, but within that sequence, the radar data underestimate the rainfall amounts, especially at peak values.
- In the study of the empirical variance model, it is found that contrary to the literature, empirical variance does not increase when the distance between radar and station increases. The scarcity of rain gauge stations, particularly after 60 km, and the presence of fewer observed events are likely the reason for this outcome.
- In the BCR (I) dataset, the majority of the results converge to the observed ones in cumulative rainfall amounts. However, the application of KF (first step) does

not yield remarkable improvement in r computations, although the correlations between the radar and the gauge datasets are acceptable.

- In the BCR (II) dataset, the majority of the stations have similar cumulative rainfall amounts and higher r results concerning the gauge statistics, similar to the previous case. Moreover, an improvement in the bias computation is observed.
- The sensitivity of the ρ_x and σ_x^2 parameters shows that the stability and magnitude of r have a decreasing pattern as the parameters increase. However, the parameters are more sensitive in the results of cumulative and maximum rainfall amounts.
- The success of the filter in spatial sense has not been investigated due to the inadequate number of events. However, correlation results of the stations in Table 4.5 show that the filter is successful in temporal sense.

CHAPTER 5

HYDROLOGIC MODELING

5.1 General

Hydrologic system covers complex movement of water through the Earth. Hydrologic models try to conceive and represent these complex behaviors using relatively simple mathematical equations. Hydrologic model, from the simplest to the most complex, is essentially needed for forecasting, simulating and quantifying the effects of different inputs for a watershed. Models are in general designed to meet two primary objectives; to understand the hydrologic phenomena operating in a catchment and to generate synthetic sequences of hydrologic data for use in forecasting or facility design (Xu, 2002). In flood studies, there are several hydrologic rainfall-runoff models with different levels of uncertainty (Bartholmes and Todini, 2005). In this chapter, two hydrologic models are used for the flood simulations; the Hydrologic Engineering Center's Hydrologic Modeling System (HEC-HMS) and the Weather Research and Forecasting model hydrological extension package (WRF-Hydro). The reasons these specific models are selected can be listed as follows: HEC-HMS is easily accessible, has wide usage in the literature and is used as an empirical based lumped model; whereas WRF-Hydro has open source code, is expected to be used in the near future at the continental level and is used as a physic-based distributed model.

5.2 HEC Hydrologic Modeling System

The Hydrologic Modeling System (HEC-HMS) is a product of the Hydrologic Engineering Center within the United States Army Corps of Engineers (USACE).

Under different soil and climatic conditions with different datasets, HEC-HMS has proved its ability to forecast and simulate the streamflow (Anderson et al., 2002; Yusop et al., 2007; Chu and Steinmann 2009; Soytekin, 2010; Choudhari et al., 2014). HEC-HMS is a lumped and uncoupled surface water model. HEC-HMS contains four components: Data Manager, Control Specification, Basin Model and Meteorologic Model. All components have different subcomponents. Depending on the characteristics of the study area, necessary subcomponents can be selected. Before the application of HEC-HMS, it is necessary to define the basin area, sub-basins, stream network, diversions and junctions. The Geospatial Hydrologic Modeling Extension (HEC-GeoHMS) and ArcHydro extension can be used to delineate the watersheds and generate the stream network. This process is commonly referred as terrain preprocessing based on digital elevation model (DEM). In the form of sub-basin boundaries, HEC GeoHMS is used to create input files. To determine physical characteristics of the sub-basins, 25 m spatial resolution DEM data retrieved from 1/25000 scaled topographic maps are used. Figure 5.1 shows the preprocessing steps. The steps can be listed in the order given below;

1. Dem Reconditioning (grid)
2. Fill Sinks (grid)
3. Flow Direction (grid)
4. Flow Accumulation (grid)
5. Stream Definition (grid)
6. Stream Segmentation (grid)
7. Catchment Grid Delineation
8. Catchment Polygon
9. Drainage Line
10. Adjoint Catchment
11. Drainage Point

After the completion of the terrain preprocessing, a project point which is the outlet of the study area is defined (Figure 5.2). Based on the project point location on the drainage line, HEC-GeoHMS extension defines the project area.

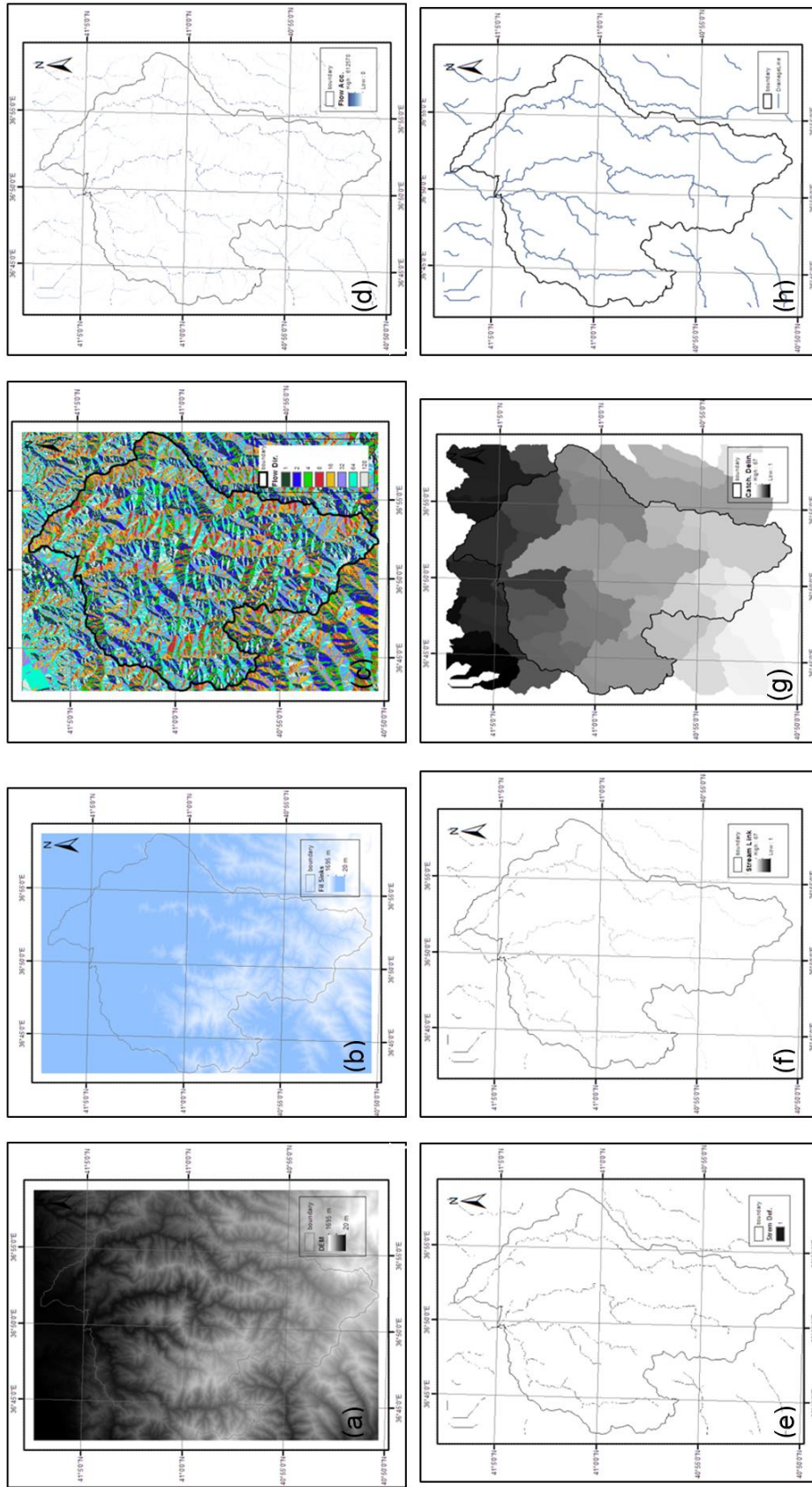


Figure 5.1 Preprocessing Steps (Dem Reconditioning (a), Fill Sinks (b), Flow Direction (c), Flow Accumulation (d), Stream Definition (e), Stream Segmentation (f), Catchment Delineation (g) and Drainage Line (h))

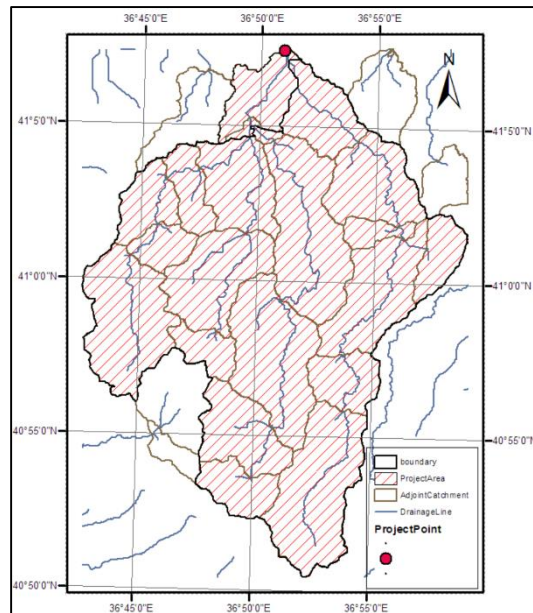


Figure 5.2 Project Area with Project Point and Drainage Line

The resulting project area has a total area of 383 km² including 39 sub-basins. For stream segments and the sub-basins, physical characteristics like the lengths and the slopes of each river segment, the average basin slope and the longest flow path of each sub-basin are computed using DEM data and HEC-GeoHMS extension.

In order to perform rainfall-runoff modeling, NRCS Curve Number model, NRCS Unit Hydrograph model and Muskingum flow routing model are selected for loss, transform and routing computations respectively.

5.2.1 Parameters Defined in the Model

Parameters in loss and routing computations are determined in the model calibration procedure. In this procedure, firstly, curve number is specified considering the soil data and observed runoff volume, then routing parameters are defined considering the reach properties, observed hydrograph shape and peak discharge time. In the model, only rainfall data are used as a forcing input in meteorological model component.

5.2.1.1 Curve Number (CN) Determination

The runoff curve number (CN) is an empirical parameter and used to predict direct runoff from excess rainfall. It was developed by the USDA Natural Resources Conservation Service, formerly called the Soil Conservation Service (SCS). CN is based on soil group, land use, treatment and hydrologic condition. CNs were developed for many soil-covers and published in the NRCS National Engineering Handbook (NEH-4). (1986). CN may also be defined as Antecedent Moisture Condition (AMC II) or CN (II). It describes the average soil moisture. The other conditions CN I and CN III describe the dry and wet soil condition respectively.

In environmental impact assessment report of Salıpazarı Dam, planned to construct on the outlet of the sub-basin 1 (sub-basin located on the far left), the CN (II) and CN (III) of upstream part of the dam are defined as 86 and 94 respectively (DSI, 2014). The geology map and existing soil materials; land use and land cover indicate that the study area has uniform soil type and land cover. In Figure 2.8 (a), it is seen that majority of the study area has basalt-andesite agglomerate soil type. In Figure 2.8 (b) and (c), it can be inferred that forest and podzolic soil (grey and brown) take part in almost all area. The podzolic soil is the typical soil of the coniferous or boreal forests (Chesworth, 2008). This information confirms the relevance of the soil materials; land cover and land use. Assignment of CN for a certain soil type is directly related to infiltration rate of the soil. Pratama et al. (2016) classify the average infiltration rate measurements into 5 groups considering the origin of the soil (Figure 5.3). According to their study, basalt and andesit soil type have low porosity that cause low infiltration capacity.

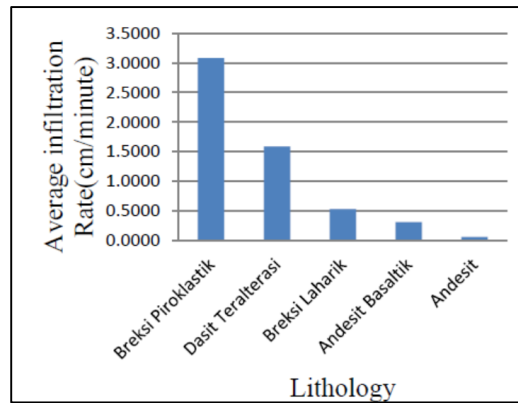


Figure 5.3 Average Infiltration Rate vs. Lithology (Source: Pratama et al., 2016)

Information about the soil data and literature review support the high curve numbers defined in environmental impact assessment report of Salıpazarı Dam. In modeling, average curve number that corresponds to CN (II) is generally used in the loss calculation. However, to see the effect on the discharge and to find the appropriate curve number for the study area, more than one specific value is used. The optimum curve number is defined with calibration procedure using observed discharge values. As defined in the assessment report, the curve number is started with a value of 86 and incremented by 2 at each iteration until it reaches 94.

5.2.2.2 Parameters in Routing Procedure

Routing is a mathematical procedure that predicts the flood magnitude, speed and shape as a function of time along the stream bed (Maidment, 1993). Flood routing methods can be classified into two categories; hydraulic routing (distributed system method) and hydrologic routing (lumped system method). In hydraulic routing procedure, conservation of mass and conservation of momentum equations are used. Whereas, in hydrologic routing procedure, conservation of mass and storage-discharge relation equations are used.

In HEC-HMS model, there are five available hydrologic routing methods: the Kinematic Wave Routing, Lag Routing, Modified Puls Routing, Muskingum Routing, and Muskingum-Cunge Routing methods. Muskingum method is selected for routing procedure because of its common use and reasonable results for floods propagating

through mild to steep sloping stream beds (Maidment, 1993). The expression of the continuity equation in Muskingum method is given as follows,

$$I - Q = \frac{dS}{dT} \quad \text{Equation (5.1)}$$

$$\frac{(I_1 + I_2)}{2} \Delta t - \frac{(Q_1 + Q_2)}{2} \Delta t = S_2 - S_1 \quad \text{Equation (5.2)}$$

Where I is the inflow rate, Q is the outflow rate and S is the storage. This method assumes that the amount of storage is related to inflow and outflow discharge. The total storage in the reach can be expressed as follows:

$$S = KQ + KX(I - Q) \quad \text{Equation (5.3)}$$

Where K is the storage constant and X is the weighting factor (dimensionless). K value is close to flow travel time through the stream. It is sensitive to the channel length. The value of X ranges from 0 to 0.5 which gives the maximum and the minimum attenuation respectively.

In ungauged basins, the Muskingum parameters (K and X) can be estimated using inflow hydrographs and channel dimensions estimated from empirical equations (Tewolde and Smithers, 2006). In our case, input data about the channel characteristics and inflow hydrographs are not available. To get proper outflow hydrograph, K and X parameters are described using basic channel properties and empirical equations. Slope and length of the reaches are calculated using DEM data in terrain preprocessing step.

Muskingum K parameter can be estimated using the equation (Fread, 1983),

$$K = \frac{\Delta L}{V_W} \quad \text{Equation (5.4)}$$

Where K is the wave travel time (s), ΔL is the reach length (m) and V_W is the celerity (m/s). The celerity (V_W) may be estimated from the equation constituted by Viessman et al. (1989),

$$V_w = \frac{11}{9} V_{av} \quad \text{Equation (5.5)}$$

where V_{av} is the average velocity and can be calculated from Manning Equation (Te Chow, 1959),

$$V_{av} = \frac{1}{n} R^{2/3} \sqrt{S} \quad \text{Equation (5.6)}$$

where n is the manning roughness coefficient (dimensionless), R is the hydraulic radius (m) and S is the slope of the reach. Substituting Equation 5.5 and Equation 5.6 into Equation 5.4, this can be obtained,

$$K = \frac{9(\Delta L n)}{11 R^{2/3} \sqrt{S}} \quad \text{Equation (5.7)}$$

From Equation 5.7, it can be inferred that increasing the channel length or decreasing the slope reach increase the K parameter.

Another routing parameter, the weighting factor (X), is a physical parameter and defines the attenuation and shape of the hydrograph. In 1969, Cunge defined X as,

$$X = \frac{1}{2} - \frac{Q_0}{2SPV_w\Delta L} \quad \text{Equation (5.8)}$$

where Q_0 is the reference discharge and P is the wetted perimeter.

In order to start the calibration procedure, K and X parameters are defined roughly using only the reach properties (length and slope). Then, for all reach segments in the model, routing parameters are changed by putting additive or subtractive factors. Calibration is continued until the simulated hydrograph shape and peak discharge time approach to the observed one.

5.2.2 Calibration of the Model

As defined in the previous section, calibration procedure starts with CN application. Model is run for each numbers defined in the range. Visual and statistical results for this procedure are given in Figure 5.4 and Table 5.1. The rainfall values over the study area obtained using Thiessen Polygon method (Figure 3.9 (a)).

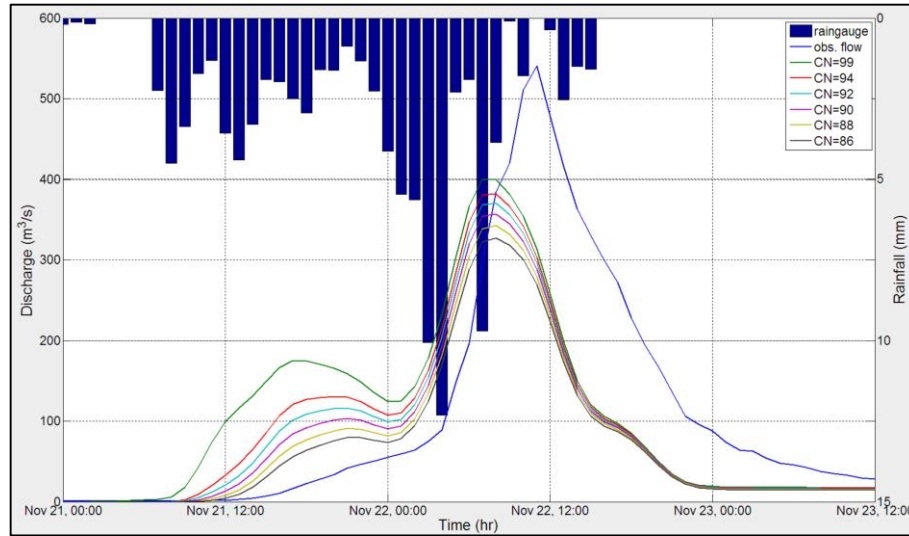


Figure 5.4 Simulated hydrographs obtained from CN calibration

Table 5.1 Amount of Runoff Volume for Observed and Simulated Discharges (10^6 m^3)

Observed	CN=99	CN=94	CN=92	CN=90	CN=88	CN=86
24.9	24.3	21.0	19.7	18.5	17.3	16.2

In Figure 5.4, it is seen that, as expected, the increase in curve number value rises the simulated discharge values in the rising limb of the hydrographs noticeably. In the falling limb of the hydrograph (especially time after 12:00, Nov 22), regardless of the CN value, all simulated hydrographs converge to each other. The main effect of the CN value is seen in the rising limb and peak of the hydrographs. Apart from the defined range of the CN, as an upper bound, CN value is selected as 99 for a specific run to see the effect on discharge and runoff volume. At this point, it is observed that model gives very quick response and almost whole rainfall received in studied time returns

to discharge with very few infiltration. The runoff volume results show that even an upper bound of CN value does not catch the observed runoff volume value, which is 24.9 m⁶ (Table 5.1). Therefore, it can be inferred that, rainfall data prepared with Thiessen polygon cannot represent the spatial distribution of the rainfall very well. At this stage, statistical computations like correlation coefficient (r), root mean square error (RMSE) and Nash and Sutcliffe efficiency (NSE) are not carried on. Because, the main aim is to simulate the discharge that has similar runoff volume to the observed one. From Table 5.1, it is seen that none of the CN values catches the observed runoff volume completely. Among these results, to provide proper runoff volume and to be consistent with the environmental report, CN is selected as 94. This CN value implies that soil condition is wet.

In the second stage, routing parameters are calibrated. In the studied area, there is only one discharge observation station (2245-Gökçeli AGI) located in the outlet of sub - basin 3. Discharge data represents the sub-basin 1, sub-basin 2 and sub-basin 3. In previous section, formulation of K and X parameters are defined. In these equations, to find the necessary parameters which are slope, channel length, manning's roughness coefficient, hydraulic radius, reference discharge and wetted perimeter are required. However, apart from the stationary physical characteristics of the streams supplied from the DEM data, there is no further available data to compute the routing parameters precisely. In the upstream part of the gauging station, depicted with blue identifier in Figure 5.5, there are 11 reaches convey flow through the outlet.

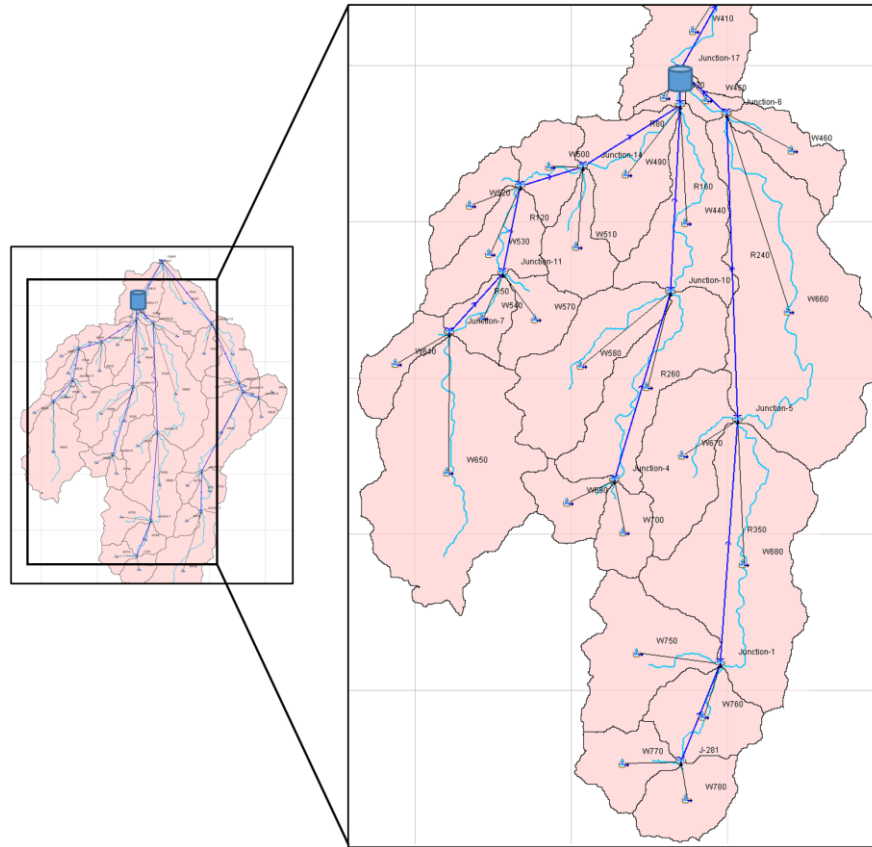


Figure 5.5 Location of the Sub-basins, Reaches and Gauging Station

In K and X computations, values like reference discharge, hydraulic radius, wetted parameter and manning's roughness coefficient are considered to be uniform for each reach. Routing parameters are estimated roughly, using only reach length (ΔL) and slope information. Then, calibration is applied by putting additive or subtractive factors to the routing parameters. In calibration procedure, stepwise technique is applied. Firstly, storage constant, K parameter is calibrated by additive factor ± 0.1 . Then, weighting factor, X parameter is calibrated by additive factor ± 0.05 . Figure 5.6 shows the effect of K and X parameter on discharge.

Figure 5.6 (a) shows that the increase in K parameter causes decrease in peak discharge and also runoff volume due to the increase in infiltration. However, this situation causes increase in lag time and postponing the time of peak discharge. The increase in X parameter decreases the attenuation slightly (Figure 5.6 (b)). Generally, it can be stated that X parameter changes the hydrograph shape with a minor effect. The

optimum simulated flow is obtained with the values given in Table 5.2 for each reach. Computations like correlation coefficient (r) and root mean square error (RMSE) are the objective functions in the calibration study. According to the objective functions, the optimal simulated flow is depicted in Figure 5.7.

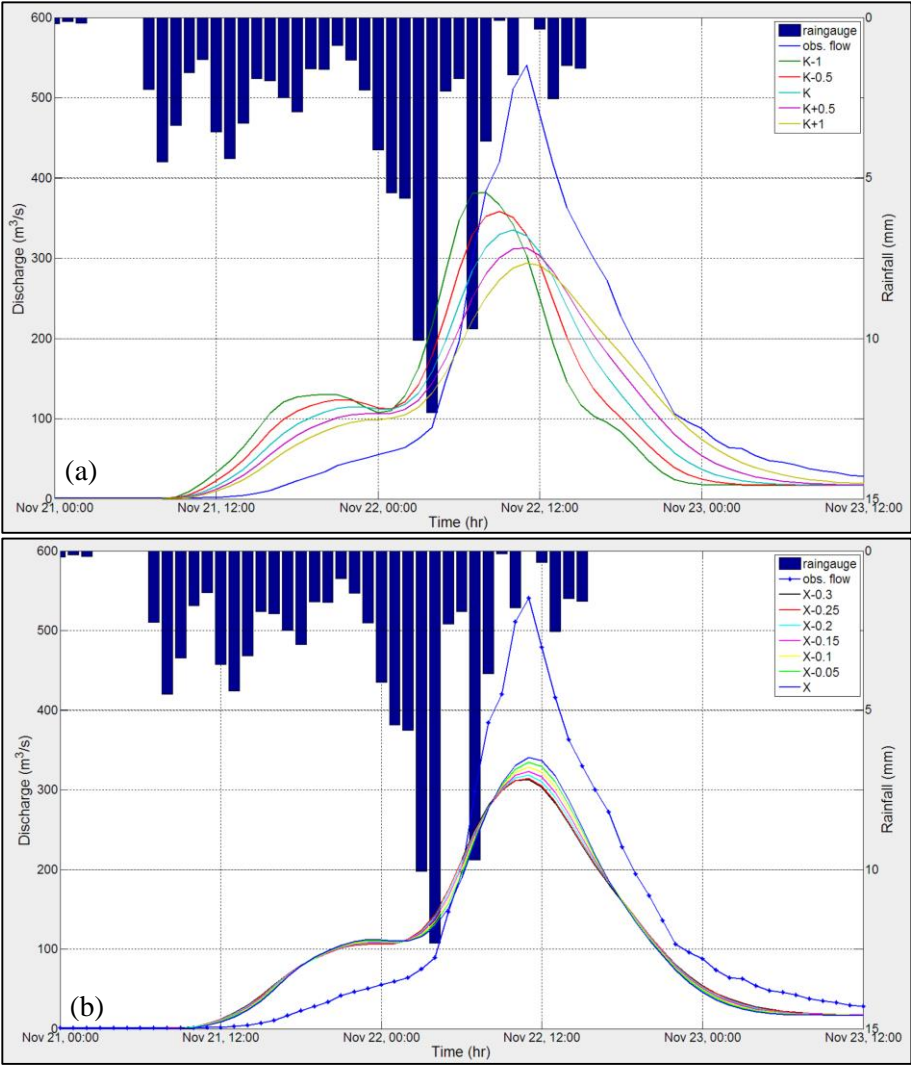


Figure 5.6 The Effect of K (a) and X (b) Parameters on Discharge

Table 5.2 Calibrated Routing Parameters for each Reach

Reach	ΔL (km)	Slope (%)	K (hr)	X
R50	2.97	0.040	1.57	0.496
R120	3.49	0.037	1.67	0.496
R100	2.46	0.008	2.11	0.475
R80	4.57	0.018	2.13	0.494
R260	8.21	0.080	1.81	0.499
R160	7.77	0.019	2.46	0.497
R30	1.16	0.002	2.20	0.326
R360	3.97	0.041	1.69	0.497
R350	10.75	0.028	2.49	0.498
R240	15.33	0.016	3.21	0.498
R40	2.29	0.010	1.97	0.478



Figure 5.7 The Optimal Simulated Flow

Figure 5.7 shows the optimal simulated flow along with the observed one. It is seen that model overestimates the discharge at the beginning and then underestimates the discharge after Nov. 22 at 06:00 AM. RMSE and r values for the simulated flow are 60.91 m³/s and 0.95 respectively. To assess the power of hydrological model, the Nash–Sutcliffe model efficiency (NSE) coefficient can be used,

$$NSE = 1 - \frac{\sum_{t=1}^T (Q_o^t - Q_m^t)^2}{\sum_{t=1}^T (Q_o^t - \bar{Q}_o)^2} \quad \text{Equation (5.9)}$$

where, $\overline{Q_m}$ is the mean of observed discharge, Q_m is the modeled discharge and Q_o is the observed discharge at time t. Using this equation, the NSE coefficient is calculated as 0.82 for rain gauge data that belongs to 2014 flood event in HEC-HMS. For other rainfall products, events and hydrologic model, the NSE results will be given in section 5.4

5.3 WRF-Hydro Modeling System

WRF-Hydro has been developed by the National Center for Atmospheric Research and its research partners. It is originally designed to facilitate easier coupling between the WRF mesoscale meteorological model and components of terrestrial hydrological models. Currently, WRF-Hydro is both a stand-alone hydrological modeling architecture and a coupling architecture with atmospheric models. It has been developed to represent hydrologic processes with spatial redistribution of surface, subsurface and channel waters across the land surface and to couple hydrologic models with atmospheric models (Gochis et al., 2015). System contains baseflow, lake and reservoir routing options. Model has an ability to simulate soil moisture (liquid and frozen), soil temperature, skin temperature, snowpack water equivalent (snowpack density), canopy water content and the energy flux and the water flux terms of the surface energy (Senatore et al., 2015).

The structure of WRF-Hydro is illustrated in Figure 5.8. The process starts with reading the static land surface physiographic data into the WRF-Hydro system. In this stage, computational arrays are constructed. After that, in stand-alone system (uncoupled), the forcing data are read and 1-D gridded land surface model (LSM) is executed. In the next stage, land surface states are disaggregated to high resolution terrain routing grids using spatial weighting method. After that, if activated, physics options are executed in this order: subsurface routing physics, surface routing physics, the conceptual base flow model and channel and reservoir routing components. In the last stage, updated land surface states are aggregated from the terrain routing grid to the LSM grid and model simulation results are written to the model output files (Gochis et al., 2015).

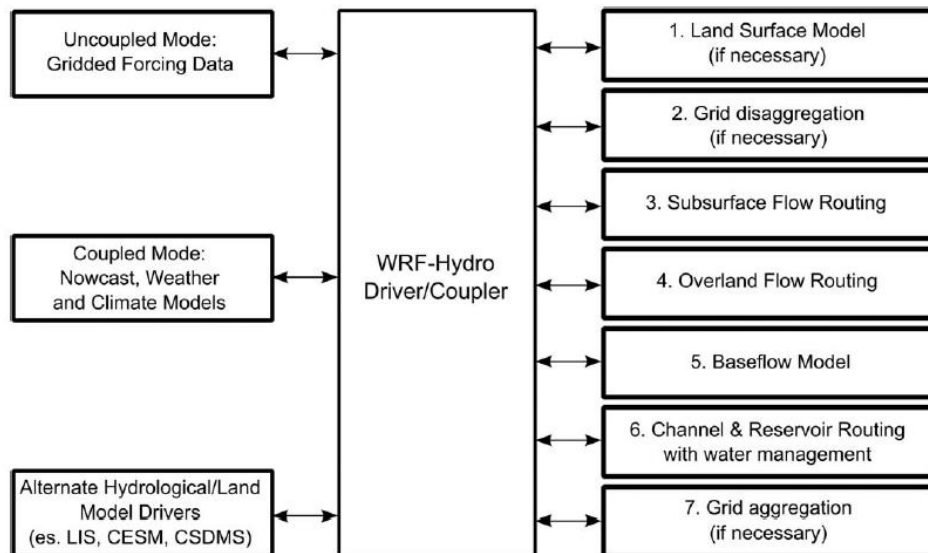


Figure 5.8 WRF-Hydro Architecture with Model Components (from Gochis et al., 2015)

5.3.1 WRF Model Physics Description

Version 3.0 of WRF-Hydro includes the 1-Dimensional land surface model, the subsurface routing routines, the overland routing routines, the channel routing routines, the lake/reservoir routing and the base flow model routine. In this study, the WRF-Hydro is used in an uncoupled manner with activated options of surface flow, subsurface flow and channel routing.

5.3.1.1 Land Surface Model (LSM) Description

LSM is a 1-D model that simulates soil moisture (liquid and frozen), soil temperature, skin temperature, snowpack depth, snowpack water equivalent canopy water content, and the energy flux and water flux terms of the surface energy balance and surface water balance (Figure 5.9). As an input data, near-surface atmospheric forcing data are required. Model has a long heritage starting from the mid-1980's. The earliest predecessor of NOAA LSM calculated latent and heat flux using two-layer soil model and simplified plant canopy model. With recent development and community participation, numerous changes in LSM has been evolved. Advancements like representation of soil with four layer (Ek et al., 2003), formulation of the canopy

conductance (Chen et al., 1996), bare soil evaporation and vegetation phenology (Betts et al., 1997), surface runoff and infiltration (Schaake et al., 1996), thermal roughness length treatment in the surface layer exchange coefficients (Chen et al., 1997), frozen soil processes (Koren et al., 1999), the snow-surface energy budget calculation (Ek et al., 2003) and seasonal variability of the surface emissivity (Tewari et al., 2005) have been implemented. The reliability and sensitivity of this model has been assessed various researchers in coupled modes (Gochis et al., 2015).

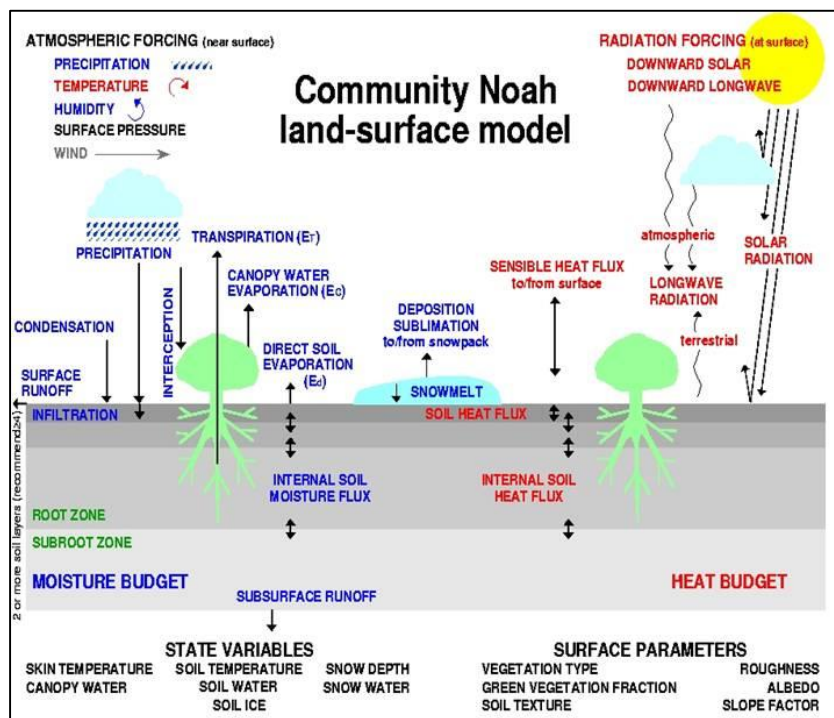


Figure 5.9 NOAH Land Surface Model Structure (source form: <http://ldas.gsfc.nasa.gov/nldas/NLDAS2model.php>)

5.3.1.2 Subsurface Routing Description

Prior to the routing of overland flow, subsurface lateral flow is calculated. Lateral flux and exfiltration process is shown in Figure 5.10. Lateral flow in saturated soil employs a quasi-three-dimensional flow representation. Topography, saturated soil depth and saturated hydraulic conductivity affect the calculation.

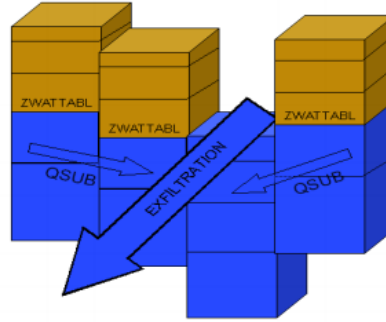


Figure 5.10 Saturated Subsurface Flow Components (from Gochis et al., 2015)

The rate of saturated subsurface flow can be calculated using Dupuit-Forcheimer assumptions.

$$q_{i,j} = \begin{cases} -T_{i,j} \tan \beta_{i,j} w_{i,j} & \beta_{i,j} < 0 \\ 0 & \beta_{i,j} > 0 \end{cases} \quad \text{Equation (5.10)}$$

where,

$q_{i,j}$ is the flow rate from cell i, j ,

$T_{i,j}$ is the transmissivity of cell i, j ,

$\beta_{i,j}$ is the water table slope of cell i, j and

$w_{i,j}$ is the width of the cell

The transmissivity is given by:

$$T_{i,j} = \begin{cases} \frac{K_{sat_{i,j}} D_{i,j}}{n_{i,j}} \left(1 - \frac{z_{i,j}}{D_{i,j}} \right) & z_{i,j} \leq D_{i,j} \\ 0 & z_{i,j} > D_{i,j} \end{cases} \quad \text{Equation (5.11)}$$

where,

$D_{i,j}$ is the soil thickness,

$z_{i,j}$ is the depth of the water table and

$n_{i,j}$ power law exponent (governs the decay rate of $Ksat_{i,j}$).

When both equations combined in x direction, the flow rate can be expressed like this:

$$q_{x(i,j)} = \gamma_{x(i,j)} h_{(i,j)} \beta_{x(i,j)} < 0 \quad \text{Equation (5.12)}$$

where,

$$\gamma_{x(i,j)} = - \left(\frac{w_{i,j} Ksat_{i,j} D_{i,j}}{n_{i,j}} \right) \tan \beta_{x(i,j)} \quad \text{Equation (5.13)}$$

$$h_{(i,j)} = \left(1 - \frac{z_{i,j}}{D_{i,j}} \right)^{n_{i,j}} \quad \text{Equation (5.14)}$$

Using two dimensional routing method, same calculation is repeated for y-direction.

The total saturated subsurface moisture becomes:

$$Q_{net(i,j)} = h_{(i,j)} \sum_x \gamma_{x(i,j)} + h_{(i,j)} \sum_y \gamma_{y(i,j)} \quad \text{Equation (5.15)}$$

Then, the change in water table depth can be calculated as:

$$\Delta z = \frac{1}{\phi_{(i,j)}} \left[\frac{Q_{net(i,j)}}{A} - R_{i,j} \right] \Delta t \quad \text{Equation (5.16)}$$

where,

ϕ is the soil porosity,

R is the soil column recharge rate from infiltration and

A is the grid cell area.

5.3.1.3 Surface Overland Flow Routing Description

WRF-Hydro uses a fully-unsteady, explicit, finite difference, diffusive wave formulation for surface overland flow routing (Figure 5.11). Diffusive wave formulation is superior to the kinematic wave equation and the simplification of the

more general St. Venant equations of continuity and momentum for a shallow water wave.

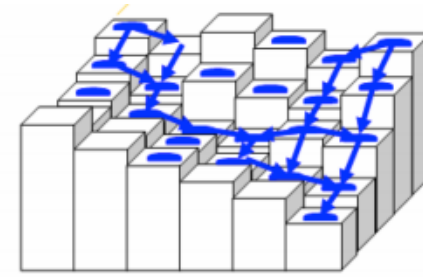


Figure 5.11 Overland Flow Routing (from Gochis et al., 2015)

The two-dimensional continuity equation for a flood wave can be described as:

$$\frac{\partial h}{\partial t} = \frac{\partial q_x}{\partial t} + \frac{\partial q_y}{\partial t} = i_e \quad \text{Equation (5.17)}$$

where

h is the surface flow depth,

q_x and q_y are the unit discharges in the x and y directions and

i_e is the infiltration excess.

In WRF-Hydro, to find unit discharge, Manning's equation is implemented,

$$q_x = a_x + h^\beta \quad \text{Equation (5.18)}$$

where,

$$a_x = \frac{S_{fx}^{0.5}}{n_{OV}} ; \quad \beta = \frac{5}{3} \quad \text{Equation (5.19)}$$

where,

n_{OV} is the land surface roughness coefficient and

β is the unit dependent coefficient.

In the diffusive wave calculation, the momentum equation for the x-dimension can be described as:

$$S_{fx} = S_{ox} - \frac{\partial h}{\partial x} \quad \text{Equation (5.20)}$$

where,

S_{fx} is the friction slope (slope of energy grade line),

S_{ox} is the terrain slope and

$\frac{\partial h}{\partial x}$ is the depth of surface water change in x direction.

5.3.1.4 Channel Routing Description

When the ponded water depth of stream channel exceeds the retention depth, stream channel starts. The ponded water depth is a combination of local infiltration excess, water from overland flow and exfiltration from groundwater flow. Channel routing module in WRF-Hydro allows for one-dimensional distributed stream flow routing. Module uses explicit, 1D, variable time stepping diffusive wave formulation. This formulation is a simplified form of St. Venant equations. The continuity equation is given as:

$$\frac{\partial A}{\partial t} + \frac{\partial Q}{\partial x} = q_{lat} \quad \text{Equation (5.21)}$$

where,

A is the flow area of the cross section,

t is the time,

Q is the flow rate,

x is the stream wise coordinate and

q_{lat} is the lateral inflow rate into the channel.

The momentum equation is:

$$\frac{\partial Q}{\partial t} + \frac{\partial(\beta Q^2/A)}{\partial x} + gA \frac{\partial Z}{\partial x} = -gAS_f \quad \text{Equation (5.22)}$$

where,

β is the momentum correction coefficient,

g is the gravity,

Z is the water surface elevation and

S_f is the friction slope.

$$S_f = \left(\frac{Q}{K}\right)^2 \quad \text{Equation (5.23)}$$

where, K is the conveyance and computed from the Manning's equation:

$$K = \frac{C_m}{n} AR^{2/3} \quad \text{Equation (5.24)}$$

where,

C_m is the dimensional constant (1.0 for metric units),

n is the Manning's roughness coefficient and

R is the hydraulic radius.

The simplified momentum equation (ignoring convective term):

$$Q = -SIGN\left(\frac{\partial Z}{\partial x}\right) K \sqrt{\left|\frac{\partial Z}{\partial x}\right|} \quad \text{and} \quad \begin{cases} SIGN = 1 & \frac{\partial Z}{\partial x} > 0 \\ SIGN = 0 & \frac{\partial Z}{\partial x} < 0 \end{cases} \quad \text{Equation (5.25)}$$

Continuity equation over raster cell is defined as:

$$A^{n+1} - A^n = \frac{\Delta t}{\Delta x} \left(Q^n_{i+\frac{1}{2}} - Q^n_{i-\frac{1}{2}} \right) + \Delta t q_{lat}^n \quad \text{Equation (5.26)}$$

where, $Q^n_{i+\frac{1}{2}}$ is the flux between point i and $i + 1$ and computed from:

$$Q^n_{i+\frac{1}{2}} = -SIGN(\Delta Z^n_{i+1}) K_{i+\frac{1}{2}} \sqrt{\frac{|\Delta Z^n_{i+1}|}{\Delta x}} \quad \text{Equation (5.27)}$$

where,

$$\Delta Z^n_{i+1} = Z^n_{i+1} - Z^n_i \quad \text{Equation (5.28)}$$

$$K_{i+\frac{1}{2}} = 0.5[(1 + SIGN(\Delta Z^n_{i+1}))K_i + (1 - SIGN(\Delta Z^n_{i+1}))K_{i+1}] \quad \text{Equation (5.29)}$$

5.3.2 Description of Input Data Files

WRF-Hydro requires two individual input data files in model domain for running process. These are land surface model grid and terrain routing grid. Land surface model grid or coarse grid contains information about topography, green vegetation fraction, latitude, longitude, land use, albedo and etc. It can be created in WRF Preprocessing system (WPS). It can also be custom created by user using software like ArcGIS and Matlab. In this study, using WPS tool, the coarse grid data are prepared. For this process, from NCAR Research Data Archive (NCAR RDA) the WPS geographical input data are obtained. Terrain routing grid or high resolution grid data are necessary for routing procedure across the landscape and through the stream channels. Terrain routing grid is in Network Common Data Form (NetCDF) grid format and contains the information like latitude, longitude, topography, flow

direction, channel grid, stream order, lake grid and etc. Terrain routing grid file has a higher spatial resolution than the land surface model grid file. However, the spatial extent of the files should be the same for disaggregation/aggregation procedure defined in running process. Apart from the model domain input files, WRF-Hydro requires meteorological forcing data for simulation and forecasting. Forcing data includes the variables of incoming short wave radiation (W/m^2), incoming longwave radiation (W/m^2), specific humidity (kg/kg), air temperature (K), surface pressure (pa) near surface wind (m/s) and liquid water precipitation rate (mm/s). For testing purposes, idealized forcing data can be selected.

5.3.2.1 The WRF Preprocessing System (WPS)

The WRF Preprocessing System (WPS) is a set of programs whose main aim is to prepare input for the simulation. The system, depicted in Figure 5.12, contains three independent programs: ungrib, metgrid and geogrid. The geogrid program defines the simulation domains and interpolates datasets to model domains. The ungrib program reads GRIB files (GRIdded Binary or General Regularly-distributed Information in Binary form), data format used in meteorology to store weather data, and writes in a simple format. The metgrid program interpolates the data created by ungrib program onto the simulation domain defined by geogrid program.

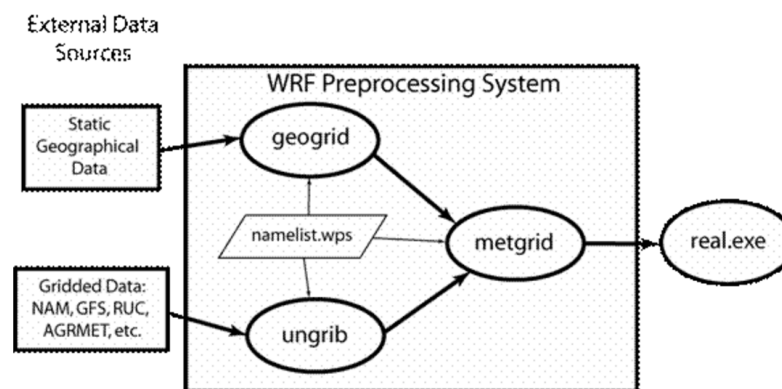


Figure 5.12 The WRF Preprocessing System Flowchart
 (source: http://www2.mmm.ucar.edu/wrf/users/docs/user_guide_V3/users_guide_chap3.htm)

The namelist.wps is a file that contains information about domain (parent id, grid ratio, coordinates, and reference lat/lon), simulation start and end times, intervals, path names and etc. Data specified in this file forms the model inputs. For this reason, to compose compatible data extent and resolution, conscious decisions should be made by the user.

The programs, ungrib and metgrid, are not used in the study because the gridded data, wrfout, required for forcing files are recognized by the WRF-Hydro. Thus, ungrib procedure performed by geogrid program and data transformation carried by metgrid program are not conducted.

The geogrid program is utilized in linux environment with required dataset. The dataset is downloaded from the WRF WPS geographical input data downloads page (http://www2.mmm.ucar.edu/wrf/users/download/get_sources_wps_geog.html). It includes data about terrestrial information like albedo, land use, soil type and green fraction. For Turkey and surroundings, some of the terrestrial data like soil categories in bottom and top layer, land use index, land mask, topography and surface albedo are visualized in visual browser for netCDF files (ncview program) and these are depicted in Figure 5.13. The resolution of terrestrial dataset is 4500 meters which is the same resolution as wrfout dataset acquired from TSMS. The explanation for class numbers or indexes defined in the soil categories and textures, land use, surface albedo and vegetation fraction datasets are given in the Appendix E. In albedo calculation, WRF uses vegetation fraction bounded by the maximum and minimum values of the vegetation parameter table (Table E.2).

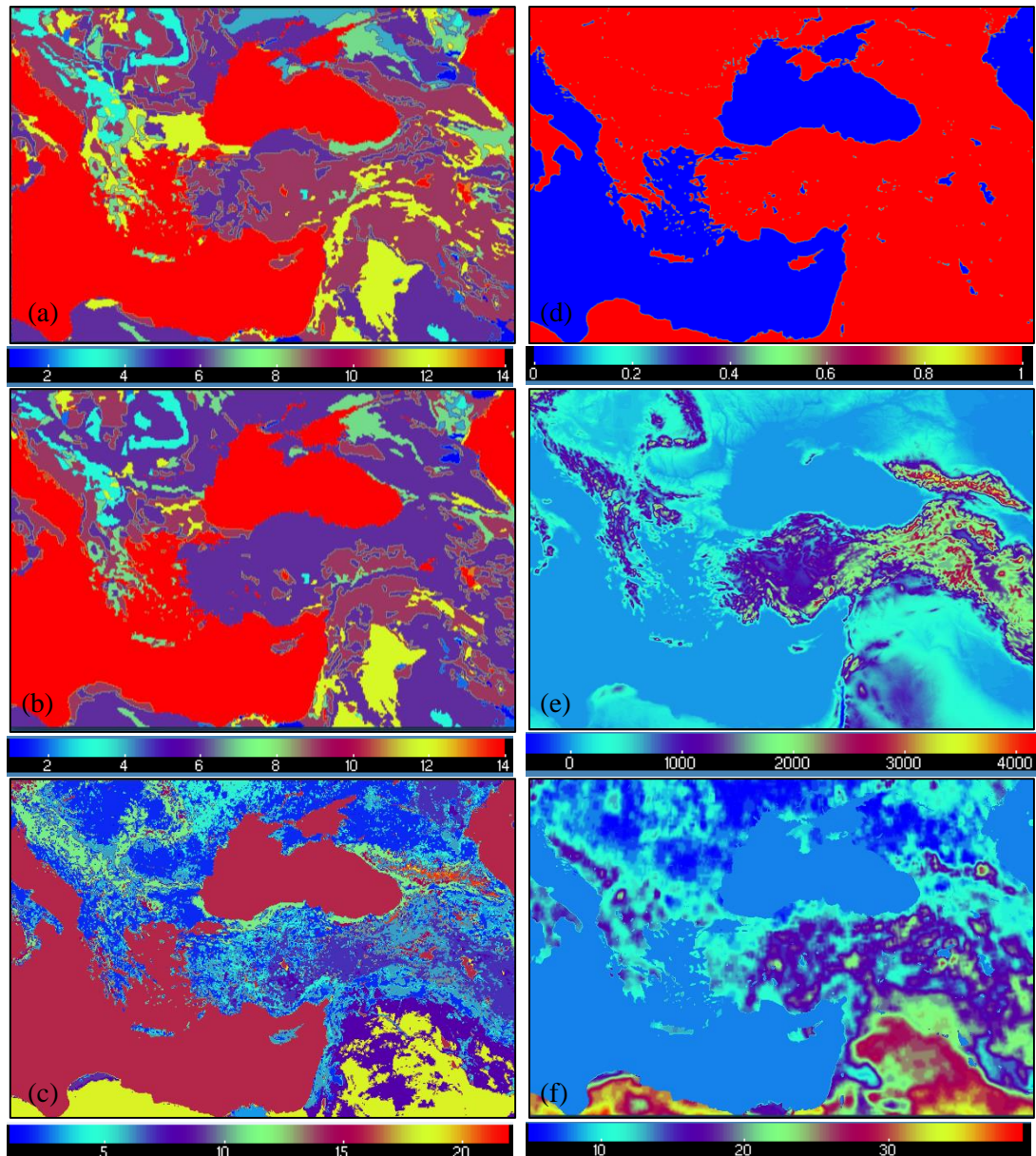


Figure 5.13 Terrestrial Information for Turkey and Surroundings (Dominant Soil Categories in the Bottom Layer (a) (numbered) and the Top Layer (b) (numbered), Land Use Index (Dominant Vegetation Types) (c) (numbered), Land Mask (d), Topographic Elevation (units of m)(e) and Surface Albedo (units of %) (e)) (The explanations for class numbers are given in Appendix E)

For the model domain, the necessary coarse grid data are clipped from the general terrestrial dataset. Figure 5.14 (a) and (b) show the elevation and land use index of the model domain.

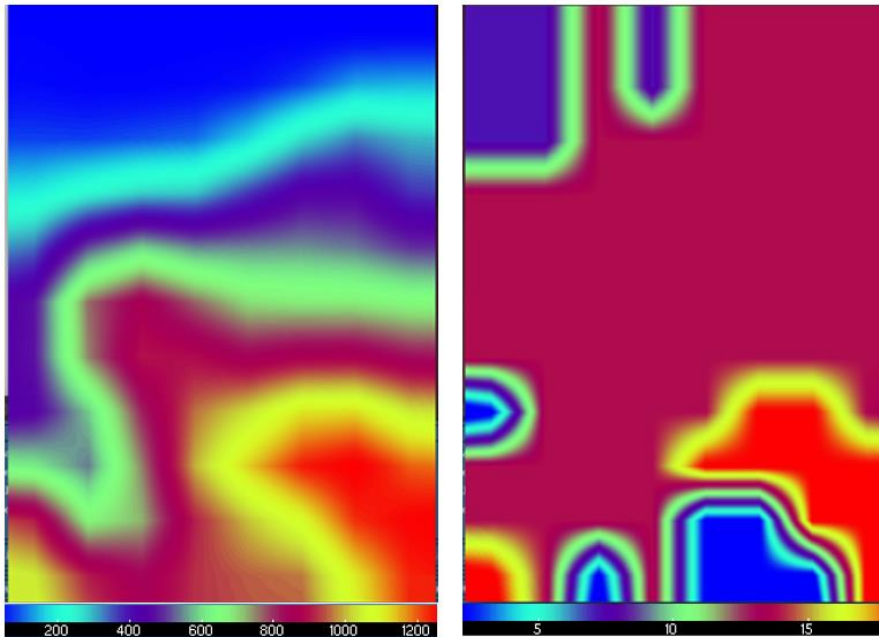


Figure 5.14 (a) Elevation Data (on the left), (b) land use index (on the right)

5.3.2.2 Terrain Routing Grid Data (High Resolution Grid Data)

In this step, the necessary data used in the routing procedure is constructed in ArcGIS environment. For this purpose, DEM data are downloaded from USGS HydroSHEDS (Hydrological data and maps based on Shuttle Elevation Derivatives at multiple Scales) mapping product. It offers georeferenced vector or raster datasets at various scales. It is a high resolution elevation data obtained from Space Shuttle flight for NASA's Shuttle Radar Topography Mission (SRTM). The used HydroSHED data are hydrologically processed elevation data at 3 arc-second (~90m) resolution.

In model runtime, defined variables are passed from coarse grid to the fine grid via disaggregation/aggregation procedure. In this procedure, there are two significant points that should be satisfied before the model run: coarse grid should exactly match the extent of fine grid and the dimension of coarse grid (spatial resolution) must be an integer multiple of fine grid dimension. The multiplication constant is called aggregation factor in the model and varies from 1 to n. In two separate special loops, disaggregation/aggregation steps are implemented after the land surface model loop. The reason behind disaggregation loop is to divide hydrologic variables coarse grid

square into integer number specified in by AGGFACTR (Figure 5.15). After disaggregation process, the routing procedure is carried out using fine grid values. Next, the aggregation procedure is achieved after the completion of computations in fine grid. Values calculated in routing are then used on the next iteration of the coarse grid.

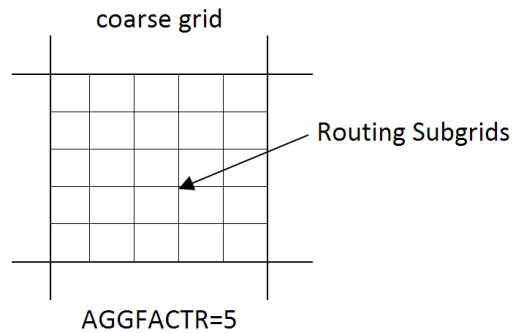


Figure 5.15 Implementation of Routing Sub-grid within Coarse Grid

As stated before, the resolution of the course grid data, namely wrfout data, is 4500 m. For model run operation, the AGGFACTR is selected as 30. This means one coarse grid square is disaggregated into 900 squares. In this way the resolution of the fine grid data is built as 150 m. In ArcGIS program, layers which are latitude, longitude, topography, flow direction, channel grid, stream order, basin mask, overland flow roughness scaling factor (OVROUGHRTFAC) and surface retention depth factor (RETDEPRTFAC) are created. For land use layer creation, the geogrid layer, mentioned in the previous section, is used. Then, the created layers are exported to netcdf format in ArcGIS program. The view of topography, flow accumulation, channel grid, flow direction, basin mask and land use are depicted in Figure 5.16 using ncview program. According to land use data downloaded from WRF WPS geographical input data web page, the majority of studied area has a silty clay soil type (soil number 11 in Figure 5.16 (f), marked as bright green). The soil texture information in the downloaded data is defined by the State Soil Geographic soil database (STATSGO) that is generated from United States Department of Agriculture, Natural Resources Conservation Service (USDA- NRCS). The dataset was generated by detailed soil survey maps. In region where detailed soil maps are unavailable, Land

Remote Sensing Satellite (LANDSAT) images are assembled. In order to work with fine grid in the WRF-Hydro, the defined layers in the netcdf format must be in the concatenated form. The merging process can be done any netcdf operators that make netcdf files into a single netcdf file. The extent and the resolution of coarse and fine grids can be seen in Figure 5.17. The extent of the datasets is verified by Matlab.

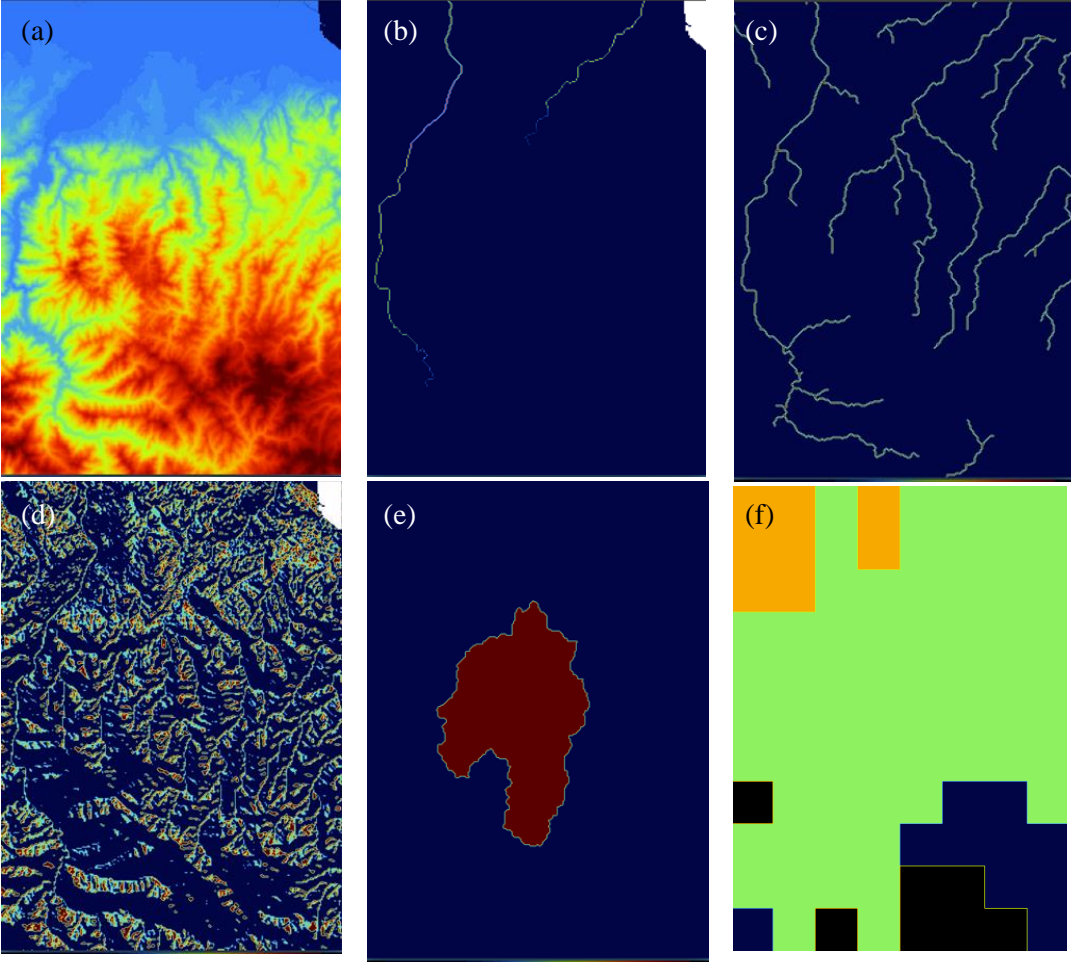


Figure 5.16 Topography (a), Flow Accumulation (b), Channel Grid (c), Flow Direction (d), Basin Mask (e) and Land Use (f)

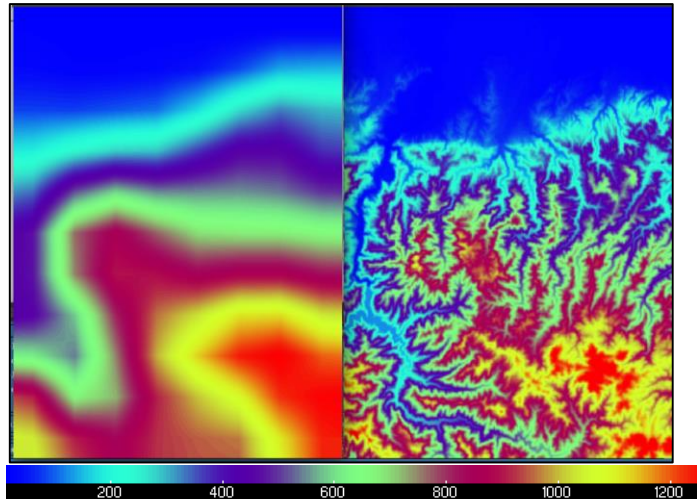


Figure 5.17 The Topography of Coarse Grid (on the left) and Fine Grid (on the right) in the Model Domain

5.3.2.3 Forcing Data Input Files

Unlike the HEC-HMS model that uses only rainfall data as a forcing input, the WRF-Hydro model uses 7 different variables. The mandatory meteorological forcing variables required by the model can be listed as below;

1. Incoming shortwave radiation (W/m^2),
2. Incoming longwave radiation (W/m^2),
3. Specific humidity (kg/kg),
4. Air temperature (K),
5. Surface pressure (Pa),
6. Near surface wind components (m/s) and
7. Liquid water precipitation rate (mm/s).

In the model, meteorological forcing data can be provided in one of the options; 1) HRLDAS (High Resolution Land Data Assimilation System) hourly input files, 2) HRLDAS minute format input files, 3) wrfout file (from WRF program), 4) Idealized HRLDAS, 5) Idealized HRLDAS with specific precipitation, 6) hourly HRLDAS input file with specified precipitation and 7) WRF output file with specified precipitation. The third option, wrfout, is selected for the forcing data input option in the model namelist file as this option is used to read a WRF model output file and

extract appropriate fields. “wrfout_d01_2014-11-22_17:00:00” is an example of forcing data format. The filename formats for each hour are turned into to the required form in linux environment. Because, the punctuation mark, colon (:), cannot be used in the filenames in windows.

In the calibration procedure, the gauge values, distributed over the study area by Thiessen polygon method are used. The extent of the Thiessen polygon does not cover the model domain defined in the WRF-Hydro. For this reason, the edge of the polygons are stretched out through the model domain and the area of polygons are split over the coarse grid. The steps are demonstrated in Figure 5.18. The rainfall values for each grid are computed considering the area ratio of the pixel. The wrfout template with mandatory variables except the rainfall data is used for forcing data. The writing process of the gauge data is achieved in Matlab. After this step, the calibration study is implemented.

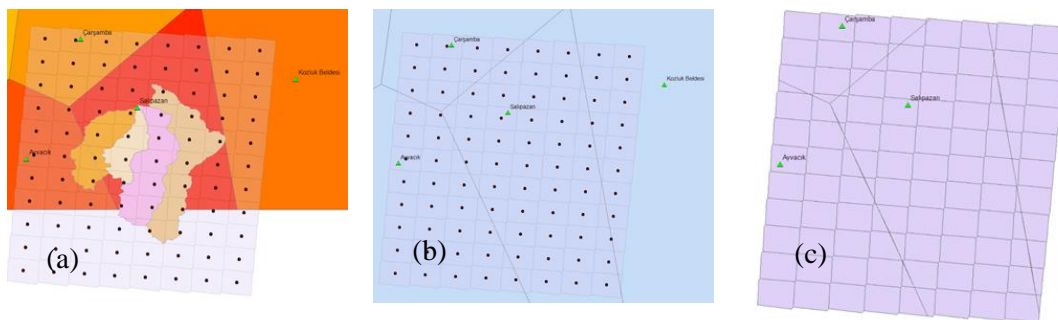


Figure 5.18 Model Domain over the Thiessen Polygon (a), Stretching the Edge of the Polygons (b), Splitting the Polygons over the Coarse Grid (c)

5.3.3 WRF-Hydro Model Calibration Approach

Using predefined parameter sets and forcing data containing gauge rainfall data, WRF-Hydro model is calibrated. In this process, manual calibration is performed with the aim of reproducing observed hydrograph of Gökçeli (2244) gauging station and is applied in two steps:

- In the first step, relevant parameters that control the total water volume are calibrated. These parameters are infiltration scaling factor (REFKDT), surface

runoff parameter (REFDK) and surface retention depth (RETDEPRTFAC). REFDK and REFKDT are scaling parameters for surface runoff within the WRF model. These are interlocking parameters which means, If REFKDT is changed, then REFDK must be adapted to that new value (Mitchell, 2001). For this reason, the effects of both parameter on water volume are analyzed simultaneously. When the optimum pair acquired with respect to observed water volume, the other parameter, RETDEPRTFAC, is examined. The reason behind taking some parameters as a set is to see the parameter interaction and its influence on the results that is stated in detail in the study of Yucel et al (2015).

- In the second step, parameters that control hydrograph shape are calibrated simultaneously like in the previous step. These are surface roughness (OVROUGHRT) and channel Manning roughness (MANN).

In the model, REFDK, REFKDT and MANN parameters are in tabulated form for model domain, whereas RETDEPRTFAC and OVROUGHRT are in pixel format which means they can be distinct for each sub-basin or specific area. Optimum parameter or parameter sets in calibration procedure are defined by using statistical measures. Since the implementation of WRF-Hydro in the research is very recent, the studies on modeling are not abundant. As for uncoupled mode, Yucel et al (2015) calibrated the parameters: REFKDT, RETDEPRTFAC, OVROUGHRT and MANN in step-wise manner and recently Silver et al (2017) calibrated the parameters: topographic slope (SLOPECAT), REFDK and REFKDT whereas, for coupled mode, Givati et al (2016) calibrated the parameters: REFKDT and REFDK

5.3.3.1 Model Calibration Part I

As mentioned before, calibration study is started by changing the parameters, REFKDT and REFDK. Initially, model default values are used. The calibration range for REFDK is selected between 2×10^{-6} and 2×10^{-3} . Due to the wide range, the increment is selected as 10^{-1} and the effect of results are analyzed visually in logarithmic scale (Figure 5.19 (a)). The nominal range for REFDK mentioned by Mendoza et al. (2015) is between 2×10^{-8} and 2×10^{-4} . The chosen values exceed the

nominal range but the purpose is to realize the influence of parameters on the results. For REFKDT, the selected calibration range is between 0.1 and 1.0. The feasible ranges of REFKDT, mentioned in the Rosero et al. (2009), is between 0.1 and 10. This span contains the chosen values in the calibration. Model is executed for the selected ranges of the parameters. In calibration, simulation time interval starts with 20.11.2014-00:00 and ends with 24.11.2014-00:00, which takes 120 hrs. However, statistical measures are done with considering the time span interval of the gauging station, 64 hrs. The main aim of enlarging the time interval is to reduce the model spin up effect. However, in validation stages of WRF-Hydro, due to the time span of WRF model precipitation forecasts, 72 hours of simulations are performed. At this stage, the main purpose is to calibrate the aforementioned parameters and get proper runoff volume in simulation outputs. Therefore, the statistical evaluations like correlation coefficient (r), root mean square error (RMSE) and Nash-Sutcliffe Efficiency (NSE) are not calculated. Instead of this, the ratio of simulated and observed runoff volume is calculated for each run. Runoff volume is the amount of total water volume that is beneath the hydrograph plot. For the flood observed on 22nd November 2014, 24.92 hm³ volume of runoff in total passed through the Gökçeli AGI in 64 hours. Figure 5.19 shows the simulation results for the runoff volume ratios. To prepare surface data, linear interpolation technique is used between the points shown as blue dots in the figure. It is seen that model ratio results do not change extremely in the line where the value of REFDK is greater than 10^{-4} (Figure 5.19 (a)). Besides, the nominal range, mentioned at the beginning, does not enclose this range. On the other hand, the line where the value of REFDK is lower than 2×10^{-5} , model gives unsuccessful results. Thus, to examine REFDK parameter in detail, model run is performed for the range between 2×10^{-5} and 2×10^{-4} with an increment of 2×10^{-5} . The runoff volume ratios of this range are given in Figure 5.19 (b). It is noticed that the use of lower REFKDT values and higher REFDK values in the model increases the efficiency. In other words, the ratio results in these conditions approach the appropriate values. The optimum point that has the highest ratio in the computation is seen in the bottom right corner (0.1 for REFKDT and 2×10^{-4} for REFDK).

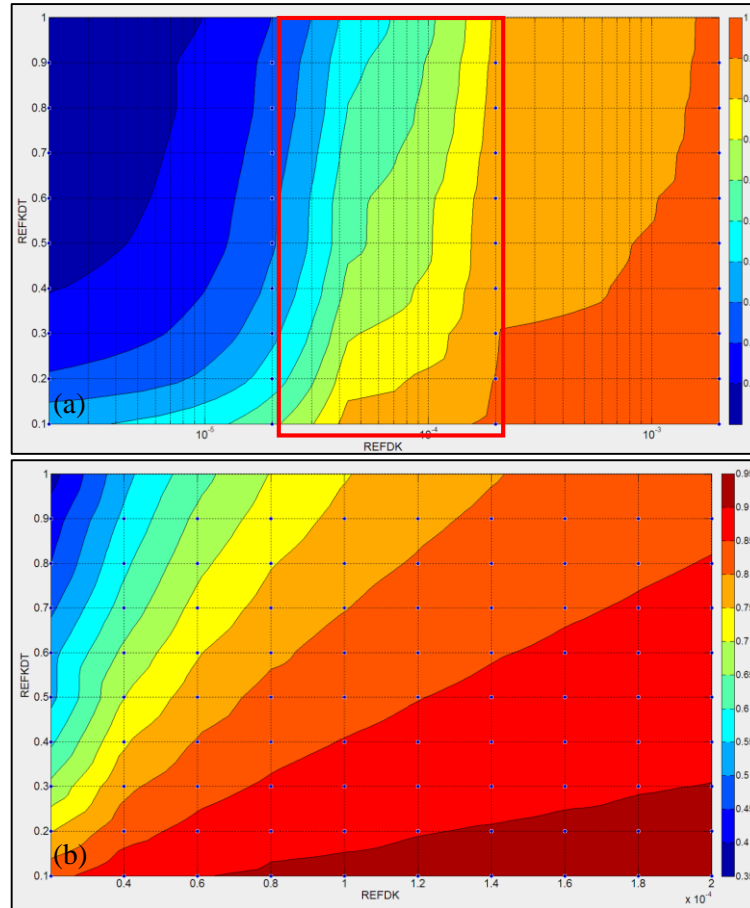


Figure 5.19 Simulation Results for the Runoff Volume Ratios

In the model, REFDK is defined as reference saturated hydraulic conductivity of the silty-clay-loam soil texture and has a default value of 2×10^{-6} m/s. The land use datasets show that the study area has a similar soil texture, silty clayey soil. In order to remain close to the reference REFDK value, REFKDT is taken as 0.1 which is the minimum value in calibration process and feasible ranges. Later, improvement in runoff volume ratios with increasing the REFDK values is taken into consideration (Table 5.3). When REFDK is 4×10^{-5} , the runoff volume ratio is calculated as 0.89. Beyond this value, the improvement of the results decreases. As a result, the optimum values for REFDK and RERKDT are determined as 4×10^{-5} and 0.1 respectively.

Table 5.3 Runoff Volume Ratios and Improvements for REFDK Values

REFDK (m/s)	Ratio	Improvement
2.0E-06	0.38	-
2.0E-05	0.83	54.3
4.0E-05	0.89	6.0
6.0E-05	0.90	1.4
8.0E-05	0.91	0.9
1.0E-04	0.91	0.4
1.2E-04	0.91	0.4
1.4E-04	0.92	0.4
1.6E-04	0.92	0.1
1.8E-04	0.92	0.2
2.0E-04	0.92	0.1

In the second stage of the part I, RETDEPRTFAC parameter (surface detention depth) is calibrated. Surface detention depth is a threshold value in millimeters and below this value, overland flow does not start. The selected range of this parameter in the model is between 0 and 1 mm. At first, the selected boundary values are studied to discern the effect in the model. For maximum and minimum values of RETDEPRTFAC parameter, the runoff volume ratios are calculated as 0.89 and 0.90 respectively. The results are similar to each other. As mentioned in the study of Yucel et al. (2015), steep slopes in Western Black Sea Region of Turkey dominate the domain and this value can be 0. With this value, it is assumed that water moves across the terrain without infiltration.

5.3.3.2 Model Calibration Part II

In the second part of the calibration study; surface roughness parameter (OVROUGHRT) and Manning roughness parameter (MANN), together which control the hydrograph shape, are analyzed as a couple. WRF-Hydro defines OVROUGHRT parameter in the distributed form in terrain routing grid input files. The feasible range of OVROUGHRT is between 0.1 and 1. In this range, OVROUGHRT parameter is analyzed with 0.1 increment. The Model defines MANN parameter in table form that is related with Strahler stream order method. For each stream order, Manning roughness coefficient changes. With a scaling factor (MANN) ranging between 0.2

and 1.8 with 0.2 increments, parameter is tested for all sections of the river network. The default channel parameter values are given in Table 5.4.

Table 5.4 Channel Parameter Values

Stream Order	Base Width (Bw)	Initial Water Depth (HLINK)	Channel Slope (Ch SSlp)	Manning Coeff. (MannN)
1	1.5	0.02	3	0.55
2	3	0.02	1	0.35
3	5	0.02	0.5	0.15
4	10	0.03	0.18	0.1
5	20	0.03	0.05	0.07
6	40	0.03	0.05	0.05
7	60	0.03	0.05	0.04
8	70	0.1	0.05	0.03
9	80	0.3	0.05	0.02
10	100	0.3	0.05	0.01

Model is executed 90 times for the selected ranges of the parameters. Then, model evaluation that is necessary to provide a quantitative estimate of model capability and to compare model performance with previous results is done by using statistical measures. In the past decades, various statistical methods have been developed to calibrate and evaluate hydrologic model parameters (Wöhling et al., 2013). In the literature, the most widely used criteria are the mean squared error (MSE, given in Eqn (5.30)) and the Nash-Sutcliffe efficiency (NSE, given in Eqn (5.31)) used for the evaluation of hydrologic models (Wöhling et al., 2013).

$$MSE = \frac{1}{n} \sum_{t=1}^n (Q_{m,t} - Q_{o,t})^2 \quad \text{Equation (5.30)}$$

$$NSE = 1 - \frac{\sum_{t=1}^n (Q_{m,t} - Q_{o,t})^2}{\sum_{t=1}^n (Q_{o,t} - \mu_o)^2} = 1 - \frac{MSE}{\sigma_o^2} \quad \text{Equation (5.31)}$$

where n is the time step, $Q_{m,t}$ and $Q_{o,t}$ is the modelled and observed values at time step t , μ_o is the mean of the observed values and σ_o is the standard deviation of the observed values. The first criterion, MSE, is an error index that indicates error in the

units of the constituent. A value of 0 shows perfect fit. The second criterion, NSE, is a normalized statistic that detects relative magnitude of the residual variance compared to the measured variance (Nash and Sutcliffe, 1970). NSE ranges between $-\infty$ and 1.0. A value between 0-1.0 shows acceptable level of performance whereas a value lower than 0 shows unacceptable performance, because observed data are a better predictor than the simulated one. In mathematical view, these criteria are related to each other (Eqn (5.31)). Gupta et al (2009) decomposed the NSE criterion which consists of three different components, the correlation, the bias and the relative variability measure in the simulated and observed values (Eqn (5.32)).

$$NSE = 2\alpha r - \alpha^2 - \beta_n^2 \quad \text{Equation (5.32)}$$

with

$$\alpha = \sigma_m / \sigma_o \quad \text{Equation (5.33)}$$

$$\beta_n = (\mu_m - \mu_o) / \sigma_o \quad \text{Equation (5.34)}$$

where α is the relative variability in the modelled and observed values, r is the correlation coefficient and β_n is the bias normalized by the standard deviation in the observed values. The best values for these three components are $r = 1$, $\alpha = 1$ and $\beta_n = 0$. To find optimum values for the parameters, not only the NSE criterion but also its decomposition are analyzed (Figure 5.20 and Figure 5.21). In addition to this, the bias of observed and modelled flow means are also assessed (Figure 5.21 (d)). The bias of means is calculated as:

$$\beta = \mu_m / \mu_o \quad \text{Equation (5.35)}$$

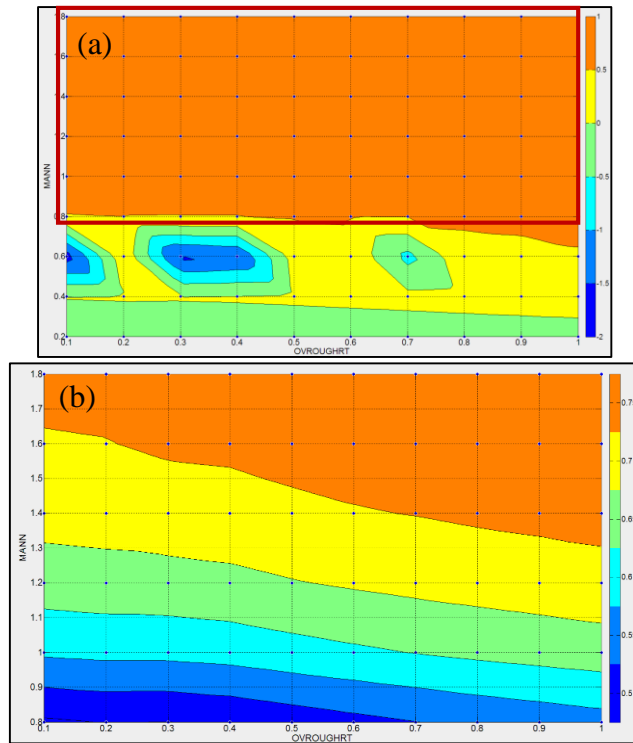


Figure 5.20 NSE Results for MANN and OVROUGHRT Parameters

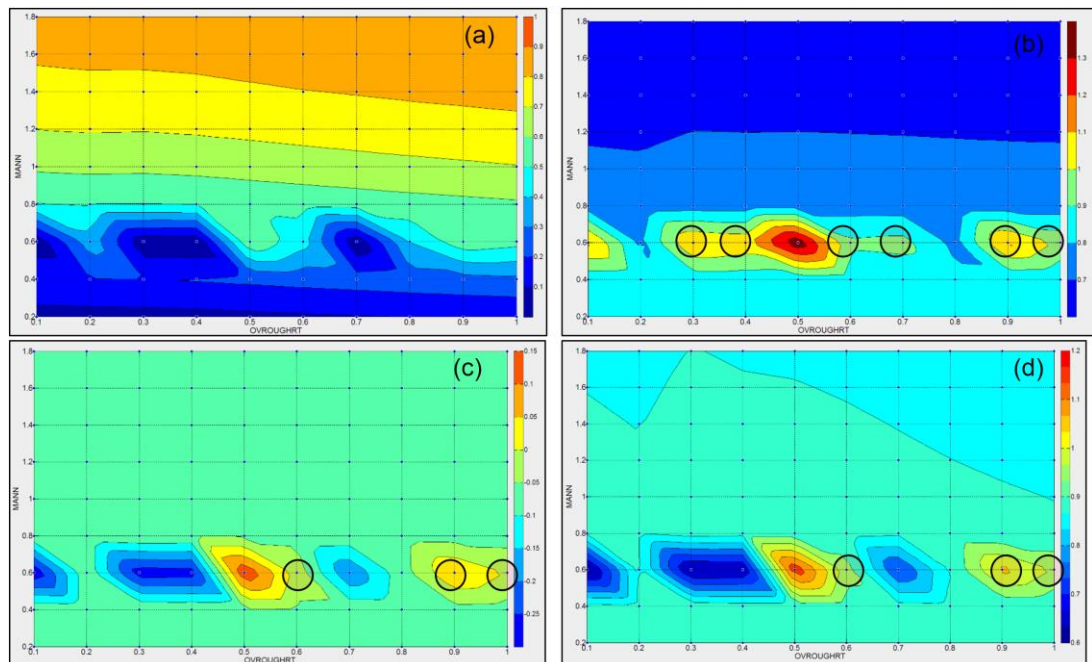


Figure 5.21 r^2 (a), α (b), β_n (c) and β (d) Results for MANN and OVROUGHRT

When the results shown in Figure 5.20 and Figure 5.21 (a) are analyzed visually, it is seen that the NSE and r^2 criterion support each other. The favored results take part

where the MANN is greater than the value of 0.8. On the other hand, there are some parameter sets at which components of the NSE criterion, α , β_n and β , have better results (Figure 5.21 (b), (c) and (d)). These sets are obtained when MANN has a value of 0.6 and OVROUGHRT has values of 0.6, 0.9 and 1.0. The hydrograph results of these sets show a spike at time after 34 hrs (Figure 5.22). This leads to increase in the variance and mean of the simulated flows, therefore NSE components' results (α , β_n and β) enhance. However, degree of collinearity between observed and modelled flows, r^2 , is lower than the value of 0.6. In hydrologic point of view, such spikes cannot be acceptable. Because rainfall pattern shows continuity in time and space and is smoothly distributed. For this reason, it can be said that WRF-Hydro model results that is obtained when MANN parameter has a value of 0.6, are not stable. Considering this outcome, the usage of optimum result of the NSE criterion seems to be more rational. Using this criterion, optimal result is obtained when MANN and OVROUGHRT parameters are equal to 1.8 and 1 respectively (Figure 5.22).

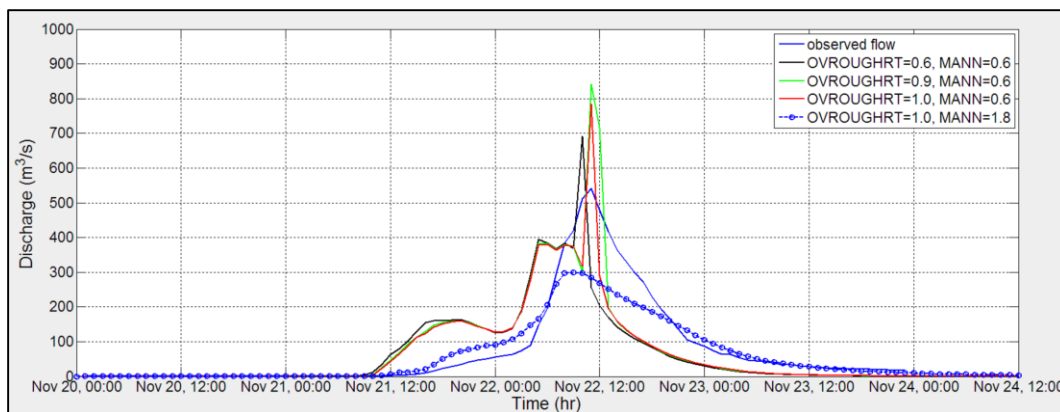


Figure 5.22 Hydrograph Results for Selected Parameters (22nd November 2014)

In conclusion, more than 210 runs are performed in model calibration stage I and II. As a result of these, 5 parameters are calibrated and findings are given in Table 5.5. In this table, nominal ranges, default values and calibrated results of the parameters can be seen.

Table 5.5 Parameters Calibrated in the Model with their Nominal Ranges, Default Values and Final Values

Parameters	Nominal Range	Default Value	Calibrated Value
REFDK	2×10^{-8} - 2×10^{-4}	2×10^{-6}	4×10^{-5}
REFKDT	0.1 - 10	1	0.1
RETDEPRTFAC	0 - 10	1	0
OVROUGHRT	0.1 - 1	1	1
MANN	0.01 - 1.8	1	1.8

5.3.4 The Effect of Stream Network Density on Simulation

Before starting the validation process, to enhance the results, the effect of stream network density on hydrograph is analyzed. For this manner, the number of pixel that defines the stream order is altered by keeping the other parameters, found in calibration stage I and II, constant. In former stages, stream segment was initiated by using 800 pixels. Therefore, stream order grid which is a part of terrain routing grid data (high resolution grid data) was constructed by adopting this threshold. In this stage, stream order grid is analyzed by different thresholds given in Table 5.6. For each threshold, terrain routing grid is regenerated. In Table 5.6, the minimum contributing area to define the stream network is calculated using the fine grid resolution, 150 m. A fine pixel has an area of 0.0225 km². Stream network density for each threshold can be seen in Figure 5.23.

Table 5.6 Stream Definition Based on Number of Pixel and Contributing Area

Number of pixel	800	400	200	150	100	50
km ²	18	9	4.5	3.38	2.25	1.13

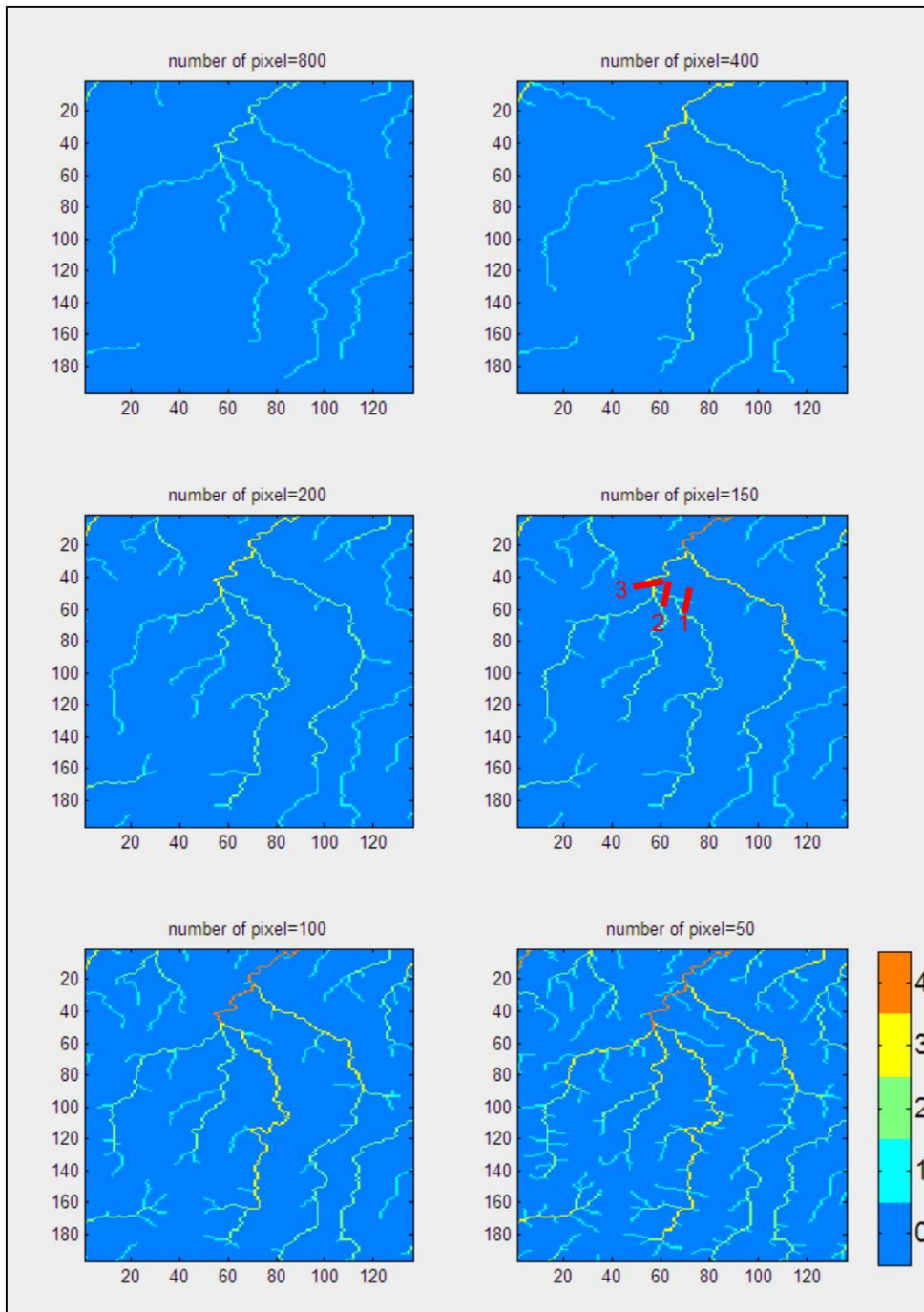


Figure 5.23 Strahler Stream Density Network for Different Thresholds

Model is executed for each regenerated fine grid data and hydrograph results are depicted in Figure 5.24. In this figure, it is seen that increase in stream density causes a rise in the peak flow and the slopes of rising and falling limb of the hydrograph. In terms of peak flows with respect to the average rainfall intensity over the entire

catchment and the point stationary rainfall intensity, efficient network density is more sensitive to storm kinematics (Seo and Schmidt, 2014). However, a stream definition with 50 pixels, which is the most detailed network, shows that the peak of the hydrograph is lower than the stream definition with 100 pixels. The main reason of this condition is the rapid contribution of sub-basin 1 and sub-basin 2 to the location of flow monitoring station since the manning roughness decreases as stream order increases. This causes rapidness in flow movement. When the results are analyzed statistically (Table 5.7), it is noticed that the stream definition with 800 pixels has the best NSE and B results. Moreover, the components of NSE, r and β , have their bests also but α has one of the lowest values.

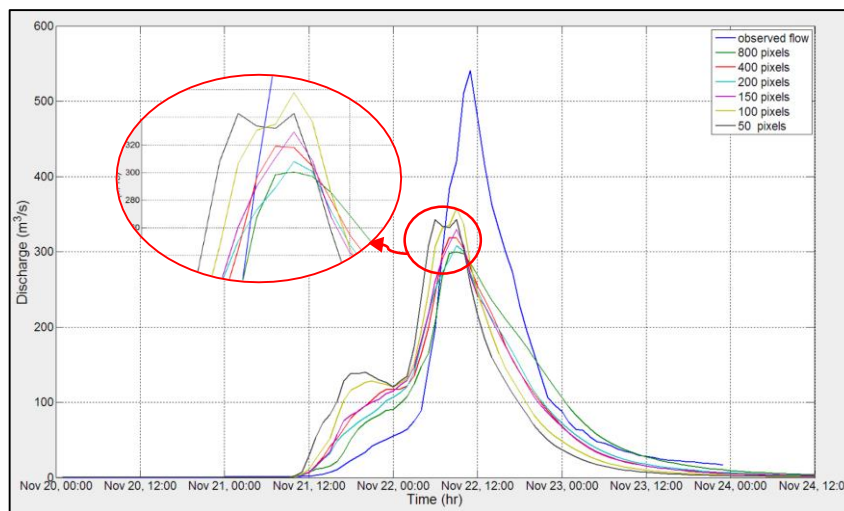


Figure 5.24 Hydrograph Simulation Results for each Stream Network Definition

Table 5.7 Statistical Results (NSE and components) for Different Stream Network Thresholds (22nd November 2014)

Criterion	800	400	200	150	100	50
r	<u>0.95</u>	0.90	0.91	0.89	0.82	0.72
α	0.64	0.65	0.63	0.65	<u>0.70</u>	<u>0.70</u>
B	<u>0.87</u>	0.84	0.82	0.84	0.85	0.85
β	<u>-0.10</u>	-0.12	-0.13	-0.12	-0.11	-0.11
NSE	<u>0.79</u>	0.73	0.73	0.71	0.65	0.51

Best results are underlined

Modeling Flood events of 2015 and 2016 with Gauge Data

In this section, WRF-Hydro model is executed with calibrated parameters and various stream order network definitions for the floods observed on 2nd August 2015 and 28th May 2016 with rain gauge data. Due to the limited number of flood events, calibration is carried with one event (22nd November 2014). Flood simulation with gauge data that belongs to 2nd August 2015 indicates that none of the stream network thresholds can catch the observed flow due to the convective type of rainfall and absence of data for the Salıpazarı Station. Therefore, statistical measures between observed and simulated hydrographs are not carried. Non-existence of the Salıpazarı Station rain data are compensated with three nearby rain gauges: Ayvacık, Çarşamba and Kozluk that are located at 19 km, 16 km and 24 km from the Salıpazarı Station (Figure 3.9 (d)). According to Thiessen polygon method, the stations Ayvacık, Çarşamba and Kozluk represent the study area by a percentage of 75.2, 23.0 and 1.8 respectively. The visual interpretation of the flow simulations shows that stream density is sensitive to the hydrograph shape and time (Figure 5.25). To get a clearer decision about the stream order, flood simulation with gauge data that belongs to 28th May 2016 is performed. For gauge data, the stations, Salıpazarı and Ayvacık are used to represent the study area by a percentage of 88.6 and 11.4 respectively. Unlike the previous case, observed flow data (28th May 2016) shows that it has a base flow probably coming from snow melting. The research about the snow melting and floods in Turkey that was conducted by Ozcan (2006) stated that the highest flow in Black Sea region is generally seen in May when the temperature rises and snow melts. The data acquired from TSMS verifies the snow existence. In 2016, at the station 18708, the average and maximum snow depth were observed as 7.5 cm and 163 cm respectively. The station 18708 is the closest station to the study area and located at 663 m of elevation. In order to make an accurate computation, simple base flow separation technique is applied to the hydrograph data. Then, flood modeling with gauge data is performed for different stream definitions (Figure 5.25 (b), Table 5.8).

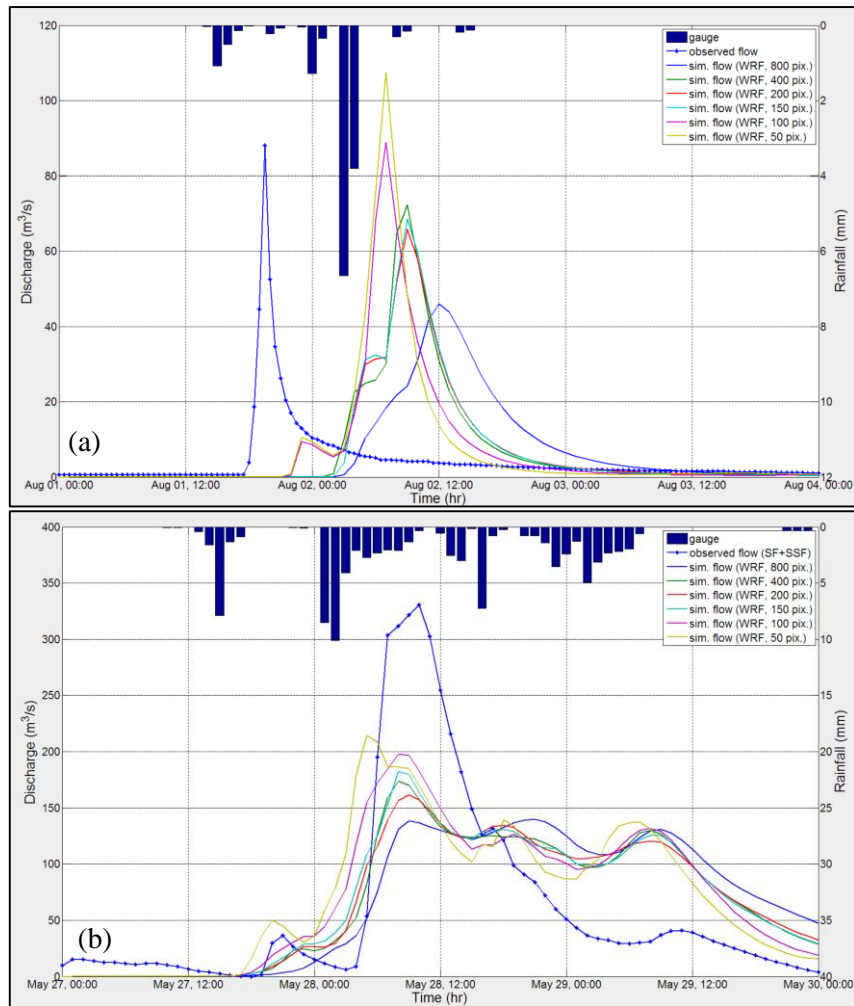


Figure 5.25 Simulated Flow for Different Stream Densities (2nd August 2015 (a), 28th May 2016 (b))

Table 5.8 Statistical Results (NSE and components) for Different Stream Network Thresholds (28th May 2016)

Criterion	800	400	200	150	100	50
r	0.53	0.71	0.69	0.73	<u>0.79</u>	0.76
α	0.64	0.64	0.63	0.65	0.69	<u>0.71</u>
B	1.10	<u>1.09</u>	1.10	1.12	1.17	1.18
β	0.070	<u>0.065</u>	0.068	0.08	0.12	0.13
NSE	0.26	0.50	0.47	0.52	<u>0.60</u>	0.56

Best results are underlined

So far, comparisons have been done with the observed and the simulated hydrographs. In addition to these comparisons, model results are analyzed between each other and

these are depicted in Figure 5.26. In HEC-HMS modeling, streams were defined with an area threshold, 3.75 km².

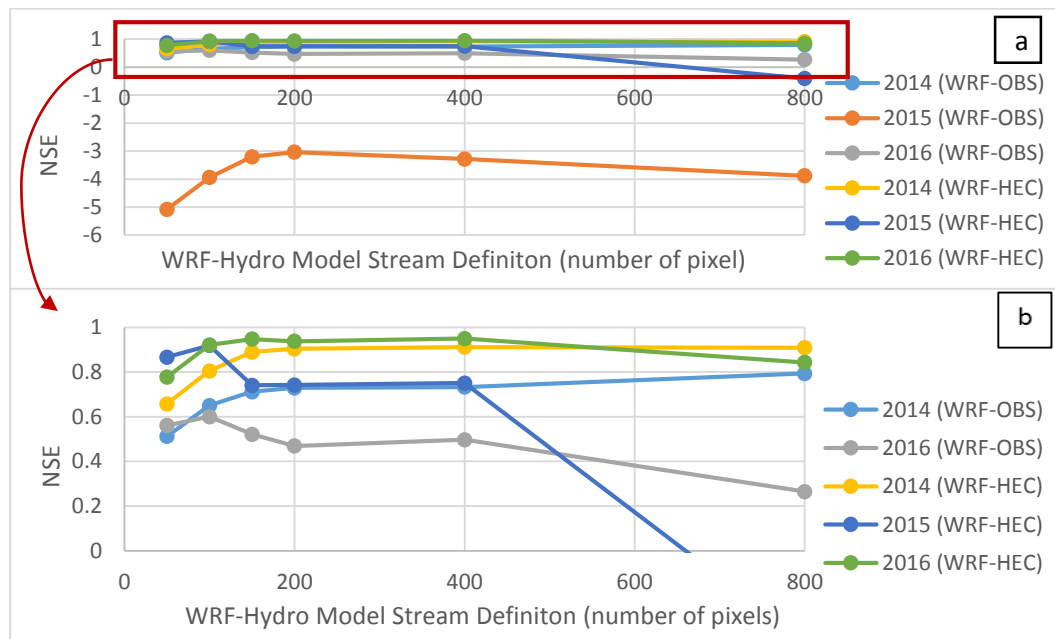


Figure 5.26 NSE Results for Models

A value of NSE lower than 0.0 shows that the mean observed value is a better predictor than the simulated value which indicates unacceptable performance (Moriasi et al., 2007). The NSE results of 2015 (WRF-OBS) shows unacceptable performance for all stream definitions (Figure 5.26 (a)). Moreover, all datasets have poor results in stream definition with 50 pixels although that is the most detailed stream network. Furthermore, generally datasets have poorer performance also in stream definition with 800 pixels that is the coarsest stream network. Besides, notable performance change between stream definition 150 pixels and 400 pixels are not observed for general dataset (Figure 5.26 (b)). Apart from the datasets, 2016 (WRF-OBS) and 2015 (WRF-HEC), nearly best NSE results are obtained stream definition with 150 pixels (3.4 km²) in all datasets and that number of pixel is nearly the same threshold selected for HEC model. However, the comparison results of WRF model and observed hydrographs for the flood events observed in 2014 and 2016 show that the stream definition greater than 100 pixels, performance of WRF model in 2014 increases but performance of WRF model in 2016 decreases. In summary, the average of the datasets

give better performance in stream definition with 150 pixels. Therefore, to enhance the simulations and to be compatible with the HEC model, stream definition with 150 pixels (3.4 km²) is selected for WRF-Hydro model.

Another outcome concerning the stream order definition is that as the stream order becomes finer, soil moisture content (SMC) shows a reduction (Figure 5.27). For example, at the stream flow station, the soil moisture differences between finest and the coarsest stream network are 0.43 mm, 0.45 mm and 0.13 mm for the events observed on 2014, 2015 and 2016 respectively (Figure 5.27 (d), (h) and (l)). The mentioned values express the reduction in soil moisture amounts.

5.4 Evaluation of Calibration with Other Rainfall Datasets

In previous sections, both WRH-Hydro and HEC-HMS model parameters are calibrated for 22nd Nov 2014 event using the gauge data. Also WRH-Hydro model stream definition are re-adjusted using 150 pixels. In here, both calibrated models (WRH-Hydro and HEC-HMS) are run for using other rainfall products namely, radar, BCR (I), BCR (II), the HE product and WRF precipitation data. In order to test the reliability of the calibrated parameters and to compare the model outputs between each other, results are evaluated using observed data. Figure 5.28, Figure 5.29 and Figure 5.30 show both model simulation results for each rainfall data related to 2014, 2015 and 2016 flood events respectively. The statistical measures for the whole study are given in Table 5.9.

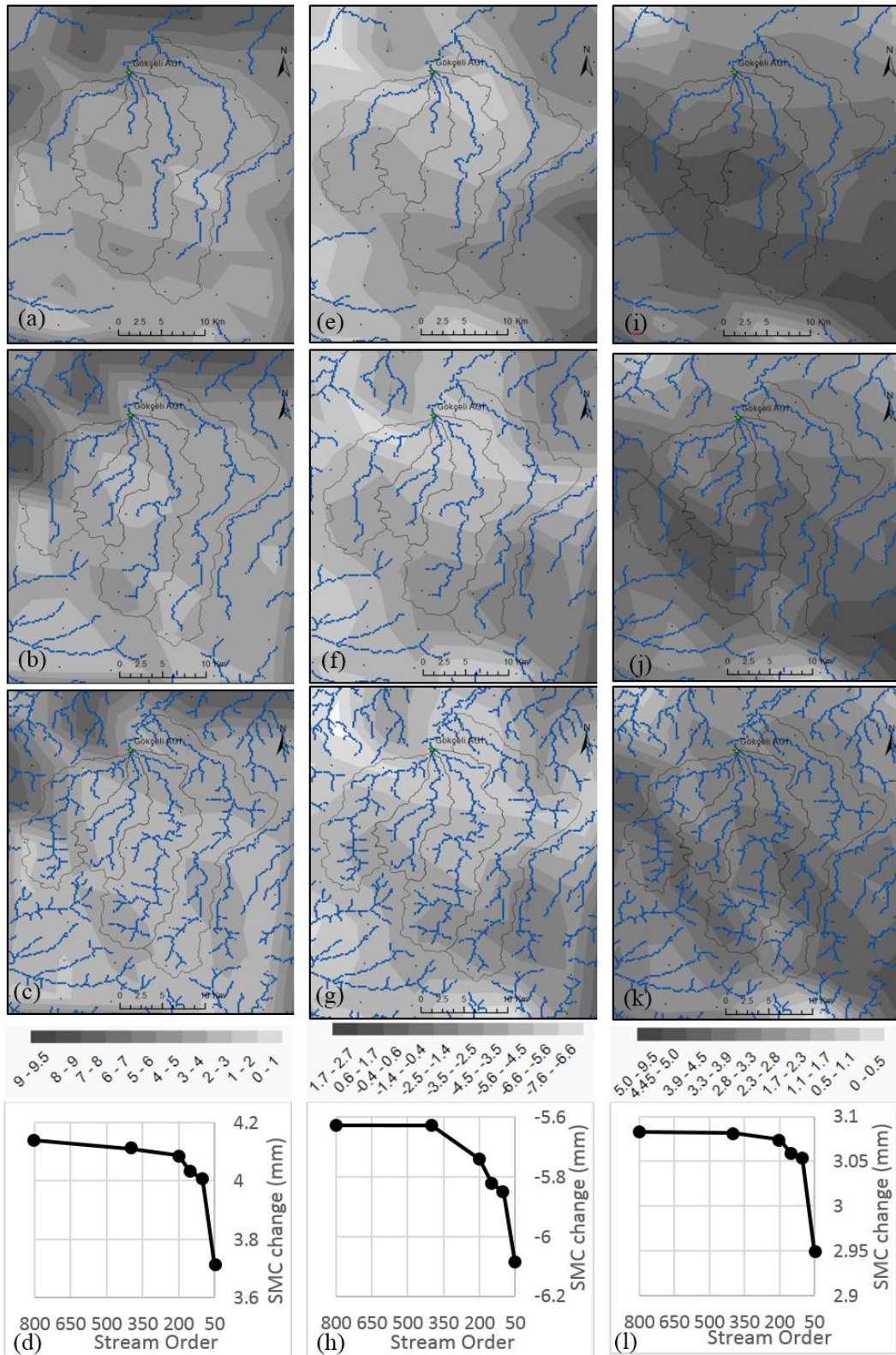


Figure 5.27 The SMC change (mm) with Stream Order (Columns (1), (2) and (3) show flood events on 22nd November 2014, 2nd August 2015 and 28th May 2016 respectively. Rows (1), (2) and (3) show threshold defining stream density 800, 150 and 50 pixels respectively. Row (4) shows SMC change in Gökçeli Station)

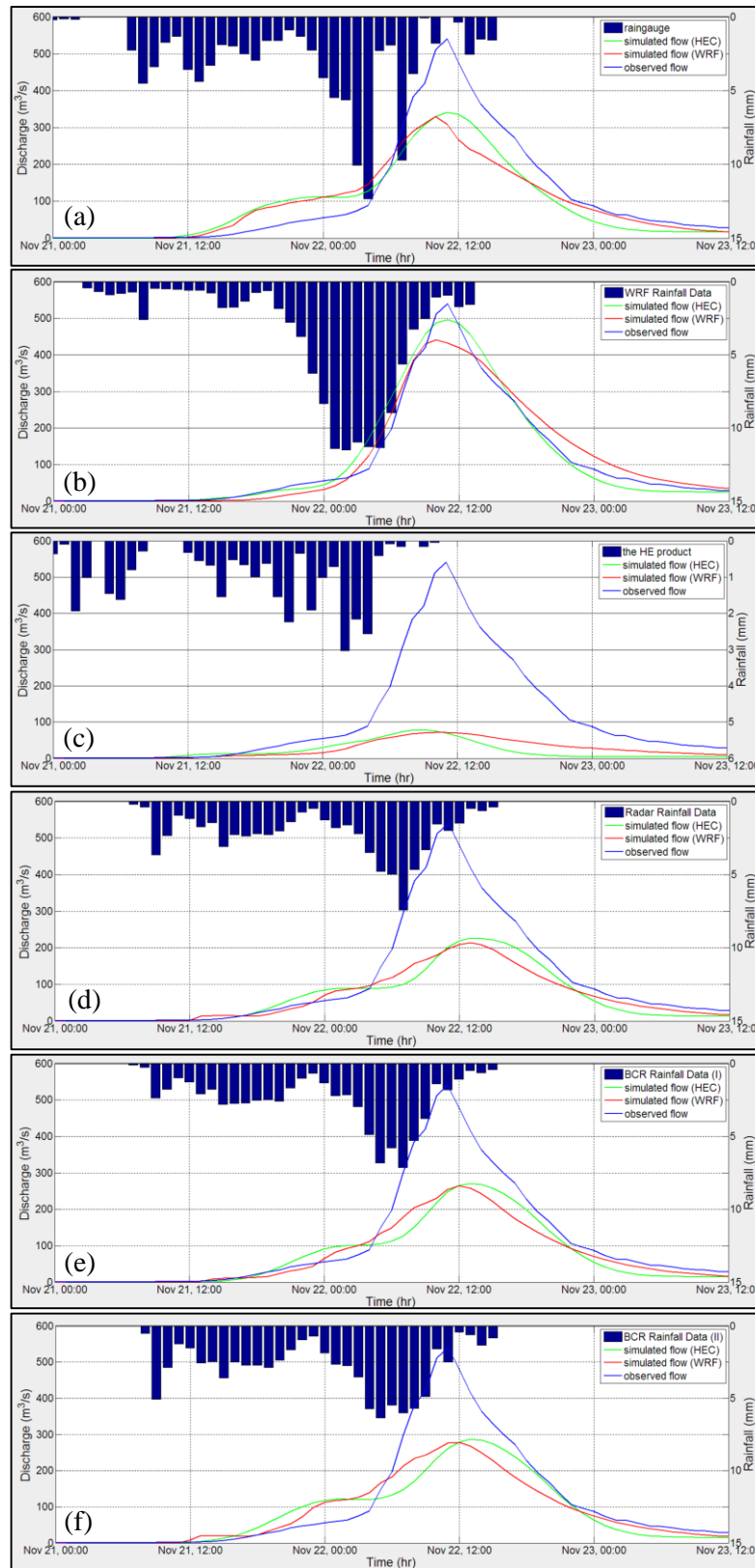


Figure 5.28 Model Simulation Results with 2014 flood data (gauge (a), WRF (b) the HE product (c), radar (d), BCR (I) (e) and BCR (II) (f))

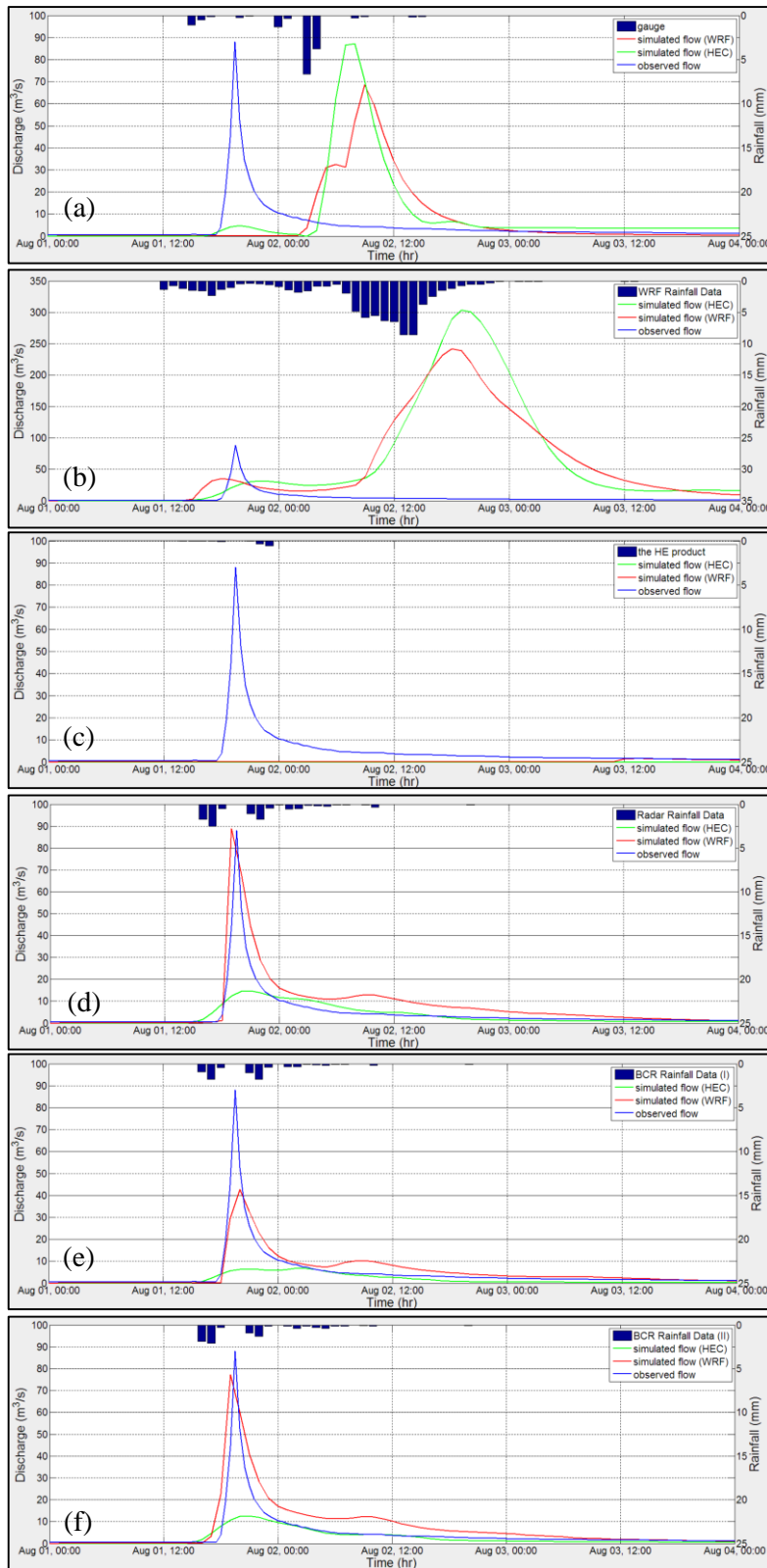


Figure 5.29 Model Simulation Results with 2015 flood data (gauge (a), WRF (b) the HE product (c), radar (d), BCR (I) (e) and BCR (II) (f))

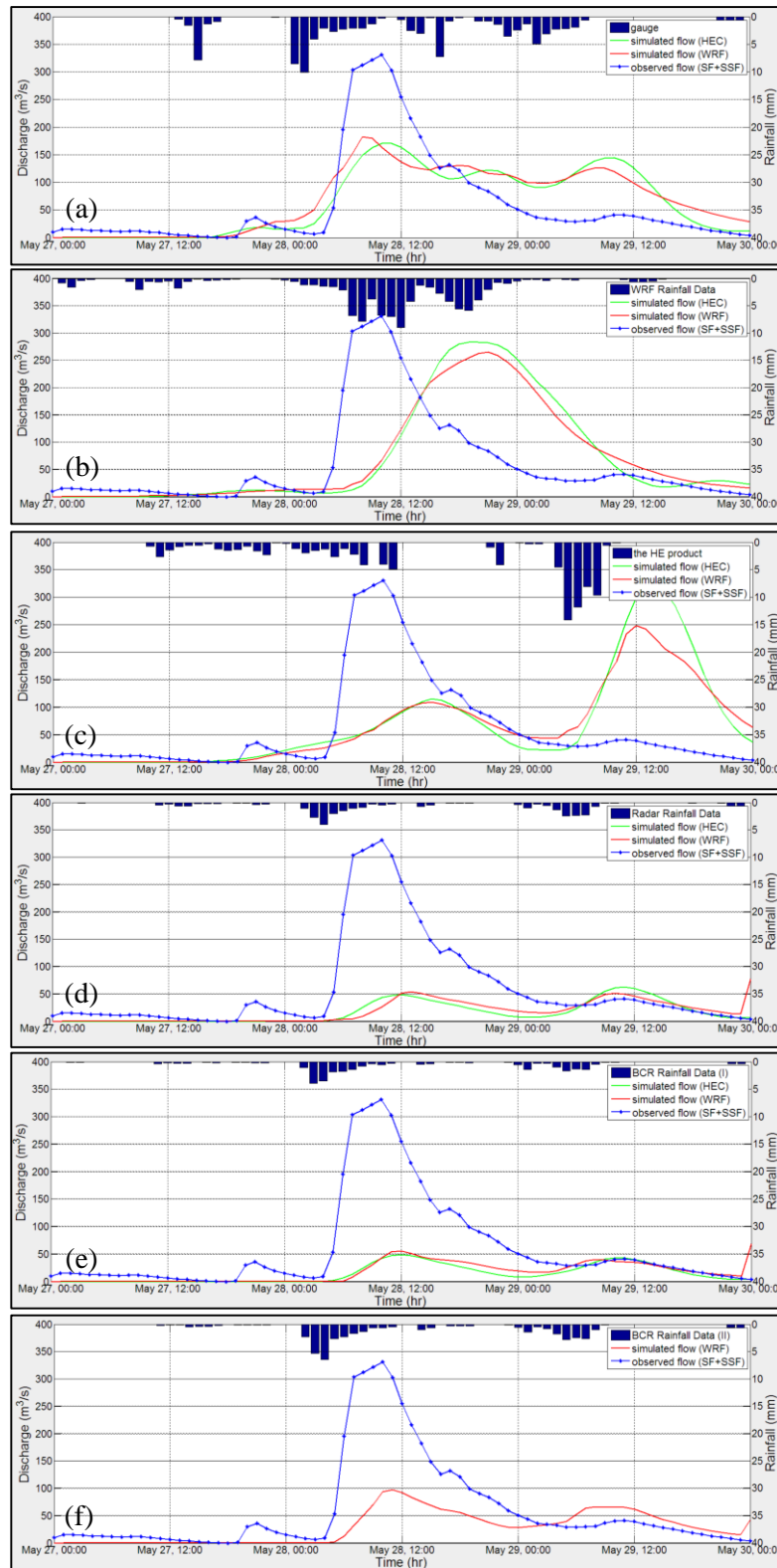


Figure 5.30 Model Simulation Results with 2016 flood data (gauge (a), WRF (b) the HE product (c), radar (d), BCR (I) (e) and BCR (II) (f))

Table 5.9 Statistical Measures for Observed and Simulated Hydrographs

Model - Rainfall Data	Peak Flow (m³/s)	Run. Vol. (hm³)	Correlation	NSE	NRMSE
22nd November 2014					
Observed Flow	541.0	24.9			
HEC - Gauge	341.0	20.8	0.95	0.83	58.93
HEC - the HE Product	78.5	4.4	0.80	-0.15	153.87
HEC - WRF Precip.	496.5	25.5	0.99	0.97	25.32
HEC - Radar	226.0	14.8	0.89	0.54	96.66
HEC - BCR (I)	271.0	16.7	0.92	0.67	81.80
HEC - BCR (II)	287.3	19.1	0.91	0.71	76.84
WRF - Gauge	329.6	20.8	0.94	0.78	67.19
WRF - the HE Product	71.4	5.5	0.94	-0.07	148.16
WRF - WRF Precip.	441.6	25.8	0.98	0.97	26.55
WRF - Radar	213.4	14.6	0.94	0.56	95.51
WRF - BCR (I)	263.7	16.5	0.97	0.70	77.80
WRF - BCR (II)	278.5	19.1	0.95	0.75	71.60
2nd August 2015					
Observed Flow	88.1	2.4			
HEC - Gauge	87.1	4.5	0.02	-3.46	2.14
HEC - the HE Product	0.0	0.0	-	-	-
HEC - WRF Precip.	303.8	32.0	-0.05	-108.00	140.39
HEC - Radar	14.8	1.7	0.67	0.37	0.71
HEC - BCR (I)	6.8	0.9	0.59	0.13	1.38
HEC - BCR (II)	12.7	1.3	0.71	0.33	0.96
WRF - Gauge	68.5	3.7	-0.02	-2.28	1.61
WRF - the HE Product	1.6	0.1	-0.15	-0.20	1.66
WRF - WRF Precip.	242.2	29.9	-0.05	-77.93	110.48
WRF - Radar	88.8	4.1	0.93	0.57	2.36
WRF - BCR (I)	42.7	2.7	0.87	0.74	1.00
WRF - BCR (II)	77.2	3.9	0.91	0.62	1.56
28th May 2016					
Observed Flow	330.8	15.9			
HEC - Gauge	170.0	16.8	0.72	0.51	60.53
HEC - the HE Product	324.3	18.4	0.09	-0.85	117.32
HEC - WRF Precip.	283.2	19.0	0.27	-0.65	110.82
HEC - Radar	62.9	4.4	0.47	-0.10	90.41
HEC - BCR (I)	48.6	3.7	0.61	-0.10	90.47
HEC - BCR (II)	91.6	6.9	0.64	0.17	78.76
WRF - Gauge	182.5	17.8	0.74	0.54	58.77
WRF - the HE Product	248.4	17.2	0.14	-0.40	102.32
WRF - WRF Precip.	265.2	18.5	0.31	-0.38	101.42
WRF - Radar	77.2	4.8	0.33	-0.14	92.32
WRF - BCR (I)	68.9	4.5	0.50	-0.09	89.95
WRF - BCR (II)	97.1	7.5	0.66	0.19	77.48

5.5 The Physical Assessment of the Channel Parameters (WRF-Hydro)

Parameters characterizing the channel network must be defined to perform channel routing. These parameters are defined in a parameter file (Table 5.4). In this table, it is seen that the physical channel parameters, base width and channel slope are related to the channel network via Strahler stream order values. In the present version of the model, stream pixel values of the same stream order have the same channel parameter values. It is known that this assumption may not be valid in many regions and future versions of the model will include parameters that are assigned to terrain grids (Gochis et al., 2015). In WRF-Hydro model, the channel routing module is performed on a pixel-by-pixel basis using predefined channel network grid in terrain routing grid file. Each channel grid cell has an assumed channel reach of trapezoidal geometry as a function of Strahler stream order. In calibration process of the MANN parameter, the physical channel parameters are kept as default.

As mentioned before, a detailed elevation model that covers the entire study area is not available, DEM data, downloaded from USGS HydroSHEDS (Hydrological data and maps based on Shuttle Elevation Derivatives at multiple Scales) mapping product with nearly 90 m (3 arc-second) resolution, is used in the model. In addition to that, there is a limited but detailed river cross section data obtained in the field survey pertaining to a downstream region of the study area. Using three different locations within this field, depicted with red line in Figure 5.23 (stream order with 150 pixels), cross section definitions in the model has been reconfigured to see the effect of physical channel parameters on routing process. For this study, channel parameters are roughly adjusted using field survey data (Figure 5.31 (1), (2) and (3)) and the numeric values of base widths and channel slopes for these three stream orders are calculated and these are given in Table 5.10.

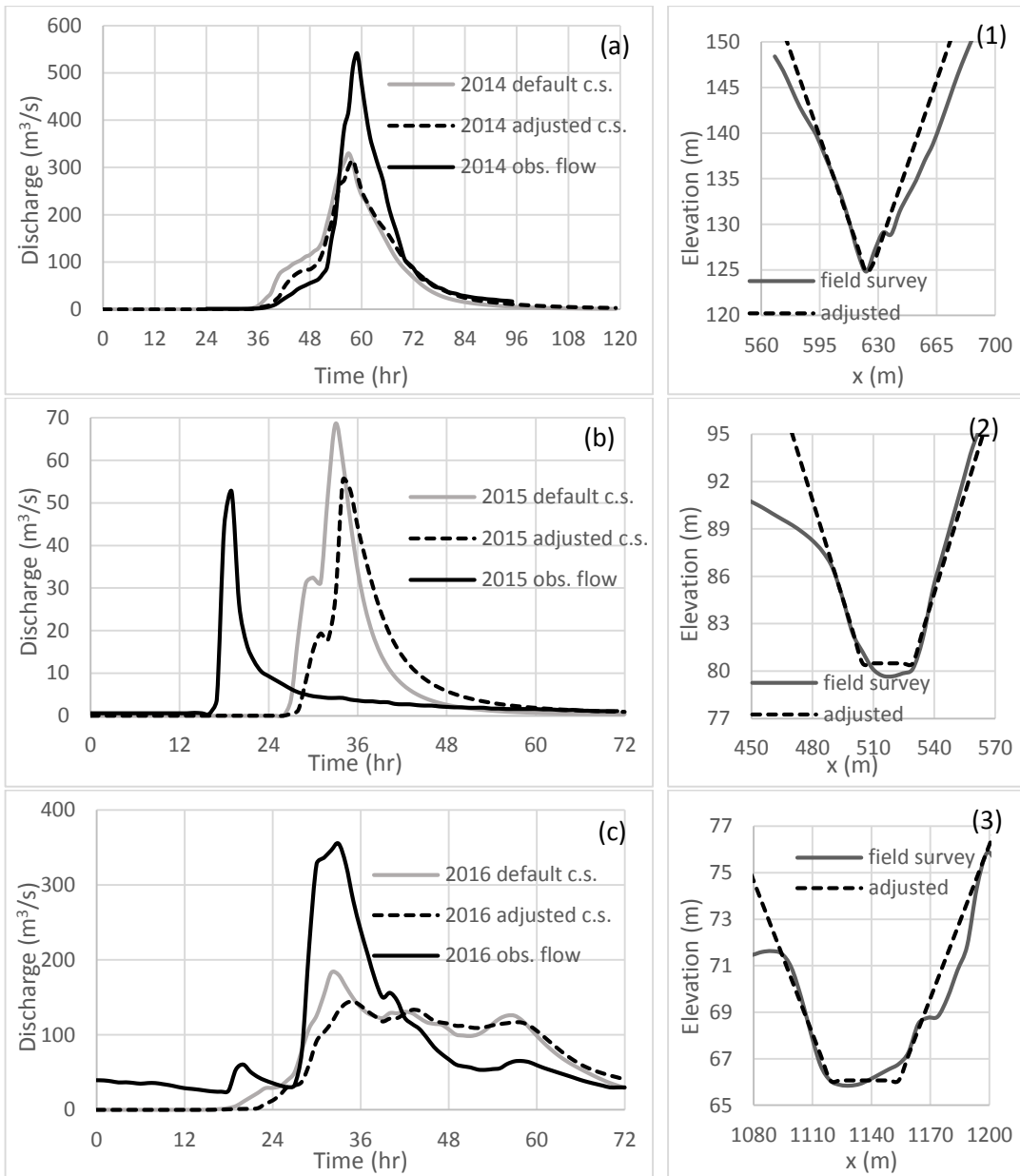


Figure 5.31 Model Simulation Results for Gauge Rainfall Data with Adjusted Cross Sections (2014 (a), 2015 (b) and 2016 (c); Stream Order 1 (1), Stream Order 2 (2), Stream Order 3 (3)) (c.s. is the abbreviation for cross section)

Table 5.10 Adjusted and Original Channel Parameters with Stream Orders

Stream Order	Parameters			
	Adjusted		Original	
	Bw (m)	Ch Slp	Bw (m)	Ch Slp
1	5	0.53	1.5	3
2	24.7	0.42	3	1
3	34.8	0.22	5	0.5

Using adjusted cross sections, model simulations for gauge rainfall datasets are performed and results are depicted with original cross sectional data in Figure 5.31 (a), (b) and (c). It is known that the effect of cross section can clearly be comprehended with discharge hydrographs taken from upstream and downstream ends of a river reach, therefore the deformation of discharge hydrographs in river channels can be evaluated using positive and negative retarding storage volumes. The results without inflow hydrographs show that the arrival time of peak water amounts shifts and peak discharges decrease. This can be explained by the fact that, the mean velocity decreases and cross sectional area increases in the rising period of the hydrograph.

5.6 Summary and Discussion of the Results

In simulations, three events are studied with six different rainfall datasets and two hydrologic models. Lumped hydrologic model and physically based distributed rainfall-runoff model are used for assessing the effect of different rainfall datasets on runoff prediction. WRF-Hydro uses rainfall data in a finer spatial resolution with respect to lump model, namely HEC-HMS. Both models are calibrated to reproduce observed hydrograph of Gökçeli gauging station with an input of observed rain gauge values obtained from averaging the rainfall values over the study area using Thiessen Polygon method. Then, using different sources of rainfall data, performance of both models are analyzed visually and statistically. The discussion of results are listed below:

- In the results of 22nd November 2014 flood data, it is seen that except the rain gauge data which is used in calibration procedure in both models, WRF precipitation data gives the best results in all aspects in both models. Among the datasets, the HE product has the poorest results. The statistical results in bias corrected radar rainfall datasets (BCR I and BCR II) show that bias correction with KF algorithm has favorable effect on results. The algorithm improves the NSE from 0.54 and 0.56 to 0.71 and 0.75 in HEC-HMS and WRF-Hydro respectively (Table 5.9). However, increasing complexity in a model that means complex interaction of water cycle on spatial and temporal scales does not increase the results of objective functions substantially. The

results in calibration part show that both models capture the similar outputs in statistical measures, r and NSE. Moreover, both model underestimate the peak flow but the result of HEC-HMS, $341.0 \text{ m}^3/\text{s}$, is better than the result of WRF model, $329.6 \text{ m}^3/\text{s}$. The difference between RMSE results is nearly $8 \text{ m}^3/\text{s}$ and HEC-HMS shows little increment in this aspect. In simulation, performed with the HE product, it is seen that all statistical measures except the peak flow results, WRF model is superior to the HEC-HMS. However, the results of simulation carried out with WRF precipitation dataset indicate that HEC-HMS gives better performance. In radar related dataset; radar, BCR (I) and BCR (II), WRF model gives better results in r computations. Moreover, WRF results of BCR (I) and BCR (II) in NSE and RMSE statistical measures are more favorable than the HEC-HMS results. In peak flow estimation, HEC-HMS is more successful. However, both models have good results compared to each other in statistical measures; r , NSE, RMSE and runoff volume ratios.

- According to WRF precipitation data, flood that was occurred on 2nd August 2015 is almost convective. 91% of the rainfall data estimated in Salpazarı location is described as convective. It is known that the storm dynamic of convective rain is spatially unstable. In such circumstances, high number of rain gauge data that defines the spatial distribution of rainfall pattern is desired. However, even Salpazarı Station was not in operation during the 2015 flood event. Therefore, stations that are located in remote distances are used to obtain rain data. Using acquired rain gauge data with Thiessen polygon method, simulations are performed and results are compared with flow monitoring station data. The comparison results show that (Figure 5.29 (a)) both models are unsuccessful in gauge simulations. Because, NSE values of both models are lower than 0 and correlations are nearly 0. Among the datasets, the statistical inference cannot be done for the HE product because the HE product did not estimate any rain for the study area. Indeed, the HE product is powerful in convective rainfall mesoscale systems (Kuligowski, 2014), such success is not observed for 2015 flood case in this study area. When simulations are examined with wrfout data, it is seen that there are two peaks

in the hydrographs. In the first one, the peaks in HEC and WRF models are nearly a value of $40 \text{ m}^3/\text{s}$ and in the second one, peaks are greater than $200 \text{ m}^3/\text{s}$ for both models. Among these peaks, the first ones nearly place at the right time with respect to observed hydrograph. Apart from these datasets, radar, BCR (I) and BCR (II) datasets show good performance in the simulations. Without correction, radar-based QPE has the best hydrograph shape, timing in peak and peak amount. As it is analyzed earlier in 2014 dataset, BCR (II) is superior to BCR (I). The success of bias correction in radar-based QPE diminishes in convective system. However, if the Salipazarı station was in operation, the BCR (II) data would have probably been superior to the radar-based QPE itself. Because, radar data estimated rainfall in a region that is specifically close to the station. In radar related datasets, the outcome of WRF model is better than the outcome of HEC model. The reason behind this state is the difference in maximum retention calculation that is a measure of the ability to abstract and retain storm precipitation. In WRF model; it is defined as 0 whereas in HEC model it is calculated by using the CN value. Even if for the maximum CN value, which is 99, HEC model calculates retention depth.

- According to WRF precipitation data, 21% of the rainfall amount estimated in the Salipazarı Station location is convective for the flood observed on 28th May 2016. In the upstream part of the study area, the effect of convective rain diminishes (Figure 3.18 (g)). The statistical results and visual interpretations show that in terms of peak value and peak time, gauge data are superior to the other rainfall sources. However, the amount of peak is better represented by wrf data with 12 hours delay. The HE product is better than the 2015 year simulation because of rain estimation but accuracy and timing of the peak value show unsuccessful results for both models. On the other hand, radar related datasets have flow trends that follow the observed flow but the amount of these datasets have poor results. However, like in the previous cases, bias corrected radar data using the gauging station in close proximity to the studied one has an affirmative effect on the results.

- The models are prepared with minimum required data. Although the same forcing input data (rainfall) are used in the two models, additional effort is needed to build WRF-Hydro model. Furthermore, to calibrate parameters manually in WRF-Hydro model takes more effort. Hourly runoff computations in WRF-Hydro requires more time compared to runoff computations in HEC-HMS.
- A major advantage of physical based model over empirical based model is that it has distributed outputs of major hydrologic states; such as infiltration, and surface runoff, at high spatial resolutions.
- It is seen that the assigned threshold for stream network density significantly affects the model response. The increase in stream network density accelerates the flow and therefore raises the water volume under the simulated hydrographs.

CHAPTER 6

CONCLUSIONS AND RECOMMENDATIONS

6.1 Summary

One of the major problems in mountainous regions is damages caused by floods that are related to intense rainfall. These events in the Black Sea region have been responsible for loss of life and property. On 22nd November 2014, 2nd August 2015 and 28th May 2016, catastrophic flood events occurred in the Terme River basin, which is located in the eastern Black Sea region. As a consequence of the river overflows; many people were affected, homes and workplaces were flooded, roads collapsed and electricity could not be supplied to the region due to damage in energy transmission lines. These consequences all point to the importance of flood discharge estimation in such regions for property and life savings. However, flood estimation in developing countries has difficulties due to lack of data. Radar-based QPE, numerical forecast rainfall data and satellite products are valuable data sources for hydrologic studies in ungauged or poorly gauged regions. The aim of this study is to evaluate the rainfall datasets at hourly time intervals in a small catchment with different rainfall types that caused severe consequences in Samsun – Terme. In developing and managing water resources on a commensurate scale, WMO defined the minimum densities of stations (area in km² per station) to avoid serious deficiencies (1994). According to this guide, the minimum area per recording rain gauge station is defined as 2500 km² to satisfy specific needs for mountainous areas. Although the study region fulfills the condition, in some cases rainfall cannot be detected by rain gauges as a result of station malfunction or convective rain.

In the evaluation, a total of six rainfall products, which are weather radar, the Hydro-Estimator (HE) product, gauge data, rainfall data obtained from Weather Research and Forecasting (WRF) model, and two different bias corrected radar-based QPE obtained by Kalman Filtering (KF) algorithm, were used in two different hydrological models; Weather Research and Forecasting model hydrological extension package (WRF Hydro) and Hydrologic Engineering Center's Hydrologic Modeling System (HEC-HMS).

Before the hydrological model simulations, rainfall products were evaluated by using statistical measures. For this, first, radar-based QPE was analyzed using the matching techniques mentioned in the literature. Then, based on the technique giving best results (WCMM with 5X5 space window), radar data extraction was done for all flood events. Second, comparison of rainfall products was performed in point and areal based manner. Among the products, radar-based QPE, having better spatial resolution, proved to be successful in point and areal based analyses in this research. The reason for this can be explained by the general trend of the rainfall being captured best by the radar rainfall estimation in rainfall-time graphics. Although rainfall types affected the success of the radar-based QPE; radar and rain gauge data generally followed the same pattern in hourly time series. Third, the success of radar-based QPE that shows the best spatio-temporal variation in the duration of flooding was improved using the KF algorithm in frontal rainfall type that had less dynamics throughout the event duration. Then, it was found that the application of KF with gauges that had high correlation between each other could improve the radar-based QPE better in mixed rainfall types. However, another rainfall source, the HE product generally showed poor performance in rain detection in point and areal based comparisons. Apart from the nowcast products, the forecast product, WRF data, demonstrated success in cumulative rainfall amounts in the study area. Although WRF data was less accurate at following the rain gauge data in time series manner, this data could still give information about the probability of high rainfall before the flood occurrence. In the fourth and final step, hydrologic models were calibrated and rainfall products were evaluated.

In model calibration procedure, three parameters; wave travel time (K), weighting factor (X) and curve number (CN) for HEC-HMS and five parameters; infiltration scaling factor (REFKDT), surface runoff parameter (REFDK), surface retention depth (RETDEPRTFAC), surface roughness (OVROUGHRT) and channel Manning roughness (MANN) for WRF Hydro were calibrated to reproduce the observed hydrograph of Gökçeli gauging station with an input of observed rain gauge values obtained from averaging the rainfall values over the study area using Thiessen Polygon method for 2014 flood event. It was found that the parameters; MANN and REFKDT for WRF Hydro and the parameters; CN and K for HEC HMS were sensitive in defining the hydrograph shape and total water volume respectively. With the calibration of both models' parameters, runoff volume in stream flow and slope of rising and falling limb of the simulated hydrographs were improved. In terms of model evaluation, the most obvious difference was observed in radar based model simulations in 2015 flood event that is mainly convective rain. In mentioned event, WRF-Hydro showed distinct success with respect to HEC HMS. The average value of correlation (r) and root mean square error (RMSE) for all events and rainfall products indicated that WRF Hydro (0.61 for r, 62.6 m³/s for RMSE) showed a slight success compared to the HEC HMS (0.59 for r, 67.6 m³/s for RMSE).

6.2 Conclusions

It is known that in radar-based QPE simulations, a large amount of peak underestimation is common due to the problems in mixture of raindrop distribution, orographic enhancement and attenuation (Zhu et al., 2014). However, timing of the flow peaks with precision is an advantage of radar-based QPE in ungauged basins where the radar rainfall is only available sources of rainfall. Simulation done for the convective flood (2nd August 2015) supported the utility of radar-based QPE in ungauged basins and showed the limited-spatial extent of the rain gauge data that represent the basin.

The approach in KF algorithm was in contrast to study of Chumchean (2006) that defined the empirical variance considering the distance between radar location and the rain gauges. The proposed approach implemented a different way to define the

empirical variance for sparsely gauged areas. Using the gauges that had better correlations with the studied gauge made a contribution to the study. The simulation results of the hydrologic models showed that bias corrected radar (BCR) data had an affirmative effect in statistical measures.

As a *now-casting product*, the HE algorithm had poor performance in the events by exhibiting inaccurate rainfall detection in the study area; whereas, as a *forecasting product*, WRF precipitation data, which has the same spatial resolution with the HE product, generally performed well at predicting rainfall amount but not necessarily timing. The capabilities of the NWP model precipitation estimates vary considerably with forecast lead time. Generally, forecast skill decreases with the lead time and increases with rising rainfall accumulation periods due to the compensation of timing errors in individual periods (Shrestha et al., 2013). The cumulative rainfall amounts in sub-basins and averaged bias results in stations supported the WRF precipitation data forecast skill in rainfall accumulation periods in the study.

Distributed models need vast amount of data, knowledge about the initial conditions, effort and time; but guidelines, available input datasets and GIS based preprocessing tools make them usable. Among the physics-based distributed hydrologic models, WRF-Hydro, has several advantages such as having open source and community maintained code, integrating multiple physics options, being adjustable for multi-spatial scale and multi-temporal resolution and lastly supporting multiple computing platforms. However, there are difficulties in the model setup procedure and model runs take considerable time. On the other hand, lumped models average spatial characteristics but they are incapable of incorporating the spatial heterogeneity. HEC-HMS has advantages like easy basin model development and calibration process and less time requirement in model runs; whereas, HEC-HMS model uses fewer parameters and represents spatial variation of the catchment characteristics inefficiently. Lumped or distributed models have relative strengths and weaknesses. Depending on the problem type, either of them can be the best choice. In addition to problem type, user knowledge and the data availability should be considered carefully in model selection. However, the lumped models should be used with caution because

of their limited capability in expressing the spatial change in complex topography. In the light of information provided, it was seen that the study area has uniform soil characteristics, so the results of model simulations were close to each other except the flood event that was observed on 2nd August 2015, which was mainly in convective origin. Radar-based QPE data showed better performance in WRF-Hydro model compared to HEC-HMS model. In HEC-HMS model, initial abstraction in the loss computation is defined by an empirical relationship, which is 20% of the potential storage ($I_a = 0.2S$). The amount of water storage must be compensated by the rainfall for the flow to start. However, loss method defined in the model (SCS CN) held the water and slowed down the flow speed. This situation proves that although HEC-HMS model is easy in calibration phase; it does not work well with other storms due to parameters not always fitting the catchment physics and complex topography.

Another part of the research placed importance on the calibration of WRF-Hydro model. Unlike the WRF-Hydro model calibration steps defined in the literature, calibration was performed using the parameters as a couple to indicate the parameter interaction on simulated hydrograph. The results showed that the channel parameter (MANN) is more sensitive than the surface roughness parameter (OVROUGHRT) in defining the hydrograph shape and the infiltration scaling factor (REFKDT) is more sensitive than the surface runoff parameter (REFDK) and the surface detention depth (RETDEPRTFAC) in calculating the total water volume.

High drainage density may indicate that surface runoff moves rapidly from the catchment and the soil has low infiltration capacity. It depends on climate and physical characteristics of the catchment (Subramanya, 2005). In the model, the increase in stream network density accelerated the flow depending on the increase of the MANN coefficient, reduced the time water stayed in the catchment and therefore raised the water volume under the simulated hydrographs. The effect of network density was clearly seen in the 2015 flood due to the rainfall pattern that was observed close to the outlet. The increase in MANN coefficient in sub basin 3 made rapid flow contribution to the outlet and changed the time of peak flow. In terms of changes in total soil moisture content, it was seen that the increase in stream density caused a moisture

reduction in the soil. The decrease in number of pixels from 800 to 50 causes a reduction in soil moisture.

With this study, it is shown that the WRF precipitation forecast data allows to obtain hydrographs with peak values close to observed hydrograph, 36 hrs. prior to the flood occurrence. This information might be worth to be used in a possible early warning system and help to take initial precautions in the study area and in similar catchments that are prone to flood. The usage of radar-based QPE in simulations can correct the peak time of the hydrograph forecasted by the WRF data. In addition to that, BCR data can improve the results. Therefore, it can be concluded that the use of hourly WRF, radar and gauge data in combination through a data assimilation schema may help to take necessary precautions against flooding in settlement areas in advance and provide benefit in saving life and property.

6.3 Recommendations

It is known that the success of the proposed approach in the KF application and the reliability of the hydrologic models increase with data availability. It would be interesting in future studies to improve the application of KF algorithm for similar scenarios by defining more stable parameters; correlation coefficient and empirical variance with more data. However, this statement may reveal contradiction in poorly gauged regions. It is considered that the increase in the weather radar stations and gauge data will benefit the studies in the forthcoming years. Yet, for now, to the best of our knowledge, the use of BCR data in this study in a hydrologic application is the first in Turkey.

In pre-processing stages of the models' setup, DEM data with same spatial resolution could not be used due to technical reasons. For HEC-HMS model, DEM data with 25 m.; whereas, for WRF-Hydro model, DEM data with 90 m. spatial resolution were used. Although the algorithm of these models to produce routing structure are completely different, the use of the same DEM data in both models would increase the similarity of the physical basin configuration in stream definition process.

In Turkish State Meteorological Service (TSMS), WRF model is operated daily; meaning 72 hours of forecasted rainfall data are provided by the WRF model at the end of each day. However, in this study the lead time is selected as nearly one and a half day before the flood occurrence. The use of different forecast lead times in WRF precipitation data may reveal the effect of sensitivity on forecast skill in the study area.

Furthermore, use of more than one flood event data in model calibration stage may enhance the model parameters that were suppressed in the boundaries of the feasible region. Regardless of the poor data, usage of various rainfall forecasts obtained from different WRF microphysical schemes may reveal the effect of physical mechanisms on the rainfall pattern. Although this is more related to WRF coupled model, such study will increase the performance of WRF data on complex topography.

Knowing that the annual economic loss is around 160 million \$, whereas the investment for flood prevention is around 30 million \$, developing flood warning systems in flood prone areas of Turkey is essential. Recently, 12 meteorological satellites are working. These satellites and radars must be used in flood warning systems. The calibration of radar rainfall estimates must be done. With well calibrated hydrologic models, radar rainfall estimates can be helpful to establish flood warning systems wherever they are needed. Moreover, data assimilation which combines radar, satellite, WRF model precipitation data and other observations can improve the precipitation forecast that is essential to make accurate hydrological forecast.

REFERENCES

- Ahnert, P. R., Krajewski, W. F., & Johnson, E. R. (1986). Kalman filter estimation of radar-rainfall field bias. In *Preprints, 23rd Conf. On Radar Meteor., Snowmass, CO, Amer. Meteor. Soc., JP33-JP37*.
- Akçelik, M. (2013). *Improving Remotely-Sensed Precipitation Estimates over Mountainous Regions* (MSc, Middle East Technical University).
- Anagnostou, E. N., Krajewski, W. F., Seo, D. J., & Johnson, E. R. (1998). Mean-field rainfall bias studies for WSR-88D. *Journal of Hydrologic Engineering*, 3(3), 149-159.
- Anderson, M. L., Chen, Z. Q., Kavvas, M. L., & Feldman, A. (2002). Coupling HEC-HMS with atmospheric models for prediction of watershed runoff. *Journal of Hydrologic Engineering*, 7(4), 312-318.
- Andrieu, H., Creutin, J. D., Delrieu, G., & Faure, D. (1997). Use of a weather radar for the hydrology of a mountainous area. Part I: radar measurement interpretation. *Journal of Hydrology*, 193(1), 1-25.
- Atlas, D., Rosenfeld, D., & Jameson, A. R. (1997). Evolution of radar rainfall measurements: steps and mis-steps. *Weather Radar Technology for Water Resources Management, IRTCUD/University of Sao Paulo, Brazil and IHP-UNESCO*.
- Austin, P. M. (1987). Relation between measured radar reflectivity and surface rainfall. *Monthly Weather Review*, 115(5), 1053-1070.
- Bartholmes, J., & Todini, E. (2005). Coupling meteorological and hydrological models for flood forecasting. *Hydrology and Earth System Sciences Discussions*, 9(4), 333-346.

- Battan, L. J. (1973). Radar observation of the atmosphere. The University of Chicago Press, 324 pp.
- Bech, J., Codina, B., Lorente, J., & Bebbington, D. (2003). The sensitivity of single polarization weather radar beam blockage correction to variability in the vertical refractivity gradient. *Journal of Atmospheric and Oceanic Technology*, 20(6), 845-855.
- Betts, A. K., Chen, F., Mitchell, K. E., & Janjić, Z. I. (1997). Assessment of the land surface and boundary layer models in two operational versions of the NCEP Eta model using FIFE data. *Monthly Weather Review*, 125(11), 2896-2916.
- Beven, K. J. (2011). *Rainfall-runoff modelling: the primer*. John Wiley & Sons.
- Bozoğlu, B. (2015). *1-D and 2-D Flood Modeling Studies and Upstream Structural Measures for Samsun City Terme District* (MSc, Middle East Technical University).
- Calheiros, R. V., & Zawadzki, I. (1987). Reflectivity-rain rate relationships for radar hydrology in Brazil. *Journal of climate and applied meteorology*, 26(1), 118-132.
- Chen, F., Mitchell, K., Schaake, J., Xue, Y., Pan, H. L., Koren, V., & Betts, A. (1996). Modeling of land surface evaporation by four schemes and comparison with FIFE observations. *Journal of Geophysical Research: Atmospheres*, 101(D3), 7251-7268.
- Chen, F., Janjić, Z., & Mitchell, K. (1997). Impact of atmospheric surface-layer parameterizations in the new land-surface scheme of the NCEP mesoscale Eta model. *Boundary-Layer Meteorology*, 85(3), 391-421.
- Chen, C. S., Lin, Y. L., Peng, W. C., & Liu, C. L. (2010). Investigation of a heavy rainfall event over southwestern Taiwan associated with a subsynoptic cyclone during the 2003 Mei-Yu season. *Atmospheric Research*, 95(2), 235-254.
- Chesworth, W. (Ed.). (2008). *Encyclopedia of soil science* (Vol. 207). Berlin: Springer.

- Choudhari, K., Panigrahi, B., & Paul, J. C. (2014). Simulation of rainfall-runoff process using HEC-HMS model for Balijore Nala watershed, Odisha, India. *International Journal of Geomatics and Geosciences*, 5(2), 253-265.
- Chu, X., & Steinman, A. (2009). Event and continuous hydrologic modeling with HEC-HMS. *Journal of Irrigation and Drainage Engineering*, 135(1), 119-124.
- Chumchean, S., Sharma, A., & Seed, A. (2003). Radar rainfall error variance and its impact on radar rainfall calibration. *Physics and Chemistry of the Earth, Parts A/B/C*, 28(1), 27-39.
- Chumchean, S., Seed, A., & Sharma, A. (2006). Correcting of real-time radar rainfall bias using a Kalman filtering approach. *Journal of Hydrology*, 317(1), 123-137.
- Collier, C. G. (1996). Applications of weather radar systems: a guide to uses of radar data in meteorology and hydrology. 406 pp.
- Creutin, J. D., & Borga, M. (2003). Radar hydrology modifies the monitoring of flash-flood hazard. *Hydrological processes*, 17(7), 1453-1456.
- Cunge, J. A. (1969). On the subject of a flood propagation computation method (Muskingum method). *Journal of Hydraulic Research*, 7(2), 205-230.
- Derin, Y. (2014). *Advancement of Satellite-Based Rainfall Applications for Basin-Scale Hydrologic Modeling* (MSc, Middle East Technical University).
- Derin, Y., & Yilmaz, K. K. (2014). Evaluation of multiple satellite-based precipitation products over complex topography. *Journal of Hydrometeorology*, 15(4), 1498-1516.
- Derin, Y., Anagnostou, E., Berne, A., Borga, M., Boudevillain, B., Buytaert, W., Chang, C.H., Delrieu, G., Hong, Y., Hsu, Y.C. and Lavado-Casimiro, W. (2016). Multiregional Satellite Precipitation Products Evaluation over Complex Terrain. *Journal of Hydrometeorology*, 17(6), 1817-1836.

- Devia, G. K., Ganasri, B. P., & Dwarakish, G. S. (2015). A review on hydrological models. *Aquatic Procedia*, 4, 1001-1007.
- DSİ VII. Bölge Müdürlüğü., (2014). Samsun İli, Salıpazarı İlçesi, Kayaköprü Mevkii, ÇED Raporu, DSİ, p. 223.
- Ek, M. B., Mitchell, K. E., Lin, Y., Rogers, E., Grunmann, P., Koren, V., ... & Tarpley, J. D. (2003). Implementation of Noah land surface model advances in the National Centers for Environmental Prediction operational mesoscale Eta model. *Journal of Geophysical Research: Atmospheres*, 108(D22).
- Evans, J. D. (1996). *Straightforward statistics for the behavioral sciences*. CA: Brooks/Cole Publishing.
- Fread, D. L. (1983, February). A unified coefficient routing model. In *Paper present at seminar, Department of Civil Engineering, Pa. State University, University Park*.
- Gerstner, E. M., & Heinemann, G. (2008). Real-time areal precipitation determination from radar by means of statistical objective analysis. *Journal of Hydrology*, 352(3), 296-308.
- Givati, A., Gochis, D., Rummler, T., & Kunstmann, H. (2016). Comparing One-Way and Two-Way Coupled Hydrometeorological Forecasting Systems for Flood Forecasting in the Mediterranean Region. *Hydrology*, 3(2), 19.
- Gjertsen, U., Salek, M., & Michelson, D. B. (2004). Gauge adjustment of radar-based precipitation estimates in Europe. In *Proceedings of ERAD* (Vol. 7, No. 11).
- Gochis, D. J., Yu, W., & Yates, D. N. (2015). The WRF-Hydro Model Technical Description and User's Guide, Version 3.0. NCAR Technical Document, 120 pp.
- Grewal, M. S., & Andrews, A. P. Kalman Filtering: Theory and Practice. 1993.
- Gupta, H. V., Kling, H., Yilmaz, K. K., & Martinez, G. F. (2009). Decomposition of the mean squared error and NSE performance criteria: Implications for improving hydrological modelling. *Journal of Hydrology*, 377(1), 80-91.

- Habib, E., Qin, L., Seo, D. J., Ciach, G. J., & Nelson, B. R. (2012). Independent assessment of incremental complexity in NWS multisensor precipitation estimator algorithms. *Journal of Hydrologic Engineering*, *18*(2), 143-155.
- Hand, W. H., Fox, N. I., & Collier, C. G. (2004). A study of twentieth-century extreme rainfall events in the United Kingdom with implications for forecasting. *Meteorological Applications*, *11*(01), 15-31.
- Harrold, T. W., English, E. J., & Nicholass, C. A. (1974). The accuracy of radar-derived rainfall measurements in hilly terrain. *Quarterly Journal of the Royal Meteorological Society*, *100*(425), 331-350.
- Heinemann, T., Latanzio, A., & Roveda, F. (2002, September). The Eumetsat multi-sensor precipitation estimate (MPE). In *Second International Precipitation Working group (IPWG) Meeting* (pp. 23-27).
- Hildebrand, P. H. (1978). Iterative correction for attenuation of 5 cm radar in rain. *Journal of Applied Meteorology*, *17*(4), 508-514.
- Hong, Y., & Adler, R. F. (2007). Towards an early-warning system for global landslides triggered by rainfall and earthquake. *International journal of remote sensing*, *28*(16), 3713-3719.
- Hong, Y., Adler, R. F., & Huffman, G. (2007). An experimental global prediction system for rainfall-triggered landslides using satellite remote sensing and geospatial datasets. *IEEE Transactions on Geoscience and Remote Sensing*, *45*(6), 1671-1680.
- Hooijer, A., Klijn, F., Pedroli, G. B. M., & Van Os, A. G. (2004). Towards sustainable flood risk management in the Rhine and Meuse river basins: synopsis of the findings of IRMA-SPONGE. *River research and applications*, *20*(3), 343-357.
- Houze Jr, R. A. (1997). Stratiform precipitation in regions of convection: A meteorological paradox?. *Bulletin of the American Meteorological Society*, *78*(10), 2179-2196.

- Huffman, G (2015). Sorting out the Variety of Precipitation Datasets. In *2015 GSA Annual Meeting* Baltimore, Maryland, USA (1-4 November 2015). Paper No: 296-4.
- Ide, K., P. Courtier, M. Ghil, A. Lorenc, Unified notation for data assimilation: operational sequential and variational, *J. Meteorol. Soc. Jpn.*, 75, 181–189, 1997.
- Jajarmizadeh, M., Harun, S., & Salarpour, M. (2012). A review on theoretical consideration and types of models in hydrology. *Journal of Environmental Science and Technology*, 5(5), 249.
- Joss, J., & Waldvogel, A. (1970, November). A method to improve the accuracy of radar measured amounts of precipitation. In *14th Conference on radar meteorology (preprints)* (pp. 237-238).
- Kalman, R. E. (1960). A new approach to linear filtering and prediction problems. *Journal of basic Engineering*, 82(1), 35-45.
- Kim, J., & Yoo, C. (2014). Use of a dual Kalman filter for real-time correction of mean field bias of radar rain rate. *Journal of Hydrology*, 519, 2785-2796.
- Kitchen, M., Brown, R., & Davies, A. G. (1994). Real-time correction of weather radar data for the effects of bright band, range and orographic growth in widespread precipitation. *Quarterly Journal of the Royal Meteorological Society*, 120(519), 1231-1254.
- Koren, V., Schaake, J., Mitchell, K., Duan, Q. Y., Chen, F., & Baker, J. M. (1999). A parameterization of snowpack and frozen ground intended for NCEP weather and climate models. *Journal of Geophysical Research: Atmospheres*, 104(D16), 19569-19585.
- Krajewski, W. F., & Smith, J. A. (1991). On the estimation of climatological Z–R relationships. *Journal of applied meteorology*, 30(10), 1436-1445.

- Kuligowski, B.(2014, March 27). *STAR Satellite Rainfall Estimates Hydro-Estimator - Technique Description*. Retrieved from <http://www.star.nesdis.noaa.gov/smcd/emb/ff/HEtechnique.php> Last accessed 04/20/2017.
- Lau, C. L., Smythe, L. D., Craig, S. B., & Weinstein, P. (2010). Climate change, flooding, urbanisation and leptospirosis: fuelling the fire?. *Transactions of the Royal Society of Tropical Medicine and Hygiene*, 104(10), 631-638.
- Li, L., Ngongondo, C. S., Xu, C. Y., & Gong, L. (2013). Comparison of the global TRMM and WFD precipitation datasets in driving a large-scale hydrological model in Southern Africa. *Hydrology research*, 44(5), 770-788.
- Li, J., Chen, Y., Wang, H., Qin, J., Li, J., & Chiao, S. (2017). Extending flood forecasting lead time in a large watershed by coupling WRF QPF with a distributed hydrological model. *Hydrology and Earth System Sciences*, 21(2), 1279.
- Lighezzolo, A. (2014). Manual descriptivo sobre la implementación experimental del modelo numérico de predicción del tiempo wrf y sus productos. *Manual, CAEARTE-CONAE*, 30.
- Liu, J., Bray, M., & Han, D. (2013). A study on WRF radar data assimilation for hydrological rainfall prediction. *Hydrology and Earth System Sciences*, 17(8), 3095.
- Maidment, D. R. (1992). *Handbook of hydrology*. McGraw-Hill Inc.
- Marshall, J. S., & Palmer, W. M. K. (1948). The distribution of raindrops with size. *Journal of meteorology*, 5(4), 165-166.
- Maynard, R. H. (1945). Radar and weather. *Journal of Meteorology*, 2(4), 214-226.

- Mendoza, P. A., Clark, M. P., Mizukami, N., Gutmann, E. D., Arnold, J. R., Brekke, L. D., & Rajagopalan, B. (2015). How do hydrologic modeling decisions affect the portrayal of climate change impacts?. *Hydrological Processes*.
- Mitchell, K. (2001). The community Noah land-surface model (LSM). *Users Guide Public Release Version 2.7. 1*.
- Moel, H. D., Alphen, J. V., & Aerts, J. C. J. H. (2009). Flood maps in Europe—methods, availability and use. *Natural Hazards and Earth System Sciences*, 9(2), 289-301.
- Moriasi, D. N., Arnold, J. G., Van Liew, M. W., Bingner, R. L., Harmel, R. D., & Veith, T. L. (2007). Model evaluation guidelines for systematic quantification of accuracy in watershed simulations. *Trans. Asabe*, 50(3), 885-900.
- Nash, J. E., & Sutcliffe, J. V. (1970). River flow forecasting through conceptual models part I—A discussion of principles. *Journal of hydrology*, 10(3), 282-290.
- Nasrollahi, N., AghaKouchak, A., Li, J., Gao, X., Hsu, K., & Sorooshian, S. (2012). Assessing the impacts of different WRF precipitation physics in hurricane simulations. *Weather and Forecasting*, 27(4), 1003-1016.
- Negenborn, R. (2003). *Robot localization and Kalman filters* (Doctoral dissertation, Utrecht University).
- Ozcan, E. (2006). Sel olayı ve Türkiye. *Gazi Üniversitesi Gazi Eğitim Fakültesi Dergisi*, 26(1).
- Pereira Fo, A. J., Crawford, K. C., & Hartzell, C. L. (1998). Improving WSR-88D hourly rainfall estimates. *Weather and Forecasting*, 13(4), 1016-1028.
- Petrow, T., Thielen, A. H., Kreibich, H., Merz, B., & Bahlburg, C. H. (2006). Improvements on flood alleviation in Germany: Lessons learned from the Elbe flood in August 2002. *Environmental management*, 38(5), 717-732.

- Piman, T., Babel, M. S., Gupta, A. D., & Weesakul, S. (2007). Development of a window correlation matching method for improved radar rainfall estimation. *Hydrology and Earth System Sciences Discussions*, *11*(4), 1361-1372.
- Pratama, A., Irawan, D. E., Susanto, A., & Ardi, R. D. W. (2016). Influence of Lithology and Slope Gradient to Infiltration of the Mount Malabar, West Java. In *IOP Conference Series: Earth and Environmental Science* (Vol. 29, No. 1, p. 012025). IOP Publishing.
- Rosenfeld, D., Wolff, D. B., & Atlas, D. (1993). General probability-matched relations between radar reflectivity and rain rate. *Journal of applied meteorology*, *32*(1), 50-72.
- Rosenfeld, D., Wolff, D. B., & Amitai, E. (1994). The window probability matching method for rainfall measurements with radar. *Journal of applied meteorology*, *33*(6), 682-693.
- Rosero, E., Yang, Z. L., Gulden, L. E., Niu, G. Y., & Gochis, D. J. (2009). Evaluating enhanced hydrological representations in Noah LSM over transition zones: Implications for model development. *Journal of Hydrometeorology*, *10*(3), 600-622.
- Schaake, J. C., Koren, V. I., Duan, Q. Y., Mitchell, K., & Chen, F. (1996). Simple water balance model for estimating runoff at different spatial and temporal scales. *Journal of Geophysical Research: Atmospheres*, *101*(D3), 7461-7475.
- Scofield, R. A., & Kuligowski, R. J. (2003). Status and outlook of operational satellite precipitation algorithms for extreme-precipitation events. *Weather and Forecasting*, *18*(6), 1037-1051.
- Senatore, A., Mendicino, G., Gochis, D. J., Yu, W., Yates, D. N., & Kunstmann, H. (2015). Fully coupled atmosphere-hydrology simulations for the central Mediterranean: Impact of enhanced hydrological parameterization for short and

- long time scales. *Journal of Advances in Modeling Earth Systems*, 7(4), 1693-1715.
- Sensoy, S. (2004, May). The mountains influence on Turkey climate. In *Balwois Conference on Water Observation and Information System for Decision Support, Ohrid* (pp. 25-29).
- Seo, D. J., Breidenbach, J. P., & Johnson, E. R. (1999). Real-time estimation of mean field bias in radar rainfall data. *Journal of Hydrology*, 223(3), 131-147.
- Seo, Y., & Schmidt, A. R. (2014). Evaluation of drainage networks under moving storms utilizing the equivalent stationary storms. *Natural hazards*, 70(1), 803-819.
- Shrestha, D. L., Robertson, D. E., Wang, Q. J., Pagano, T. C., & Hapuarachchi, H. A. P. (2013). Evaluation of numerical weather prediction model precipitation forecasts for short-term streamflow forecasting purpose. *Hydrology and Earth System Sciences*, 17(5), 1913-1931.
- Silver, M., Karnieli, A., Ginat, H., Meiri, E., & Fredj, E. (2017). An innovative method for determining hydrological calibration parameters for the WRF-Hydro model in arid regions. *Environmental Modelling & Software*, 91, 47-69.
- Skamarock, W. C., Klemp, J. B., & Dudhia, J. (2001). Prototypes for the WRF (Weather Research and Forecasting) model. In *Preprints, Ninth Conf. Mesoscale Processes, J11–J15, Amer. Meteorol. Soc., Fort Lauderdale, FL*.
- Smith, J. A., & Krajewski, W. F. (1991). Estimation of the mean field bias of radar rainfall estimates. *Journal of Applied Meteorology*, 30(4), 397-412.
- Soytekin, A. (2010). *Evaluating the use of satellite-based precipitation estimates for discharge estimation in ungauged basins* (Master Thesis, Middle East Technical University).
- Subramanya, K. (2005). *Engineering Hydrology, 4e*. Tata McGraw-Hill Education.

- Sun, X., Mein, R. G., Keenan, T. D., & Elliott, J. F. (2000). Flood estimation using radar and raingauge data. *Journal of Hydrology*, 239(1), 4-18.
- Te Chow, V. (1959). Open channel hydraulics.
- Tewari, M., Chen, F., Wang, W., Dudhia, J., LeMone, M. A., Mitchell, K., ... & Cuenca, R. H. (2005, January). Numerical experiments with upgraded WRF/NoahLSM model. In *Preprints of the Proceedings 19th Conference on Hydrology, San Diego, CA, Am. Meteorol. Soc.*(<http://ams.confex.com/ams/pdfpapers/87342.pdf>).
- Tewolde, M. H., & Smithers, J. C. (2006). Flood routing in ungauged catchments using Muskingum methods. *Water SA*, 32(3), 379-388.
- Thompson, W. R. (1935). On a criterion for the rejection of observations and the distribution of the ratio of deviation to sample standard deviation. *The Annals of Mathematical Statistics*, 6(4), 214-219.
- Todini, E. (1988). Rainfall-runoff modeling—Past, present and future. *Journal of Hydrology*, 100(1), 341-352.
- Todini, E. (2001). A Bayesian technique for conditioning radar precipitation estimates to rain-gauge measurements. *Hydrology and Earth System Sciences Discussions*, 5(2), 187-199.
- US Army Corps of Engineers. 2000. *Hydrologic Modeling System HEC-HMS: Technical reference manual*. CPD-74B. Hydrologic Engineering Center, Davis, California.
- USDA Soil Conservation Service, 1986. National Engineering Manual. US Government Printing Office, Washington, DC, Hydrology Section 4.
- Van Alphen, J., & Van Beek, E. (2006). From flood defence to flood management—prerequisites for sustainable flood management. *Floods, from defence to management*. Taylor & Francis Group, London, 11-15.

- Verworn, A., & Haberlandt, U. (2011). Spatial interpolation of hourly rainfall—effect of additional information, variogram inference and storm properties. *Hydrology and Earth System Sciences*, 15(2), 569-584.
- Vicente, G. A., Scofield, R. A., & Menzel, W. P. (1998). The operational GOES infrared rainfall estimation technique. *Bulletin of the American Meteorological Society*, 79(9), 1883-1898.
- Vicente, G. A., Davenport, J. C., & Scofield, R. A. (2002). The role of orographic and parallax corrections on real time high resolution satellite rainfall rate distribution. *International Journal of Remote Sensing*, 23(2), 221-230.
- Vieux, B. E., Cui, Z., & Gaur, A. (2004). Evaluation of a physics-based distributed hydrologic model for flood forecasting. *Journal of Hydrology*, 298(1), 155-177.
- Viessman, W., Lewis, G.L., & Knapp, J.W., (1989). Introduction to Hydrology. Harper and Row, New York, p. 780.
- Vieux, B. E., & Bedient, P. B. (1998). Estimation of Rainfall for Flood Prediction from WSR-88D Reflectivity: A Case Study, 17-18 October 1994. *Weather and Forecasting*, 13(2), 407-415.
- Vieux, B. E., Cui, Z., & Gaur, A. (2004). Evaluation of a physics-based distributed hydrologic model for flood forecasting. *Journal of Hydrology*, 298(1), 155-177.
- Wagener, T., Wheater, S. H., & Gupta, V. K. (2004). Rainfall-runoff modelling—a review. *Rainfall-runoff modelling in gauged and ungauged catchments*. Imperial College Press, London, 1-8.
- Welch, G., & Bishop, G. (2006). An introduction to the kalman filter. Department of Computer Science, University of North Carolina.
- World Meteorological Organization (WMO). (1994). Guide to hydrological practices, data acquisition and processing, analysis forecasting and other applications, design and evaluation of hydrological networks. 168, Geneva.

- Wöhling, T., Samaniego, L., & Kumar, R. (2013). Evaluating multiple performance criteria to calibrate the distributed hydrological model of the upper Neckar catchment. *Environmental earth sciences*, 69(2), 453-468.
- Xu, C. Y. (2002). Hydrologic models. *Uppsala University, Department of Earth Sciences and Hydrology*.
- Yilmaz, K. K., Hogue, T. S., Hsu, K. L., Sorooshian, S., Gupta, H. V., & Wagener, T. (2005). Intercomparison of rain gauge, radar, and satellite-based precipitation estimates with emphasis on hydrologic forecasting. *Journal of Hydrometeorology*, 6(4), 497-517.
- Yoo, C., Park, C., Yoon, J., & Kim, J. (2014). Interpretation of mean-field bias correction of radar rain rate using the concept of linear regression. *Hydrological Processes*, 28(19), 5081-5092.
- Yucel, I., Kuligowski, R. J., & Gochis, D. J. (2011). Evaluating the hydro-estimator satellite rainfall algorithm over a mountainous region. *International journal of remote sensing*, 32(22), 7315-7342.
- Yucel, I., & Onen, A. (2014). Evaluating a mesoscale atmosphere model and a satellite-based algorithm in estimating extreme rainfall events in northwestern Turkey. *Natural Hazards and Earth System Sciences*, 14(3), 611-624.
- Yucel, I. (2015). Assessment of a flash flood event using different precipitation datasets. *Natural Hazards*, 79(3), 1889-1911.
- Yucel, I., Onen, A., Yilmaz, K. K., & Gochis, D. J. (2015). Calibration and evaluation of a flood forecasting system: Utility of numerical weather prediction model, data assimilation and satellite-based rainfall. *Journal of Hydrology*, 523, 49-66.
- Yusop, Z., Chan, C. H., & Katimon, A. (2007). Runoff characteristics and application of HEC-HMS for modelling stormflow hydrograph in an oil palm catchment. *Water Science and Technology*, 56(8), 41-48.

Zhu, D., Xuan, Y., & Cluckie, I. (2014). Hydrological appraisal of operational weather radar rainfall estimates in the context of different modelling structures. *Hydrology and Earth System Sciences*, 18(1), 257-272.

APPENDICES

Appendix A: CDF Curves

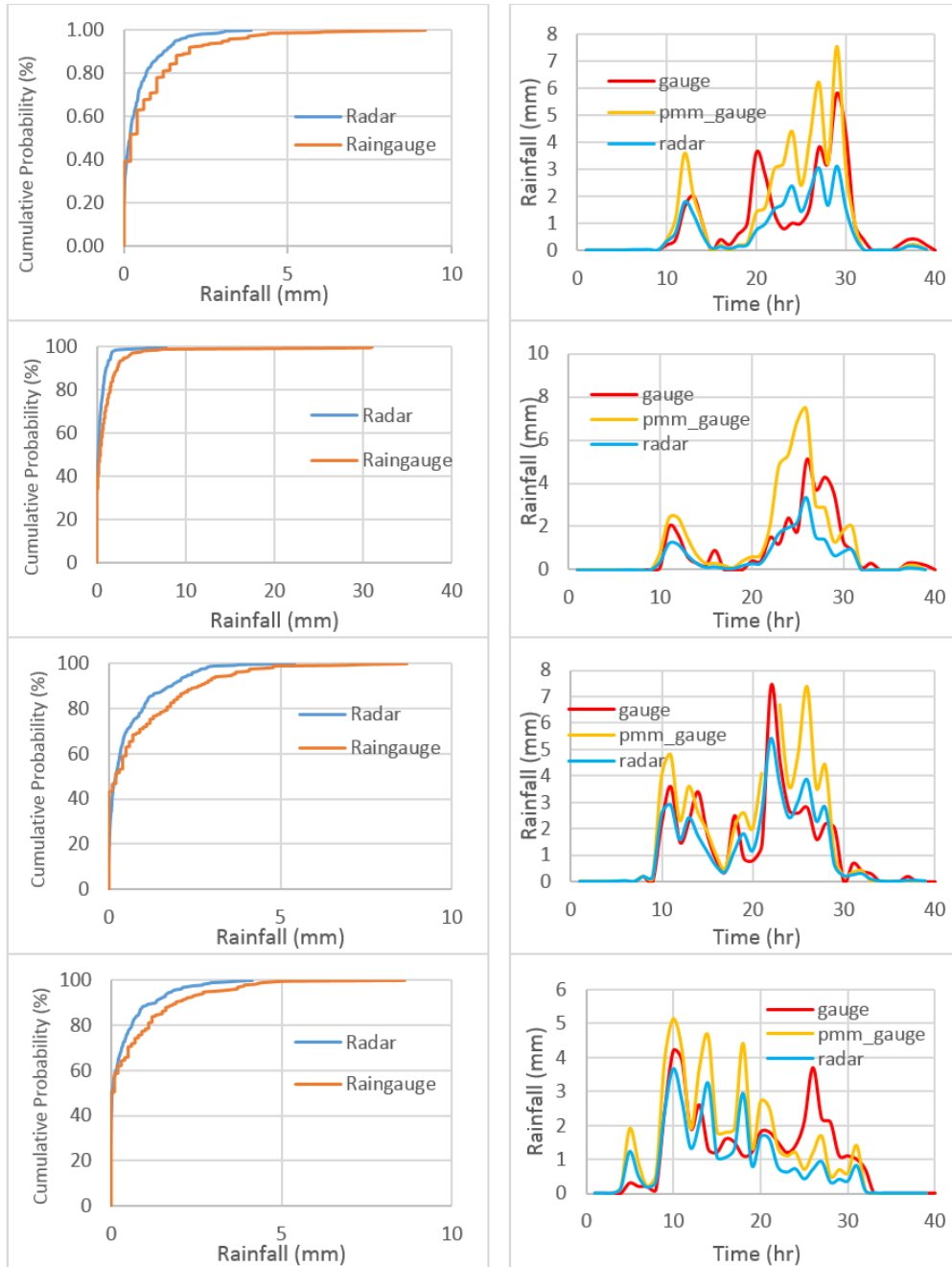


Figure A. 1 Columns (1) and (2) show CDF Curve of Stations and Rainfall Distribution with three Datasets for 2014 Flood Event Day respectively; Rows (1), (2), (3) and (4) show stations: Bafra, Ondokuz M., Karadeniz A. and Havza respectively.

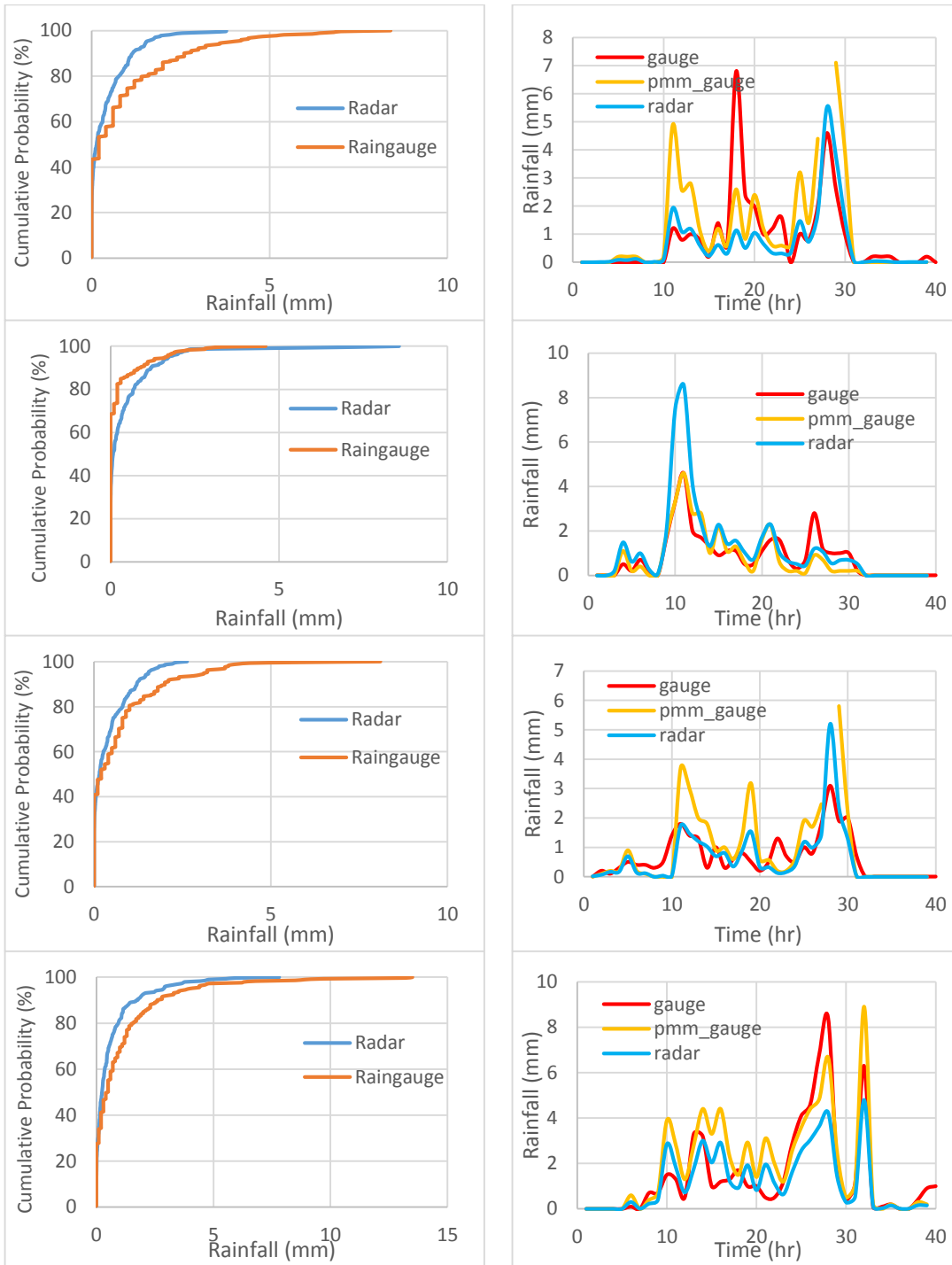


Figure A.2 Columns (1) and (2) show CDF Curve of Stations and Rainfall Distribution with three Datasets for 2014 Flood Event Day respectively; Rows (1), (2), (3) and (4) show stations: Alaçam, Vezirköprü, Yakakent and Çarşamba respectively.

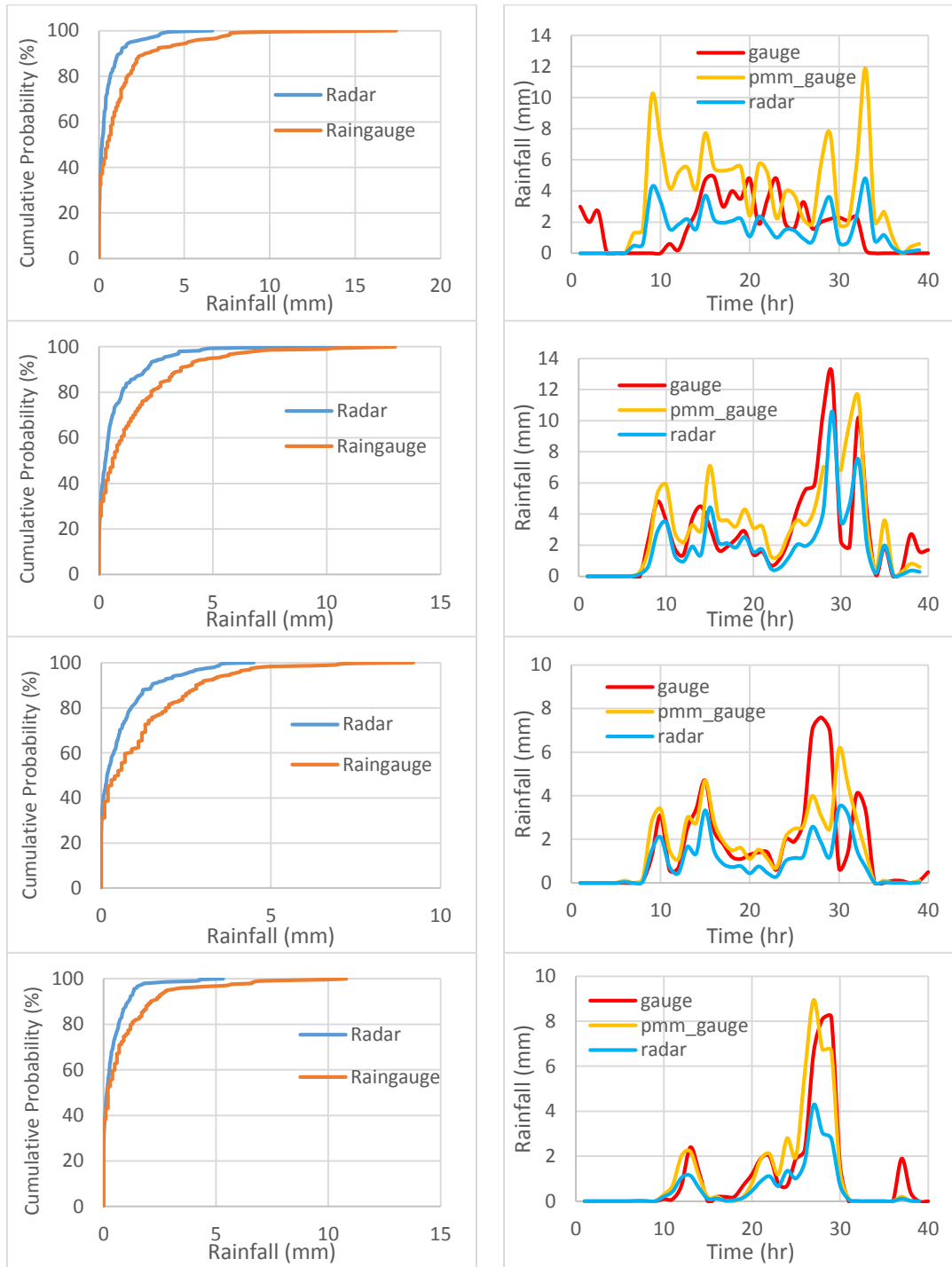


Figure A.3 Columns (1) and (2) show CDF Curve of Stations and Rainfall Distribution with three Datasets for 2014 Flood Event Day respectively; Rows (1), (2), (3) and (4) show stations: Ayvacık, Salıpazarı, Kozluk Beldesi and Topraksu Araş. respectively.

Appendix B: Statistical Measures for Stations

Table B.1 Statistical Measures for the flood observed on 22nd November 2014

Stations	BIAS (1 hr)			RMSE (mm)			r			Cum. Rainfall (mm)			
	Radar	WRF	HE	Radar	WRF	HE	Radar	WRF	HE	Gauge	Radar	WRF	HE
Vezirköprü	0.36	-0.05	0.6	1.09	0.81	1.92	0.87	0.63	-0.04	33.5	48	31.4	56.1
Yakakent	-0.04	-0.33	-0.58	0.55	0.82	0.96	0.81	0.18	0.06	26.6	25	13.6	4.2
Alaçam	-0.2	-0.54	-0.84	1.06	1.53	1.56	0.66	-0.02	0.53	33.8	25.7	12.3	1.5
Havza	-0.27	-0.61	-0.01	0.88	1.4	1.53	0.58	0.25	0.29	45.4	34.5	21.2	45
Topraksu	-0.53	-0.52	-1.14	1.35	2.33	2.35	0.9	-0.18	-	43.5	22.1	22.7	0
Bafra	-0.32	-0.42	-1.03	0.95	1.66	1.75	0.74	-0.1	-	39.4	26.6	22.8	0
Kavak	0.43	-0.34	-0.12	0.84	1.1	1.41	0.88	0.14	0.12	37.6	55	23.9	32.7
Ondokuz M.	-0.31	-0.37	-0.83	0.83	1.5	1.55	0.83	-0.08	0.02	33.4	20.9	18.8	1.8
Karadeniz	-0.09	-0.78	-0.76	0.67	1.59	1.88	0.9	0.57	0.03	49.2	45.5	17.9	20.1
Ayvacak	-0.27	-0.38	-1.07	1.88	1.9	1.87	0.34	0.25	0.36	67.4	56.4	52	26.4
Çarşamba	-0.31	-0.34	-1.13	1.14	1.33	2.28	0.85	0.77	0.24	59.8	47.4	46.3	16.8
Salıpazarı	-0.86	0.01	-2.25	1.81	2.86	3.51	0.83	0.65	0.45	107.7	73.5	108.1	21.9
Kozluk Bel.	-0.78	-0.29	-0.97	1.79	2.66	2.24	0.55	0.27	0.21	66	34.9	54.5	29.1

Table B.2 Statistical Measures the flood observed on 2nd August 2015

Stations	BIAS (1 hr)			RMSE (mm)			r			Cum. Rainfall (mm)			
	Radar	WRF	HE	Radar	WRF	HE	Radar	WRF	HE	Gauge	Radar	WRF	HE
	0.02	0.49	0	0.06	1.33	0	-	-	-	-	0	1.2	35.1
-0.01	0.84	-0.02	0.22	2.21	0.22	-0.01	-0.06	-0.02	-0.02	2.2	1.6	62.8	0.6
0.01	0.91	0	0.03	2.29	0	-	-	-	-	0	0.7	65.2	0
0.01	0	0	0.04	0	0	-	-	-	-	0	0.8	0.1	0
0.04	1.09	-0.01	0.27	2.67	0.09	0.85	0.23	-0.03	-0.03	1.2	4	79.6	0.3
0.01	0.93	0.02	0.02	2.32	0.11	-	-	-	-	0	0.7	66.8	1.5
0.02	0.33	0	0.07	1.03	0.03	0.52	-0.04	-	-	0.3	1.6	24.2	0
0.02	1.06	0.04	0.06	2.48	0.25	0.51	0.07	0.93	0.2	1.3	76.7	3	3
-0.25	0.06	-0.43	1.74	3.18	2.69	0.99	-0.04	-	-	30.9	13	34.9	0
0	1.09	-0.05	0.13	2.61	0.22	0.81	0.08	-	-	3.4	3.4	81.6	0
-0.52	0.45	-0.64	3.45	4.66	3.84	0.78	-0.06	-	-	45.8	8.4	78.5	0
-	-	-	-	-	-	-	-	-	-	-	56.4	145.7	0.6
-1.08	-0.73	-1.48	5.84	7.95	7.93	0.96	0.07	0.19	0.19	109.3	31.7	57	2.4

Table B.3 Statistical Measures for the flood observed on 28th May 2016

Stations	BIAS (1 hr)			RMSE (mm)			r			Cum. Rainfall (mm)			
	Radar	WRF	HE	Radar	WRF	HE	Radar	WRF	HE	Radar	Gauge	HE	
Vezirköprü	-0.35	-0.34	-0.4	0.76	1.08	1.11	0.88	0.13	0.14	0.14	42.7	17.8	18.2
Yakakent	-0.63	-0.86	-0.79	1.7	2.33	2.14	0.88	0.34	0.53	0.53	76.7	31.6	14.9
Alaçam	-0.47	-0.75	-0.73	1.3	2.06	2.1	0.93	0.39	0.27	0.27	68.8	34.8	14.6
Havza	-0.21	-0.2	-0.26	1.13	0.74	1.18	0.4	0.68	0.1	0.1	37.3	22.4	22.6
Topraksu	-0.78	-0.9	-0.85	1.76	2.25	2.39	0.8	0.23	0.27	0.27	87.1	30.6	22.6
Bafra	-0.6	-0.75	-0.75	1.69	2.65	2.81	0.94	0.07	0.09	0.09	77.8	34.9	23.5
Kavak	-0.2	-0.11	-0.09	0.58	1.02	1.13	0.85	0.05	0.14	0.14	35.1	20.7	27.2
Ondokuz M.	-0.4	-0.14	-0.39	1.37	1.65	1.5	0.42	-0.01	0.17	0.17	44.1	15.2	33.8
Karadeniz	-0.78	-0.73	-0.37	1.92	2.73	2.63	0.85	-0.14	0.15	0.15	90.4	34.5	38.2
Ayvacık	-0.48	0.23	-0.23	1.64	2.79	2.09	0.54	0.04	0.08	0.08	65.8	31.5	82.2
Çarşamba	-1.87	-1.78	-2.15	6.8	7.74	7.63	0.63	-0.1	-0.01	-0.01	189.7	55.1	61.6
Salıpazarı	-0.72	0.19	-0.27	2.03	3.42	3.01	0.61	0.01	0.1	0.1	95.2	43.7	108.7
Kozluk Bel.	-1.62	-1.08	-1.96	5.27	6.77	5.74	0.55	-0.08	0.3	0.3	173.1	56.1	95.2

Appendix C: Rainfall Distributions for Sub-basins

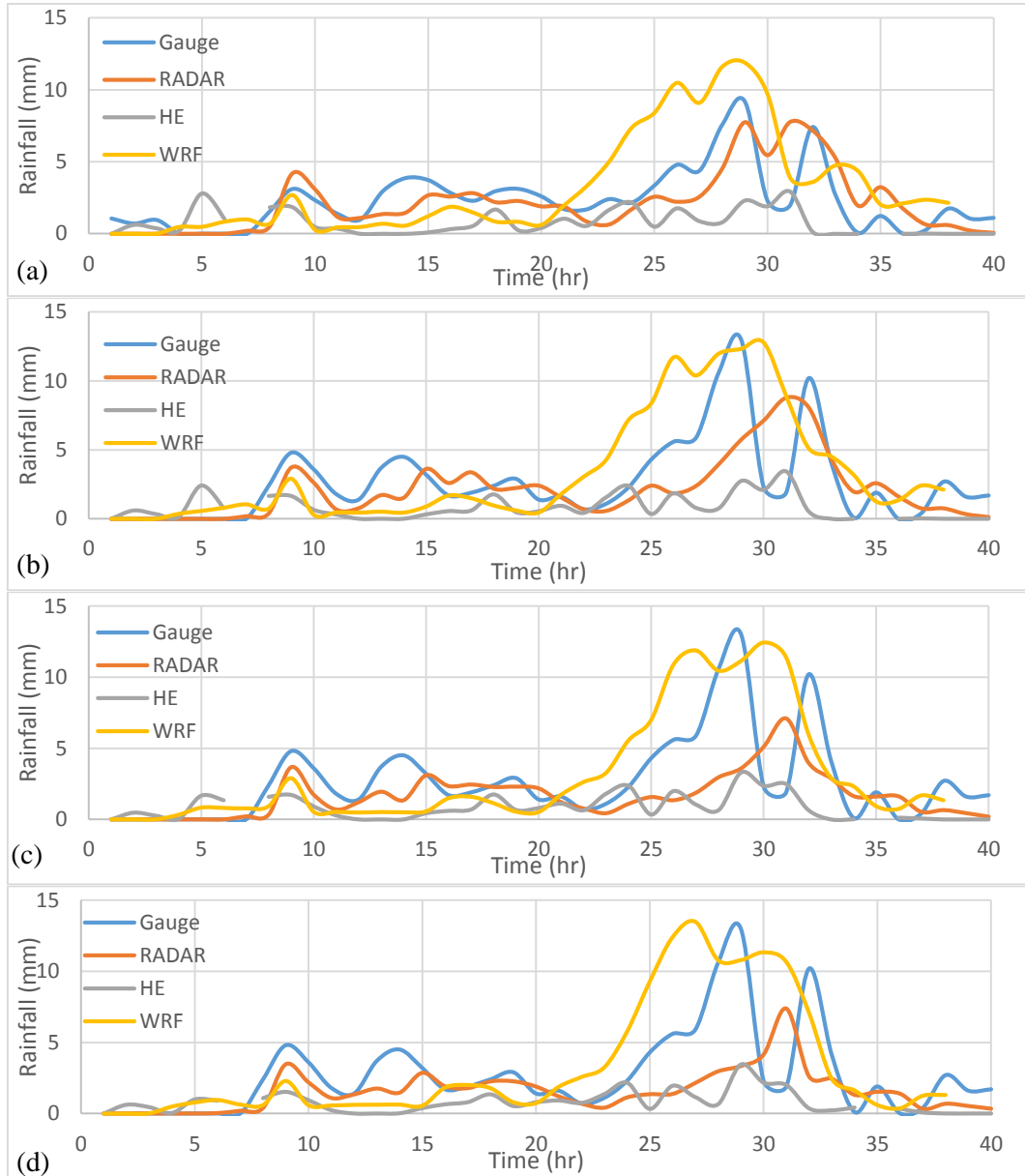


Figure C.1 2014 Flood Event Rainfall Distribution with Time for Four Sub-basins (Sub-basin 1 (a), Sub-basin 2 (b), Sub-basin 3 (c) and Sub-basin 4 (d))

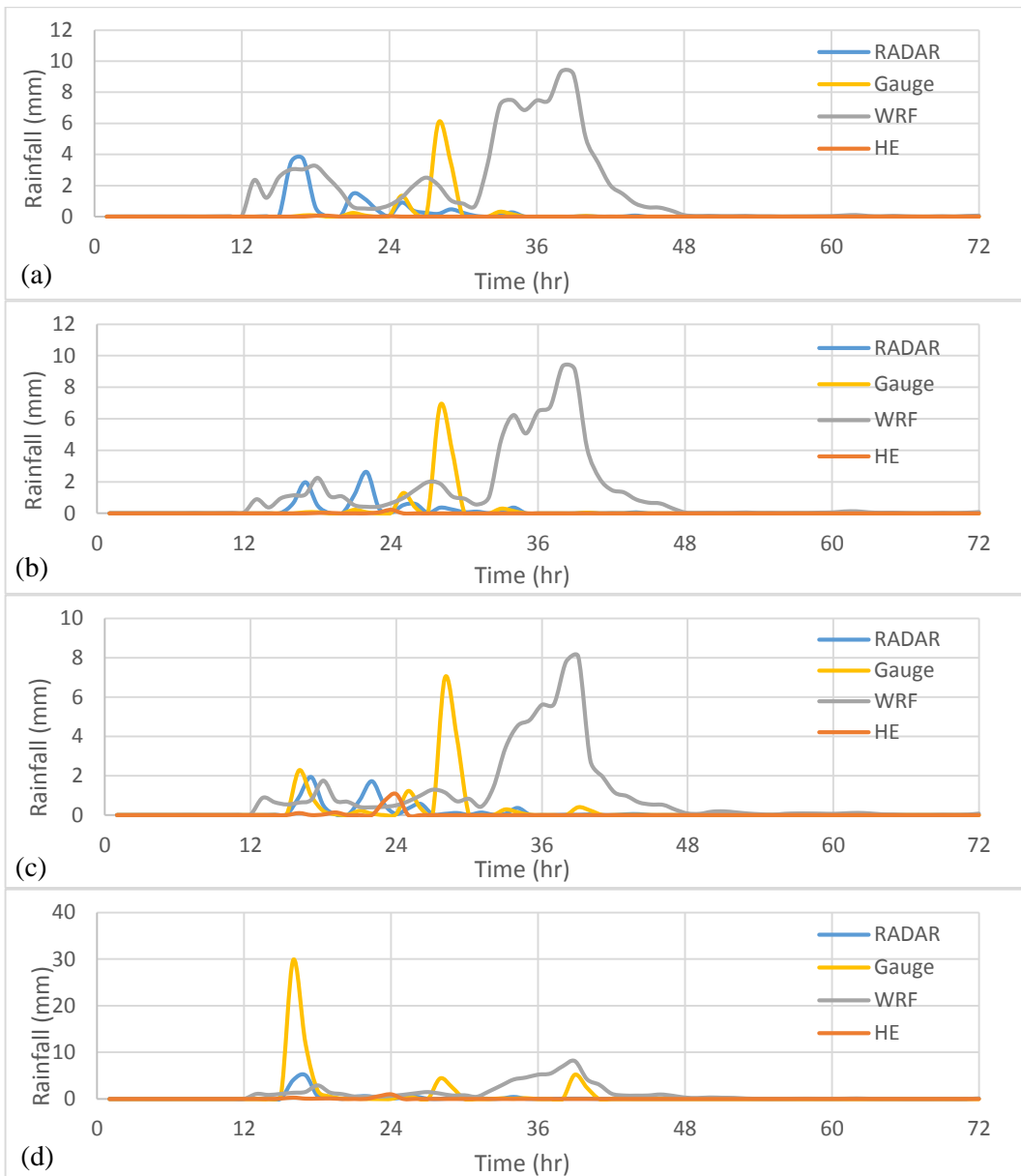


Figure C.2 2015 Flood Event Rainfall Distribution with Time for Four Sub-basins (Sub-basin 1 (a), Sub-basin 2 (b), Sub-basin 3 (c) and Sub-basin 4 (d))

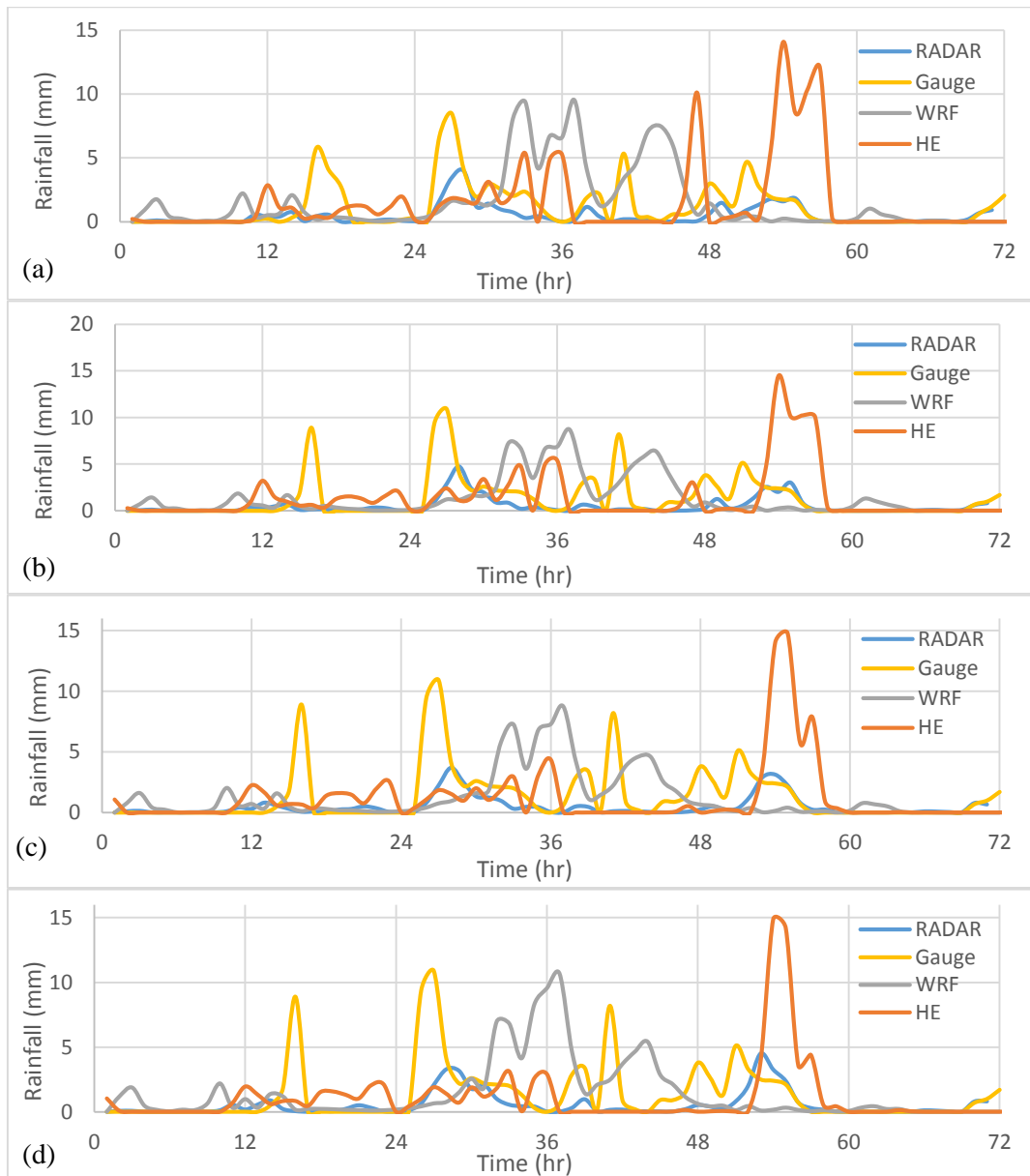


Figure C.3 2016 Flood Event Rainfall Distribution with Time for Four Sub-basins (Sub-basin 1 (a), Sub-basin 2 (b), Sub-basin 3 (c) and Sub-basin 4 (d))

Appendix D: KF Application Results for Stations

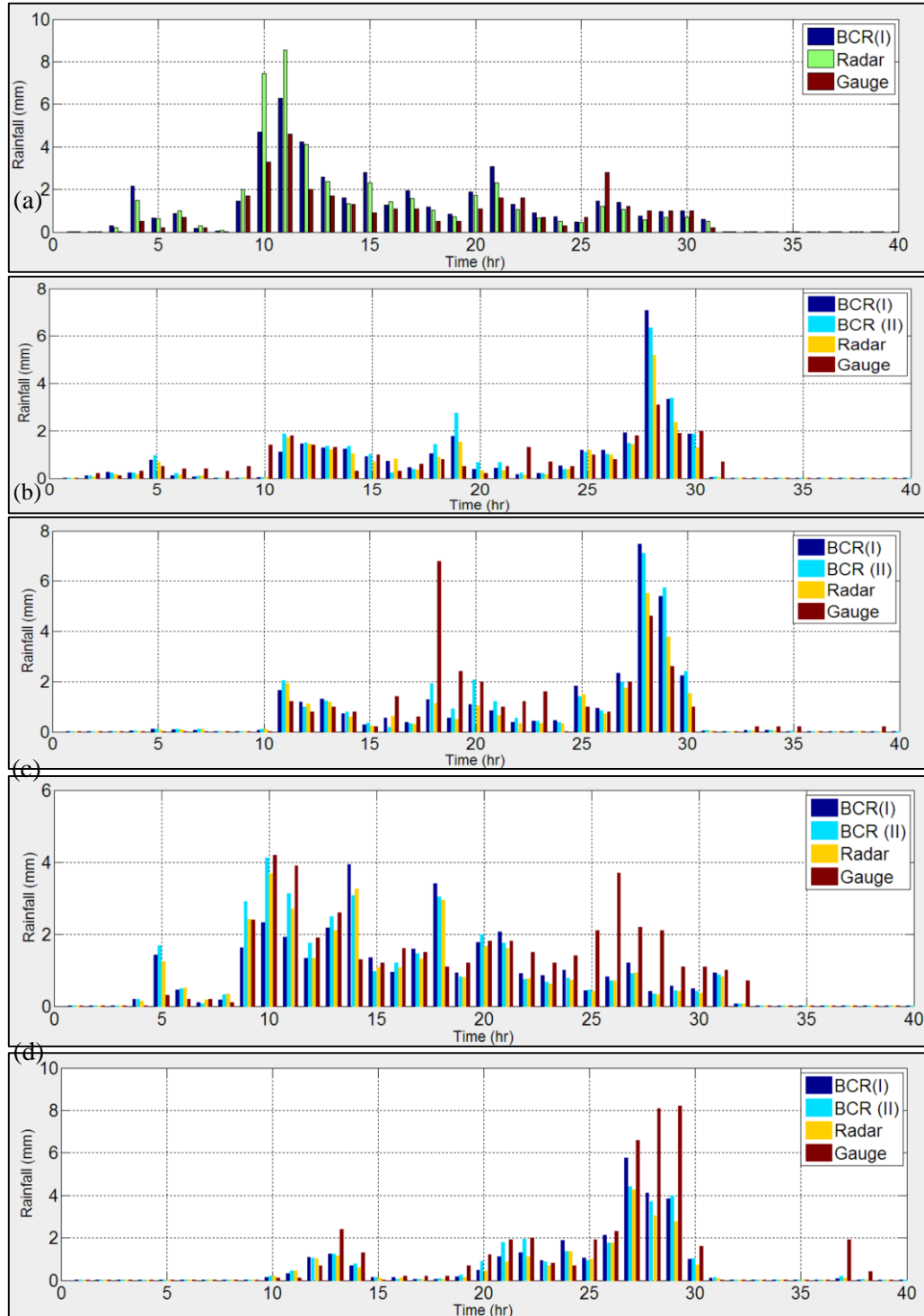


Figure D.1 KF Application Results in 2014 Flood Event for Stations: Vezirköprü (a), Yakakent (b), Alaçam (c), Havza (d) and Topraksu Araştırma (e)

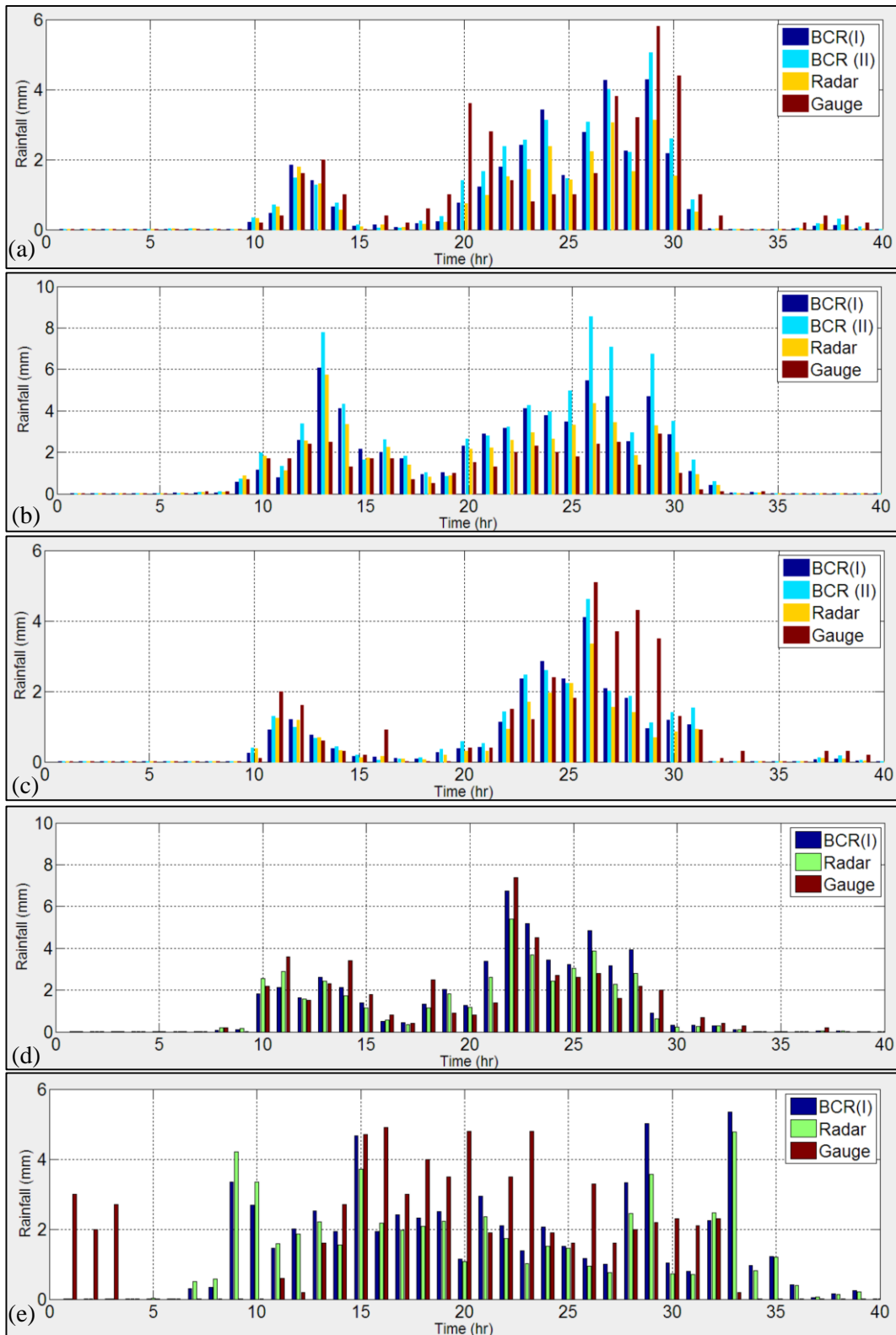


Figure D.2 KF Application Results in 2014 Flood Event for Stations: Bafra (a), Kavak (b), Ondokuz Mayıs (c), Karadeniz Araştırma (d) and Ayvacık (e)

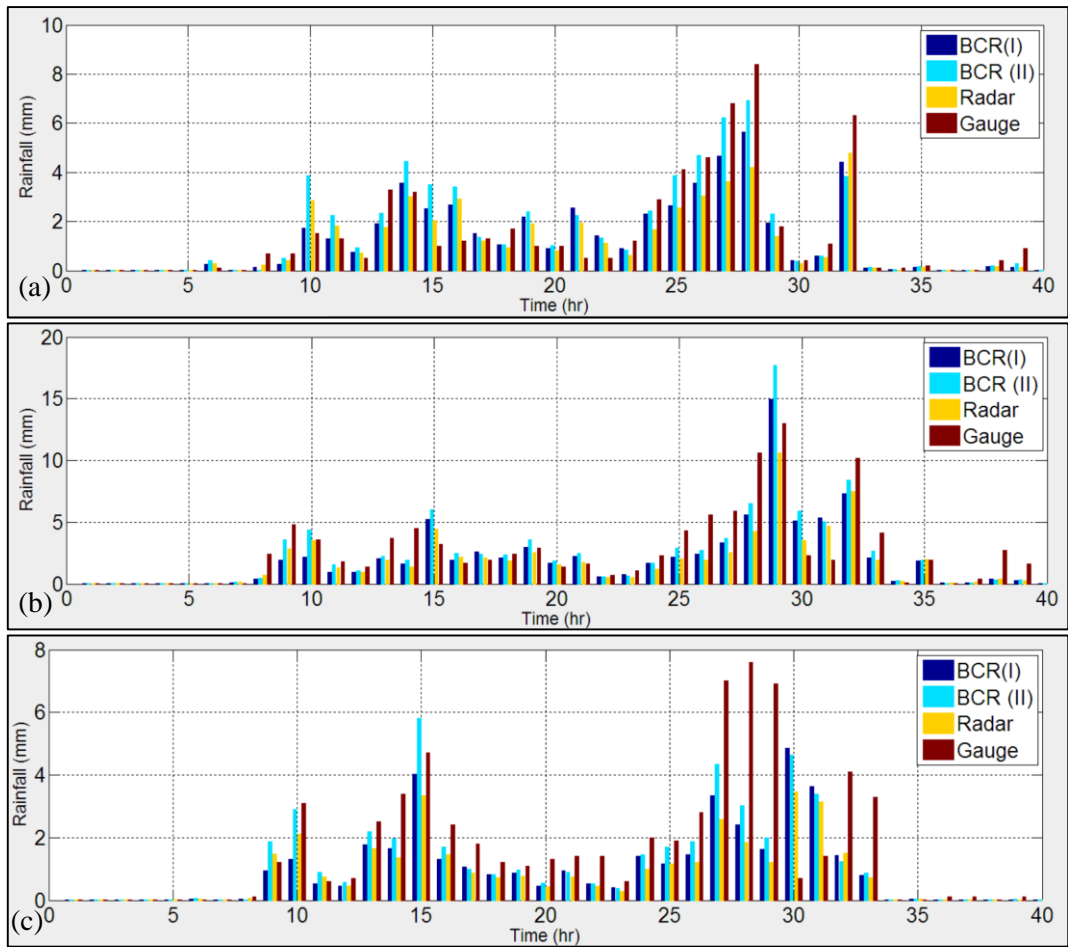


Figure D.3 KF Application Results in 2014 Flood Event for Stations: Çarşamba (a), Salıpazarı (b) and Kozluk (c)

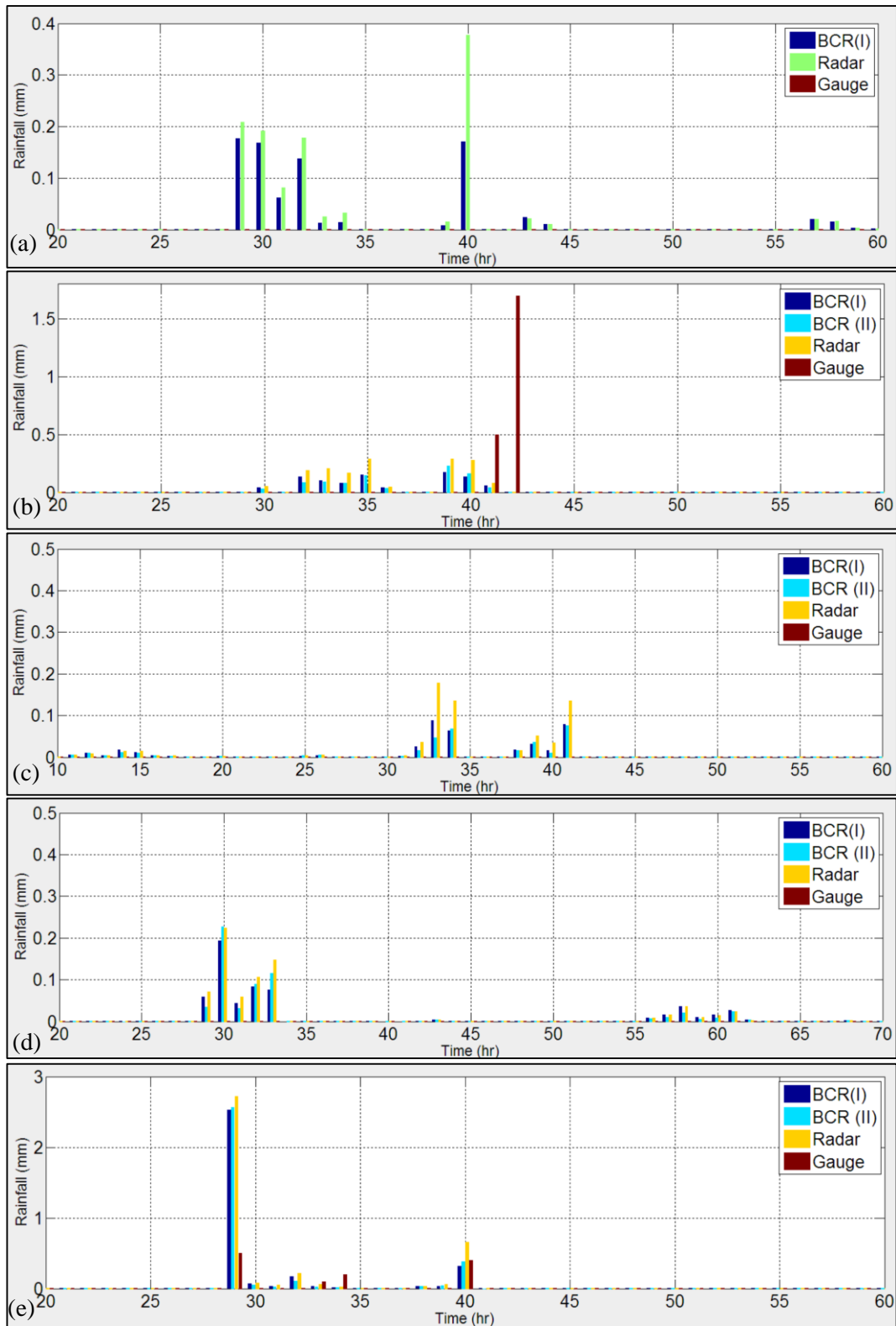


Figure D.4 KF Application Results in 2015 Flood Event for Stations: Vezirköprü (a), Yakakent (b), Alaçam (c), Havza (d) and Topraksu Araştırma (e)

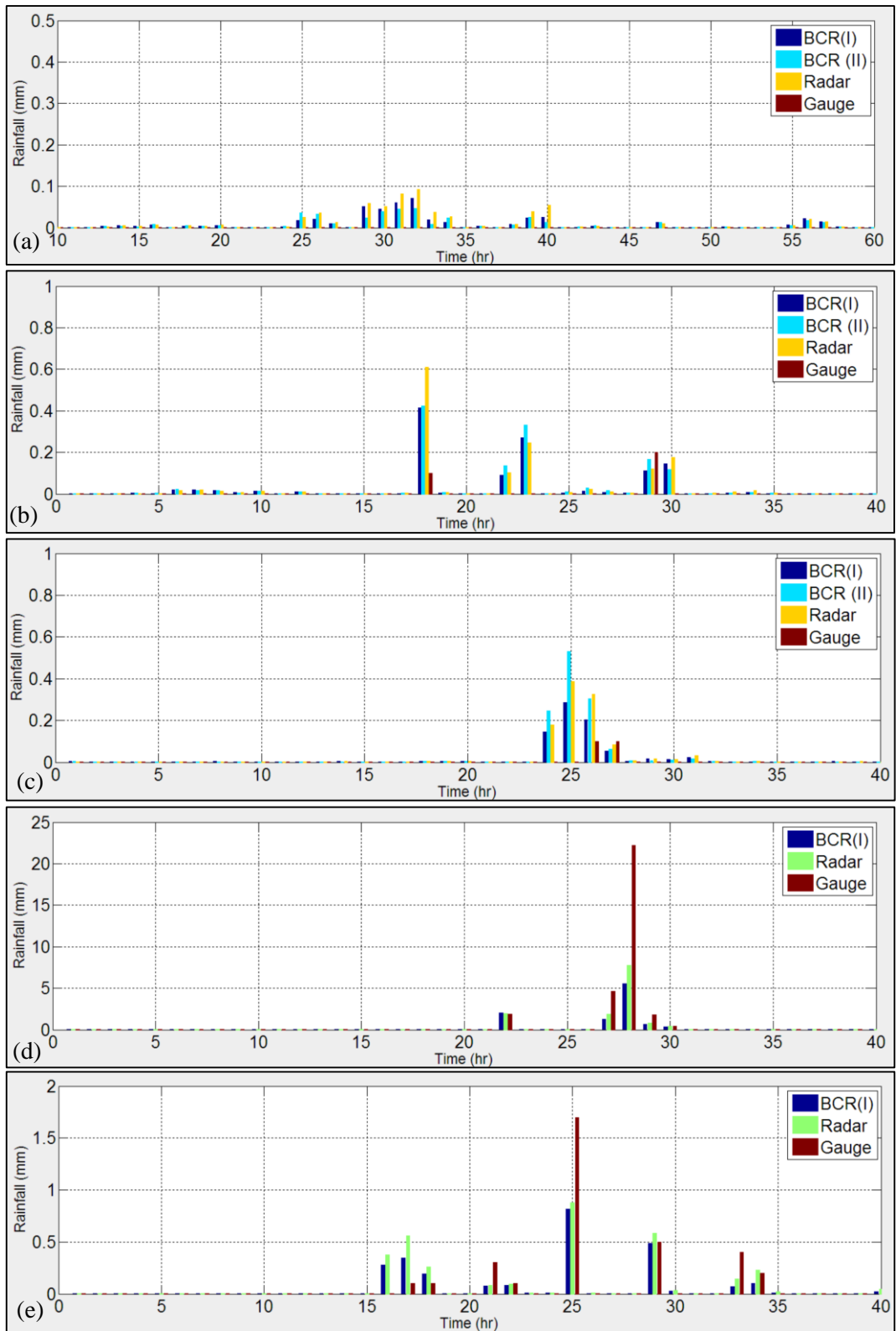


Figure D.5 KF Application Results in 2015 Flood Event for Stations: Bafra (a), Kavak (b), Ondokuz Mayıs (c), Karadeniz Araştırma (d) and Ayvacık (e)

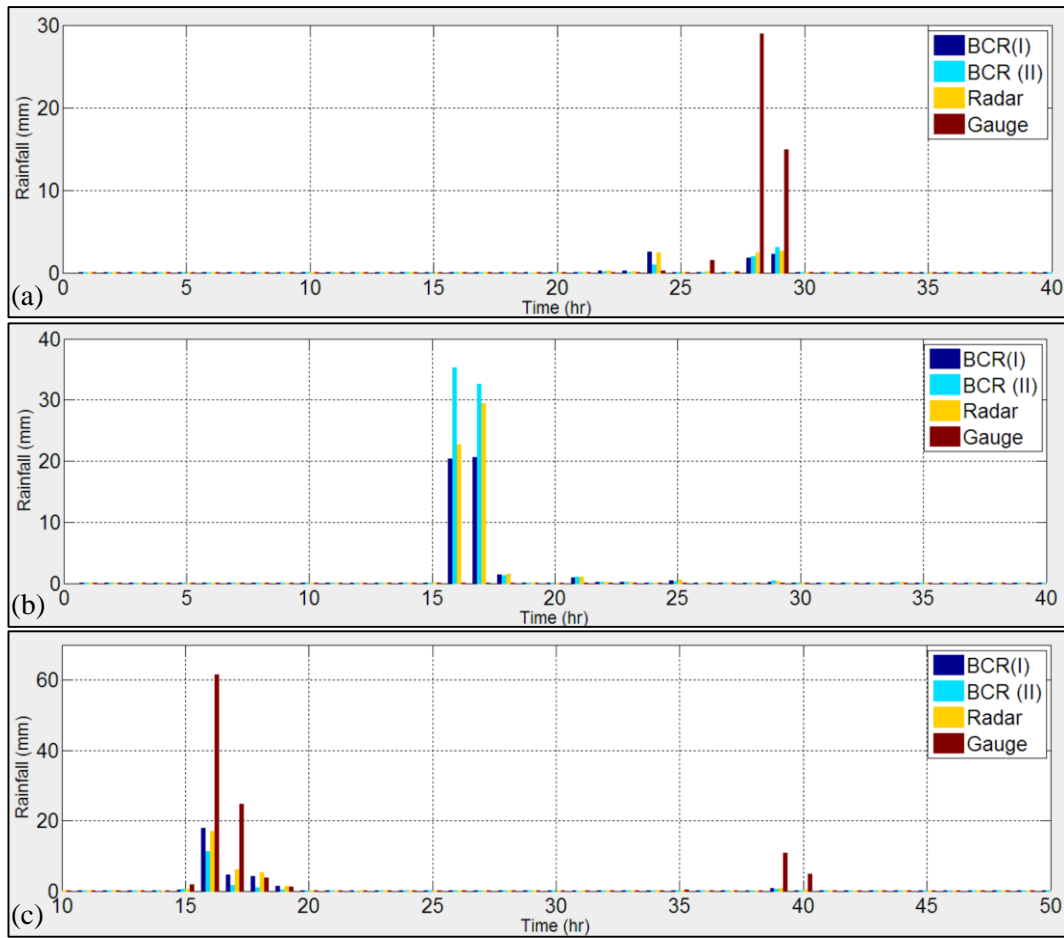


Figure D.6 KF Application Results in 2015 Flood Event for Stations: Çarşamba (a), Salıpazarı (b) and Kozluk (c)

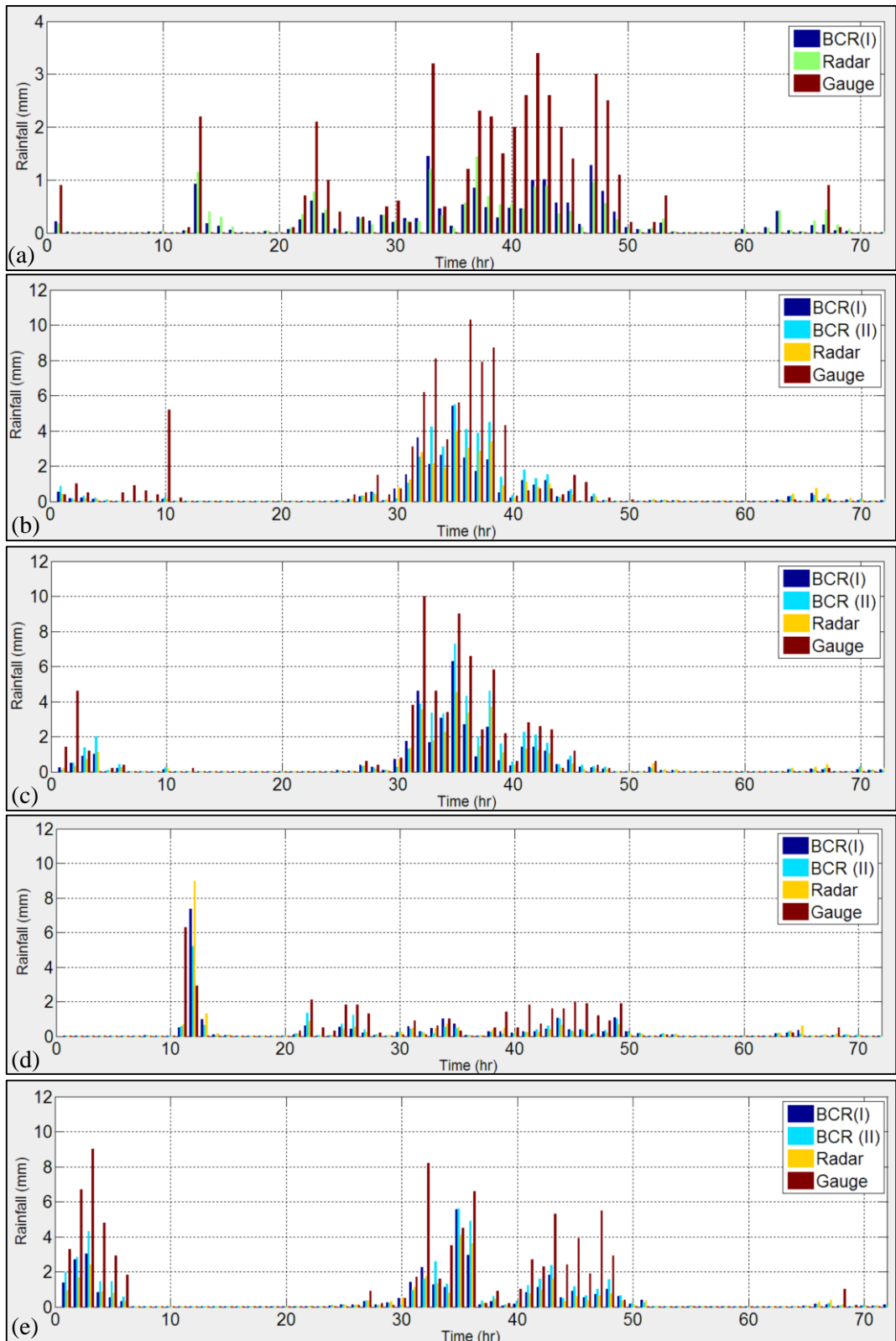


Figure D.7 KF Application Results in 2016 Flood Event for Stations: Vezirköprü (a), Yakakent (b), Alaçam (c), Havza (d) and Topraksu Araştırma (e)

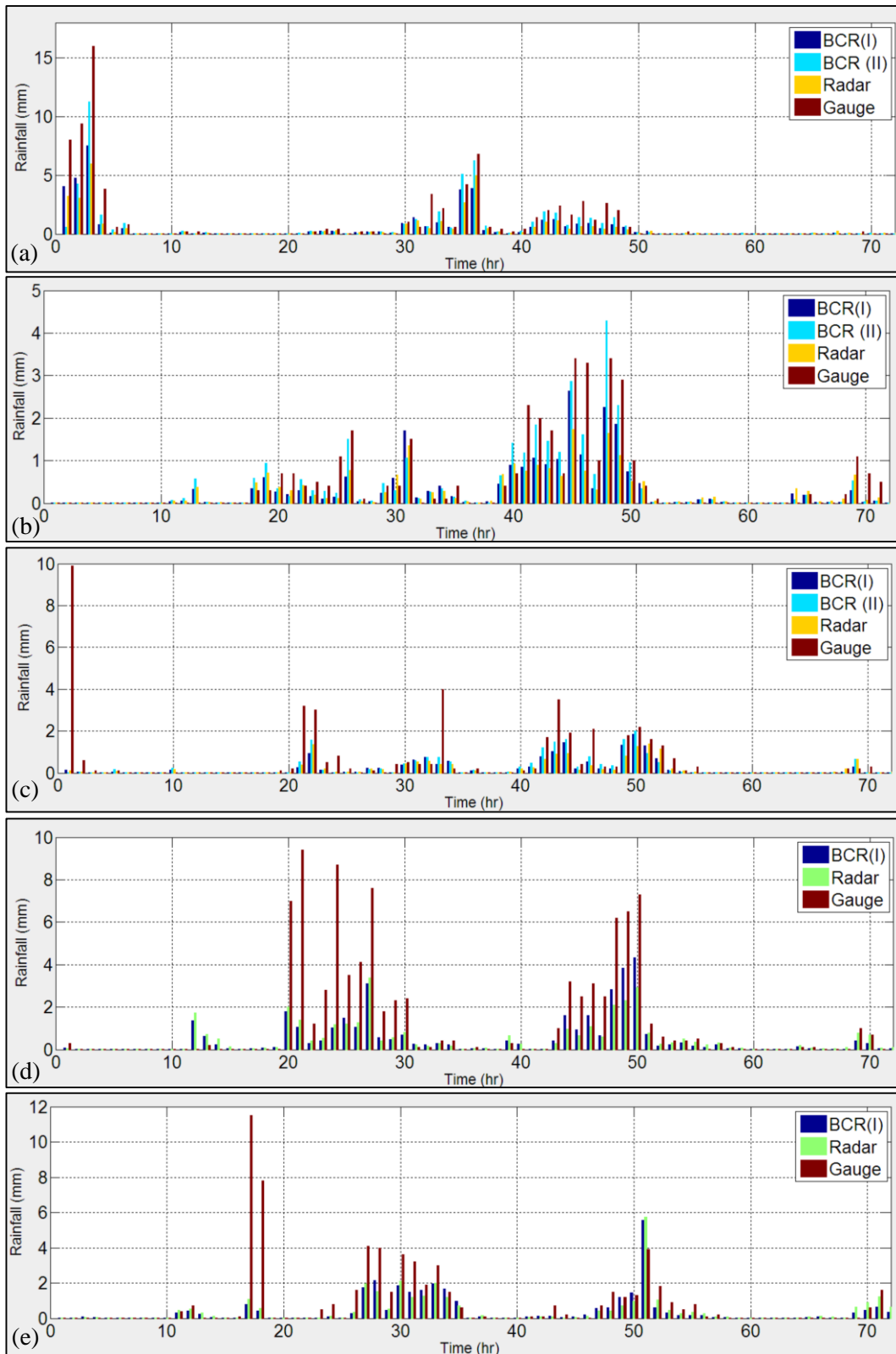


Figure D.8 KF Application Results in 2016 Flood Event for Stations: Bafra (a), Kavak (b), Ondokuz Mayıs (c), Karadeniz Araştırma (d) and Ayvacık (e)

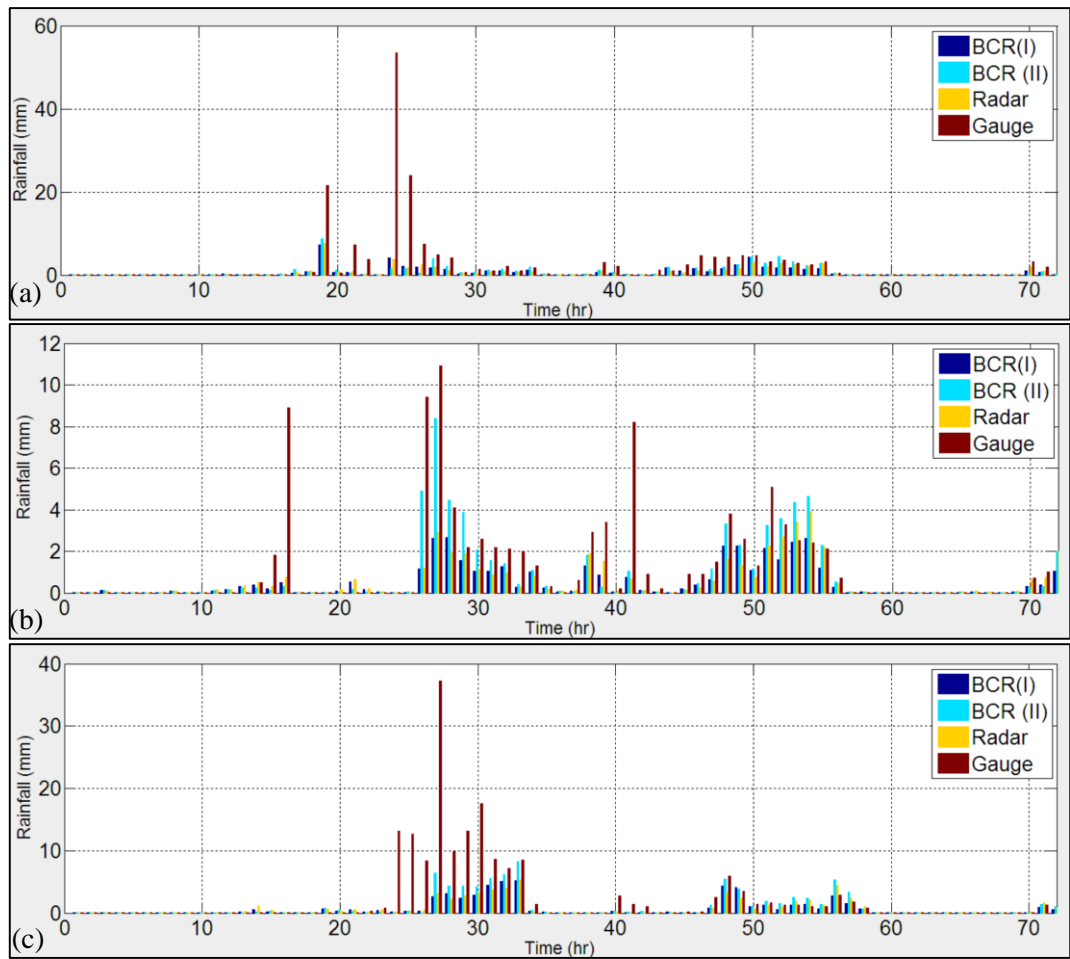


Figure D.9 KF Application Results in 2016 Flood Event for Stations: Çarşamba (a), Salıpazarı (b) and Kozluk (c)

Appendix E: Soil Categories and Vegetation Type Tables

Table E.1 Soil Categories and Textures

Class No.	Soil texture class	% Sand	% Silt	% Clay	Quartz Content (Peters-Lidard et al, 1998, JAS)	Estimated Quartz content (F. Chen subjective method)
1	Sand	92	5	3	0.92	
2	Loamy Sand	82	12	6	0.82	
3	Sandy Loam	58	32	10	0.6	
4	Silt Loam	17	70	13	0.25	
5	Silt	10	85	5	0.1	
6	Loam	43	39	18	0.4	
7	Sandy Clay Loam	58	15	27	0.6	
8	Silty Clay Loam	10	56	34	0.1	
9	Clay Loam	32	34	34	0.35	
10	Sandy Clay	52	6	42	0.52	
11	Silty Clay	6	47	47	0.1	
12	Clay	22	20	58	0.25	
13	Organic Material	0	0	0		0.05 (mostly peat, muck, mineral soils are not dominant)
14	Water	0	0	0		
15	Bedrock	0	0	0		
16	Other	0	0	0		
17*	Playa					0.60 (as sandy loam)
18*	Lava					
19*	White sand					0.92 (as sand)

*Note: *: Not originally in STATSGO data base*

Table E.2 Vegetation Type (Class), LAI and Albedo Parameters with Explanations

class	LAI MIN	LAI MAX	ALBEDO MIN	ALBEDO MAX	Explanation
1	5	6.4	0.12	0.12	Evergreen Needleleaf Forest
2	3.08	6.48	0.12	0.12	Evergreen Broadleaf Forest
3	1	5.16	0.14	0.15	Deciduous Needleleaf Forest
4	1.85	3.31	0.16	0.17	Deciduous Broadleaf Forest
5	2.8	5.5	0.17	0.25	Mixed Forests
6	0.5	3.66	0.25	0.3	Closed Shrublands
7	0.6	2.6	0.22	0.3	Open Shrublands
8	0.5	3.66	0.25	0.3	Woody Savannas
9	0.5	3.66	0.2	0.2	Savannas
10	0.52	2.9	0.19	0.23	Grasslands
11	1.75	5.72	0.14	0.14	Permanent wetlands
12	1.56	5.68	0.17	0.23	Croplands
13	1	1	0.15	0.15	Urban and Built-Up
14	2.29	4.29	0.18	0.23	cropland/natural vegetation mosaic
15	0.01	0.01	0.55	0.7	Snow and Ice
16	0.1	0.75	0.38	0.38	Barren or Sparsely Vegetated
17	0.01	0.01	0.08	0.08	Water
18	0.41	3.35	0.15	0.2	Wooded Tundra
19	0.41	3.35	0.15	0.2	Mixed Tundra
20	0.41	3.35	0.25	0.25	Barren Tundra

source: modified MODIS NOAH

VITA

PERSONAL INFORMATION

Surname, Name: Özkaya, Arzu
Nationality: Turkish (TC)
Date and Place of Birth: 1985, Ankara
Marital Status: Married

EDUCATION

Degree	Institution	Year
PHD	METU Civil Engineering	2012-2017
MS	METU Civil Engineering	2008-2010
BS (Major)	METU Civil Engineering	2004-2008
BS (Minor)	METU GIS/RS	2005-2008

WORK EXPERIENCE

Year	Place	Enrollment
2012-2014	METU Department of Civil Eng.	Project Assistant
2010-2012	Su-Yapı Engineering & Consulting Inc.	Design Engineer
2007 August	Inta-Spaceturk	Intern
2006 August	Akkan Construction	Intern

ACHIEVEMENTS

TUBITAK (BIDEB-2211A) Ph.D. Scholarship: 2013-2016
TUBITAK Summer School Grant, Gabriel Lippmann Hydrocourse Summer School, Luxembourg: 2014, May
ERE Group, Master Research Scholarship (Hydropower Engineering): 2008-2010
METU, Dean's List High Honor Student 2006-2007 Fall, 2007-2008 Spring
METU, Dean's List Honor Student: 2005-2006 Fall, 2005-2006 Spring, 2007-2008 Fall

FOREIGN LANGUAGES

Advanced English, Basic French

PUBLICATIONS

Refereed Papers in Journals

1. **Özkaya, A.**, Akyürek, Z., (2017) Evaluating the Use of Bias Corrected Radar Rainfall Data in Flood Simulation, Hydrological Sciences Journal (submitted).
2. **Özkaya, A.**, Akyürek, Z., Yucel, İ. and Yilmaz K., (2017) Assessment of Different Rainfall Products in Flood Simulations using WRF-Hydro Modeling, (in preparation)

Papers in Conference Proceedings

1. Akyurek, Z., **Özkaya, A.** (2016, December). Evaluating the use of different precipitation datasets in simulating a flood event. In AGU Conference Abstracts.
2. **Özkaya, A.**, Akyürek, Z., (2016, October). Evaluating the use of radar precipitation data in simulating a flood event in Terme, Samsun-Turkey. In 9th Europ. Conf. on Radar in Meteorology and Hydrology, Antalya-Turkey (pp. 1-8).
3. Akyurek, Z., **Özkaya, A.** (2016, April). Evaluating the use of different precipitation datasets in flood modelling. In EGU General Assembly Conference Abstracts (Vol. 18, p. 6125).

Papers in Conference Proceedings (National)

1. **Özkaya, A.**, Akyürek, Z., (2016, November). Farklı Yağış Veri Setlerinin Taşkın Modellemesindeki Kullanımının Değerlendirilmesi. IV. Ulusal Taşkın Sempozyumu, Rize, Türkiye
2. **Özkaya, A.**, Bolat, K., Demir, G., Akyürek, Z., (2015, October) Meteoroloji RADAR yağış verisinin Hidrolojik modellemede kullanımı açısından değerlendirilmesi. UZALMET 2015.
3. **Soytekin A.**, Z. Akyürek (2010, September) Çoruh Havzası ve Çevresinde Yer ve Uydu Tabanlı Yağış Verilerinin Zamansal ve Mekânsal Olarak Karşılaştırılması. VI. Ulusal Hidroloji Kongresi, Denizli, Türkiye.

Technical Reports

1. Akyurek, Z., **Özkaya, A.**, (2014, September). Kızılırmak Havzasında Akım Ölçümü Yapılmayan Akarsu Kollarında Coğrafi Bilgi Sistemleri Tabanlı Akım Tahmin Modellerinin Geliştirilmesi ve Ön Havza Yönetim Planının Oluşturulması. TUJBB-TUMEHAB 01-11 Result Report, 58 pp.
2. Akyurek, Z., **Özkaya, A.**, Sürer, S., Bozoğlu, B. (2013, July). Kızılırmak Havzasında Akım Ölçümü Yapılmayan Akarsu Kollarında Coğrafi Bilgi Sistemleri Tabanlı Akım Tahmin Modellerinin Geliştirilmesi ve Ön Havza Yönetim Planının Oluşturulması. TUJBB-TUMEHAB 01-11 Progressing Report (2), 49 pp.

HOBBIES

Quilling, embroidery